

# An Integrated Quantum Dot Barcode Smartphone Optical Device for Wireless Multiplexed Diagnosis of Infected Patients

by

Kevin Ming

A thesis submitted in conformity with the requirements  
for the degree of Doctor of Philosophy

Institute of Biomaterials & Biomedical Engineering  
University of Toronto

© Copyright by Kevin Ming 2015

# An Integrated Quantum Dot Barcode Smartphone Optical Device for Wireless Multiplexed Diagnosis of Infected Patients

Kevin Ming

Doctor of Philosophy

Institute of Biomaterials & Biomedical Engineering  
University of Toronto

2015

## Abstract

Integrating mobile-cellular devices with multiplex molecular diagnostics can potentially provide the most powerful platform for tracking, managing and preventing the transmission of infectious diseases. With over 6.9 billion subscriptions globally, handheld mobile-cellular devices can be programmed to spatially map, temporally track, and transmit information on infections over wide geographical space and boundaries. Current cell phone diagnostic technologies have poor limit of detection, dynamic range, and cannot detect multiple pathogen targets simultaneously, limiting their utility to single infections with high load. Here we combined recent advances in quantum dot barcode technology for molecular detection with smartphones to engineer a simple and low-cost chip-based wireless multiplex diagnostic device. We validated our device using a variety of synthetic genomic targets for the respiratory virus and blood-borne pathogens, and demonstrated that it could detect clinical samples after simple amplification. More importantly, we confirmed that the device is capable of detecting patients infected with a single or multiple infectious pathogens (e.g., HIV and hepatitis B) in a single test. This device advances the capacity for global surveillance of infectious diseases and has the potential to accelerate knowledge exchange-transfer of emerging or exigent disease threats with healthcare and military organizations in real-time.

## Acknowledgments

First of all, I would like to thank my mentor Professor Warren Chan, without whom none of this would be possible. I sincerely appreciate his guidance, patience, and support over the years. I have learnt a great deal, both academically and personally, under his tutelage.

I would like to thank my committee members Professors Christopher Yip and Lidan You for their advice and suggestions over the years. Their input, especially from Prof. Yip, have greatly improved and refined my thesis.

I would like to thank my colleagues Jisung Kim, Abdullah Syed, Kun Chen, and Albert Lam for their amazing contributions toward this project. All of them, especially Jisung, have gone above and beyond in their respective parts, and I truly thank them.

I would like to thank my collaborators Doctors Mia Biondi, Anu Rebbapragada, Mario Ostrowski, and Jordan Feld for all their input on clinically-related topics.

I would like to thank all of my colleagues at the Chan lab for their feedback, support, and friendship over the years. In particular, I would like to thank those who started the program with me in the Fall of 2008: Alexandre Albanese, for bringing great joy and mental stimulation to my life the past six years; Edward Sykes, for always lending a hand when I needed one; and Leo Chou, for our discussions about science and everything else. Our time together will be greatly missed.

Finally, I would like to thank my parents, for their unconditional love, understanding, and support, always. They were there with me all along the way, in their encouragements and in spirit. I hope to make them proud.

# Table of Contents

Acknowledgments.....	iii
Table of Contents .....	iv
List of Tables .....	x
List of Figures .....	xi
List of Equations .....	xiv
List of Abbreviations .....	xv
Chapter 1 Introduction .....	1
1 Infectious Diseases.....	1
2 Infectious Disease Diagnostics .....	4
2.1 Current Diagnostic Technologies .....	4
2.2 Limitations of Current Diagnostic Technologies.....	5
3 Point-of-Care Mobile Phone Diagnostic Technologies .....	8
3.1 Current Phone-based Diagnostic Technologies .....	10
3.2 Limitations of Current Phone-based Diagnostic Technologies .....	15
4 Thesis Overview.....	15
5 Choice of Infectious Diseases .....	18
Chapter 2 Quantum Dot Barcodes .....	20
1 Introduction .....	20
2 Experimental Methods .....	26
2.1 Organic Fluorophore Particles .....	26
2.2 Quantum Dot Synthesis .....	26
2.3 Quantum Dot Barcode Synthesis .....	26
2.4 Excitation, Absorption, and Emission Spectra Measurement.....	27
2.5 Photobleaching Measurements .....	27



2.6 Sample Imaging .....	27
3 Results & Discussion .....	27
3.1 Spectral Properties .....	27
3.2 Effects of Varying Excitation on Emission .....	29
3.3 Photobleaching.....	29
3.4 Single-Source Imaging.....	32
4 Chapter Summary.....	34
5 Author Contributions .....	34
Chapter 3 Quantum Dot Barcode Readout and Resolution Algorithm.....	35
1 Introduction .....	35
2 Experimental Methods .....	36
2.1 Quantum Dot Synthesis .....	36
2.2 Quantum Dot Barcode Synthesis .....	36
2.3 Barcode Microbead Deposition on Microwell Chip.....	36
2.4 Microwell Fill Efficiency.....	38
2.5 Sample Imaging .....	38
2.6 Image Processing and Analysis .....	39
2.7 Image Registration .....	39
2.8 Barcode Image Extraction.....	39
2.9 Barcode Identification using Maximum Intensity Approach.....	39
2.10Barcode Identification using Euclidean Distance Approach .....	40
2.11Barcode Identification using Two-Step Maximum Intensity or Euclidean Distance Approach.....	41
2.12Barcode Identification Accuracy Confirmation using Flow Cytometry.....	41
3 Results & Discussion .....	42
3.1 Microwell Chip Platform .....	42

3.2 Approaches and Algorithms to Resolving Fluorescently-Encoded Microbeads .....	45
3.3 Overview of Imaging-Based Approach and Algorithm.....	48
3.3.1 Image Alignment using Discrete Fourier Transform.....	53
3.3.2 Microbead Image Extraction using Hough Transform .....	55
3.3.3 Establishing Microbead Intensity Profiles .....	59
3.3.4 Quantum Dot Barcode Identification and Resolution.....	61
3.4 Algorithm Accuracy Validation using Flow Cytometry.....	64
4 Chapter Summary.....	66
5 Author Contributions .....	66
Chapter 4 Quantum Dot Barcode Genetic Assays on a Chip .....	67
1 Introduction .....	67
2 Experimental Methods .....	68
2.1 Quantum Dot Synthesis .....	68
2.2 Quantum Dot Barcode Synthesis .....	68
2.3 Barcode Microbead Conjugation and Validation .....	68
2.4 Solution Assay .....	72
2.5 Flow Cytometry Analysis of Solution Assay.....	74
2.6 Surface Assay Protocol for Optimization .....	74
2.7 Sensitivity Assay.....	75
2.8 Multiplexing Assay .....	76
2.9 Sample Imaging .....	77
2.10 Image Analysis.....	77
3 Results & Discussion .....	81
3.1 Solution- vs. Surface-based Genetic Assay .....	81
3.2 Assay Optimization.....	83
3.2.1 DNA Sequence and Lengths .....	83

3.2.2	Amount of Capture Strands for Conjugation .....	83
3.2.3	Amount of Detection Strands in the Assay .....	84
3.2.4	Hybridization Buffer Type.....	84
3.2.5	Hybridization Temperature .....	84
3.2.6	Hybridization Kinetics .....	84
3.2.7	Continuous Excitation of the Detection Strand Fluorophore.....	85
3.2.8	Background Intensity Adjustment .....	85
3.3	Camera Usage .....	89
3.4	Assay Sensitivity .....	92
3.5	Multiplexing and Specificity.....	93
4	Chapter Summary.....	97
5	Author Contributions .....	97
	Chapter 5 Construction and Validation of Smartphone Device.....	98
1	Introduction .....	98
2	Experimental Methods .....	98
2.1	Quantum Dot Synthesis .....	98
2.2	Quantum Dot Barcode Synthesis .....	99
2.3	Barcode Microbead Conjugation and Validation .....	99
2.4	Sensitivity Assay .....	99
2.5	Multiplexing Assay .....	104
2.6	Whole Blood Collection/Separation, Viral DNA/RNA Extraction, and Reverse Transcription .....	105
2.7	Recombinase Polymerase Amplification (RPA) and Purification.....	105
2.8	Mono-Infection Assays using Amplified Clinical Samples.....	106
2.9	Co-Infection Assays using Amplified Clinical Samples .....	107
2.10	Device Design and Construction .....	107

2.11	Sample Imaging .....	108
2.12	Image Analysis.....	108
2.13	PCR Amplification and Purification .....	111
2.14	Quantum Dot Barcode Assay in Solution .....	113
2.15	HBV/HIV Multiplexed Assay in Solution .....	113
2.16	Data Analysis for Solution-based Assay.....	114
2.17	Human Subjects .....	114
3	Results & Discussion .....	115
3.1	Device Design and Construction .....	115
3.1.1	Emission Filters and Dichroic Mirrors .....	115
3.1.2	Excitation Source and Power .....	115
3.1.3	Optical System .....	119
3.1.4	Construction .....	122
3.2	Synthetic Sample Validation.....	122
3.2.1	Assay Sensitivity.....	126
3.2.2	Microbead-Counting Analysis Approach .....	126
3.2.3	Multiplexing and Specificity.....	128
3.3	Clinical Sample Validation .....	130
3.3.1	Mono-Infection of HIV and HBV.....	130
3.3.2	Co-Infection of HIV and HBV .....	135
3.3.3	Clinical Sample Sensitivity and Specificity .....	135
3.3.4	Base Pair Mismatches .....	135
4	Chapter Summary.....	140
5	Author Contributions .....	140
	Chapter 6 Summary & Future Directions .....	141
1	Summary .....	141

2	Significance.....	141
3	Future Directions.....	142
	References.....	147

## List of Tables

Table 1.1. Comparison of diagnostic technologies. ....	7
Table 3.1. List of quantum dot barcode synthesis parameters. ....	37
Table 4.1. List of barcodes synthesized and their corresponding DNA strands. ....	70
Table 4.2. List of barcode synthesis parameters. ....	71
Table 5.1. List of barcodes synthesized and their corresponding DNA strands. ....	100
Table 5.2. List of barcode synthesis parameters. ....	103
Table 5.3. List of HBV genotypes and HBV/HIV viral loads. ....	132
Table 6.1. Comparison of Diagnostic Technologies and the Proposed System. ....	145

## List of Figures

Figure 1.1. Global distribution of infectious disease event risks. ....	2
Figure 1.2. Ebola outbreak in West Africa. ....	3
Figure 1.3. Connectivity in West Africa. ....	9
Figure 1.4. Cell phone-based microscopy system from the Fletcher group. ....	11
Figure 1.5. Smartphone cell counting system from the Ozcan group.....	12
Figure 1.6. Smartphone reader for lateral flow strips from the Ozcan group. ....	13
Figure 1.7. Smartphone reader of lab-on-chip assay from the Hashsham group.....	14
Figure 1.8. System overview. ....	17
Figure 2.1. Size of nanoparticles.....	21
Figure 2.2. Quantum dot tunability.....	22
Figure 2.3. Synthesis of a variety of quantum dot barcodes. ....	24
Figure 2.4. Quantum dot barcode synthesis setup. ....	25
Figure 2.5. Comparing excitation/absorption and emission spectra. ....	28
Figure 2.6. Comparing emission spectra under varying excitation.....	30
Figure 2.7. Comparing photobleaching. ....	31
Figure 2.8. Comparing single source imaging. ....	33
Figure 3.1. Quantum dot barcodes on glass side. ....	43
Figure 3.2. Microwell chip.....	44
Figure 3.3. Microwell fill efficiency.....	46

Figure 3.4. Colour channel intensities of barcodes. ....	50
Figure 3.5. Imaging using multiple emission filters. ....	51
Figure 3.6. The image analysis process. ....	52
Figure 3.7. Fourier transform of images. ....	54
Figure 3.8. Binary mask creation. ....	56
Figure 3.9. Feature extraction using Hough transform. ....	57
Figure 3.10. Hough transform microbead extraction. ....	60
Figure 3.11. Barcode intensity profiles. ....	62
Figure 3.12. Barcode resolution process. ....	63
Figure 3.13. Barcode resolution accuracy. ....	65
Figure 4.1. Quantum dot barcode genetic assay. ....	69
Figure 4.2. Capture strand conjugation efficiency. ....	73
Figure 4.3. Barcode intensity profiles. ....	79
Figure 4.4. Comparison of flow cytometry and CCD imaging genetic assays. ....	82
Figure 4.5. Surface assay optimization. ....	88
Figure 4.6. Microscopy-smartphone imaging setup. ....	90
Figure 4.7. Barcode genetic assay imaging on the smartphone. ....	91
Figure 4.8. Comparison of CCD and smartphone camera assay sensitivity. ....	92
Figure 4.9. Smartphone sensitivity curves. ....	94
Figure 4.10. Smartphone multiplexed detection. ....	96



Figure 5.1. Barcode intensity profiles. ....	110
Figure 5.2. Detection using histogram analysis. ....	112
Figure 5.3. Effect of dichroic mirror on intensity profiles. ....	116
Figure 5.4. LED and diode laser excitation of quantum dot barcodes. ....	117
Figure 5.5. Transillumination of quantum dot barcodes. ....	118
Figure 5.6. Excitation sources for genetic assays. ....	121
Figure 5.7. Smartphone device design. ....	123
Figure 5.8. Smartphone device and imaging. ....	124
Figure 5.9. Signal differentiation of device images. ....	125
Figure 5.10. Device sensitivity assays. ....	127
Figure 5.11. Device multiplexing assays. ....	129
Figure 5.12. Detection of HIV and HBV clinical mono-infections. ....	133
Figure 5.13. Detection of HIV and HBV clinical mono-infections in solution. ....	134
Figure 5.14. Detection of HIV and HBV clinical co-infections. ....	136
Figure 5.15. Detection of HIV and HBV clinical co-infections in solution. ....	138
Figure 5.16. Single-nucleotide polymorphisms in clinical samples. ....	139
Figure 6.1. Device procedures flow chart. ....	144
Figure 6.2. Envisioned diagnostic unit. ....	146

## List of Equations

Equation 3.1 .....	40
Equation 3.2 .....	40
Equation 3.3 .....	41
Equation 3.4 .....	55
Equation 3.5 .....	58
Equations 3.6.....	58
Equation 3.7 .....	58
Equation 3.8 .....	59
Equations 3.9.....	59
Equation 4.1 .....	78
Equation 5.1 .....	109
Equation 5.2 .....	111

## List of Abbreviations

**PCR:** polymerase chain reaction

**HIV/AIDS:** human immunodeficiency virus/acquired immune deficiency syndrome

**HBV:** hepatitis B virus

**HCV:** hepatitis C virus

**DD:** double-distilled

**CCD:** charge-coupled diode

**DNA:** deoxyribonucleic acid

**EDC:** 1-ethyl-3-(3-dimethylaminopropyl) carbodiimide hydrochloride

**TE:** Tris-Ethylenediaminetetraacetic acid

**MES:** 2-(N-morpholino)ethanesulfonic acid

**DMSO:** dimethyl sulfoxide

**LED:** light-emitting diodes

**cDNA:** complementary DNA

## Chapter 1 Introduction

### 1 Infectious Diseases

Infectious diseases are the types of diseases caused by pathogenic microorganisms (i.e. bacteria, viruses, parasites, or fungi) that can spread directly or indirectly from person to person or from animal to person<sup>1</sup>. Despite the advent of modern medicine, these infections continue to pose a significant threat to the health and safety of people worldwide, accounting for millions of deaths each year, impacting global health<sup>2,3</sup> (**Figure 1.1**). In particular, they constitute one of the major causes of morbidity and mortality in the developing countries<sup>4</sup>. With globalization and the ease of international travel, undiagnosed and misdiagnosed infectious diseases can spread rapidly, worsening economic burdens, morbidity, and mortality. The SARS outbreak of 2003, the H1N1 flu pandemic of 2009, along with the ongoing fight against human immunodeficiency virus/acquired immune deficiency syndrome (HIV/AIDS), malaria, and many others, dramatically highlight the threat of infectious diseases on a global scale. The current Ebola epidemic, which continues to ravage through West Africa, serves to illustrate the threat of infectious diseases. It started with the infection of a single child living in a forested area of Guinea in December 2013. Contracted and spread by travelers, by June 2014 it had infected 759 and killed 467. As of January 4<sup>th</sup> 2015, only a year since the initial infection, 20,747 cases and 8,235 deaths had been reported worldwide (**Figure 1.2**), including countries outside of the West African region as far as Spain, the United Kingdom, and the United States<sup>5</sup>.

While this can be attributed to many factors such as the poor-functioning health systems in these regions and slow initial response<sup>6</sup>, much of the effort to control and contain the infection is heavily hindered by poor diagnostics, as the World Health Organization has stated<sup>7</sup>:

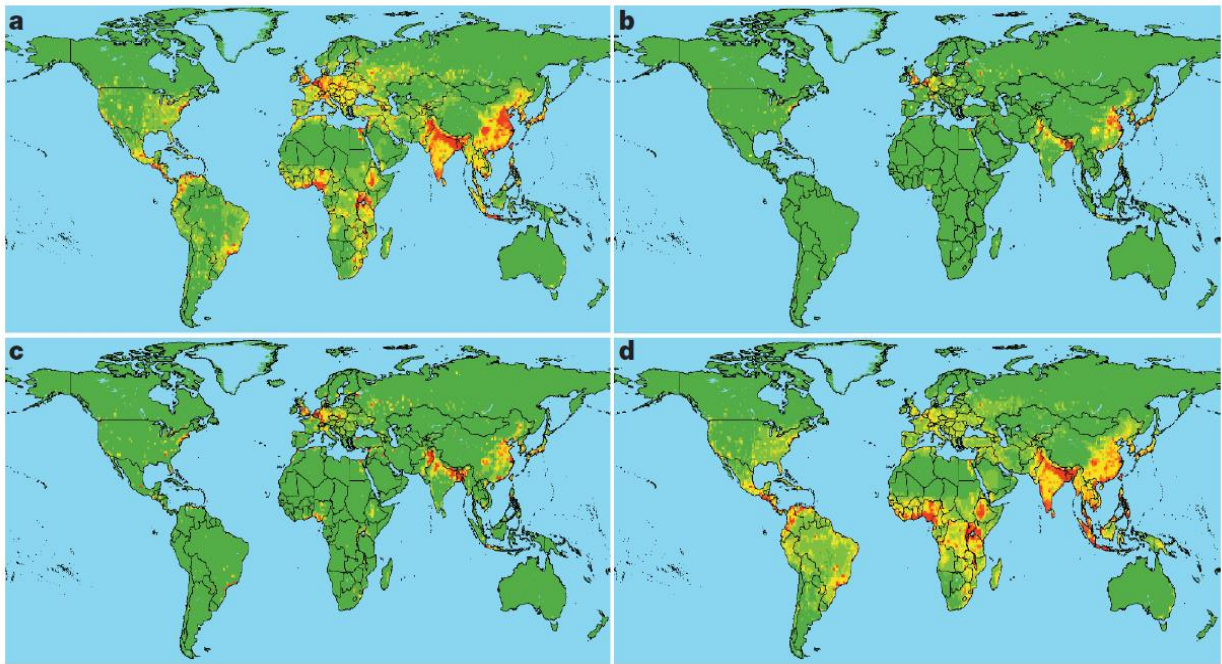


**Figure 1.1. Global distribution of infectious disease event risks.**

Distribution derived for (a) zoonotic pathogens from wildlife, (b) zoonotic pathogens from non-wildlife, (c) drug-resistant pathogens, and (d) vector-borne pathogens. Figure and description adapted from source<sup>3</sup> and not created by the author.

(Removed)

**Figure 1.2. Ebola outbreak in West Africa.**

Data, as of December 14<sup>th</sup> 2014, showing the toll of Ebola on Africa. Figure adapted from source<sup>5</sup> and not created by the author. (**Note:** It has been removed due to copyright restrictions, please refer to citation.)

Efforts to contain the Ebola outbreaks in West Africa are currently hampered by cumbersome, slow and complex diagnostic tests that impose a number of additional logistical challenges, including requirements for a high level of laboratory biosafety and staff expertise in using sophisticated machines.

The standard molecular assays currently used in mobile and other laboratories supporting the Ebola response include the reverse-transcriptase polymerase chain reaction, or RT-PCR test. The test, which involves a number of laborious procedures, provides very accurate results when performed by trained staff. Each test requires a full tube of blood, takes from 2 to 6 hours, and costs around \$100. These requirements are difficult to meet in resource-constrained West African settings, thus severely limiting testing capacity.

That is, to effectively control Ebola, and indeed most infectious diseases, effective diagnostics are crucial.

## 2 Infectious Disease Diagnostics

The World Health Organization has outlined a list of criteria that infection diagnostics should meet in order to be effective technologies (the ASSURED criteria)<sup>4,8</sup>: affordable so that they are accessible to all; sensitive, or possess low detection limit, so that even minute amounts of pathogen can be detected; specific, or possess low cross-reactivity between the pathogens they are capable of detecting; user-friendly, such that they are simple to use and takes only a few steps to complete; robust and rapid, specifically the results should be available in under 30 minutes; equipment-free, meaning the diagnostics should be able to be performed with minimal external instrumentation; and deliverable to those who need them, i.e. at the point-of-care. In essence, these criteria illustrate an important concept: in order for a diagnostic technology to be truly effective for monitoring and ultimately controlling infectious diseases, high analytical performance (i.e. high sensitivity and specificity) is not enough. Rather than requiring laboratories or other advanced facilities, it needs to be available and accessible at the point-of-care where it is most needed, such as at the bedside, in the airport, or out in the field, in order for it to be of most use. This is especially important for developing countries where health systems and resources are not as pervasive or plentiful as those in developed countries.

### 2.1 Current Diagnostic Technologies

Traditional gold standards in infectious disease diagnostics include microscopy and cell culturing, as well as enzyme-linked immunoassays<sup>9-12</sup>. The former two work through

identification of morphological changes in diseased or viral-infected cells, whereas the latter is used to detect for the presence of a substance of interest, typically an antigen using its antibodies in a sandwich assay format. Briefly, a sandwich assay involves three main components: (1) a target molecule of interest (e.g. proteins, DNA), (2) a capturing agent that specifically binds to the target molecule in order to differentiate it from other molecules, and (3) a detection agent or secondary probe that binds to another portion of the target molecule to indicate its presence or absence.

Lateral flow immunoassays (also known as dipstick or immunochromatographic tests)<sup>13–15</sup> are simple tests, typically in strip format, that allow the transport of sample liquid through its porous material in order to detect for the presence or absence of an analyte – traditionally proteins through antibody-antigen interactions in, again, sandwich assay format – on test lines. The microarrays<sup>16–19</sup> and polymerase chain reaction (PCR)<sup>20–22</sup> techniques are more recent. Microarrays involve a solid substrate (e.g. glass slide) on which a large amount of molecular detection of proteomic or genomic infected samples can be performed in an ordered or arrayed, high-throughput manner. PCR involves the amplification of a minute amount of genetic sample (e.g. viral DNA) for genomic molecular detection.

Many new approaches have emerged over the past decade, including fibre optics-based<sup>23–25</sup>, flow cytometry-based<sup>26–29</sup>, microfluidics-based<sup>30–33</sup>, and paper-based<sup>34–37</sup> technologies. The first three generally involve the use of fluorescent microbeads for detection of either proteomic or genomic samples, in once again a sandwich assay configuration, performed and whose readout are observed on various platforms: optical fibres for fibre-optics based, liquid flow stream for flow cytometry, and microfluidic chips for microfluidics-based. Paper-based techniques, inspired by the ubiquity and cost-effectiveness of lateral flow tests, are those that involve the use of a paper substrate for molecular detection, often exploiting the porosity of paper that allows for liquid flow and interactions without the use of laboratory equipment.

## 2.2 Limitations of Current Diagnostic Technologies

While these techniques are advantageous in some respects they also have their limitations. Microscopy, cell culturing, and enzyme-linked immunoassays are limited by time, need for laboratory equipment, and technical as well as operational complexities. Lateral flow tests are portable and easy to use, but have poor analytical sensitivity, and limited by their ability to



simultaneously detect for a large number of multiple diseases or strains, i.e. multiplexing<sup>4</sup>. Microarrays and PCR techniques have improved sensitivity, but with prohibitive costs. Fibre optics-based, flow cytometry-based, and microfluidics-based platforms offer speed and multiplexing capabilities. However, much of the world's population lives in resource-poor settings where advanced molecular diagnostic systems such as these are not available due to cost constraints, infrastructure limitations to sustain complex laboratory equipment, and the lack of skilled technicians to perform cumbersome procedures and accurately interpret diagnostic results<sup>38-40</sup>. Paper-based technologies, similar to the dipstick tests, are cost-effective and easily transportable, but often still lack in their sensitivity and multiplexing capabilities.

A comparison of the various technologies is shown, sorted from the least analytically sensitive to the most (**Table 1.1**). It should be noted that this serves only as an approximate guide for the overall landscape of these technologies and not intended to be exhaustive, as it is not possible to define a set of unified parameters with which comparisons are made given the diversity of the literature. For analytical sensitivity, some approaches are much more sensitive than others within the same category of technology depending on whether or not sensitivity was the focus of the study, and different measurement units (e.g. mol/L, g/mL, IU/mL, CFU/mL) that may or may not be convertible among them are used for different diseases by different authors. Here we considered only those that report in mol/L. Likewise for speed, some studies report the time required to perform the assay, while others report only the readout time, and many report a combination from different procedures. Here we considered speed as a sum of durations required to perform the assay and the readout. Portability and economy are subjective and thus presented qualitatively. Here we considered the use of dedicated readout instrumentation to be non-portable and non-economical, i.e. pumps and microscope for microfluidics; flow cytometer for flow cytometry; optical fibres and computer for fibre optics; specialized scanners for microarrays; and thermocycler for PCR, though it is not a readout device. In contrast, multiplexing can be evaluated much more objectively. And while lateral flow tests and paper-based technology can be used in 2- to 3-plex applications, they are limited to this number unless an external readout system is employed<sup>36,41,42</sup>, which reduces their portability and cost-effectiveness.

From the perspective of real-world deployment, here we see that with the exception of lateral flow tests and paper-based technologies, all other approaches are not suitable for point-of-care

**Table 1.1. Comparison of diagnostic technologies.**

<b>Platform</b>	<b>Sensitivity Range</b>	<b>Speed (Assay + Readout)</b>	<b>Portable</b>	<b>Simple to Use</b>	<b>Multiplexing</b>
Paper <sup>43,44</sup>	mM – nM	10-60 min.	Yes	Yes	No
Lateral Flow <sup>15,43,45,46</sup>	nM – pM	20-30 min.	Yes	Yes	No
Microfluidics <sup>33,47-49</sup>	nM – fM	20-60 min.	No	No	Yes
Flow Cytometry <sup>29,50-53</sup>	pM – fM	20-60 min.	No	No	Yes
Microarray <sup>19,54,55</sup>	pM – fM	2-3 hr.	No	No	Yes
Fibre Optics <sup>25,56,57</sup>	fM – zM	2-3 hr.	No	No	Yes
PCR <sup>58-60</sup>	aM – zM	2-3 hr.	No	No	Yes

diagnostics. And while they are more transportable and potentially more cost-effective, both lateral flow tests and paper-based technologies have little to no multiplexing capabilities, severely limiting their application in the field. This is because many infections exhibit similar symptoms and the ability to diagnosis one disease (e.g. a common cold) from another (e.g. SARS) quickly and efficiently is vital from an infection control perspective as well as from a drug-resistance one.

### 3 Point-of-Care Mobile Phone Diagnostic Technologies

In the last decade advances in internet technology, social media, and smartphones have significantly changed the patterns and mode of global communication. There are no more remote corners; information and events can be transmitted instantaneously across boundaries over vast distances throughout the world. The integration of mobile-cellular devices – with over 6.9 billion subscriptions worldwide<sup>61</sup>, thus extremely prevalent and accessible even in developing nations – with state-of-the-art rapid multiplexing molecular diagnostic devices would alleviate many of the problems present in current diagnostic technologies. This would be achieved by permitting clinical diagnosis and treatment in the absence of laboratory infrastructure, enable real-time global surveillance of infectious transmission events, and help predict temporal infection trends through crowd-sourced data collection<sup>62</sup>. To illustrate the potential of mobile phone-based diagnostics, we once again turn to the current Ebola epidemic in West Africa (**Figure 1.3**). As can be observed in **Figure 1.3a**, the most recent outbreak had unfortunately taken place in a region of high physical connectivity (low travel times to settlements of high population), potentially a factor in its rapid spread. However, **Figure 1.3b** shows that over the same region, there exists a moderate to high amount of mobile phone connectivity. This suggests that the mobile phone could have been an invaluable tool in controlling and predicting the spread of Ebola, through call record information that can be used to model population movement, as well as diagnostic tools that are readily deployable among the populace.

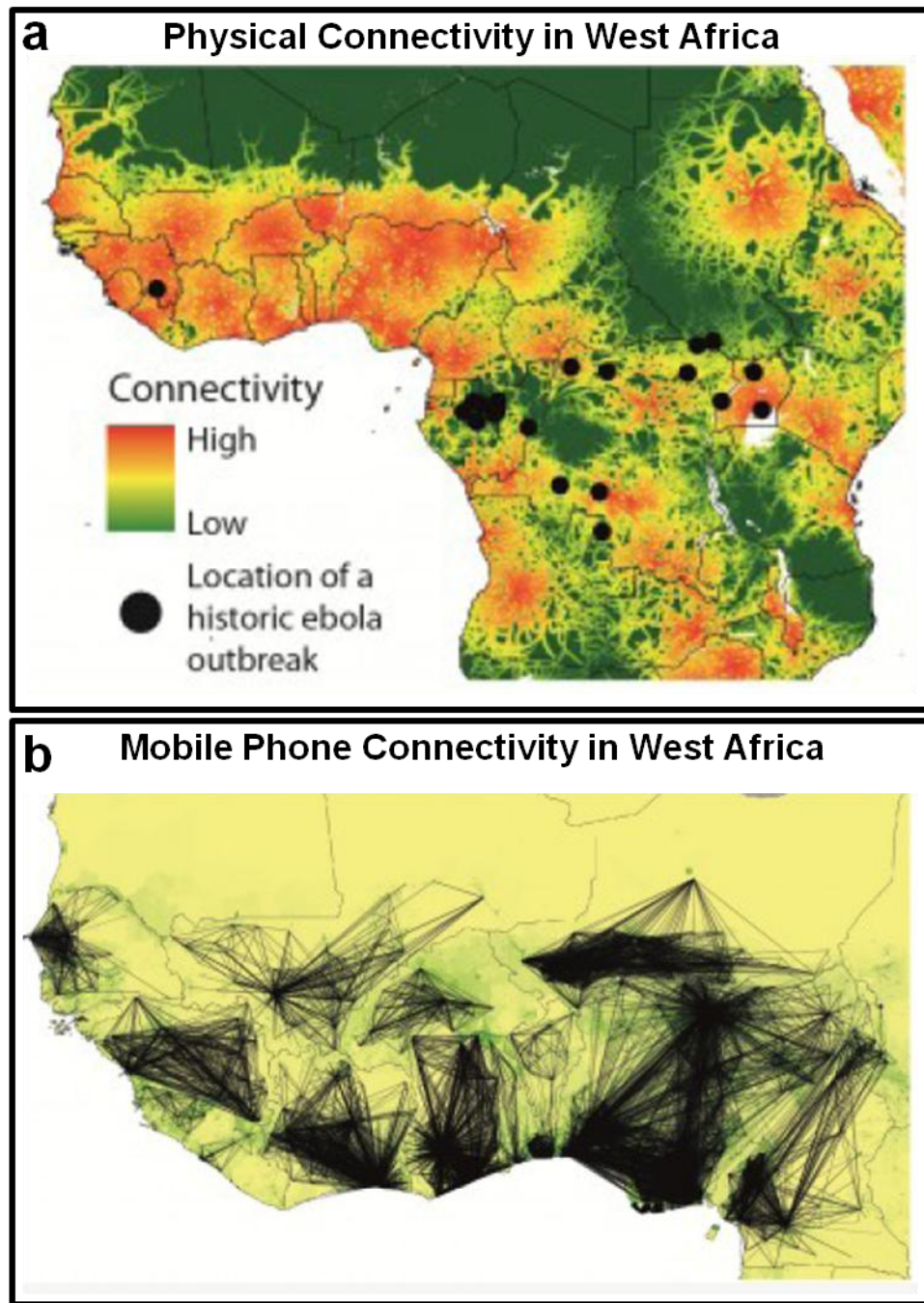


**Figure 1.3. Connectivity in West Africa.**

Information on the West African region showing (a) physical connectivity as measured by the amount of travel time required to reach a settle of high population, with locations of historic Ebola outbreaks highlighted; and (b) mobile phone connectivity as measured by call detail records. Figure adapted from source<sup>63</sup> and not created by the author.

### 3.1 Current Phone-based Diagnostic Technologies

In the past five years, there has been a surge of publications relating to the use of cell phones or smartphones for infectious disease diagnostics<sup>64,65</sup>. Thus far, they have primarily been used in direct imaging applications, such as the identification of bacteria or viruses labeled with a fluorophore<sup>66,67</sup>. The Fletcher group constructed a cell phone microscope system using existing microscope components to demonstrate bright-field and fluorescence imaging of 6  $\mu\text{m}$  fluorescent microbeads<sup>66</sup>. They then used the system to identify sickle red blood cells from blood smear samples, as well as tuberculosis bacilli from fluorescent dye-stained sputum samples (**Figure 1.4**).

The use of smartphones for cell counting has also been popular<sup>68–70</sup>. The Ozcan group built a smartphone blood analyzer that has three sets of interchangeable components that can count white blood cells under fluorescence mode, red blood cells under bright-field mode, and hemoglobins under absorbance mode, respectively<sup>70</sup>. They verified their results against those from a commercially-available analyzer (**Figure 1.5**).

Another smartphone diagnostics technology from the Ozcan group involved the construction of a smartphone reader for the test lines on lateral flow strips testing for malaria, human immunodeficiency virus (HIV), or tuberculosis<sup>71</sup>. The reader digitally processed and enhanced the images of the test lines to improve reading accuracy and sensitivity. They then demonstrated its ability to quantify the antigen amount by showing different intensity results from 1x, 2x, and 3x dilutions of the sample (**Figure 1.6**).

Moving beyond the imaging of bacteria, cells, or strip tests, other approaches using the smartphone to read/image custom-made lab-on-chip assays also exist<sup>72–74</sup>. For example, the Hashsham group constructed a smartphone-based genetic tester for bacteria DNA<sup>73</sup>. After incubation and amplification they demonstrated the detection of two different marker genes for each of *S. aureus* and *E. coli* in a parallel manner (**Figure 1.7**).

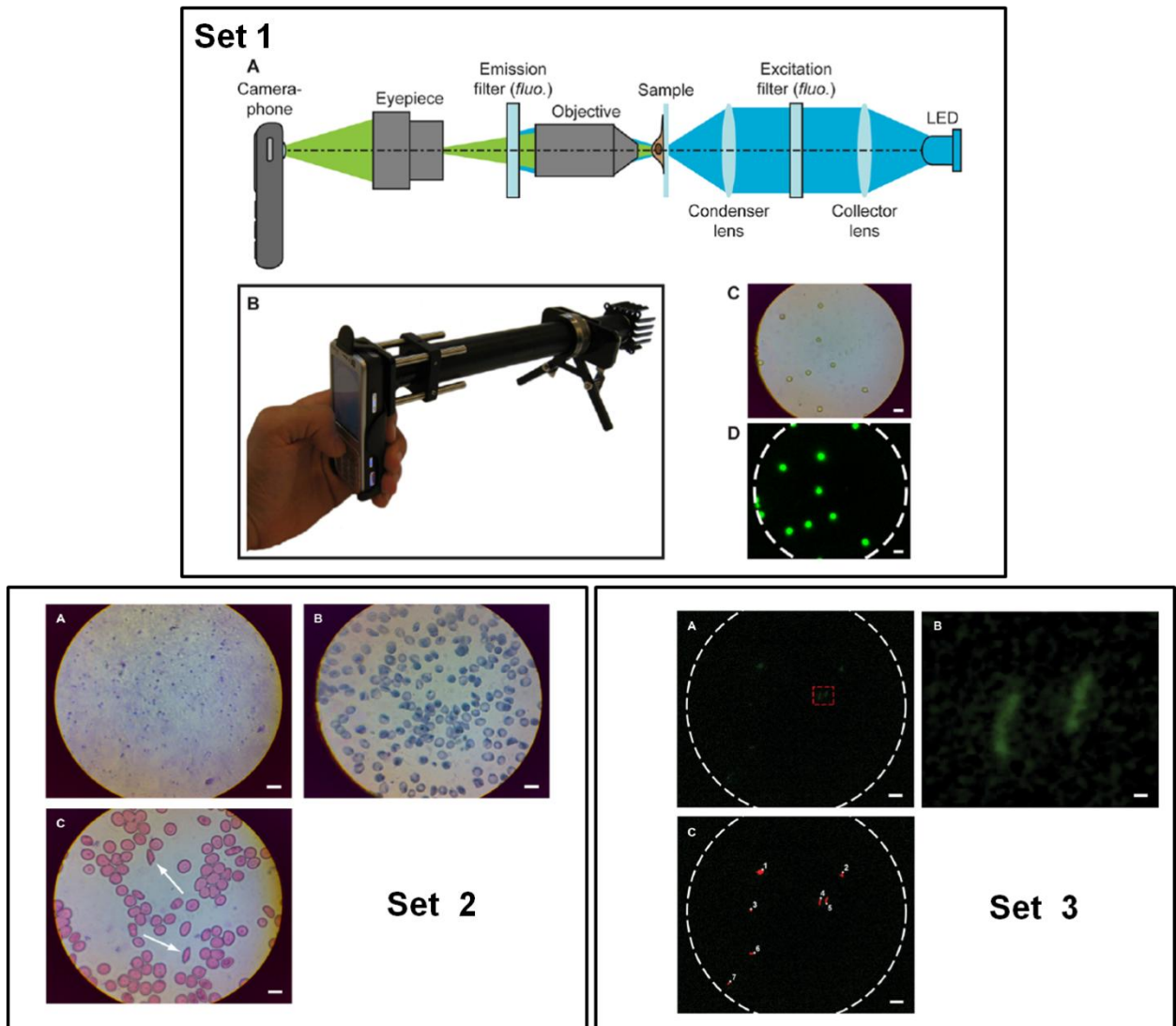


**Figure 1.4. Cell phone-based microscopy system from the Fletcher group.**

Cell phone-based microscopy system from the Fletcher group. Set 1 shows the system setup and imaging of 6  $\mu\text{m}$  fluorescent microbeads. Set 2 shows results from the identification of sickle red blood cells. Set 3 shows results from tuberculosis bacilli from dye-stained sputum samples. Figures adapted from source<sup>66</sup> and not created by the author.

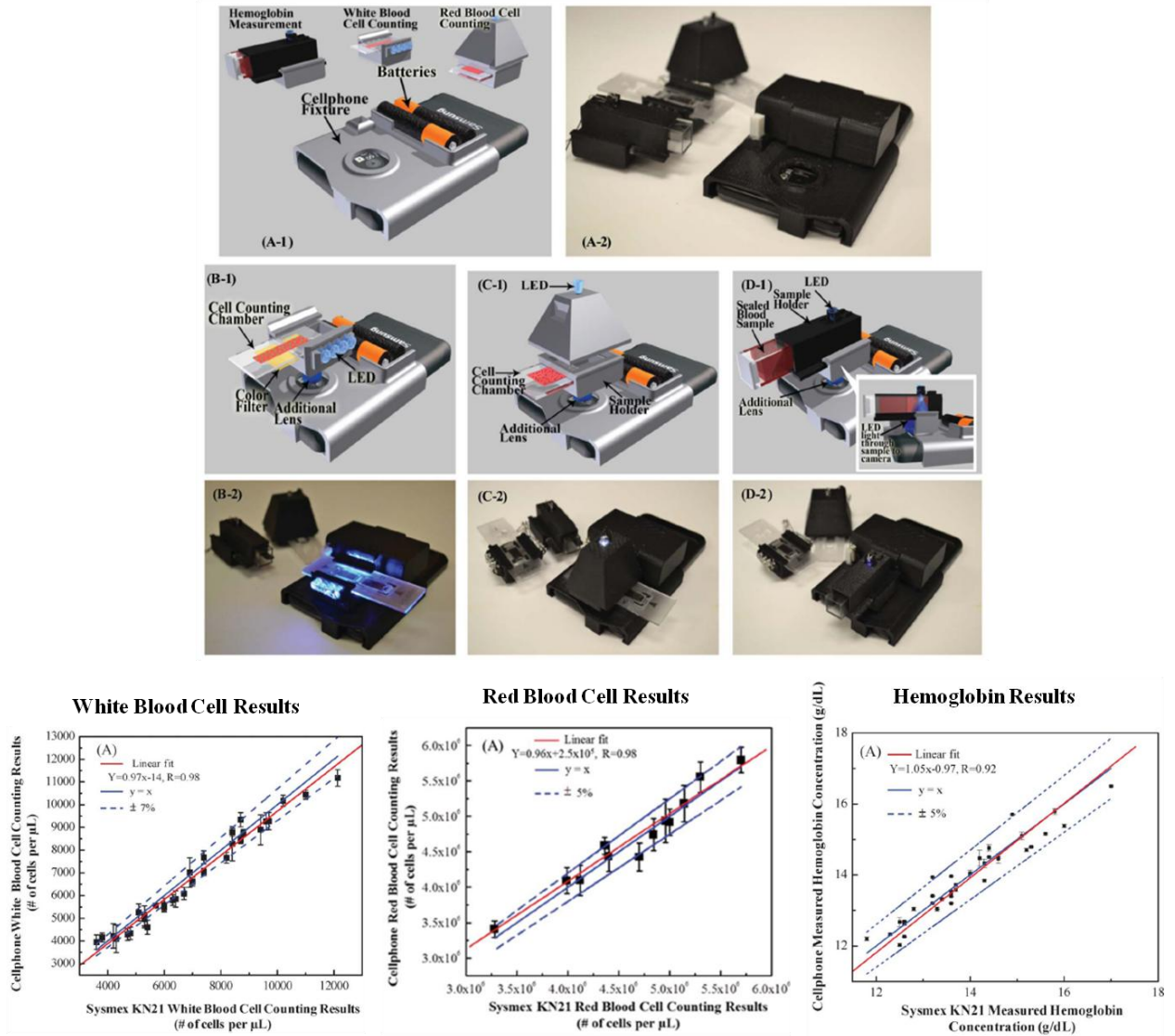


**Figure 1.5. Smartphone cell counting system from the Ozcan group.**

Top eight figures show the various components for each of white blood cell counter, red blood cell counter, and hemoglobin counter. The bottom three figures show the corresponding results and compare them with those from commercially-available analyzers. Figures adapted from source<sup>70</sup> and not created by the author.



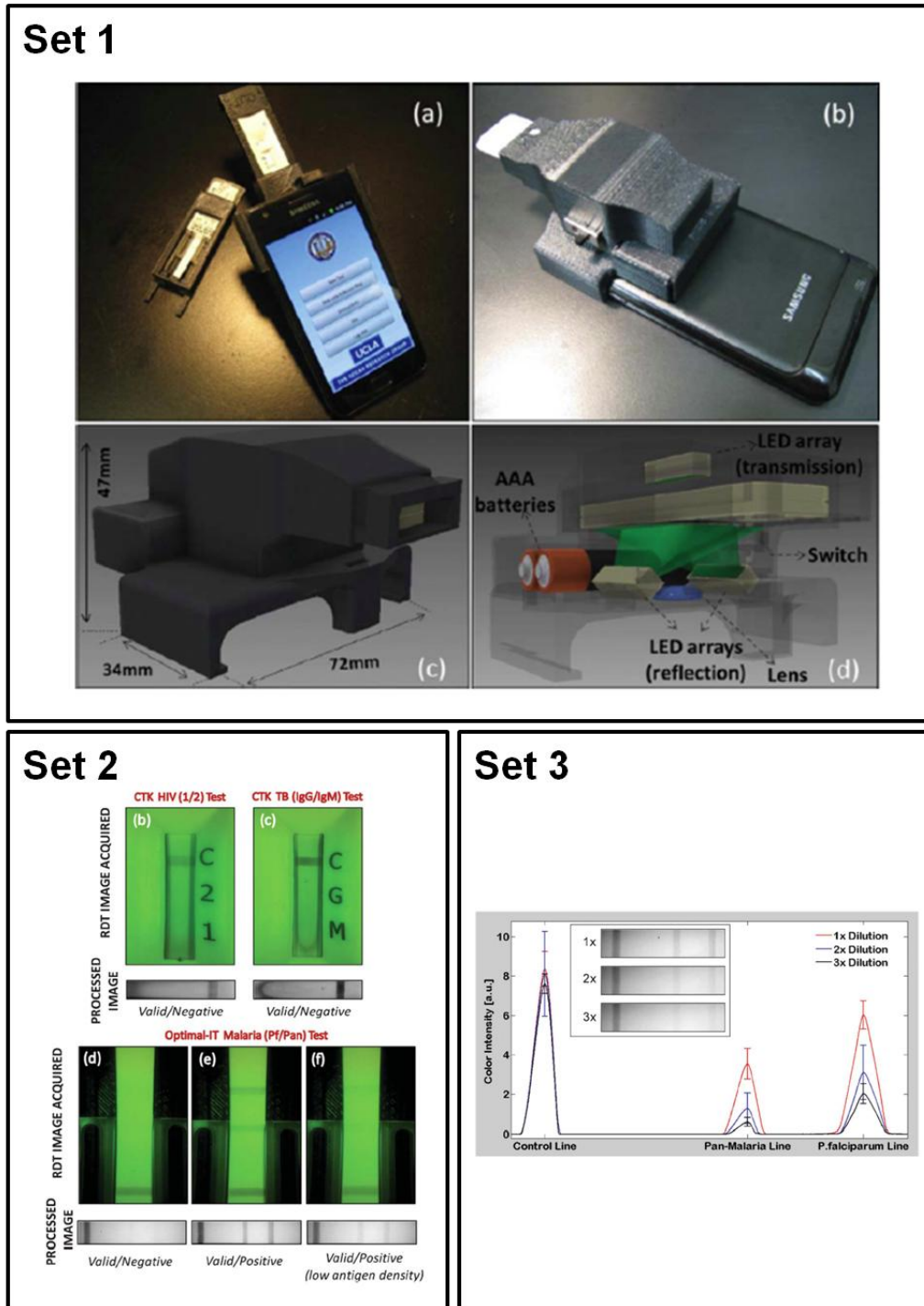


**Figure 1.6. Smartphone reader for lateral flow strips from the Ozcan group.**

Set 1 shows the reader system setup. Set 2 shows results from test strip results before and after image processing and enhancement. Set 3 shows the reader's basic ability in quantifying antigen amount. Figures adapted from source<sup>71</sup> and not created by the author.



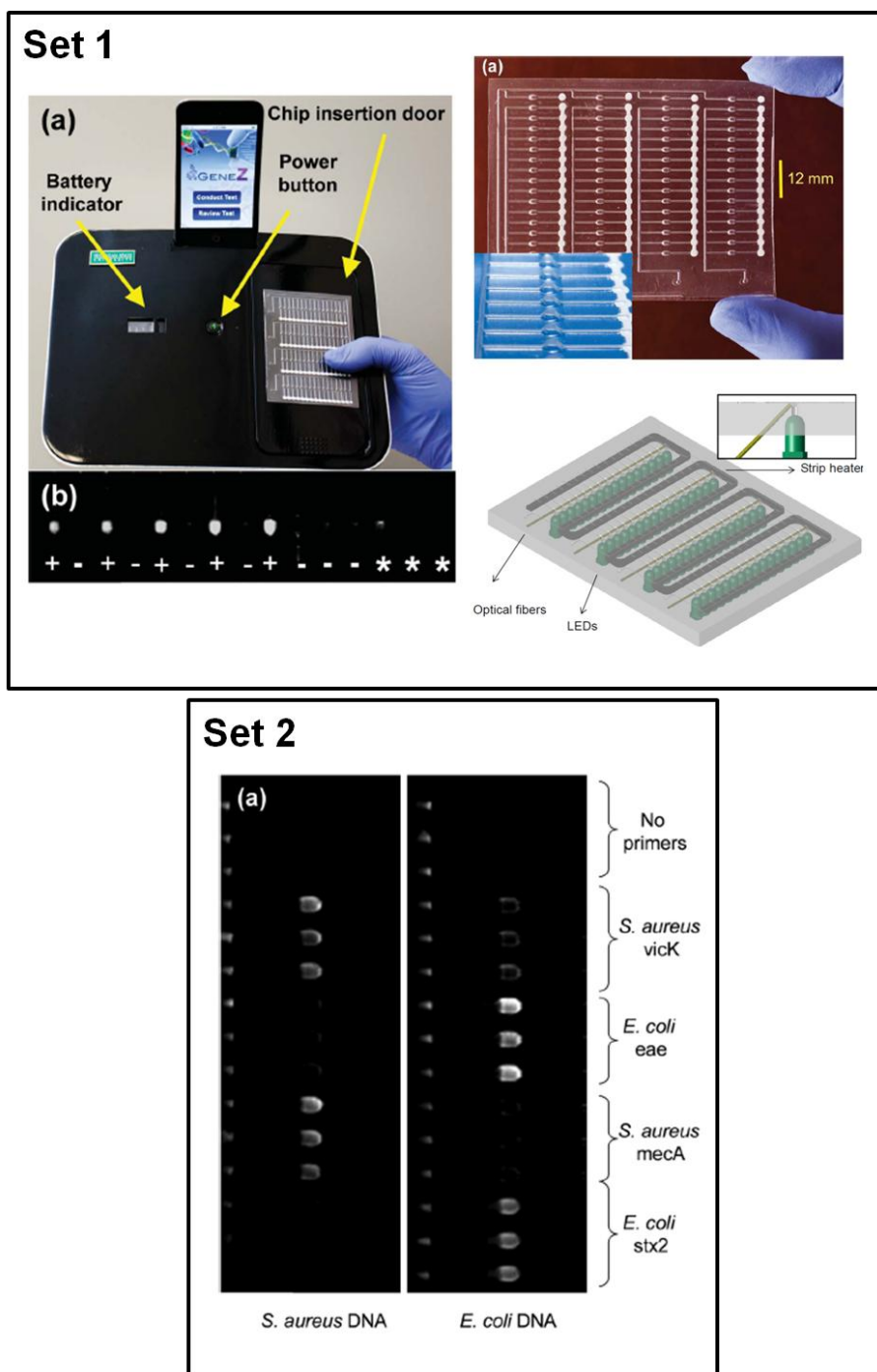


**Figure 1.7. Smartphone reader of lab-on-chip assay from the Hashsham group.**

Set 1 shows the reader system and lab-on-chip setup. Set 2 shows results from parallel detection of bacterial DNA. Figures adapted from source<sup>73</sup> and not created by the author.

### 3.2 Limitations of Current Phone-based Diagnostic Technologies

While these studies advance the field of mobile phone diagnostics, they are still in many ways limited by their ability to be widely utilized for molecular detection of infectious diseases, i.e. quantitative analysis of proteomic or genomic samples. For one, as stated above, many of these involve basic direct imaging applications, either of samples themselves (e.g. cells, bacteria) or enhancement of commercially-available test kits, without being able to perform molecular detection. While this reduces complexity, it also confines them to simple qualitative analyses of images. Many of these technologies are also constrained by their poor analytical sensitivity, which prevents them from diagnosing early stages of infections. Most crucially, they have limited multiplexing capabilities, i.e. inability to simultaneously detect different pathogens in “one pot” or from a single sample. The low throughput nature of this means the diagnosis would be done very inefficiently, ultimately impacting the precision and accuracy of diagnosis. The lack of multiplexing also means that sample collection and volume requirements would be an issue, as samples from a patient would need to be taken multiple times in order to be tested for multiple diseases, which may not always be possible (e.g. for children). Additionally, the lack of a simple multiplexing mechanism means that the diagnostic instrumentation itself would need to be physically enlarged in order to accommodate the detection of multiple pathogens, reducing portability.

## 4 Thesis Overview

The objective of this thesis, therefore, was to develop a proof-of-concept infectious disease diagnostic device that exploit the imaging and wireless capabilities of modern-day smartphones, combined with the molecular detection and multiplexing capabilities of a platform known as “quantum dot barcodes”. Quantum dot barcodes – which shall be simply referred to as “barcodes”, “microbeads”, or simply “beads” – discussed in more detail later, are easily synthesized, have the capacity for high degrees of multiplexing, as well as provide a platform on which both genomic and proteomic molecular detections can be performed<sup>75</sup>. On the other hand the smartphone, as described previously and when compared to traditional barcode readout systems such as microfluidics<sup>76</sup> or flow cytometry<sup>29,50,77</sup>, is more ubiquitous, portable, and easy to use, as well as allowing for data transmission. By combining the advantages of the quantum

dot barcode for molecular detection and smartphone for its readout, we were able to create a potentially powerful point-of-care diagnostic system for infectious diseases.

In Chapter 2, we briefly outline the method with which quantum dot barcodes are synthesized and present rationales as to why quantum dot barcodes are more advantageous for barcoding compared to traditional fluorophores. To do this, we demonstrate the superiority of quantum dot over traditional fluorophores for barcoding purposes on the bases of absorption spectra, emission spectra, photobleaching, and imaging.

In Chapter 3, we describe the algorithm we developed for quantum dot barcode readout. We begin by first describing the method to array the quantum dot barcodes onto a surface chip substrate, as a means to increase the portability and ease of handling (as compared to storage in solution) of our diagnostic system. We then illustrate the algorithm through which the barcode microbeads are imaged, processed, and ultimately identified and resolved on a surface. Finally, we demonstrate the effective of our algorithm by resolving a set of different barcodes arrayed on the chip.

In Chapter 4, we demonstrate the ability to perform genetic assays on our quantum dot barcode chip platform by first comparing the analytical performance of traditional solution-based barcode assay with our surface-based approach. After describing our assay optimization process, we compare the performance of different imaging setups by examining the resulting assay analytical sensitivity. We then conclude the chapter by demonstrating the ability for our system to perform multiplexed detection.

In Chapter 5, we illustrate the design and construction process to our point-of-care smartphone diagnostics device that incorporates the various components described in the preceding chapters. We then characterize our device's analytical sensitivity, and validate its multiplexing capabilities, both using synthetic samples. Finally, we demonstrate the ability of our device to be used in a clinical setting, with both mono- and co-infection patient samples. An overview of the preceding three main components of our diagnostic system is illustrated in a diagram (**Figure 1.8**).

We conclude the thesis, in Chapter 6, with a brief summary of the achievements illustrated in the preceding chapters, and provide an outline of future work and vision.

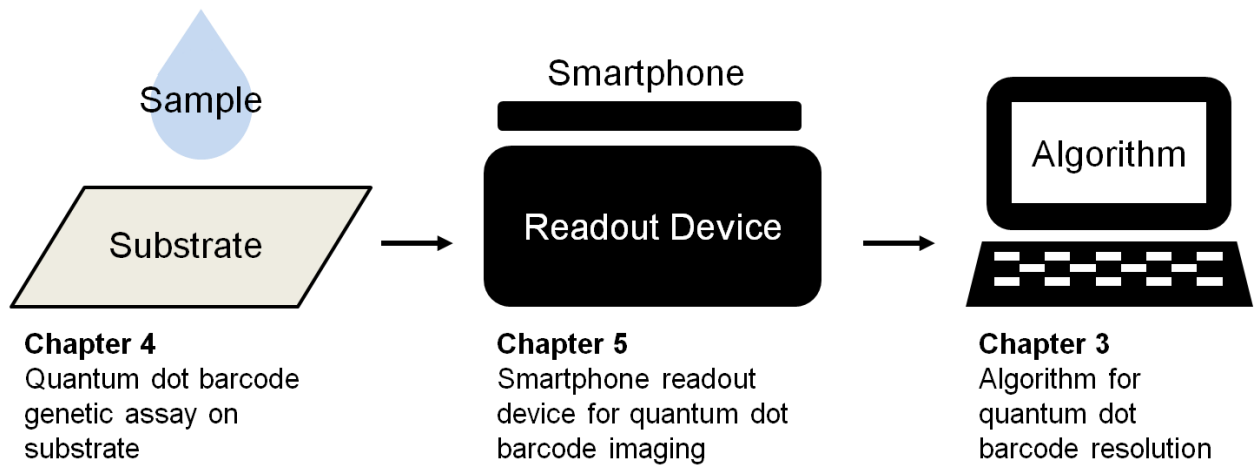


**Figure 1.8. Overview of thesis components.**

An overview of the three main components of our diagnostic system, corresponding to three chapters of the thesis.

## 5 Choice of Infectious Diseases

We elected to use seven different types of prevalent infectious diseases to test for the feasibility of our device. These include the influenza A viruses H1N1 (commonly known as “swine flu”), H3N2, and H5N1 (commonly known as “bird flu”), influenza B virus, human immunodeficiency virus/acquired immune deficiency syndrome (HIV/AIDS), as well as the hepatitis B and C virus (HBV and HCV). They were chosen because they constitute a significant burden of communicable illnesses. Many of them also exhibit common symptoms such as fever and fatigue, and thus it becomes important to be able to diagnose the patient accurately and quickly in order to devise the correct countermeasure and stop further spreading.

The influenza viruses are airborne and highly contagious, and they have posed significant difficulty in clinical differential diagnosis<sup>78,79</sup>. H5N1 remains a pandemic risk due to its high rate of mutation<sup>80,81</sup>. In addition, H1N1, H3N2, and influenza B have frequently been included in the seasonal vaccines in recent years for their likelihood of reoccurrence<sup>82–84</sup>.

HIV/AIDS, as well HBV and HCV infections comprise the majority of bloodborne infections worldwide, especially in resource-limited settings<sup>85</sup>. These infections are also difficult to differentiate clinically since they share common symptoms such as general malaise, jaundice, and nausea and/or vomiting<sup>86</sup>. They also share the same routes of transmission including blood transfusions/contact, sharing of contaminated needles (drug-use) or instruments (tattoos, piercings, acupuncture, etc.), sexual contact (debatable for HCV), and mother-to-child transmission during pregnancy<sup>87–89</sup>. Furthermore, the mortality and loss of life quality associated with HIV/AIDS alone has decimated generations and economies in the developing world. While voluntary counseling and testing centres for HIV are available in Africa and Asia, delays in test turnaround time and partner notification represents a loss of valuable time when transmission continues, treatment initiation is delayed, and health deteriorates<sup>90,91</sup>. However, people screened for HIV in the developing world are not aware or simultaneously tested for hepatitis B/C even though co-infections are common and accelerate disease progression. A combined rapid diagnostic test for HIV and hepatitis B/C has been proposed as a key measure for national screening programs in low-income countries with high prevalence of these infections<sup>92</sup>. Coupling early diagnosis of HIV and hepatitis B/C through sensitive molecular testing that is also portable

and simple to use with rapid notification via current mobile phone infrastructures provides an innovative and integrated approach to fight the spread of HIV/AIDS globally.

To summarize, all of the pathogen targets used in this thesis represent major infectious threats to the global community, necessitating the development of an effective and innovative means for detection and informatics to identify infected patients, enable proper treatment, notify at-risk individuals, accelerate clinical management, implement infection control measures and enhance surveillance to curb the rampant spread of these diseases.

## Chapter 2 Quantum Dot Barcodes

### 1 Introduction

In the last decade, researchers have developed a wide-array of barcoding structures and have demonstrated the detection of multiple biological targets in buffer, simultaneously. These barcodes comprise of graphical<sup>93,94</sup>, optical<sup>95,96</sup>, or magnetic<sup>97,98</sup> structures with unique patterns that identify surface coated bio-recognition molecules. The coated bio-recognition molecule can selectively recognize biological targets of interest (e.g. whole virus, antigen, or genetic sequence). Detection occurs when a fluorescently labeled secondary targeting agent is added to the barcode, forming a sandwich structure. The code identifies the coated recognition molecule, which identifies the target; and the secondary probe confirms the presence of the disease and the quantity. The advantage of using barcodes in a diagnostic setting is that multiple targets from patient samples can be detected simultaneously (i.e. multiplexing), which increase the speed of analysis as well as improve the precision and accuracy of diagnosis. Despite advances with the chemical design of barcodes, nanotechnology-based barcoding technologies have not advanced to patient care. The poor sensitivity (limit of detection of fmol to amol) limits their utility in a clinically relevant setting and their readout devices remain expensive, described previously.

In addition to the ones introduced above, barcodes can also be engineered by infusing polystyrene microbeads with different emitting quantum dots to create what has been called “quantum dot barcodes”<sup>99,100</sup>. Briefly, quantum dots are semiconductor crystals in the nanometer size range (**Figure 2.1**). By definition, they are particles whose physical dimensions are smaller than the exciton Bohr radius (i.e. electron-hole pair), which is usually below 100 nm<sup>101</sup>. They possess highly tunable optical properties as a result of their tunable size and composition (**Figure 2.2**). Quantum dots provide significant advantages over organic fluorophores for barcoding. They are brighter, have wider excitation spectra and narrower emission spectra, and are more resistant to photobleaching<sup>102–104</sup>. From a device perspective, these properties are attractive because they reduce the costs of manufacturing the diagnostic device and simplify the design of the readout system while giving high precision in identifying the optical code. This strategy also provides quantum dots with greater multiplexing capabilities, as the use of quantum dot in a non-barcoded detection system can differentiate only 5-6 unique signals<sup>103,104</sup> versus the potentially

(Removed)

**Figure 2.1. Size of nanoparticles.**

An illustration of the size scale of quantum dots and other nanoparticles. Figure adapted and modified from source<sup>105</sup> and not created by the author. (**Note:** Figure has been removed due to copyright restrictions, please refer to citation.)



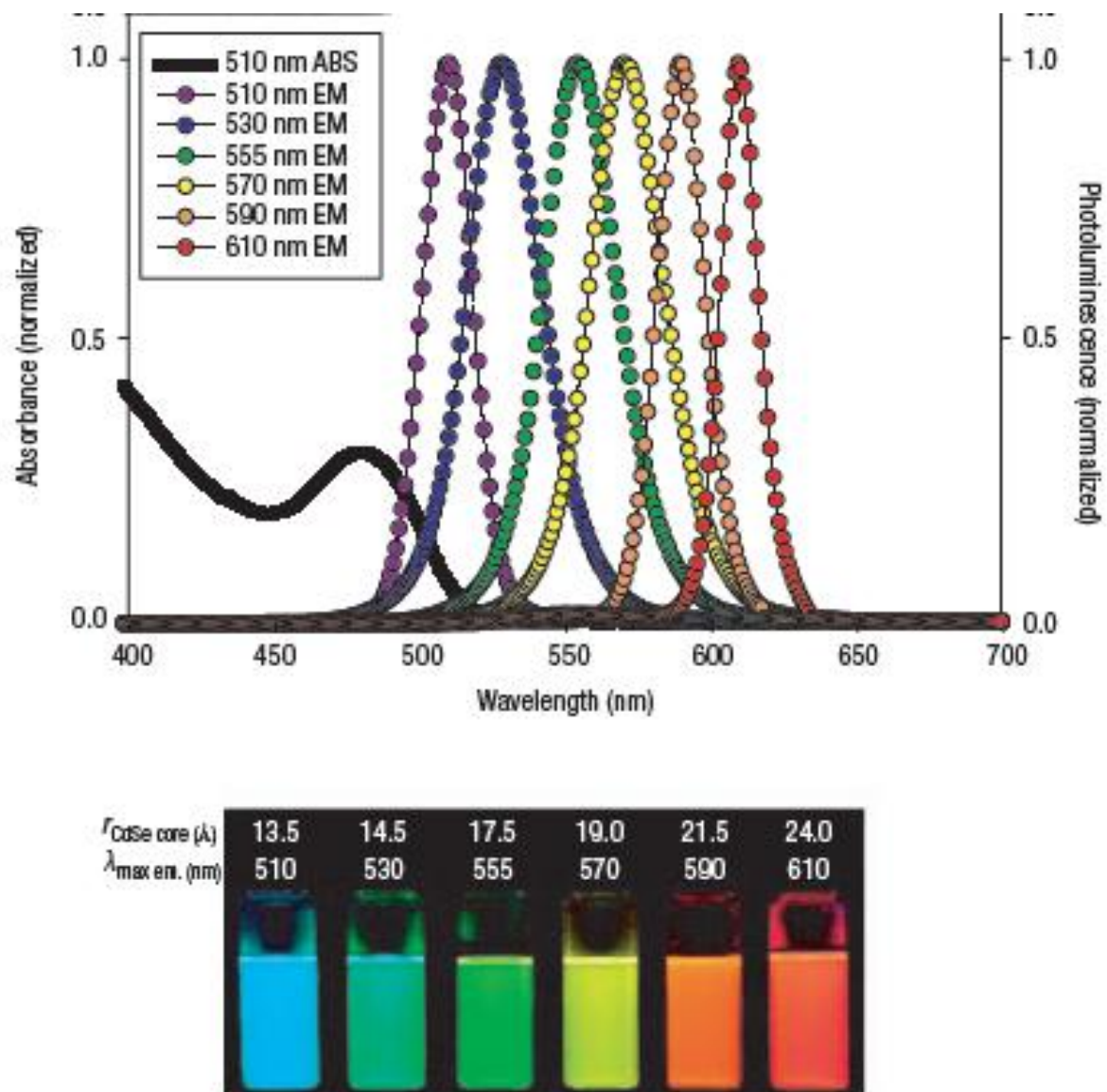


**Figure 2.2. Quantum dot tunability.**

An illustration of the optical tunability of quantum dots as a result of their size. Figures adapted from source<sup>106</sup> and not created by the author.

millions in a barcode format<sup>99</sup>. In fact, our group has previously demonstrated the ability to synthesize 105 optically-unique quantum dot barcodes using only five different quantum dot wavelengths at three intensity levels (**Figure 2.3**). Furthermore, the optical signals of the quantum dots are protected in the microbead from fluorescence fluctuations – which affect detection reproducibility – as the polystyrene reduces the interaction of the quantum dots with ions, proteins, and other biological molecules<sup>107,108</sup>. The microbeads themselves are also versatile in molecular detection and can detect both genomic or proteomic targets<sup>29,76,99</sup>.

Unfortunately, since its introduction in 2002, the quantum dot barcode has so far not translated well into the field. This is due to challenges associated with the synthetic reproducibility, lack of appropriate readout system, and analytical sensitivity. As a result, quantum dots barcodes have not advanced far for testing in patient samples. Through the last ten years, our group has optimized and solved the chemistry design issues and demonstrated their utility for detecting both genomic and proteomic targets using synthetic targets<sup>75,109</sup>. We have also developed a simple barcode synthesis process. Briefly, quantum dots dissolved in chloroform are mixed together in different ratios with a polymer-based solution. When this chloroform solution intersects with a high-pressure water stream inside a nozzle, microfluidic instability causes the fluid to “pinch off” and form microbeads<sup>110</sup>. The optical properties of these quantum dot microbeads reflect the combination and concentration of the quantum dots in the chloroform solution (**Figure 2.4**). Therefore, as a continuation of work done by our group, the aim of this thesis was to further the use of quantum dot barcodes for diagnostics in the field.

Thus far in literature, benefits of using quantum dot barcodes, particularly for use in point-of-care diagnostics where instrument portability and simplicity are crucial, have only been inferred through theoretical comparisons between quantum dots and organic fluorophores. In this chapter we compare the optical properties of microbeads encapsulated with organic fluorophores (“Yellow” with  $\lambda_{em} = 480$  nm, and “Nile Blue” with  $\lambda_{em} = 630$ nm) against those with quantum dots (“QD540” with  $\lambda_{em} = 530$  nm and “QD640” with  $\lambda_{em} = 640$  nm) on the bases of their absorption/excitation and emission spectral properties, as well as effects of photobleaching and imaging under single wavelength excitation.

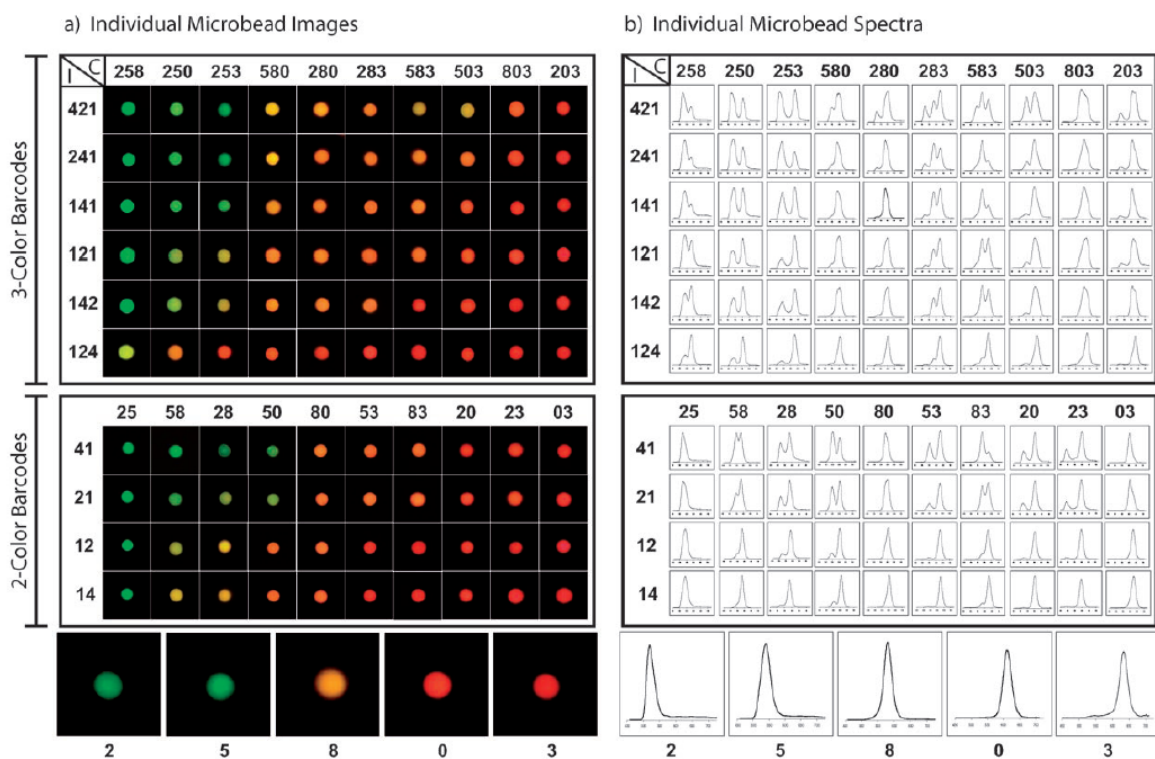


**Figure 2.3. Synthesis of a variety of quantum dot barcodes.**

A demonstration of the synthesis of 105 unique quantum dot barcodes using only five quantum dot wavelengths and three intensity levels. Figure adapted from source<sup>75</sup> and not created by the author.

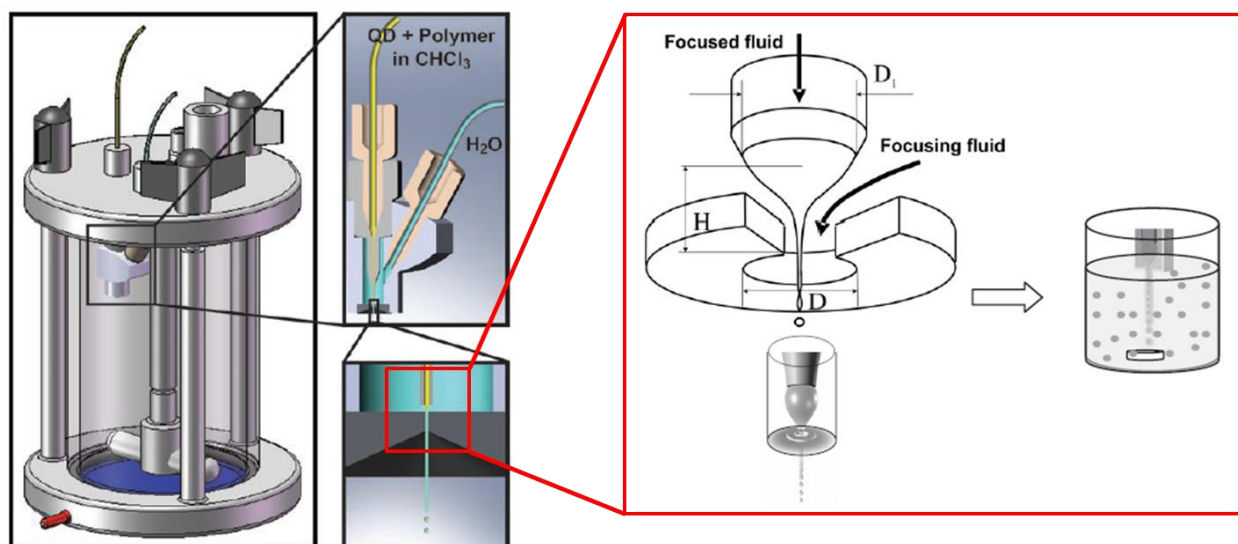


**Figure 2.4. Quantum dot barcode synthesis setup.**

An illustration of the apparatus with which quantum dot barcodes used in this thesis were synthesized. Figures adapted from sources<sup>75,110</sup> and not created by the author.

## 2 Experimental Methods

### 2.1 Organic Fluorophore Particles

The carboxyl functionalized, organic fluorophore-impregnated particles “Carboxyl Fluorescent Yellow Particles, Medium Intensity” ( $\lambda_{em} = 480$  nm, CFP-5052-2) and “Carboxyl Fluorescent Nile Blue Particles, Medium Intensity” ( $\lambda_{em} = 630$  nm, CFP-5065-2) were purchased from Spherotech. They were stored as instructed – in the dark, at room temperature – and used without additional processing.

### 2.2 Quantum Dot Synthesis

Quantum dots (CdSeS alloyed-ZnS capped) of peak emission wavelength 540 nm (“QD540”) were purchased from CytoDiagnostics and used as instructed. Quantum dots of peak emission wavelength 640 nm (“QD640”) were synthesized and characterized according to published procedures<sup>111,112</sup> and stored in chloroform at room temperature until later use. Quantum dot synthesis and characterization performed by **D. Li**.

### 2.3 Quantum Dot Barcode Synthesis

ZnS-capped CdSeS quantum dot barcodes were incorporated into polystyrene microbeads using a flow-focusing strategy, as described in a previous publication by our group<sup>75</sup>. Briefly, quantum dots (“QD540” and “QD640”) were mixed together in different ratios with a polymer-based solution: for barcode “QD540”, 6  $\mu$ L/mL of “QD540” was added to the solution; for barcode “QD640”, 910  $\mu$ L/mL of “QD640” was added to the solution. The polymer solution consisted of poly(styrene-co-maleic anhydride) (32%, cumene terminated) from Sigma-Aldrich dissolved in chloroform, with the polymer concentration at 4-wt%. The resultant quantum dot polymer solution was then introduced into a nozzle system from Ingeniatics using a syringe pump from Harvard Apparatus at a rate of 0.9 mL/hour, as well as double-distilled water as the focusing fluid at a rate of 180 mL/hour. The nozzle system was then submerged inside a beaker partially filled with double-distilled (DD) water. The polymeric barcode microbeads were synthesized in situ, and the microbeads formed a white colloidal suspension in the water. After synthesis, the valve was closed and the microbeads were stabilized by overnight stirring and then collected. The microbeads were filtered using 35  $\mu$ m BD Falcon nylon mesh strainer cap, and characterized using an automated Beckman Coulter Vi-Cell counter, and stored in DD water at 4 °C until use.

Note that the microbead size can be increased by increasing the polystyrene solution injection rate.

## 2.4 Excitation, Absorption, and Emission Spectra Measurement

The excitation and emission spectra of the “Yellow” and “Nile Blue” fluorescent particles were measured using the “Excitation Acquisition” and “Emission Acquisition” modes, respectively, on Horiba Jobin Yvon FluoroMax-3 fluorometer. The fluorophores used in the “Yellow” and “Nile Blue” fluorescent particles could not be obtained to perform absorption measurements due to proprietary reasons. The quantum dot absorption spectra were measured using Shimadzu UV-1601PC UV-Visible spectrophotometer. The quantum dot barcode emission spectra were measured using the “Emission Acquisition” mode on Horiba Jobin Yvon FluoroMax-3 fluorometer.

## 2.5 Photobleaching Measurements

To measure photobleaching, the samples were excited continuously for 3 minutes while images were being acquired at 10-second intervals. The mean intensity of all microbeads in the image for each sample was calculated using image processing performed on MATLAB from MathWorks.

## 2.6 Sample Imaging

To image the microbead samples, 1  $\mu\text{L}$  of it was deposited on a chip surface and let dry for 1 hour. The chip was placed under a microscopy-based setup such that the micrometer-sized microbeads were excited using a 405 nm diode laser and imaged through a  $\lambda_{\text{em}} = 430\text{LP}$  emission filter using a smartphone camera iPhone 4S from Apple.

# 3 Results & Discussion

## 3.1 Spectral Properties

As the spectra demonstrate, the quantum dots have a continuous absorption profile while the organic fluorophore equivalent has peak-like profiles (**Figure 2.5**). The absorbance profile presents a significant advantage for quantum dots for engineering point-of-care device. This would reduce the size and thus costs of the final device as a quantum dot barcode device will

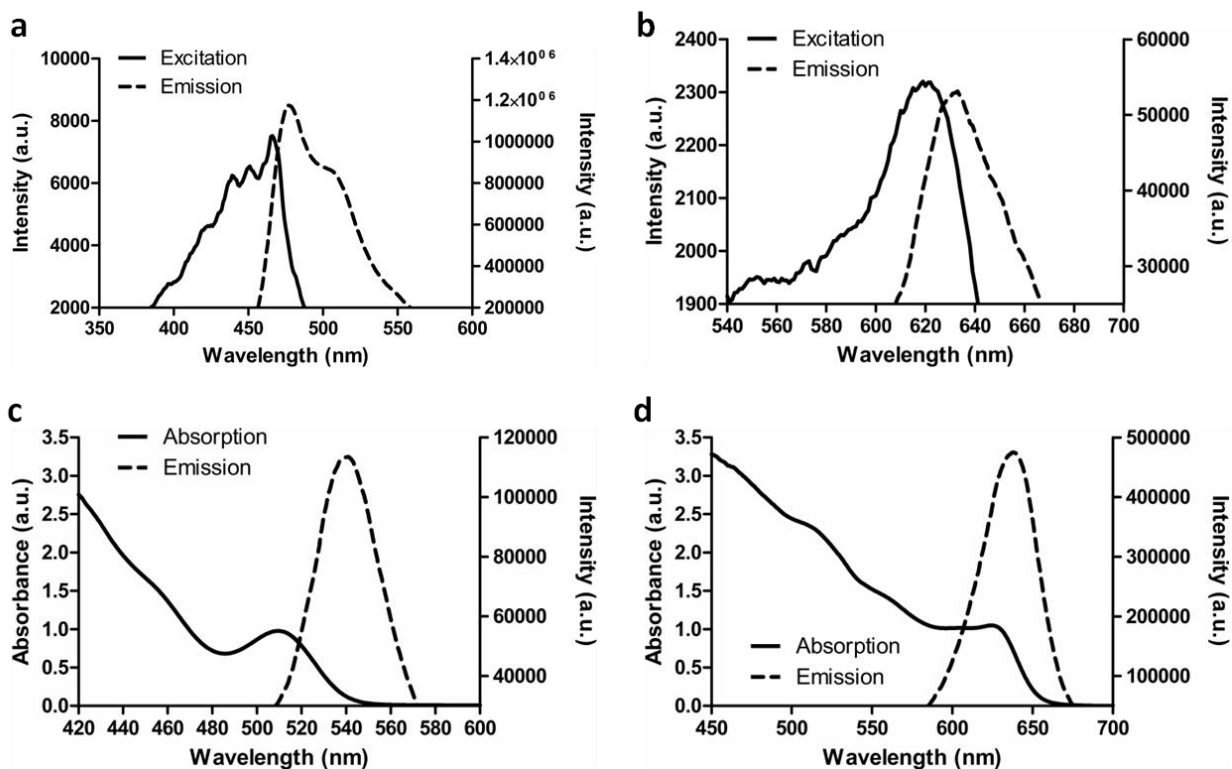


**Figure 2.5. Comparing excitation/absorption and emission spectra.**

Polymeric particles impregnated with fluorophores (a) "Yellow" and (b) "Nile Blue" were compared with quantum dot barcodes impregnated with (c) "QD540" and (d) "QD640", in terms of their excitation/absorption and emission spectra. Figure created by the author. Reprinted (adapted) with permission from source<sup>113</sup>. Copyright 2015 American Chemical Society.

only require a single energy source to excite all of the barcodes while similar particles using organic fluorophores will require multiple emitting diodes or lasers to maximally excite different wavelengths. The organic fluorophore particles' peak excitation and emission wavelengths are also near overlaying, unlike those of the quantum dot barcodes'. This means that appropriate wavelength channels/filters need to be implemented to ensure that the excitation wavelength is blocked from interfering or overpowering the sample emission wavelength if maximal excitation is desired.

### 3.2 Effects of Varying Excitation on Emission

The quantum dot barcodes also have narrower emission profiles (**Figure 2.6**). This is more apparent between the full-width half-maximum of "QD540" (~35 nm) and "Yellow" (~60 nm). Furthermore, the quantum dot barcodes retain their emission peaks despite being excited by different wavelengths. In the case of "Nile Blue" the peak emission wavelength varies ~10 nm between excitation wavelengths of 550 nm and 570 nm, while the peak emission wavelength remains the same for "QD640". The excitation wavelength also has a much larger impact on the fluorescent particles' emission intensity. This is most evident between "Yellow" and "QD540", which experienced a 163% and 25% change in intensity, respectively, when the excitation wavelength increased from 405 nm to 450 nm. These illustrate quantum dot barcodes' resistance to changes in the excitation. As a result, these enable greater number of quantum dot barcodes to be engineered for multiplexing analysis, and reduce the likelihood of false barcode identification.

### 3.3 Photobleaching

To study photobleaching, we excited both types of microbeads continuously and examined their intensity changes. Indeed quantum dot barcodes were much more resistant to photobleaching compared to the organic fluorophore-encapsulated particles (**Figure 2.7**). This is important for accurate barcode identification as bleaching of coded microbeads can lead to misdetection. Note that the slight increase in relative intensity for the quantum dot barcodes under continuous excitation is likely due to photoactivation<sup>114</sup>. Briefly, physical defects exist on the surface of quantum dots that act as traps for electron-hole pair recombination, resulting in non-radioactive relaxation that lowers quantum yield. Photoactivation describes the phenomenon whereby the



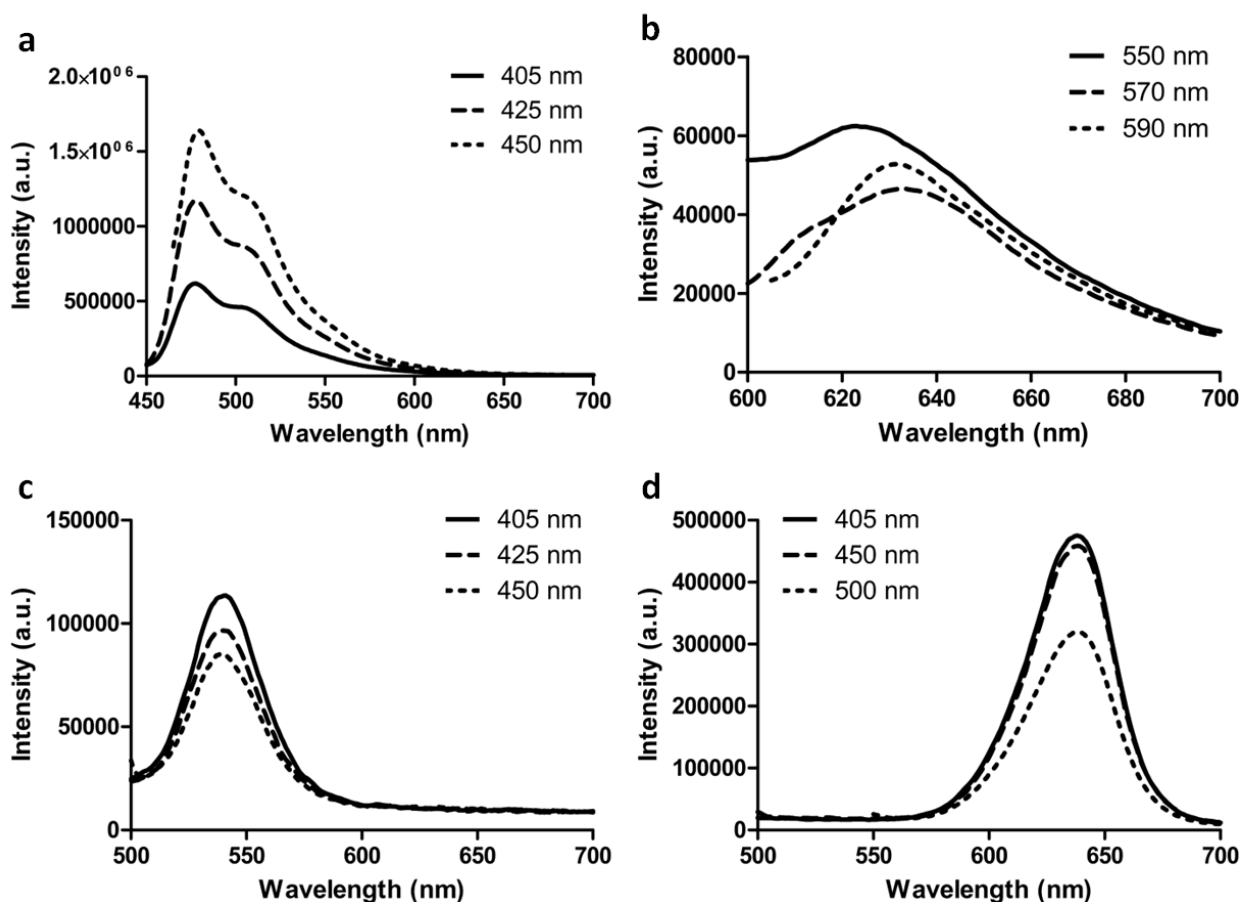


**Figure 2.6. Comparing emission spectra under varying excitation.**

Polymeric particles impregnated with fluorophores (a) "Yellow" and (b) "Nile Blue" were compared with quantum dot barcodes impregnated with (c) "QD540" and (d) "QD640", in terms of their emission spectra under varying excitation wavelengths. Figure created by the author. Reprinted (adapted) with permission from source<sup>113</sup>. Copyright 2015 American Chemical Society.

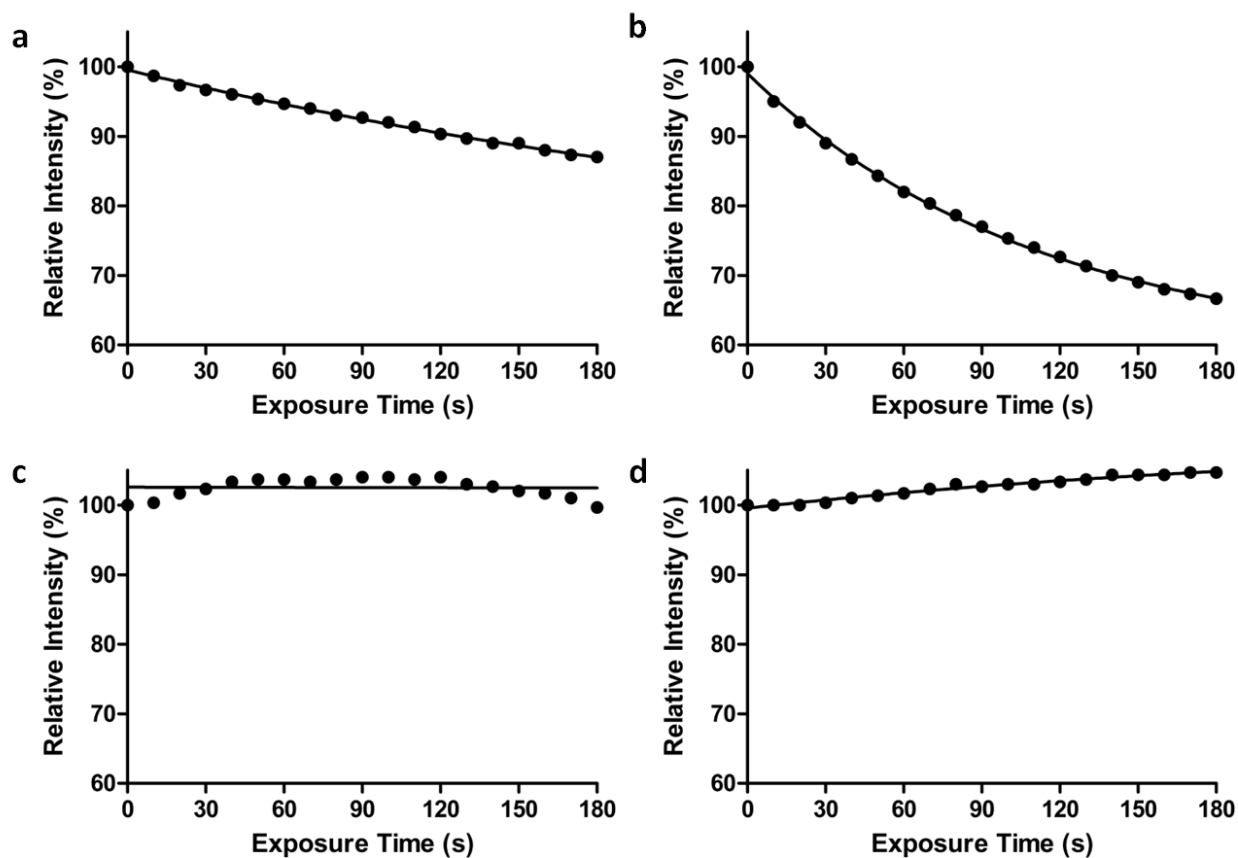


**Figure 2.7. Comparing photobleaching.**

Polymeric particles impregnated with fluorophores (a) “Yellow” and (b) “Nile Blue” were compared with quantum dot barcodes impregnated with (c) “QD540” and (d) “QD640”, in terms of photobleaching under continuous excitation. Figure created by the author. Reprinted (adapted) with permission from source<sup>113</sup>. Copyright 2015 American Chemical Society.

quantum dot surface is smoothed from continuous irritation by the excitation source, eliminating these defects and thus enhancing the quantum yield, albeit temporarily.

### 3.4 Single-Source Imaging

As a final test, both the fluorophore particles and quantum dot barcodes were excited using a 405 nm source and imaged (**Figure 2.8**). While “Yellow” fluoresced appropriately, albeit with low intensities, “Nile Blue” was not fluorescing. In fact, the grey colouration observed was likely due to auto-fluorescence of the particles’ polymer, or simply light scattered off of the particles’ surface. On the other hand, both types of quantum dot barcodes fluoresced brightly and properly. This demonstrates that even when their maximum emission wavelengths vary widely (540 nm vs. 640 nm), quantum dot barcodes can be excited using the same excitation wavelength.

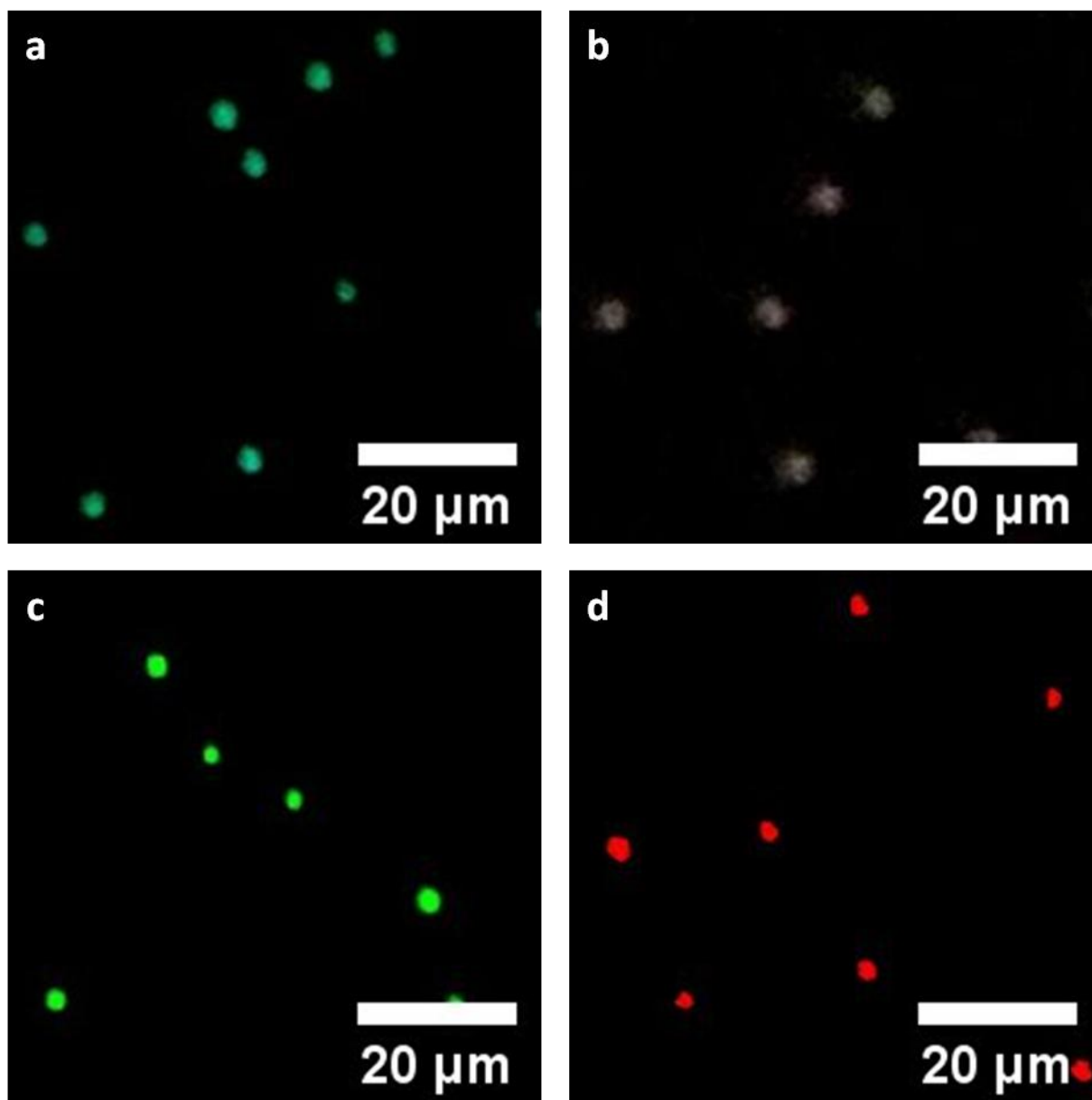


**Figure 2.8. Comparing single source imaging.**

Polymeric particles impregnated with fluorophores (a) “Yellow” and (b) “Nile Blue” were compared with quantum dot barcodes impregnated with (c) “QD540” and (d) “QD640”, in terms of their visual images under a 405 nm excitation source. Figure created by the author. Reprinted (adapted) with permission from source<sup>113</sup>. Copyright 2015 American Chemical Society.

## 4 Chapter Summary

In this chapter we demonstrated and confirmed that quantum dots are indeed more advantageous compared to traditional fluorophores because they have wider excitation spectra, narrower emission spectra, and are more resistant to photobleaching. These traits are critical for engineering point-of-care diagnostics capable of multiplexing. Specifically, these unique optical properties mean that quantum dot barcodes can be excited using the same source, engineered to allow more variety and thus multiplexing capabilities within a given range of wavelengths, and be detected with greater certainty. Combined, these desirable qualities simplify the readout device, reduce its cost and size, and enhance accuracy.

## 5 Author Contributions

The experiments were designed by the **K. Ming** and **W.C.W. Chan**. Experiments were performed by **D. Li** (quantum dot synthesis) and **K. Ming** (all others). Analyses were performed by the **K. Ming**. Algorithms were written by the **K. Ming**. This chapter was written by the **K. Ming** with contributions by **W.C.W. Chan**.

## Chapter 3

### Quantum Dot Barcode Readout and Resolution Algorithm

#### 1 Introduction

In the previous chapter we demonstrated quantum dot barcodes' advantages over that of traditional organic fluorophore particles' for point-of-care multiplex detection. Optically-encoded microbeads – infused with quantum dots or otherwise – in literature have so far been used in conjunction with flow cytometers<sup>29,50,51,115</sup>, microfluidic chips<sup>76,116–118</sup>, or optical fiber systems<sup>23,24</sup>. While many have become established laboratory practices, these techniques are not suitable for diagnostic applications in resource-limited settings. First, the microbeads are typically stored in solution before use, which add burden to transportation. Second, they all require bulky or expensive instrumentation (e.g. flow cytometers, pumps, fiber optic imaging hardware). Finally, a skilled technician is required to perform the experiments and interpret the results because subtle differences in microbead number, incubation time, and microbead stability can influence the analytical performance. The ability to array these barcoded microbeads on a chip would alleviate some of these issues and reduce complexity.

To overcome these, we developed (1) a solid-phase platform for quantum dot barcodes that can be easily transported, and (2) an image-based algorithm for barcode analysis and resolution, to take advantage of the imaging capabilities of all modern-day cell phones or smartphones. In this chapter, we describe such developments. First we identified the platform on which our barcoded microbeads can be immobilized and dispersed, with controlled number of microbeads per unit area, maintaining assay consistency. Such a platform would be a step towards reducing the burden of transportation by removing the need to transport the barcodes in solution, as well as making the system more user-friendly by reducing the number of liquids involved when performing the assay. We then demonstrate that the signals from the barcodes can be interpreted and uniquely identified using an imaging-based approach, without the need for dedicated, expensive, or bulky instrumentation. Finally, we describe the custom-written algorithm we have developed to resolve the barcodes using the images, and demonstrated the resolution of nine barcodes with high accuracy.

## 2 Experimental Methods

### 2.1 Quantum Dot Synthesis

Quantum dots (CdSeS alloyed-ZnS capped) of peak emission wavelength 540 nm (“QD540”) were purchased from CytoDiagnostics and used as instructed. Quantum dots of peak emission wavelengths 589 nm (“QD589”) and 640 nm (“QD640”) were synthesized and characterized by according to published procedures<sup>111,112</sup> and stored in chloroform at room temperature until later use. Quantum dot synthesis and characterization performed by **D. Li**.

### 2.2 Quantum Dot Barcode Synthesis

ZnS-capped CdSeS quantum dot barcodes were incorporated into polystyrene microbeads using a flow-focusing strategy, as described a previous publication by our group<sup>75</sup>. Briefly, quantum dots (“QD540”, “QD589”, and “QD640”) were mixed together the in different ratios with a polymer-based solution (**Table 3.1**). The polymer solution consisted of poly(styrene-co-maleic anhydride) (32%, cumene terminated) from Sigma-Aldrich dissolved in chloroform, with the polymer concentration at 4-wt%. The resultant quantum dot polymer solution was then introduced into a nozzle system from Ingeniatics using a syringe pump from Harvard Apparatus at a rate of 0.9 mL/hour, as well as double-distilled water as the focusing fluid at a rate of 180 mL/hour. The nozzle system was then submerged inside a beaker partially filled with DD water. The polymeric barcode microbeads were synthesized in situ, and the microbeads formed a white colloidal suspension in the water. After synthesis, the valve was closed and the microbeads were stabilized by overnight stirring and then collected. The microbeads were filtered using 35  $\mu\text{m}$  BD Falcon nylon mesh strainer cap, and characterized using an automated Beckman Coulter Vi-Cell counter, and stored in double-distilled water at 4 °C until use. Note that the microbead size can be increased by increasing the polystyrene solution injection rate.

### 2.3 Barcode Microbead Deposition on Microwell Chip

For most experiments involving imaging barcode microbeads on a microwell chip from MicroPep, samples with concentration of  $10^7$  microbeads/mL were prepared in DD water containing 0.05% Tween. Then 1  $\mu\text{L}$  of it was deposited directly on the microwell chip, which was rinsed with DD water and allowed to dry prior to deposition, and let dry for 1 hour before imaging.

**Table 3.1. List of quantum dot barcode synthesis parameters.**

<b>Barcode Name</b>	<b>QD540 Concentration (μL/mL)</b>	<b>QD589 Concentration (μL/mL)</b>	<b>QD640 Concentration (μL/mL)</b>
550	5	5	
505	5		5
055		5	5
135	1	3	5
315	3	1	5
351	3	5	1
513	5	1	3
531	5	3	1
555	5	5	5

Table created by the author. Reprinted (adapted) with permission from source<sup>113</sup>. Copyright 2015 American Chemical Society.



For studying microwell filling efficiency of barcode microbeads on the microwell chip, samples with concentration of  $10$  to  $70 \times 10^6$  microbeads/mL were prepared in DD water containing 0.05% Tween. The samples were then sonicated for 5 minutes to reduce microbead aggregation before depositing 30  $\mu$ L of each on the microwell chip, which was rinsed with DD water and allowed to dry prior to deposition. The chip was then placed in an enclosed drying chamber containing desiccant to prevent dust particle contamination, and then allowed 2 hours to dry before imaging.

## 2.4 Microwell Fill Efficiency

To characterize the filling efficiency of microwells on the microwell chip by the microbeads, an image of the chip without the microbeads was obtained. Under the 20x microscope objective we observed 80 microwells horizontally and 52 microwells vertically to obtain a total of 4160 microwells in the image. We then varied the concentration and size of the microbeads, then calculated the percentage of microwells filled with microbeads relative to the total number of microwells present.

## 2.5 Sample Imaging

All images were acquired using RETIGA EXi Fast Cooled Mono 12-bit charge-coupled diode (CCD) camera from QImaging, mounted on an Olympus IX70 Inverted microscope at 20x objective for all images (20x objective, NA = 0.50), unless specified as 32x objective (20x objective, NA = 0.50, with 1.6x further magnification). Quantum dot barcodes were excited using a 100 W mercury lamp attached to the microscope, under oblique illumination unless otherwise specified, through excitation-emission filter sets [ $\lambda_{\text{ex}} = 350/50$ ,  $\lambda_{\text{em}} = 430\text{LP}$ ] (Thorlabs), [ $\lambda_{\text{ex}} = 480/40$ ,  $\lambda_{\text{em}} = 530/10$ ] (Thorlabs), [ $\lambda_{\text{ex}} = 480/40$ ,  $\lambda_{\text{em}} = 580/10$ ] (Thorlabs), and [ $\lambda_{\text{ex}} = 480/40$ ,  $\lambda_{\text{em}} = 640/10$ ] (Thorlabs). The emission filters  $\lambda_{\text{em}} = 530/10$ ,  $\lambda_{\text{em}} = 580/10$ , and  $\lambda_{\text{em}} = 640/10$  corresponded with quantum dots “QD540”, “QD589”, and “QD640”, respectively, and were used to isolate for their fluorescence for resolving barcodes. Image exposure times, adjustable using the software Image-Pro Plus from Media Cybernetics, were 50, 200, 200, and 200 for the emission filters  $\lambda_{\text{em}} = 430\text{LP}$ ,  $\lambda_{\text{em}} = 530/10$ ,  $\lambda_{\text{em}} = 580/10$ , and  $\lambda_{\text{em}} = 640/10$ , respectively.

## 2.6 Image Processing and Analysis

All image processing and analysis were performed using MATLAB from MathWorks unless otherwise specified.

## 2.7 Image Registration

Image registration to align the various filter images was performed using the discrete-Fourier transform registration, available as an open-source MATLAB plug-in<sup>119,120</sup>. The algorithm accepts as inputs two images: a reference image and a moving image. The 430LP filter image was used as the reference image and all other filter images were inputted as the moving image to be aligned to the reference image. A registration factor of “1” (i.e. simple translation of pixels) was used over upsampling factor  $> 1$  (i.e. for sub-pixel value registration) to preserve the original intensity values, without smoothing and intensity extrapolation, as well as for simplicity.

## 2.8 Barcode Image Extraction

The binary mask approach first used the image morphological technique of erosion (“imerode” function in MATLAB) to remove small particles (i.e. debris or overly small barcodes) and smooth over sharp intensities to produce a “thinned” version of the microbeads. Then, the image morphological technique of dilation (“imdilate” function in MATLAB) was applied to “thicken” the microbeads back to their original size, ideally without re-introducing the small particles. Then a common edge detection algorithm (i.e. Sobel, Canny, Prewitt, or Roberts, all found in MATLAB and each was tested), was applied to detected the microbeads’ outlines. Finally, region filling (“imfill” function in MATLAB) was applied to “fill-in” the outlines to create a binary mask (i.e. “1” for microbead and “0” for background).

The Hough transform, available as an open-source MATLAB plug-in, (input parameters: range of radii = [0,15]; lower bound intensity = 0.15; filter radius = 8)<sup>121,122</sup>, was used to determine both the location and size of each microbead directly, without any pre- or post-processing.

## 2.9 Barcode Identification using Maximum Intensity Approach

The algorithm compares the highest intensity or highest intensity difference from the interrogated microbead’s profile against the set of known barcode intensity profiles. The barcode with the most similar maximum intensity is designated as the microbead’s barcode. Specifically,

between two possibilities “B<sub>high</sub>” (with higher mean intensities) and “B<sub>low</sub>” (with lower mean intensities) a threshold was defined for “B<sub>low</sub>”:

$$I_{barcode} = I_{mean} + I_{STD}$$

**Equation 3.1**

where

$I_{barcode}$  = Intensity threshold for “B<sub>low</sub>”.

$I_{mean}$  = Mean intensity of “B<sub>low</sub>”

$I_{STD}$  = Intensity standard deviation of “B<sub>low</sub>”.

This threshold was calculated for the highest intensity amongst the three filters  $\lambda_{em} = 530/10$ ,  $\lambda_{em} = 580/10$ , and  $\lambda_{em} = 640/10$  for “B<sub>low</sub>”. If the highest intensities were similar in value between “B<sub>low</sub>” and “B<sub>high</sub>”, the second highest filter intensity was used. With this, if the microbead’s corresponding filter intensity was equal to or lower than  $I_{barcode}$ , the barcode of interest was “B<sub>low</sub>”, otherwise “B<sub>high</sub>” was chosen.

## 2.10 Barcode Identification using Euclidean Distance Approach

The algorithm calculates the Euclidean Distance between the interrogated microbead’s intensity profile and the known barcode intensity profiles:

$$D_E = |I_{unknown} - I_{known}| = \sqrt{(I_{unknown@530/10} - I_{known@530/10})^2 + (I_{unknown@580/10} - I_{known@580/10})^2 + (I_{unknown@640/10} - I_{known@640/10})^2}$$

**Equation 3.2**

where

$D_E$  = Euclidean distance.

$I_{unknown}, I_{known}$  = Intensity profile of the unknown and known barcodes, respectively.

$I_{B@λ=530/10}$  = Intensity value of barcode  $B$  at the  $λ_{em} = 530/10$  filter.

$I_{B@λ=580/10}$  = Intensity value of barcode  $B$  at the  $λ_{em} = 580/10$  filter.

$I_{B@λ=640/10}$  = Intensity value of barcode  $B$  at the  $λ_{em} = 640/10$  filter.

The barcode of interest was identified as the barcode whose known intensity profile resulted in the smallest Euclidean distance.

## 2.11 Barcode Identification using Two-Step Maximum Intensity or Euclidean Distance Approach

A microbead was first categorized according to its highest to lowest intensities among the filters  $λ_{em} = 530/10$ ,  $λ_{em} = 580/10$ , and  $λ_{em} = 640/10$ . Then from the set of select barcodes either the maximum intensity or Euclidean distance approach, described above, was used.

## 2.12 Barcode Identification Accuracy Confirmation using Flow Cytometry

To confirm the accuracy of the barcode identification process, a mixture of barcodes was prepared by extracting and mixing 50  $μL$  of each type of barcode synthesized. Then, 200  $μL$  was analyzed using flow cytometry to determine the percentage of each type of barcode present in the mixture. And 20  $μL$  of the barcode mixture was deposited on the microwell, let dry for 4 hours, and analyzed using our algorithm. The two sets of percentages were then compared to determine the accuracy by the following equation:

$$\text{Analysis Accuracy (\%)} = \frac{(\text{Expected Count}) - |(\text{Analysis Count}) - (\text{Expected Count})|}{(\text{Expected Count})}$$

**Equation 3.3**

where

*Analysis Accuracy* = Estimated accuracy of our barcode identification approach.

*Expected Count* = Expected number of microbead count for each barcode type, obtained from flow cytometry.

*Analysis Count* = Actual number of microbead count for each barcode type, obtained by from analysis approach.

## 3 Results & Discussion

### 3.1 Microwell Chip Platform

Thus far in the thesis the microbeads had been deposited on traditional glass slides during imaging, while the samples were still in solution phase, before they dry. At low exposure times (~200 ms) the image can be acquired without issues, albeit with minor aggregations (**Figure 3.1a**). However, at high exposures (> 250 ms), the minute movements of the microbeads resulted in blurred images. Worse still, if multiple images need to be taken of the same field of view – with multiple filters for example – each microbead would not be aligned across the images, again due to their minute movements in the solution phase. To overcome these issues, we attempted to allow the microbeads to dry on the surface before imaging. While they were indeed immobilized, the microbeads experienced high levels of aggregation (**Figure 3.1b**), which can confound their signal readout as the fluorescence signals can interfere with one another. Various methods were attempted – including varying microbead concentrations, adding different concentrations of Tween, and using agarose for immobilization – to no effect. Aside from the use agarose, which hardened over the surface and thus undesirable for performing assays, microbeads under conditions of simple drying were also easily washed away, rendering the barcoded chip useless during assay conditions.

Fortunately, we were able to identify a specially-fabricated 3.0  $\mu\text{m}$ -sized microwell chip from MicroPEP (**Figure 3.2a and b**). Once the microbeads, engineered to be ~3  $\mu\text{m}$  in size, were deposited they settled into each microwell with high dispersion (i.e. reduced aggregation) (**Figure 3.2c**). This facilitated microbead image analysis as it reduced the likelihood of cross-talk between barcode signals. More importantly, the microbeads did not easily desorb from the chip once the sample dried and were bound, even during washing (**Figure 3.2d**). We believe these microbeads were held in place by non-covalent forces. But due to the proprietary nature of the

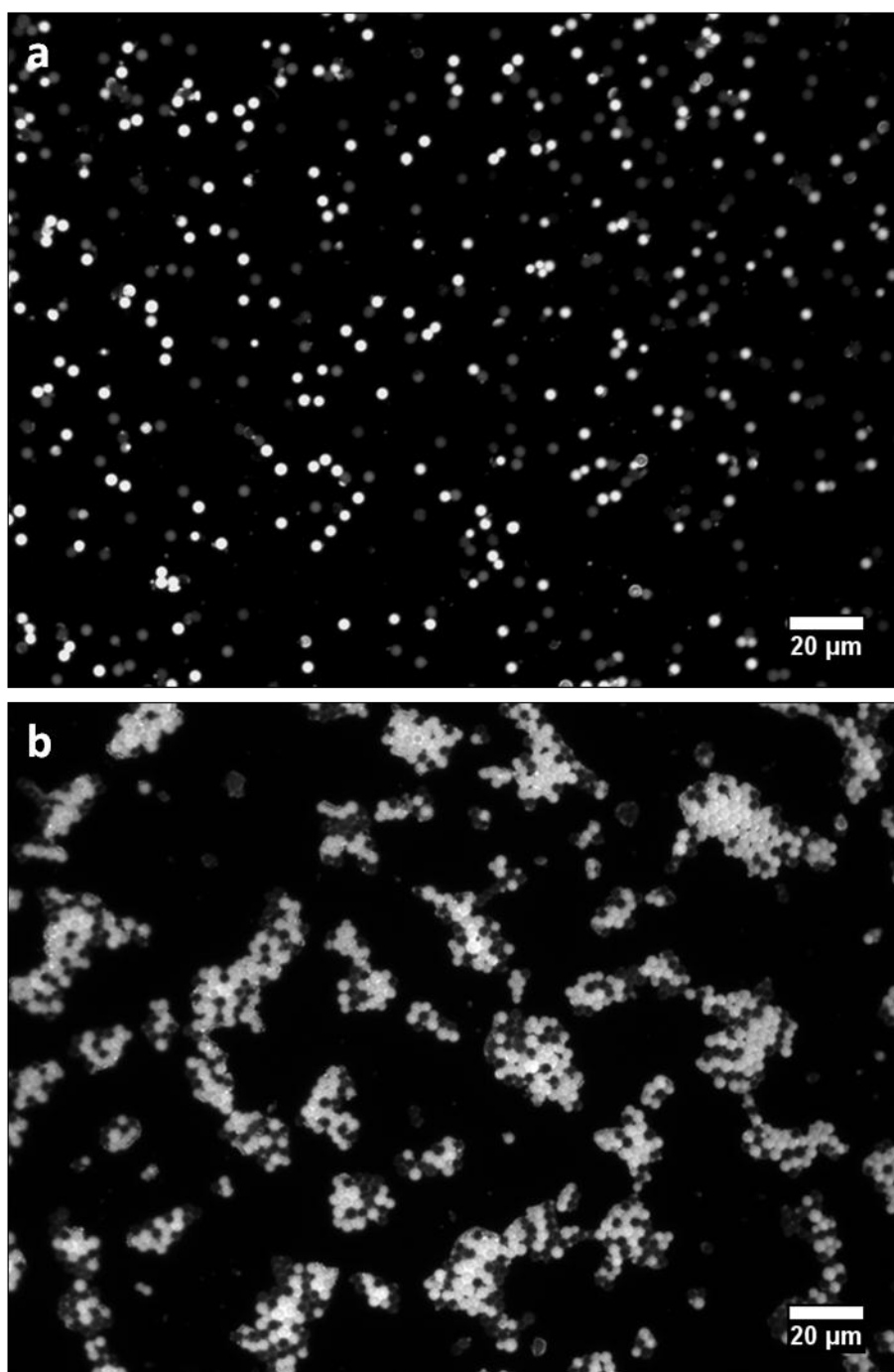


**Figure 3.1. Quantum dot barcodes on glass side.**

Two types of quantum dot barcodes deposited on a glass slide, imaged using fluorescence microscopy (a) before and (b) after the spotted sample had dried.

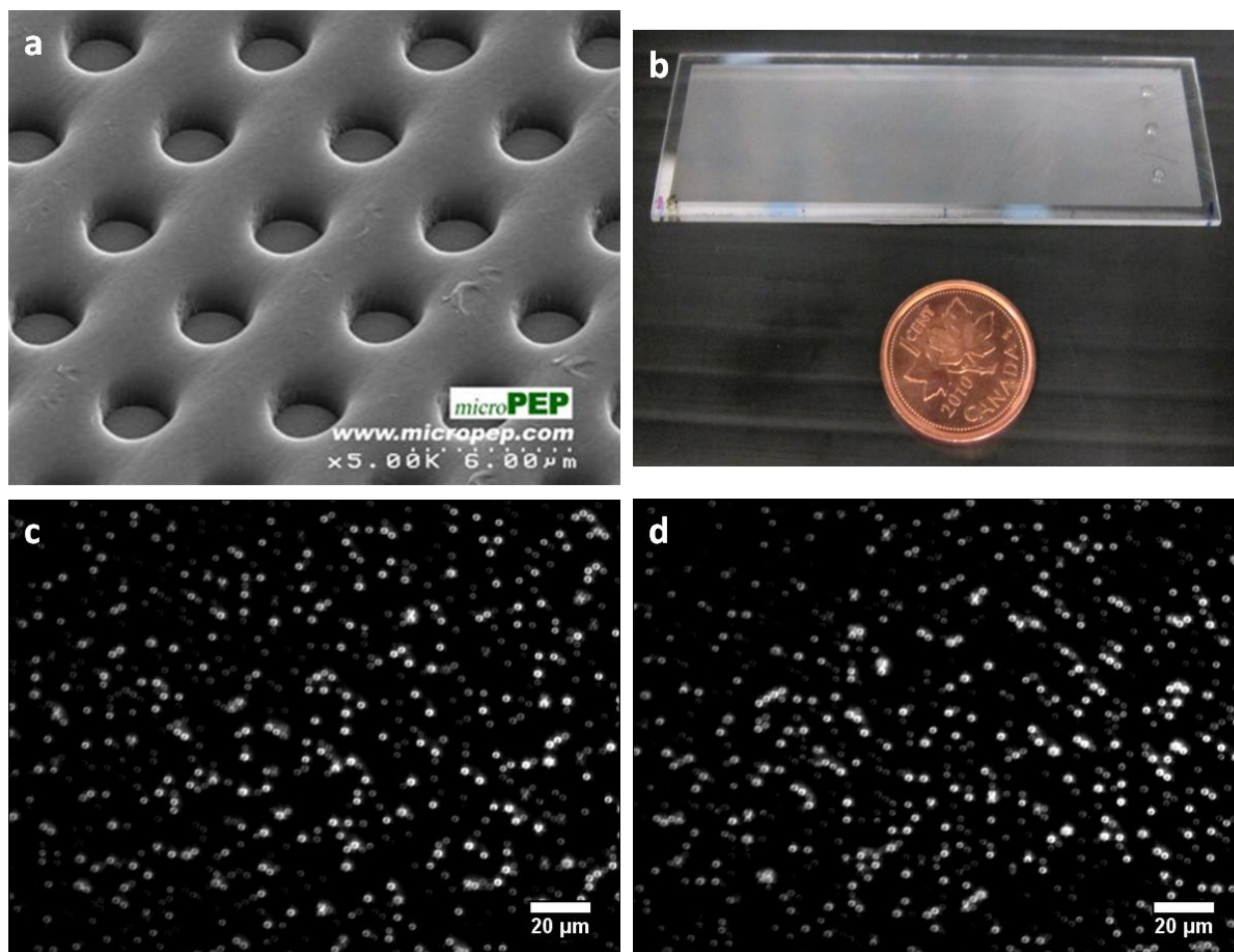


**Figure 3.2. Microwell chip.**

(a) Scanning electron microscopy of the microwell chip surface (courtesy of MicroPeP). (b) Physical size of the chip, with a penny for scale. Transillumination excitation of two types of quantum dot barcodes deposited and dried on the chip (c) before and (d) after washing with 0.05% Tween in DD water, imaged using fluorescent microscopy. Figure created by the author. Reprinted (adapted) with permission from source<sup>113</sup>. Copyright 2015 American Chemical Society.

chip we were unable to verify the precise mechanism. To characterize the filling efficiency of microwells by the microbeads on the chip, an image of the chip without the microbeads was obtained. Under the 20x microscope objective we observed 80 microwells horizontally and 52 microwells vertically to obtain a total of 4160 microwells in the image (**Figure 3.3a**). We then varied the concentration and size of the microbeads, and calculated the percentage of microwells filled with microbeads relative to the total number of microwells present (**Figure 3.3b and c**). Expectedly, the fill efficiency and microbead concentration are positively correlated and exist in a logarithmic relationship such that it is linearly increasing until  $\sim 20 \times 10^6$  microbeads/mL, then the rate of fill efficiency increase is reduced as the microbeads saturate the area affected. In terms of how microbead size affects fill efficiency, we limited our study to microbeads between 2-3  $\mu\text{m}$  in size. We found that the smaller microbeads achieved higher fill efficiency. For microbeads larger than 3  $\mu\text{m}$ , or the size of the microwells, we observed that they did not settle well into the microwells and tended to form many aggregates, and thus were not included in the study. Microbeads smaller than 2  $\mu\text{m}$ , on the other hand, are on the fringe of imaging resolution capabilities of many cell phone- or smartphone-based imaging systems<sup>64,66,68,69</sup>, and were not considered.

### 3.2 Approaches and Algorithms to Resolving Fluorescently-Encoded Microbeads

Polymeric microbeads impregnated with fluorescent agents – either organic dyes or quantum dots – in different concentrations at different emission wavelengths need to be resolved from one another in order for them to be used for multiplexed detection. That is, their fluorescence signatures need to be differentiated either spectrally or optically from one another so that they can be employed to identify their respective pathogen or analyte accurately during detection. This can be done using instrumentation that acquires the emission spectra unique to each encoded microbead<sup>117,123</sup>. This can also be done using flow cytometry, which detects fluorescence signals at different channels that correspond to the different emission wavelengths within each encoded microbead<sup>27,52,124</sup>. Such a technique is also used in commercial systems due to its popularity<sup>125,126</sup>, and has become a gold standard approach for microbead readout. Both fluorescence spectroscopy and flow cytometry yield robust and accurate results but their identification capabilities rely on the sophistication of their readout instrumentation.



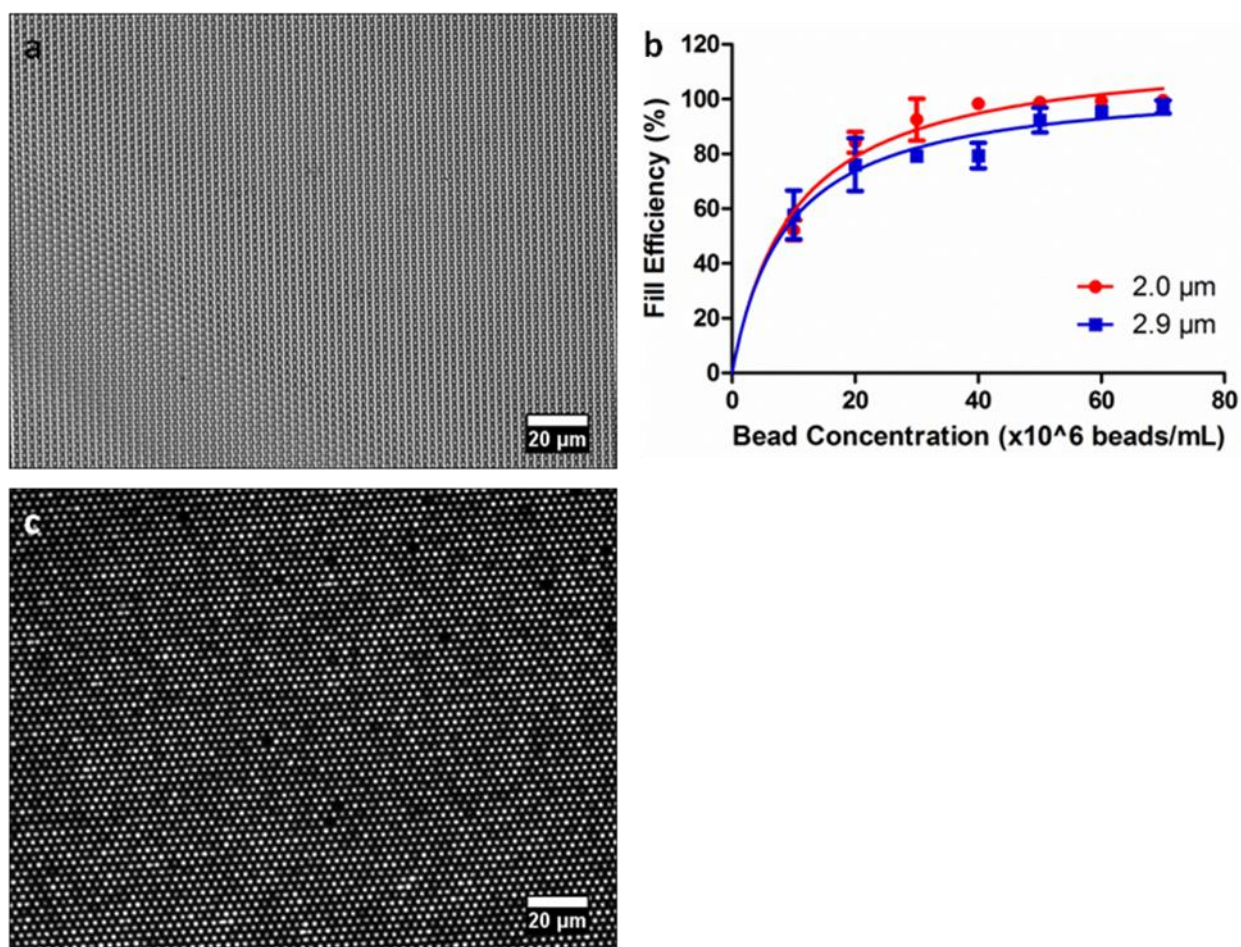


**Figure 3.3. Microwell fill efficiency.**

(a) An un-filled microwell chip imaged using bright-field microscopy. (b) Fill efficiency characterization using 2.0- and 2.9-μm microbeads. (c) An example fluorescent microscopy image of the microwell chip deposited with 2 μm microbeads at  $60 \times 10^6$  microbeads/mL. Data represent the mean and standard deviation from three replications. Figure created by the author. Reprinted (adapted) with permission from source<sup>113</sup>. Copyright 2015 American Chemical Society.

As was discussed in the Chapter 1, while such tests can be used in the laboratory in developing countries, such techniques that require expensive and bulky instruments as well as trained personnel for operation are not suitable for point-of-care purposes in resource-limited settings.

The use of software algorithms to differentiate between different encoded microbeads or fluorescence signals is another approach. Typically in these schemes, complexities in the instrumentation for data acquisition are reduced in favour of more sophistication written into the algorithm to differentiate between the fluorescence signatures. This is more attractive from the perspective of point-of-care diagnostics since unlike hardware, software does not increase transportation difficulty and can be made to be simple to use. Of course, ultimately how an algorithm functions is dependent on the data acquired, which is in turn dependent on the acquisition hardware. But in general the more “intelligence” that is built into the software means less is required from the hardware end.

Sophisticated software and hardware can be combined to resolve a high number of encoded microbeads. In one of our group’s previous studies<sup>108</sup>, the emission spectra (i.e. Gaussian profiles) of four quantum dots used to synthesize quantum dot barcodes were determined and parameterized. Then, an algorithm de-mixed the emission spectra of each barcode interrogated in a sample as a sum of the individual quantum dot spectra, i.e. a barcode’s emission spectrum is the sum of Gaussians of the quantum dots used during its synthesis. They were able to use this method to resolve a library of 150 quantum dot barcodes, made from only two-colour combinations from the four original quantum dots.

The use of charge-coupled device (CCD) camera for fluorescence readout has become popular in recent years, due to its relative small size and inexpensiveness compared to instruments such as the fluorometer or flow cytometer. It is often employed in conjunction with sophisticated algorithms for resolving fluorescence signals. One example involved reading encoded microbeads using fiber optics<sup>127</sup>. Different microbeads, encoded with varying concentrations of an organic dye (Eu), resulted in different fluorescence intensities when imaged. An algorithm then determined the mean intensity of each microbead and normalized it to the highest-concentrated microbead intensity. By comparing these with one another the algorithm was able to differentiate them from one another for applications in biological warfare agent detection.

Single-molecule binding detection was also achieved using a combination of CCD fluorescence imaging plus image processing and analysis algorithm<sup>128</sup>. Green- and red-emitting quantum dots conjugated to two complementary DNA strands were imaged on a surface. When the complementary strands were bounded, the green and red signals merge to result in yellow fluorescence. The algorithm was able to locate the yellow fluorescence, separate it into its individual colour components of green and red, then curve-fit their intensity profiles with Gaussian profiles, and thus determine their respective points of maximum intensity. Using this information and statistical analysis, they were able to deduce the DNA length based on probability.

The combination of CCD imaging and a robust algorithm was also employed to resolve dye-impregnated microbeads on a microfluidics platform in an immunoassay application<sup>118</sup>. In this study, a mixture of three colours (green, yellow, and red) of dye-encoded microbeads were run through a microfluidics platform to perform the immunoassay before being collected at the detection chamber, where they were immobilized on the same plane of view for imaging. An algorithm evaluated the likeness of a pixel's colour compared with the three possible colours (i.e. either green, yellow, red) to determine its identity. Then, using the Hough transform (discussed later), the size and location of the microbead in which the pixel resides were extracted, and the pixel's identity was assigned to that of its microbead's.

### 3.3 Overview of Imaging-Based Approach and Algorithm

In the examples listed above, the algorithms that were used often involved fitting the data with a Gaussian or a sum of Gaussian curves. While this is an applicable assumption for an encoded microbead's spectral or intensity profile, it is strongly dependent on the fidelity and robustness of the data acquisition instrumentation and process. In other words, the accompanying algorithms would be more sensitive to data irregularities such as saturations or artifacts that result in the signal being non-Gaussian, and thus unusable or contribute to poor analysis. For algorithms that used only image intensities to resolve between encoded microbeads, which is more robust than Gaussian-fitting, only one (Eu-dye)<sup>127</sup> and three (green, yellow, red)<sup>118</sup> sources of fluorescence were demonstrated. For our approach, we based it on image intensity and developed an algorithm that can be easily extended to resolve more than three principle fluorescences.

Our underlying approach to resolving the fluorescence signals from multiple sources – in our case different quantum dot emissions in a barcode – within an image is “spectral imaging” or “lambda stacking”<sup>129–131</sup>. This is the process of spectrally separating the total fluorescence into its component emission wavelength images. Our first attempt was to decompose the single  $\lambda_{\text{em}} = 430\text{LP}$  filter image into its component channels of red-green-blue. That is, to differentiate the quantum dot barcodes by their three primary colour channels. While this was possible when the barcode colours were few and distinct (e.g. “green”, “yellow”, “red”), it became increasingly difficult and prone to errors when higher multiplexing was desired, as it required barcodes to contain varying mixtures of the same quantum dots. This caused some barcodes to share similar colour channel intensities (**Figure 3.4**), due to intensity overlaps, i.e. different barcodes whose colour channel intensities overlap when error bars were considered. This increased the possibility of false identifications. In essence, the single emission filter image does not contain enough spectral information (i.e. poor spectral/wavelength resolution) to allow for high multiplexing applications.

To overcome the limitation of a single longpass filter we elected to image samples using a set of emission filters:  $\lambda_{\text{em}} = 430\text{LP}$ ,  $\lambda_{\text{em}} = 530/10$ ,  $\lambda_{\text{em}} = 580/10$ , and  $\lambda_{\text{em}} = 640/10$  (**Figure 3.5**). With these, the  $\lambda_{\text{em}} = 430\text{LP}$  was used as a reference image for all of the microbeads. The  $\lambda_{\text{em}} = 530/10$ ,  $\lambda_{\text{em}} = 580/10$ , and  $\lambda_{\text{em}} = 640/10$  filter images were for isolating wavelengths of “QD540”, “QD589”, and “QD640” quantum dots, respectively, used in our barcodes. The emission bandwidth of 10 nm for each was intentionally selected to be small so that we reduce the effect of signal overlap between each filter. This approach of using multiple emission filters, as compared with using a single colour image, allows barcode resolution to be performed with high accuracy while remaining easily scalable for greater barcode combinations. To analyze and resolve the barcodes using these filter images, our algorithm consisted of four major steps (**Figure 3.6**). The first step was image alignment, where each of the filter images was aligned with the reference  $\lambda_{\text{em}} = 430\text{LP}$  filter image so that each microbead was co-localized across all the filter images. The second step was microbead image extraction, where the size and location (i.e. centre) of each microbead within the  $\lambda_{\text{em}} = 430\text{LP}$  filter image were determined, to facilitate intensity analysis. The third step was establishing each microbead’s intensity profile, where a microbead’s mean intensity at each filter was calculated and assigned. Finally, in step four, the barcodes were resolved based on their intensity profile information. These are described in detail

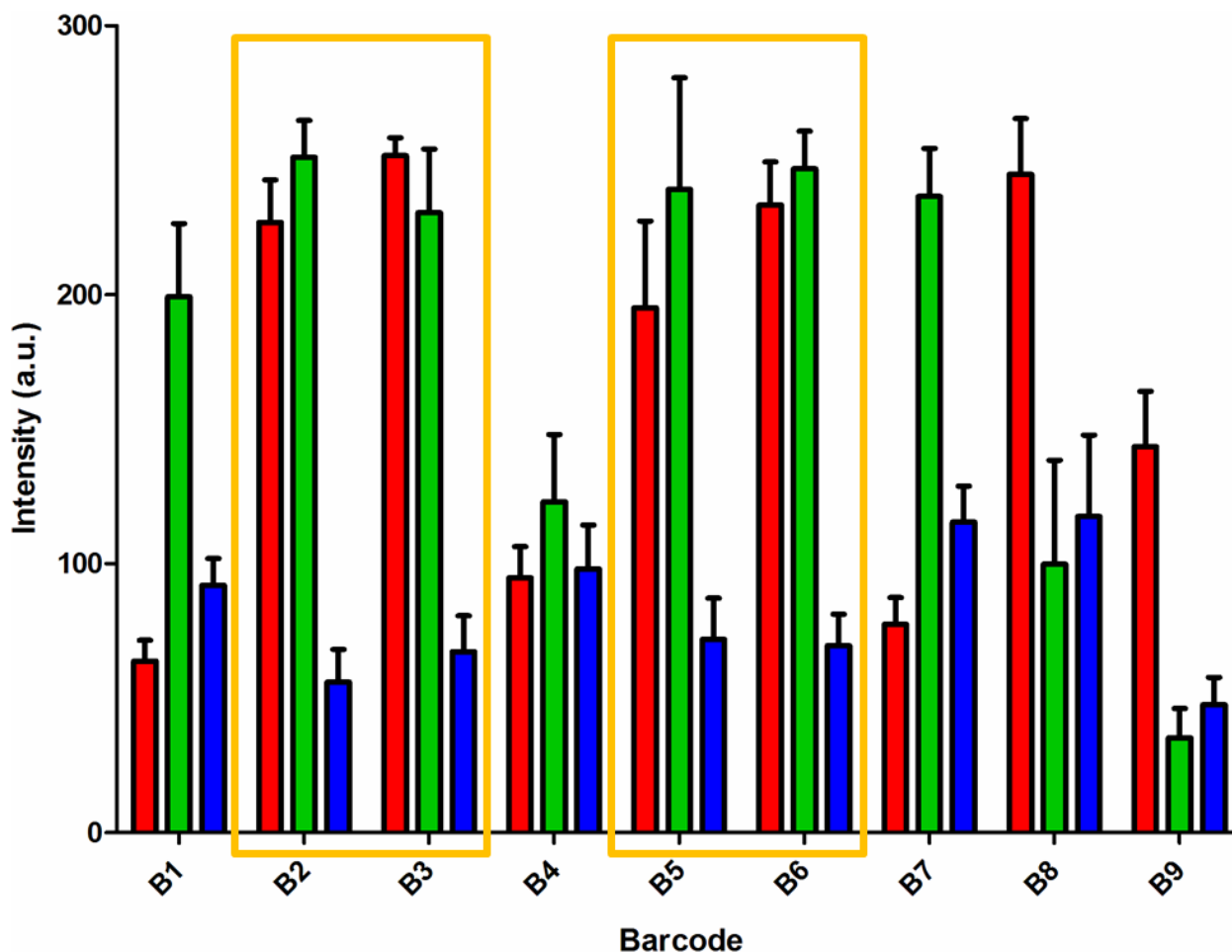


**Figure 3.4. Colour channel intensities of barcodes.**

Colour intensities for nine different quantum dot barcodes B1-B9 at the red (red bars), green (green bars), and blue (blue bars) channels of the  $\lambda_{\text{em}} = 430\text{LP}$  filter image for each barcode. The yellow boxes indicate barcodes that would be difficult to differentiate due to the similar colour channel intensities. Figure created by the author. Reprinted (adapted) with permission from source<sup>113</sup>. Copyright 2015 American Chemical Society.

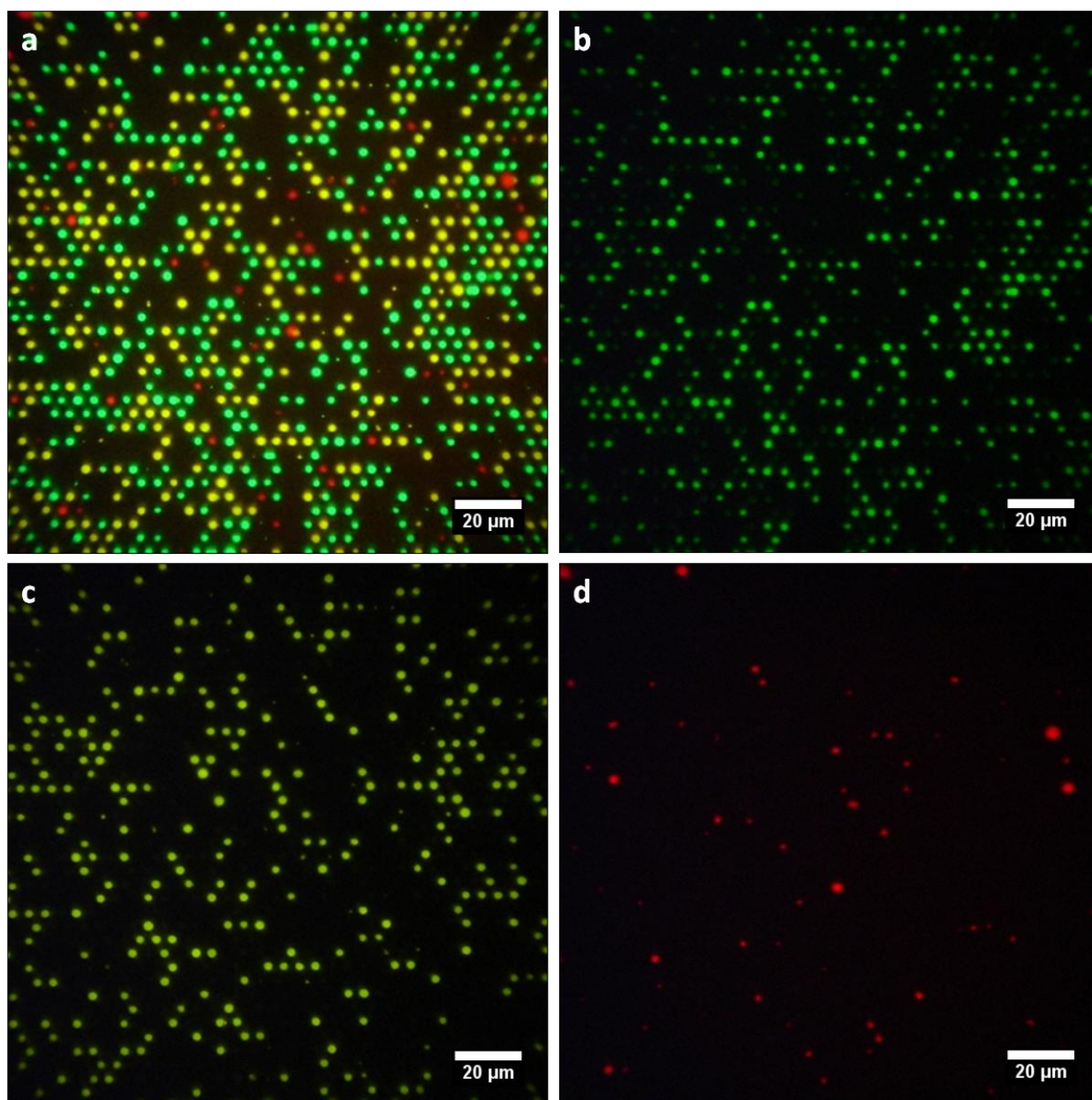


**Figure 3.5. Imaging using multiple emission filters.**

An example illustrating the optical differences of imaging different barcodes using different emission filters: (a)  $\lambda_{\text{em}} = 430\text{LP}$ , (b)  $\lambda_{\text{em}} = 530/10$ , (c)  $\lambda_{\text{em}} = 580/10$ , and (d)  $\lambda_{\text{em}} = 640/10$ .



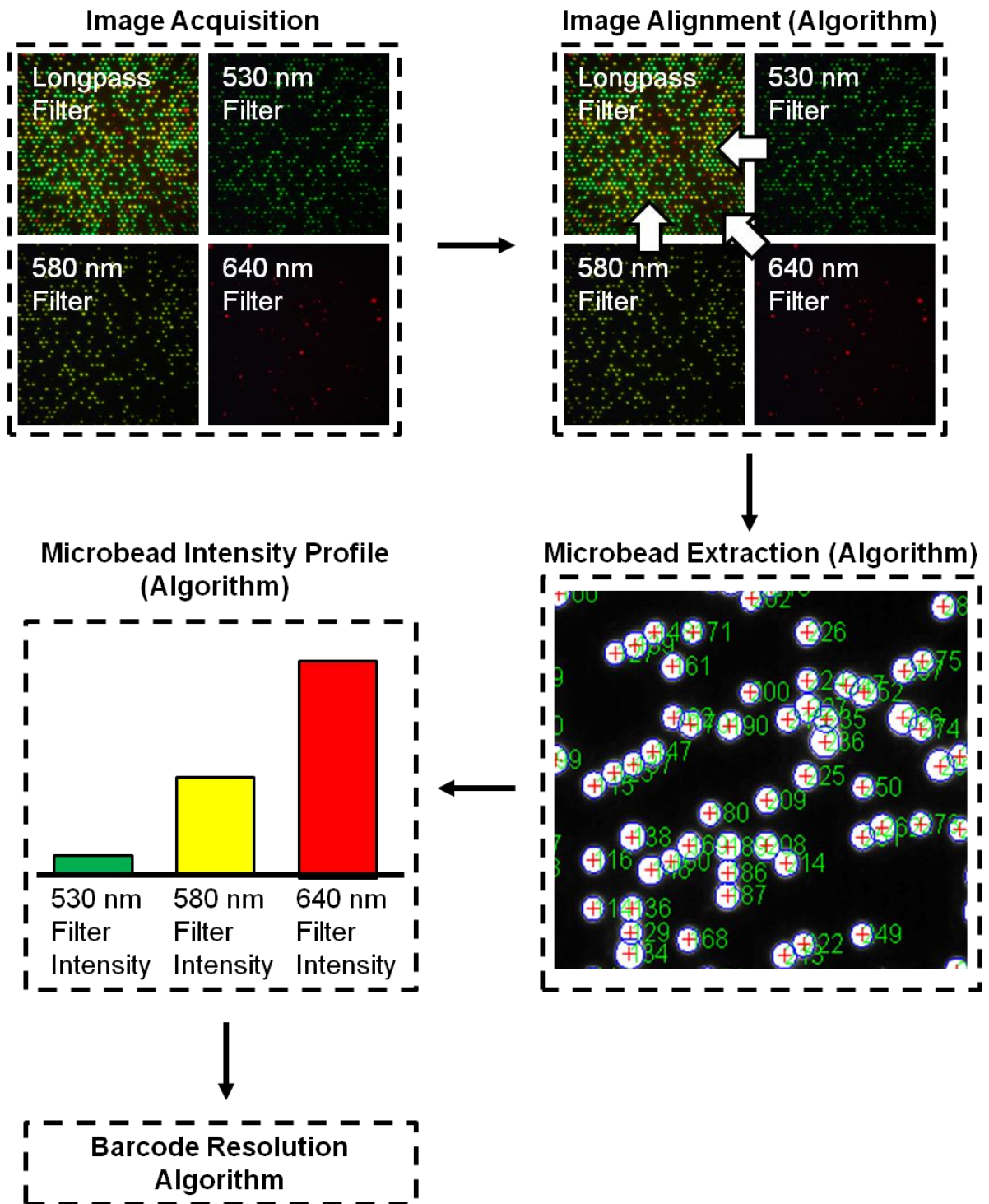


**Figure 3.6. The image analysis process.**

An overview of the algorithms involved in our image analyses.

in the sections below. Note that this algorithm is easily extendable to incorporate more than three types of emission filter images or different emission wavelengths, enabling greater multiplexing flexibility compared to the examples illustrated previously.

### 3.3.1 Image Alignment using Discrete Fourier Transform

Image registration is an image processing technique through which two images are aligned. The process finds the optimal overlay between the reference/source image and the moving image by finding the transformation (i.e. translation, rotation, affine, or deformable) that allows the moving image to resemble the reference image as closely as possible. Here we designated the  $\lambda_{em} = 430\text{LP}$  filter image as the reference image to which all other filter images were to be aligned. In doing so we ensured that minute discrepancies or movements during the image acquisition process were accounted for, and that when we performed further image processing and analysis the microbeads were aligned across all the filter images. Image registration, especially those involving translations and/or rotations only, like in our case, is typically performed in the frequency or Fourier domain. That is, both the reference and moving images first undergo Fourier transformation, to transform them from the spatial domain to the frequency domain, before attempting the overlay (**Figure 3.7**). In the Fourier domain images are represented as weighted combinations of vertical and horizontal 2-dimensional sinusoids (**Figure 3.7a**). After the transformation (**Figure 3.7b**), through computational optimization (i.e. local maximum finding), the algorithm finds the translation and/or rotation for the moving image that yield the highest similarity with the reference image.

We used the Fourier transform for image registration in our algorithm because it is more efficient computationally than using the image themselves directly, especially for complex images containing many microbeads. Furthermore, image registration performed in this manner is more resistant to effects of noise in the images<sup>132</sup>. In our case, we opted to use the discrete Fourier transform image registration technique<sup>119,120</sup>. It is based on the standard fast Fourier transform typically employed for image registrations. But since we do not expect the filter images to be misaligned from one another by a large degree, we employed this technique where the search for the optimal overlay is constrained to a smaller area about the initial estimation so as to reduce the algorithm processing time (e.g. image registration for all images can be performed in  $< 15$  s).



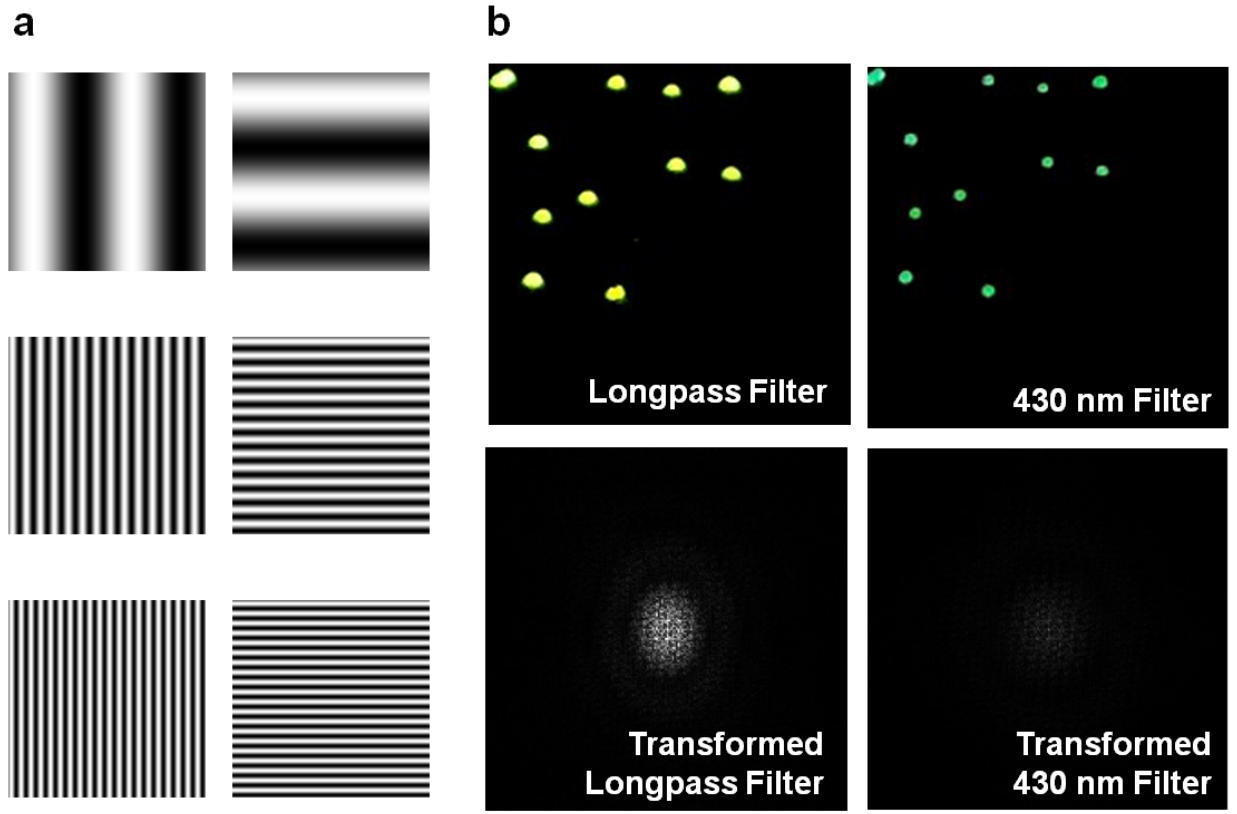


**Figure 3.7. Fourier transform of images.**

(a) Fourier domain images are represented using a series of vertical (examples in left column) and horizontal (examples in right column) 2-dimensional sinusoid images. (b) Examples of  $\lambda_{\text{em}} = 430\text{LP}$  and  $\lambda_{\text{em}} = 530/10$  filter images used in our analyses, and their corresponding Fourier-transformed images.

### 3.3.2 Microbead Image Extraction using Hough Transform

To obtain the intensity information from each individual microbead we needed to isolate them from the background and separate them from each other. Initial attempts at microbead image extraction were done using simple image processing techniques, which are computationally simple and thus reasoned to be more suitable for use on a cell phone as opposed to a dedicated personal computer. To do this we attempted to create a binary mask over the image in order to more easily determine each microbead's size and location. With this approach, however, some microbeads were lost because the morphological processes and microbead aggregations resulted in poor edge detection. Furthermore, such techniques are heavily influenced by the background intensity and noise (i.e. contrast between microbeads and background), so in the event of a high background signal or noise few microbeads would be detected. In short the lack of robustness in this approach made it unappealing (**Figure 3.8**).

The Hough transform technique was identified and used for the purpose of microbead extraction<sup>121,122</sup>. It is an image processing technique used to extract features (e.g. lines, circles, ellipses, etc.) from within an image. An example with a line as the feature of interest will be used to illustrate this process.

A line can be written as

$$y = mx + b$$

**Equation 3.4**

where

$(x, y)$  = Any given point on the line.

$(m, b)$  = The parameters defining the line, with  $m$  being its slope and  $b$  being its intercept.

This is also to say that for a given point  $(x_0, y_0)$ , there are theoretically an infinite number of parameters  $(m_1, b_1) \dots (m_n, b_n)$  that can pass through this point. Thus, for a given point  $(x_0, y_0)$  we can convert its equation from the  $(x, y)$  image space representation to the  $(m, b)$  parameter space representation (**Figure 3.9a**):

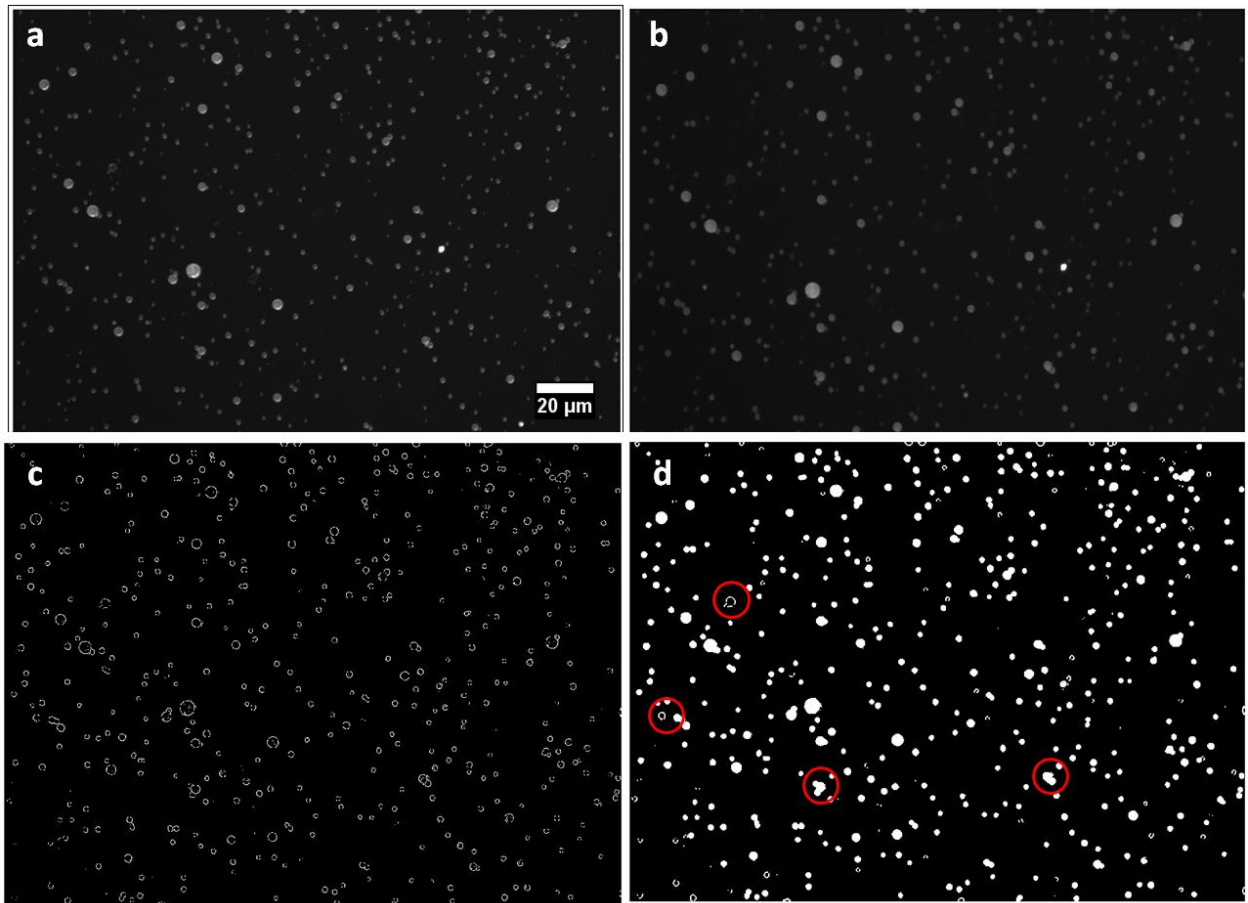


**Figure 3.8. Binary mask creation.**

An example illustrating the process of binary mask creation using simple image processing techniques. (a) Original image. (b) Original after image erosion and dilation. (c) Roberts edge detection of the eroded and dilated image. (d) Region filling of the edge detected image. Red circles provide some examples of the loss of microbeads due to either poor region filling or aggregation.

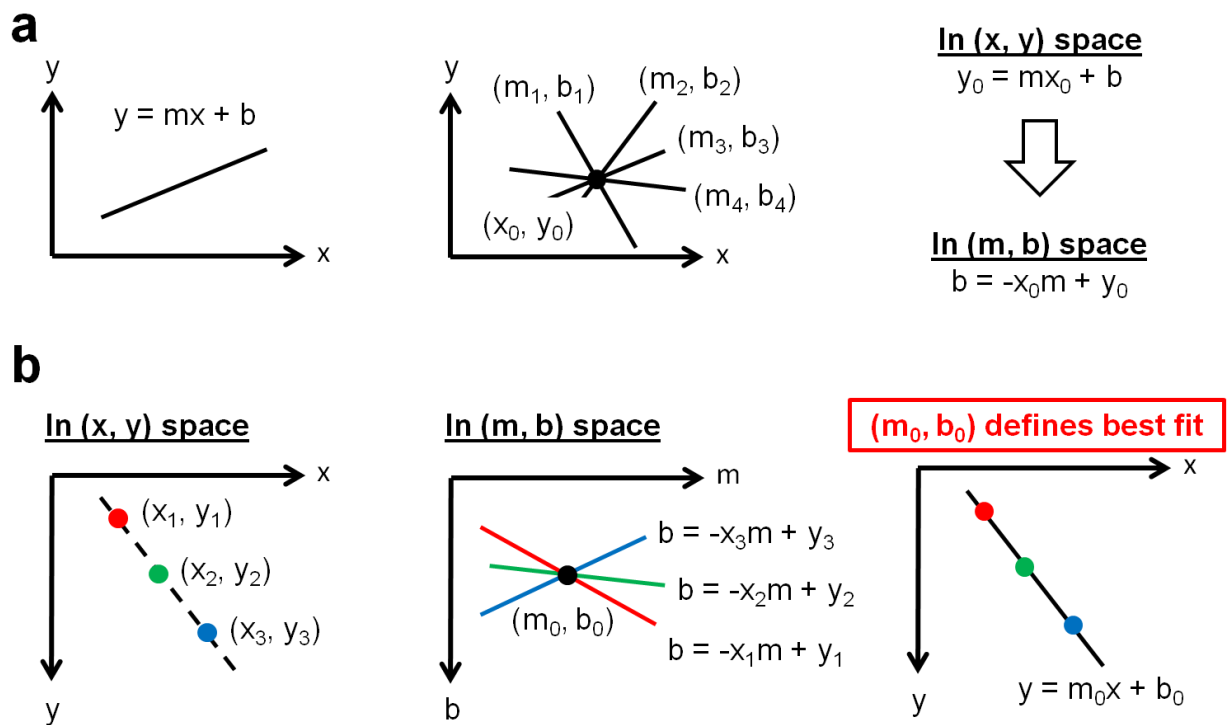


**Figure 3.9. Feature extraction using Hough transform.**

(a) An illustration of the concept of converting a line from the image coordinate space to the parameter space using the Hough transform. (b) An illustration of the concept of finding the line of best-fit, through a set of feature points on an image, using the parameter space obtained using the Hough transform.

$$y_0 = mx_0 + b \rightarrow b = -x_0m + y_0$$

### Equation 3.5

Assume we wish to extract the line feature that passes through three points  $(x_1, y_1)$ ,  $(x_2, y_2)$ , and  $(x_3, y_3)$  in the  $(x, y)$  image space. We need to find the parameter point  $(m_0, b_0)$  in the parameter space  $(m, b)$  such that  $(m_0, b_0)$  is the intersection of the three lines

$$b = -x_1m + y_1$$

$$b = -x_2m + y_2$$

$$b = -x_3m + y_3$$

### Equations 3.6

with the equations representing all possible lines that pass through the points  $(x_1, y_1)$ ,  $(x_2, y_2)$ , and  $(x_3, y_3)$ , respectively, in the  $(m, b)$  parameter space (**Figure 3.9b**). That is,  $(m_0, b_0)$  defines the line that best fits the three points  $(x_1, y_1)$ ,  $(x_2, y_2)$ , and  $(x_3, y_3)$ . Practically, the algorithm finds the list of  $n$  parameters  $(m_1, b_1) \dots (m_n, b_n)$  that pass through one or more  $m$  points of interest in the image  $(x_1, y_1) \dots (x_m, y_m)$ . The parameter  $(m_0, b_0)$  that passes through the most number of the  $m$  points is determined as the line of interest for extraction.

For extracting circular features, the same principles apply for the equation of a circle:

$$r^2 = (x - a)^2 + (y - b)^2$$

### Equation 3.7

where

$(x, y)$  = Any given point on the circle.

$(r, a, b)$  = The parameters defining the circle, with  $r$  being its radius, and  $(a, b)$  being its origin.

Note that instead of the Cartesian coordinate system, Hough transform typically uses the polar coordinate system to avoid issues with vertical lines (i.e. infinite slope  $m$ ), such that the equation of a line is represented as:

$$r = x\cos(\theta) + y\sin(\theta)$$

**Equation 3.8**

where

$(x, y)$  = Any given point on the line.

$(r, \theta)$  = The parameters defining the line.

And for a circle the equation is represented as:

$$x = a + r\cos(\theta)$$

$$y = b + r\sin(\theta)$$

**Equations 3.9**

where

$(x, y)$  = Any given point on the circle.

$(r, a, b)$  = The parameters defining the circle.

Using the Hough transform in our algorithm we were able to identify the size and location (i.e. the circumference and center) of each microbead, highlighted on the image (**Figure 3.10**). Building on this, the algorithm was improved to allow the user to manually remove erroneously-identified particles. This technique offered more sophistication and robustness compared to simple morphological and image processing techniques while still remaining computationally efficient (i.e. the microbead image extraction process can be performed in < 10 s).

### 3.3.3 Establishing Microbead Intensity Profiles

Having extracted the location and size of all the microbeads in the image, the algorithm would proceed to assign them intensity values to form their intensity profiles. Consider a microbead, extracted from  $\lambda_{em} = 430\text{LP}$  filter image and located in the  $\lambda_{em} = 530/10$  filter image, the algorithm finds the average pixel intensity within its circumference (obtained from the size information of the Hough transform algorithm), and associates this mean value as the microbead's  $\lambda_{em} = 530/10$  filter intensity. The same was done for the  $\lambda_{em} = 580/10$  and

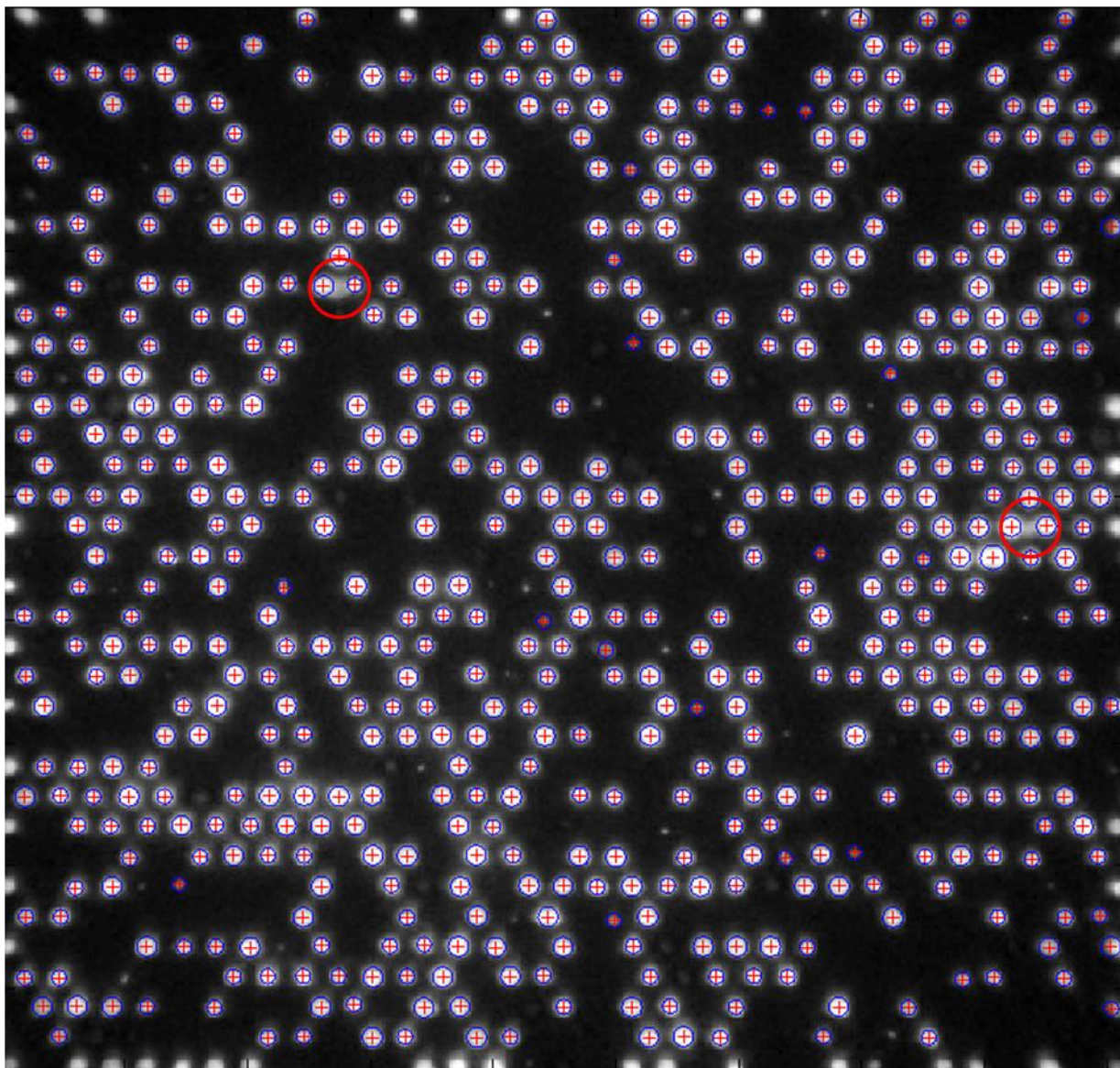


**Figure 3.10. Hough transform microbead extraction.**

An example illustrating the use of the Hough transform to extract microbeads from images. The blue outlines indicate the extracted circumference of the microbeads and the red crosshairs indicate their center. The red circle highlights provide some examples of successful extraction despite intensity crossovers that might have cofounded extraction using the edge detection approach.

$\lambda_{em} = 640/10$  filter images so that in the end, the microbead is associated with its intensity profile consisting of the mean intensity values of the  $\lambda_{em} = 530/10$ ,  $\lambda_{em} = 580/10$ , and  $\lambda_{em} = 640/10$  filter images. This algorithm was applied to nine uniquely-synthesized quantum dot barcodes (labeled as “550”, “505”, “055”, “135”, “315”, “351”, “513”, “531”, and “555”, whose names were based on concentrations of the various quantum dots used during synthesis) in order to establish their intensity profiles (**Figure 3.11**). These intensity profiles, which we called the nine “known barcode intensity profiles”, formed the basis to which a microbead was identified.

### 3.3.4 Quantum Dot Barcode Identification and Resolution

In order to identify a microbead, or unknown barcode on the chip, its intensity profile was compared against the nine known barcode intensity profiles (**Figure 3.11**). The unknown barcode’s intensity profile was compared against each known barcode’s intensity profile, and the unknown barcode was identified as the known barcode whose intensity profile best matches its own. To do this, four methods of comparisons were experimented with: 1) differentiation based on maximum intensity, 2) differentiation based on the Euclidean distance, 3) differentiation based on a two-step maximum intensity approach, and 4) differentiation based on a two-step Euclidean distance approach.

In the first comparison case, maximum intensity, the highest intensity value out of the  $\lambda_{em} = 530/10$ ,  $\lambda_{em} = 580/10$ , and  $\lambda_{em} = 640/10$  filter images was used as the basis of comparison. In the second comparison case, Euclidean distance, the Euclidean distance equation (see Section 2 *Experimental Methods*) was used as the metric to measure the difference between the intensity values of the unknown barcode and that of the known barcodes’. In the third and fourth cases, the two-step approaches, the algorithm first categorized the unknown barcode’s intensity profile according to its highest to lowest intensities among the filters  $\lambda_{em} = 530/10$ ,  $\lambda_{em} = 580/10$ , and  $\lambda_{em} = 640/10$ . Then from the set of select barcodes that followed this pattern, either the maximum intensity or Euclidean distance approach, described above, was used. An example to illustrate the barcode resolution process for the two-step maximum intensity approach (**Figure 3.12**):

A microbead B is imaged and has an intensity profile of  $[\lambda_{em} = 530/10, \lambda_{em} = 580/10, \lambda_{em} = 640/10] = [250, 325, 450]$ , so  $[\lambda_{em} = 640/10] > [\lambda_{em} = 580/10] > [\lambda_{em} = 530/10]$ . On examination of the set of barcodes used, B has a similar intensity profile (i.e. same order of highest to lowest



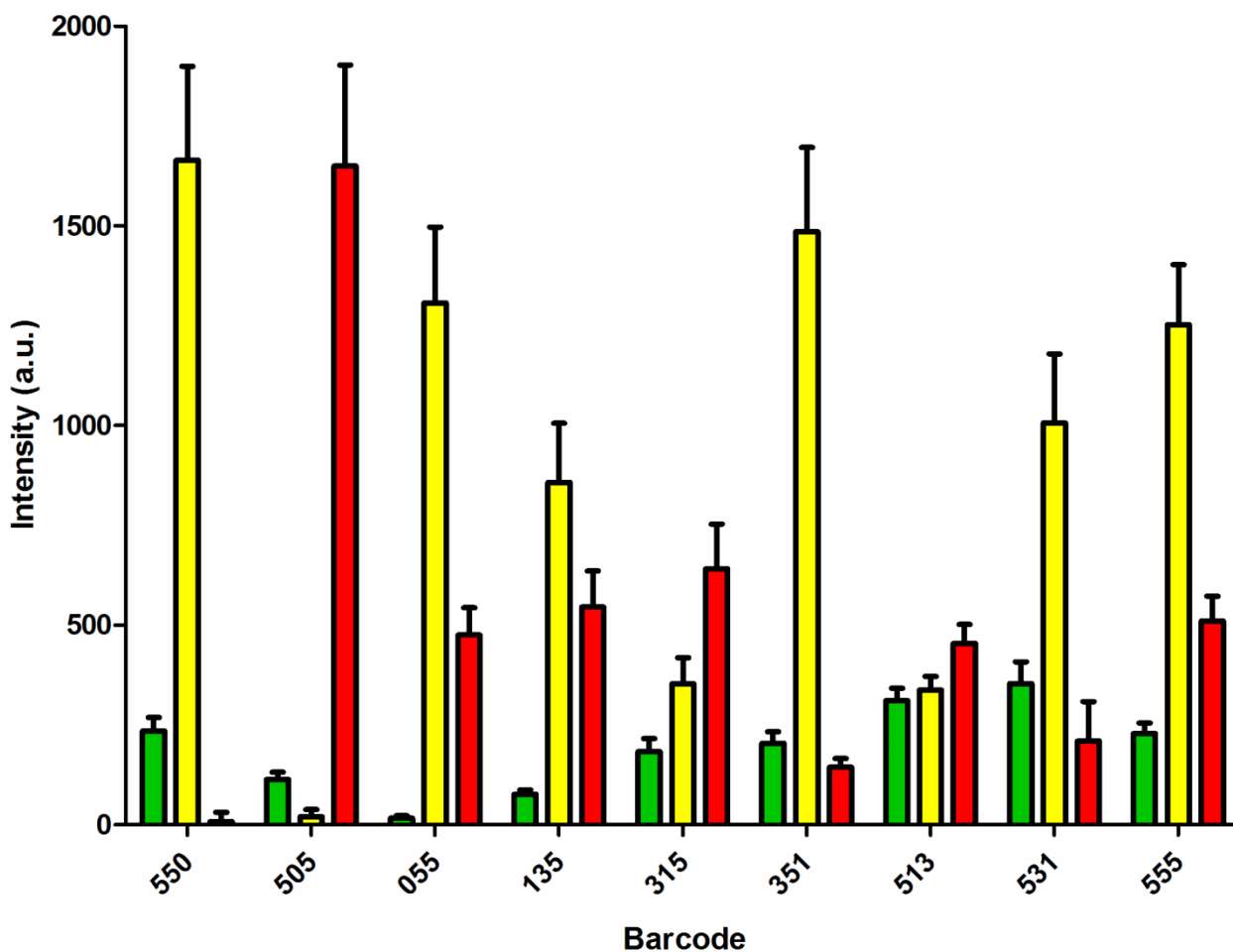


**Figure 3.11. Barcode intensity profiles.**

Barcode intensity profiles, from microscopy images, for the barcodes synthesized. From left to right the coloured bars represent intensity observed in the filter  $\lambda_{em} = 530/10$  (green),  $\lambda_{em} = 580/10$  (yellow), and  $\lambda_{em} = 640/10$  (red). Data represent the mean and standard deviation from three replications. Figure created by the author. Reprinted (adapted) with permission from source<sup>113</sup>. Copyright 2015 American Chemical Society.

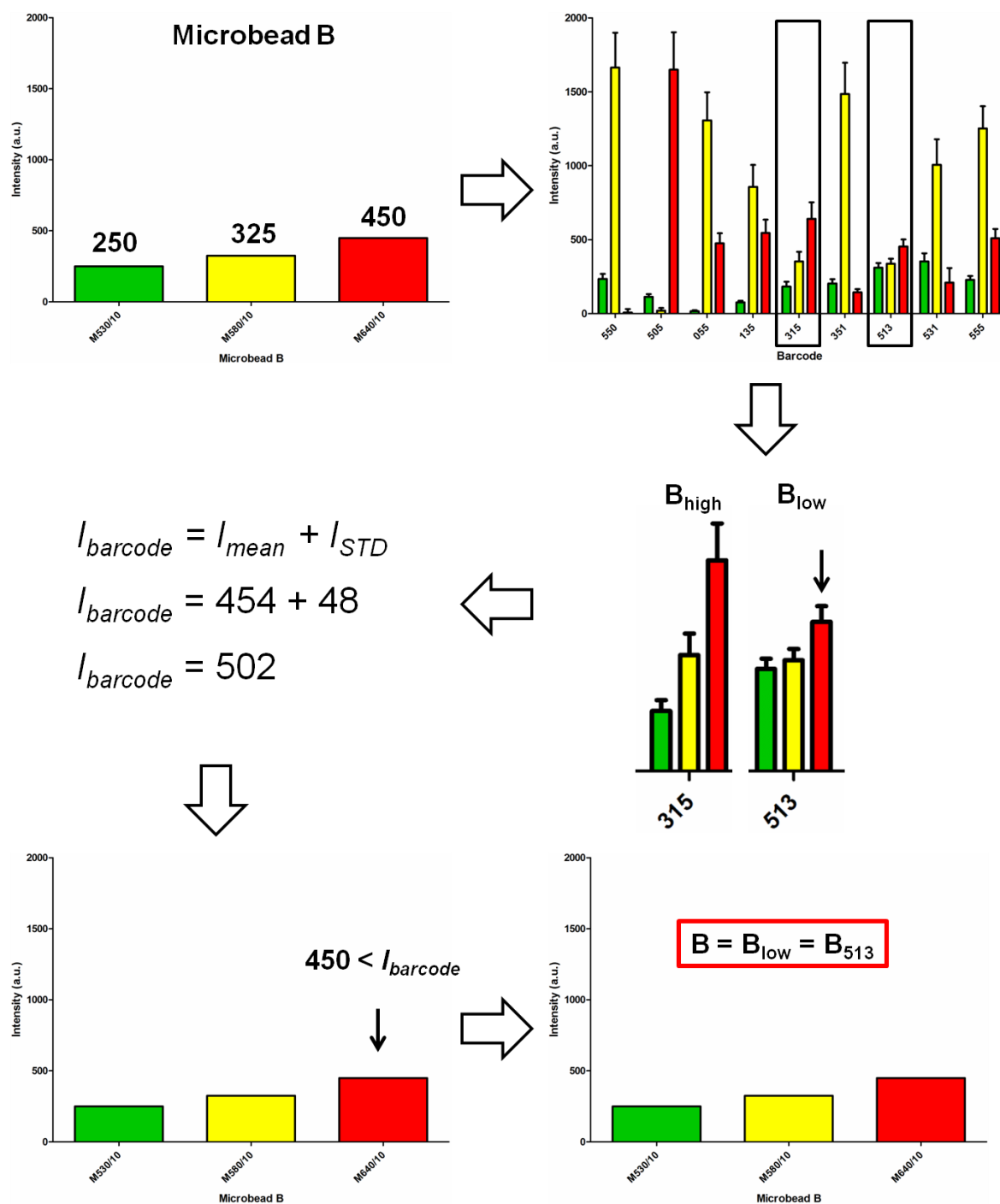


**Figure 3.12. Barcode resolution process.**

An example illustrating the process through which a microbead's barcode is identified and resolved among a mixture of the nine barcodes used in this chapter. Figure created by the author. Reprinted (adapted) with permission from source<sup>113</sup>. Copyright 2015 American Chemical Society.

filter intensities) as  $B_{315}$  and  $B_{513}$ . At the  $\lambda_{em} = 640/10$  filter (the maximum filter intensity compared to the other two filter intensities),  $B_{315}$  has  $[\lambda_{em} = 640/10] = 641$  and  $B_{513}$  has  $[\lambda_{em} = 640/10] = 454$ , so the latter is chosen as  $B_{low}$ . The intensity threshold is calculated using  $[\lambda_{em} = 640/10]$  for  $B_{low} = B_{513}$ :

$$I_{barcode} = I_{mean} + I_{STD} = 454 + 48 = 502$$

Since B's  $[\lambda_{em} = 640/10] = 450$  is less than  $I_{barcode} = 502$  of  $B_{low} = B_{513}$ , B is identified as  $B_{low} = B_{513}$ .

### 3.4 Algorithm Accuracy Validation using Flow Cytometry

We validated the accuracy of our four methods using flow cytometry, using the channels FITC-A (525 nm), PE-A (575 nm), and 7-AAD-A (650 nm) to correspond to “QD540”, “QD589”, and “QD640”, respectively. Specifically, we first obtained the percent population of each barcode within a mixture of barcodes – mixture of two to nine different barcodes were tested – and established it as our gold standard. Then we analyzed the same mixture using our algorithms and computed the difference in population data between the two approaches using an equation (**Figure 3.13a**). That is, the smaller the difference between the two approaches, the higher the accuracy of our technique. For a mixture of nine barcodes, we were able to attain an accuracy of 95% using the two-step maximum intensity approach to identify and resolve the barcodes (**Figure 3.13b**).

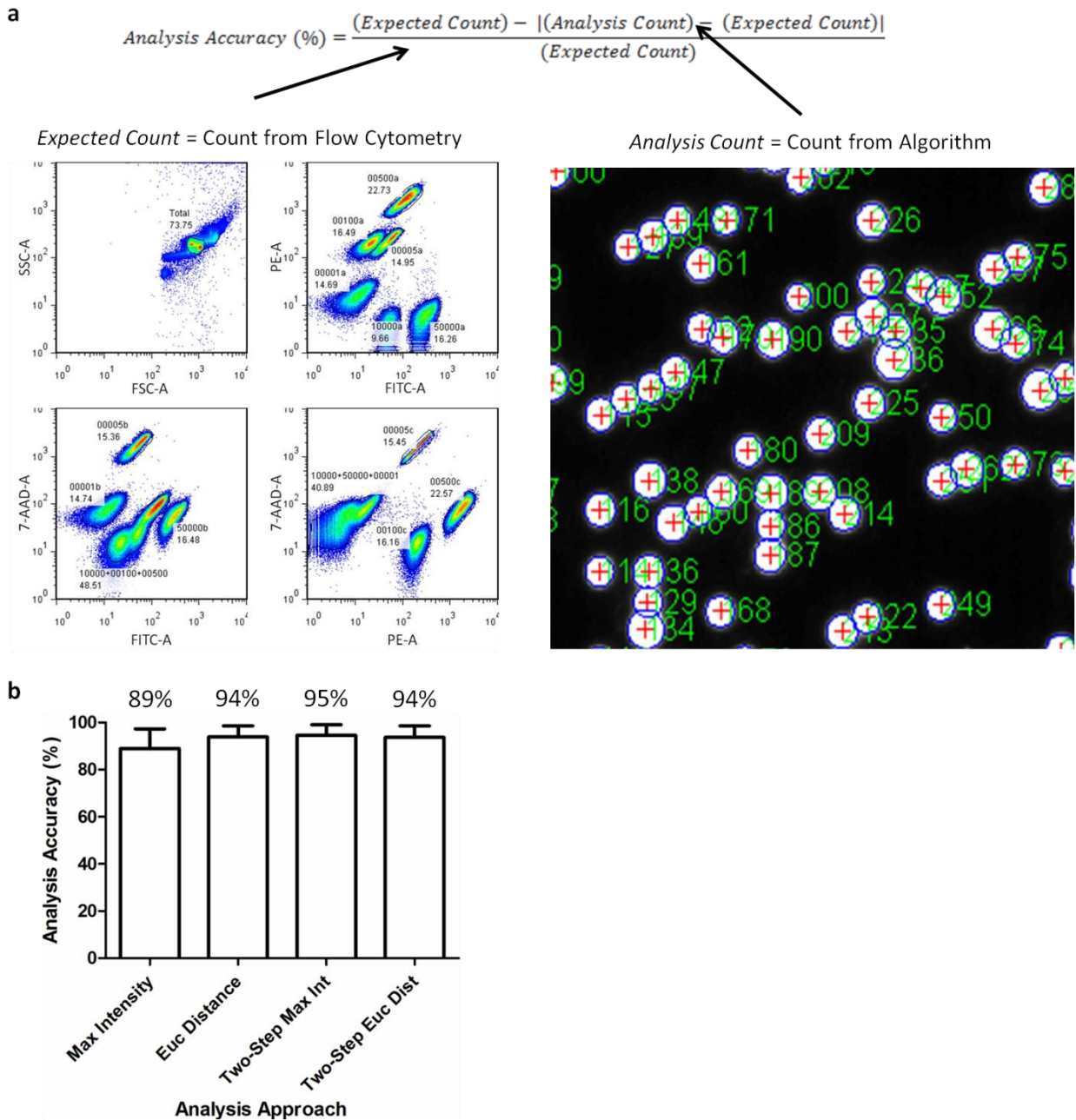


**Figure 3.13. Barcode resolution accuracy.**

(a) An example using a 6-barcode mixture illustrating the process through which we determine the accuracy of our barcode resolution algorithm. The “*Expected Count*”, our “gold standard”, was obtained from flow cytometry. The “*Analysis Count*” was obtained from our algorithm. (b) Analysis accuracy of our algorithms when used to resolve the nine barcodes used in this chapter. Data represent the mean and standard deviation from three replications.

## 4 Chapter Summary

In this chapter we functionalized a microwell chip with quantum dot barcodes to reduce the need for reagents in solutions, and characterized their filling efficiency on the chip. We developed an algorithm to align a series of microbead images taken across various filters, and to extract the microbeads from the background and each other. Using these we developed an intensity-based algorithm to identify and resolve up to nine different barcode signatures with 95% accuracy. These allow for a multiplexed diagnostic platform that is portable, easy to use, and readily analyzable with an imaging-based approach using a smartphone camera.

## 5 Author Contributions

The experiments were designed by **K. Ming** and **W.C.W. Chan**. Experiments were performed by **D. Li** (quantum dot synthesis) and **K. Ming** (all others). Analyses were performed by **K. Ming**. Algorithms were written by **K. Ming**. This chapter was written by **K. Ming**.

## Chapter 4

### Quantum Dot Barcode Genetic Assays on a Chip

#### 1 Introduction

In the previous chapter, we presented a strategy to functionalize a chip-based substrate with quantum dot barcodes and demonstrated the ability to be able to identify and resolve between nine barcodes with 95% accuracy using a simple imaging technique. To further our goal of developing point-of-care diagnostics, we need to be able to perform molecular detection using those barcodes. The quantum dot barcodes developed by our group offer many advantages in terms of diagnostics, including: (1) established synthesis protocols and methods, (2) inexpensive production, (3) flexibility due to their ability to be functionalized with and thus detect for both genomic and proteomic samples, (4) faster reaction kinetics compared to flat, surfaced-based assay platforms (e.g. microarrays), and (5) size tunability to control assay conditions<sup>50</sup>. The microbead assay, to review, involves first the functionalization or conjugation of capturing agents (e.g. oligonucleotides, antibodies, peptides, etc.). Then, the microbeads bind with or capture the complementary molecule of interest (i.e. the targeted analyte). Finally, the complex is labeled or “tagged” with a fluorescent agent. The final construct – microbead-capturing agent-target molecular-fluorescent agent – forms a “sandwich” structure around the target such that the barcoded microbead is used to identify the type of target due to the specific capturing agents functionalized on the surface, and the fluorescent agent is used to determine the presence and amount of the target.

Over the last decade, our group has optimized and solved the chemistry design issues of microbead-based assays, in particular quantum dot barcode assays, and demonstrated their utility for detecting both genomic and proteomic targets using synthetic samples<sup>29,75,76,99</sup>. In this chapter, we describe how we have built on this knowledge and extended it to our chip-based platform wherein both the genetic assay and detection were performed directly over top of our quantum dot barcode microwell chip. Specifically, each barcode contained a unique optical signature due to the incorporation of different emitting quantum dots, which identified the surface-conjugated oligonucleotide that can bind and recognize specific target deoxyribonucleic acid (DNA). In our case the polystyrene microbeads used contain maleic anhydride that converts into carboxylic acid functional groups, which allow the barcoded microbeads to conjugate to a

targeting molecule using carbodiimide chemistry. Detection occurs when a secondary label, a fluorophore-labeled oligonucleotide, also binds to the target and the overall optical signal of the microbeads comprises of both the barcode and the secondary label of the detection strand. In the absence of the target the detection strand does not bind and the fluorophore thus does not contribute to the signal detection (**Figure 4.1**). Note that in our assays, we typically use a microbead filling efficiency of 25 to 50% on the microwell chip to reduce potentials for barcode aggregation and thus signal overlap. Furthermore, for the custom-designed synthetic sequences used here, hybridization between the capture and target strands, and target with detection strands were perfectly congruent (i.e. no base pair mismatches).

## 2 Experimental Methods

### 2.1 Quantum Dot Synthesis

Same procedures as those in Chapter 3 were used. Quantum dot synthesis and characterization performed by **D. Li**.

### 2.2 Quantum Dot Barcode Synthesis

Same procedures as those in Chapter 3 were used. The barcodes synthesized are presented (**Table 4.1**) along with their synthesis parameters (**Table 4.2**). Quantum dot barcode synthesis and characterization performed by **A. Lam**.

### 2.3 Barcode Microbead Conjugation and Validation

For the synthetic samples, conjugation of DNA capture strands (i.e. amine groups present on the 5' end of the capture DNA strands) to their corresponding barcode microbeads (i.e. carboxylic acid groups present on the polymeric surface of the microbeads) was done through reaction with 1-ethyl-3-(3-dimethylaminopropyl) carbodiimide hydrochloride (EDC). DNA capture strands (**Table 4.1**) from IDT DNA Technologies, purchased high performance liquid chromatography-purified (HPLC-purified), were designed with an amine group and C12 spacer on the 5' end. They were first prepared at a concentration of 10 pmol/ $\mu$ L in Tris-Ethylenediaminetetraacetic acid (TE) buffer (pH 8) and stored at 4 °C until further use. To conjugate, EDC was first dissolved in 2-(N-morpholino)ethanesulfonic acid (MES) buffer (pH 5, 100 mM) at a concentration of 100 mg/mL. Approximately  $10^6$  microbeads were mixed with 100  $\mu$ L of the

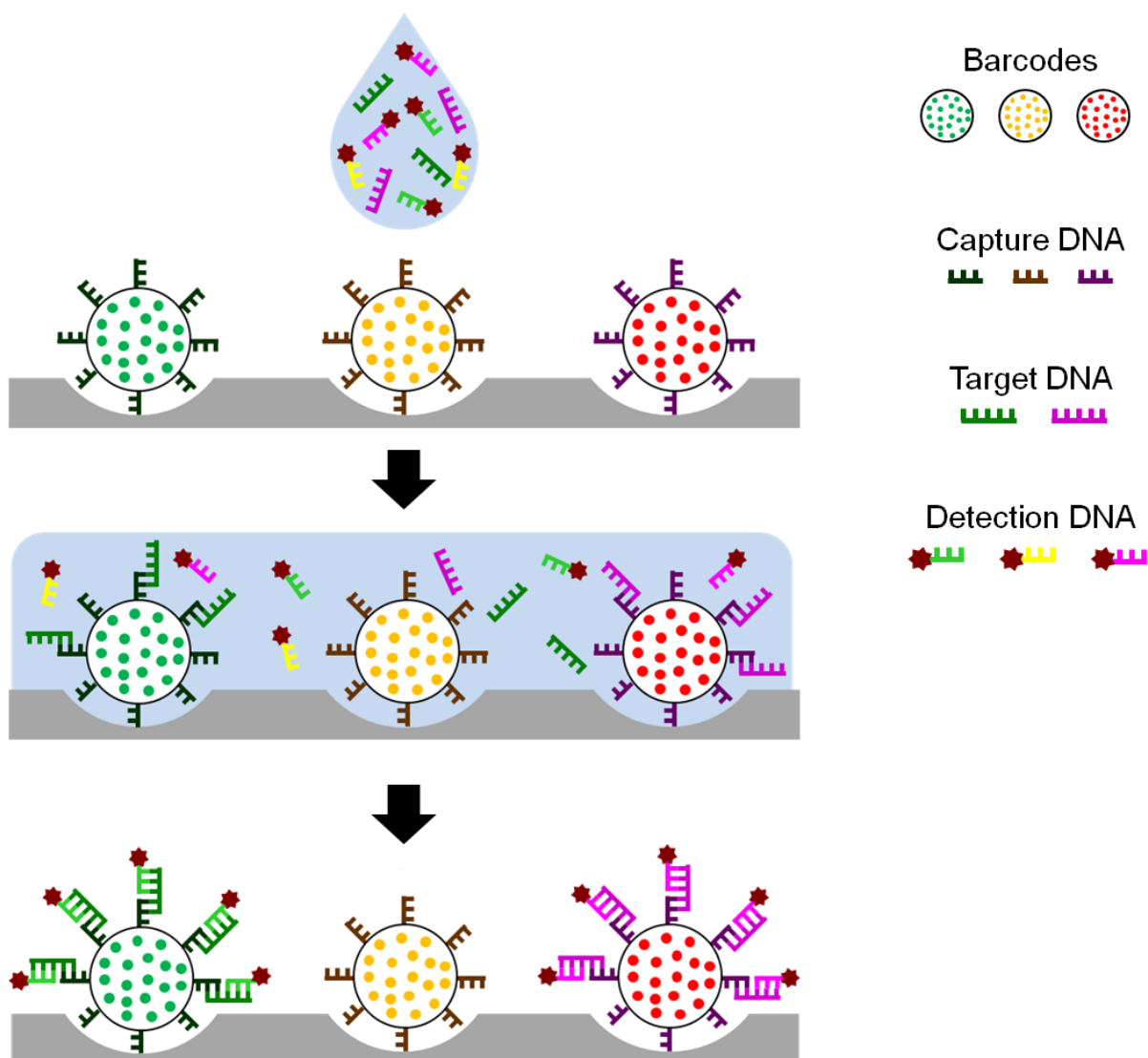


**Figure 4.1. Quantum dot barcode genetic assay.**

The assay on the microwell chip involves the addition of genetic samples to our quantum dot barcoded chip, whose microbeads are coated with molecules that recognize a target analyte. This target analyte joins the barcode to the secondary probe. Since each barcode is conjugated with a known bio-recognition molecule for a specific pathogen target, the imaging of the optical signal from the barcode would allow for the identification of the pathogen and whether it is present in a patient sample (i.e. lack of secondary probe signal indicates no pathogen present, in this case the yellow microbead). Figure created by the author. Reprinted (adapted) with permission from source<sup>113</sup>. Copyright 2015 American Chemical Society.



**Table 4.1. List of barcodes synthesized and their corresponding DNA strands.**

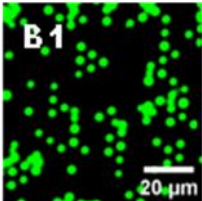
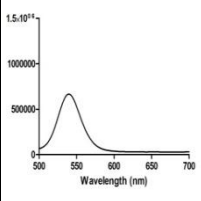
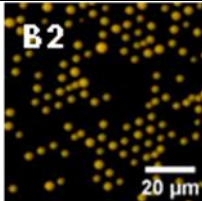
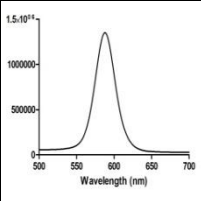
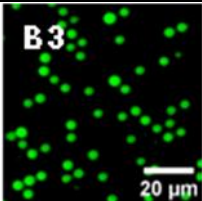
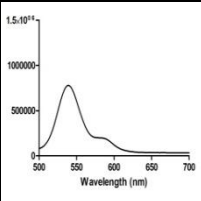
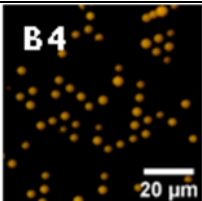
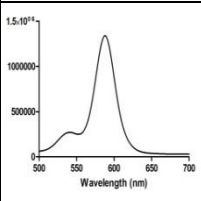
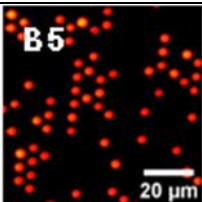
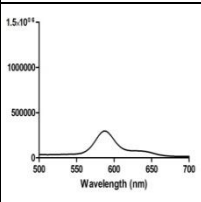
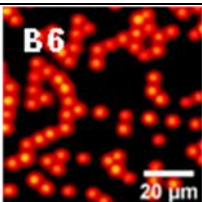
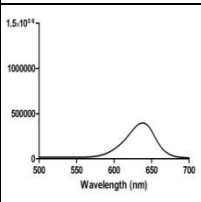
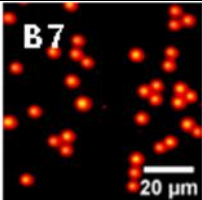
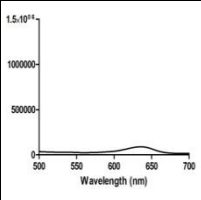
Disease	Biomarker	Capture Name/Length/Sequence	Target Name/Length/Sequence	Secondary Probe Name/Len./Sequence	Corresponding Barcode	Barcode Spectrum
Influenza	Hemagglutinin – Influenza Type A (H1N1)	<b>C1/</b> <b>30 nt/</b> CCC TCT TAG TTT GCA TAG TTT CCC GTT ATG	<b>T1/</b> <b>58 nt/</b> CGG CGA TGA ATA CCT AGC ACA CTT A CTA CA TAA CGG GAA ACT ATG CAA ACT AAG AGG G	<b>D/</b> <b>25 nt/</b> Alexa647- TAA GTG TGC TAG GTA TTC ATC GCC G	<b>B 1</b> 	
Influenza	Neuraminidase – Influenza Type A (H3N2)	<b>C2/</b> <b>30 nt/</b> ACT TGG TTG TTT GGG GGG GAG TTG AAT TCA	<b>T2/</b> <b>58 nt/</b> CGG CGA TGA ATA CCT AGC ACA CTT A CTA TG AAT TCA ACT CCC CCC CAA ACA ACC AAG T		<b>B 2</b> 	
Influenza	Hemagglutinin – Influenza Type A (H5N1)	<b>C3/</b> <b>30 nt/</b> CCA TTC CCT GCC ATC CTC CCT CTA TAA AAC	<b>T3/</b> <b>58 nt/</b> CGG CGA TGA ATA CCT AGC ACA CTT A CTA GT TTT ATA GAG GGA GGA TGG CAG GGA ATG G		<b>B 3</b> 	
Hepatitis B (HBV)	PB-2 – HBV	<b>C4/</b> <b>25 nt/</b> TCA GAA GGC AAA AAA GAG AGT AAC T	<b>T4/</b> <b>53 nt/</b> CGG CGA TGA ATA CCT AGC ACA CTT A CTA AG TTA CTC TCT TTT TTG CCT TCT GA		<b>B 4</b> 	
Hepatitis C (HCV)	KY 150 – HCV	<b>C5/</b> <b>26 nt/</b> CAT AGT GGT CTG CGG AAC CGG TGA GT	<b>T5/</b> <b>54 nt/</b> CGG CGA TGA ATA CCT AGC ACA CTT A CTA AC TCA CCG GTT CCG CAG ACC ACT ATG		<b>B 5</b> 	
Negative Control		<b>C6/</b> <b>22 nt/</b> GAC AAT GCT CAC TGA GGA TAG T	<b>T6/</b> <b>50 nt/</b> CGG CGA TGA ATA CCT AGC ACA CTT A CTA AC TAT CCT CAG TGA GCA TTG TC		<b>B 6</b> 	
Positive Control		<b>C7/</b> <b>15 nt/</b> CCA ATA TCG GCG GCC	<b>T7/</b> <b>43 nt/</b> CGG CGA TGA ATA CCT AGC ACA CTT A CTA GG CCG CCG ATA TTG G		<b>B 7</b> 	

Table created by the author. Reprinted (adapted) with permission from source<sup>113</sup>. Copyright 2015 American Chemical Society.

**Table 4.2. List of barcode synthesis parameters.**

<b>Barcode</b>	<b>Diameter (<math>\mu\text{m}</math>)</b>	<b>QD540 Concentration (<math>\mu\text{L/mL}</math>)</b>	<b>QD589 Concentration (<math>\mu\text{L/mL}</math>)</b>	<b>QD640 Concentration (<math>\mu\text{L/mL}</math>)</b>
B1	$2.70 \pm 1.61$	60		
B2	$2.70 \pm 1.36$		57	
B3	$2.70 \pm 1.60$	60	11.4	
B4	$2.70 \pm 1.60$	12	57	
B5	$2.70 \pm 1.34$		57	182
B6	$3.50 \pm 1.19$			910
B7	$2.70 \pm 1.51$			182

Table created by **A. Lam**. Reprinted (adapted) with permission from source<sup>113</sup>. Copyright 2015 American Chemical Society.

EDC solution, and it was allowed to activate the microbead carboxyl groups for 10 minutes. Then, 2.88  $\mu\text{L}$  of the DNA capture strand solution, corresponding to 28.8 pmol of DNA, was added to the microbead solution. The reaction was allowed to take place overnight.

To validate the conjugation, 1  $\mu\text{L}$  of DD water containing 5% Tween was added to the microbead solution, centrifuged at 3000 g for 5 minutes. Then, 50  $\mu\text{L}$  of the supernatant was extracted. The same conjugation procedures described above were performed for the control cases for each barcode (i.e. no conjugation), except DD water was added in place of beads. In a black 96-well plate, 10  $\mu\text{L}$  of the supernatants from all conjugation cases, 10  $\mu\text{L}$  of the supernatants from all control cases, as well as 10  $\mu\text{L}$  of four blank cases containing only DD water, were each added to individual wells. SYBR gold from Invitrogen, dissolved in dimethyl sulfoxide (DMSO), was first diluted to 0.5:10000 dilution by adding 0.5  $\mu\text{L}$  of it to 10 mL of TE buffer (pH 8), then 190  $\mu\text{L}$  of the dilution was added to each of the sample-containing wells. All reactions were incubated at room temperature for 15 minutes before being read using a plate reader from BMG Labtech. Amount of conjugation for each barcode was then determined by comparing the fluorescence of the conjugation cases with their respective controls containing no beads. That is, lower signal indicates higher amount of conjugation. Results were converted to efficiency in percentages (**Figure 4.2**).

To finish the conjugation process, after the 50  $\mu\text{L}$  of the supernatant was extracted for validation, the remaining supernatant was removed. Then, the conjugated microbeads were washed twice with 100  $\mu\text{L}$  of DD water containing 0.05% Tween and centrifuged at 3000 g for 5 minutes to remove any non-conjugated DNA capture strands. The conjugated microbeads were then stored in 100  $\mu\text{L}$  DD water containing 0.05% Tween at 4 °C until further use. Barcode microbead conjugation and validation performed by **K. Chen** and **A. Syed**.

## 2.4 Solution Assay

DNA captures strands (length: 30 nt; sequence: 5'- AAT ATA TTT GGT TTT CCC AAA CCA GTT TAA-3') were from Bio Basic Inc., purchased HPLC-purified. DNA target strands (length: 58 nt; sequence: 5'-CGG CGA TGA ATA CCT AGC ACA CTT ACT ATT AAA CTG GTT TGG GAA AAC CAA ATA TAT T-3') from Bio Basic Inc., purchased HPLC-purified, were prepared in concentrations of 0 and 100 fmol/ $\mu\text{L}$  in TE buffer (pH 8). DNA detection strand

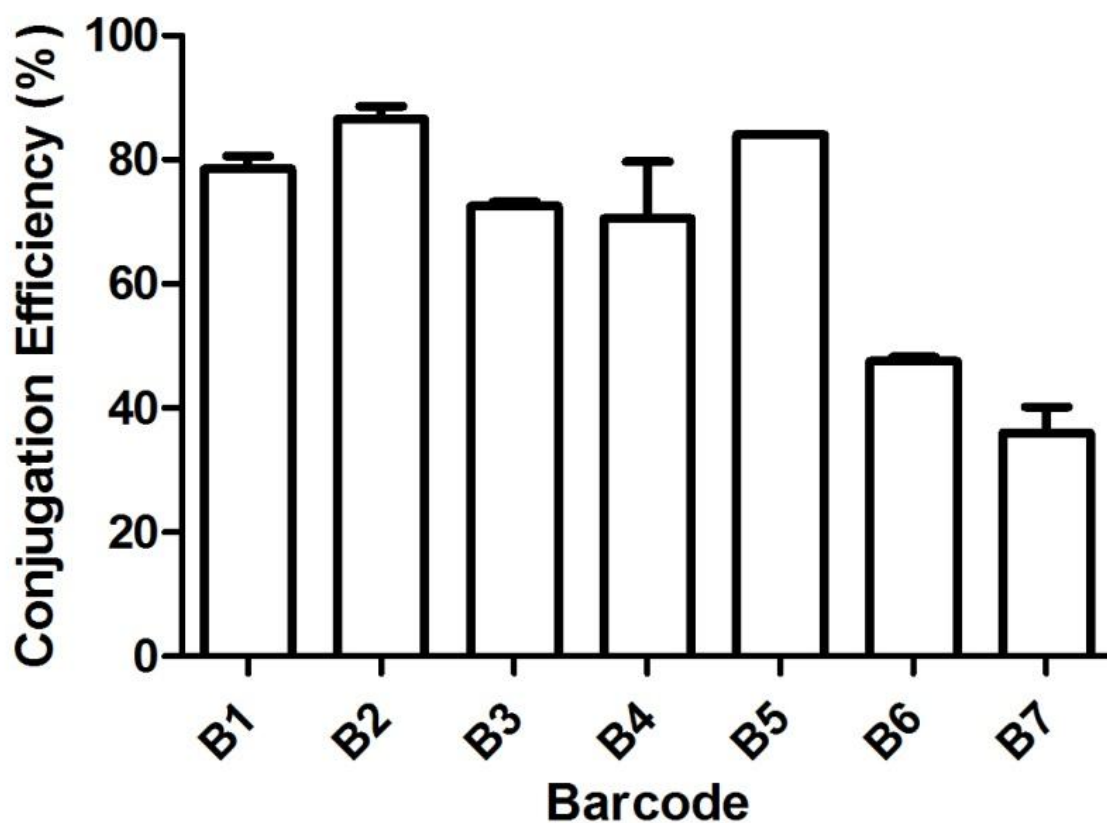


**Figure 4.2. Capture strand conjugation efficiency.**

Capture strand conjugation efficiency for each barcode. Data represent the mean and standard deviation from three replications. Figure created by **A. Syed**. Reprinted (adapted) with permission from source<sup>113</sup>. Copyright 2015 American Chemical Society.

(length: 25 nt; sequence: 5'-Alexa647-TAA GTG TGC TAG GTA TTC ATC GCC G-3') from IDT DNA Technologies with Alexa647 fluorophore on the 5' end, purchased HPLC-purified, were prepared with concentration of 100 pmol/ $\mu$ L in TE buffer (pH 8). Both DNA target and detection strand samples were stored at 4 °C until further use. To perform the assay, 1  $\mu$ L of the conjugated bead sample, corresponding to approximately  $10^4$  conjugated beads, was mixed with 1  $\mu$ L of the DNA target strand sample (100 fmol), 5  $\mu$ L of hybridization buffer (10x SSC, 0.1% SDS, pH 7, heated to 60 °C), 2  $\mu$ L of DD water, and 1  $\mu$ L of DNA detection strands (100 pmol) or DD water (for the blank condition). This resulted in a total hybridization volume of 10  $\mu$ L. This was incubated at 37 °C for 20 minutes. The samples were then washed twice with 100  $\mu$ L of washing buffer (0.5x saline-sodium citrate (SSC), 0.1% sodium dodecyl sulfate (SDS), pH 7, heated to 37 °C) and centrifuged at 3000 g for 5 minutes to remove any non-hybridized strands in the supernatant. The final 10  $\mu$ L sample was either used for flow cytometry analysis or then deposited on a microwell slide and let dry for 4 hours before imaging. Solution assay performed by **K. Chen**.

## 2.5 Flow Cytometry Analysis of Solution Assay

After the assay 190  $\mu$ L of washing buffer (0.5x SSC, 0.1% SDS, pH 7, heated to 37 °C) was added to the sample to bring it to a total volume of 200  $\mu$ L. BD FACSCalibur was used to perform the analysis. Flow cytometry analysis performed by **K. Chen**.

## 2.6 Surface Assay Protocol for Optimization

DNA captures strands (length: 30 nt; sequence: 5'- AAT ATA TTT GGT TTT CCC AAA CCA GTT TAA-3') were from Bio Basic Inc., purchased HPLC-purified. DNA target strands (length: 58 nt; sequence: 5'-CGG CGA TGA ATA CCT AGC ACA CTT ACT ATT AAA CTG GTT TGG GAA AAC CAA ATA TAT T-3') from Bio Basic Inc., purchased HPLC-purified, were prepared in concentrations of 0 and 100 fmol/ $\mu$ L in TE buffer (pH 8). DNA detection strand (length: 25 nt; sequence: 5'-Alexa647-TAA GTG TGC TAG GTA TTC ATC GCC G-3') from IDT DNA Technologies with Alexa647 fluorophore on the 5' end, purchased HPLC-purified, were prepared in desired concentration in TE buffer (pH 8). Both DNA target and detection strand samples were stored at 4 °C until further use. To perform the assay,  $10^4$  conjugated microbeads were deposited on a microwell chip for each assay condition and let dry. Then, 1  $\mu$ L

of DNA target strand sample (1 pmol) was mixed with 8  $\mu$ L of hybridization buffer (DD water; PBST, pH 7.4; 1x, 2x, 5x, or 10x SSC as the final solution concentration, pH 7), and 1  $\mu$ L of DNA detection strands (10x, 100x, 1000x, or 10000x relative to target) or DD water (for the blank condition). The 10  $\mu$ L hybridization solution for each assay condition was deposited over the conjugated bead spots on the microwell chips and incubated at the desired temperature (22 or 37 °C) for the desired amount of time (0 to 40 minutes). The microwell chips were then submerged in 10 mL of washing buffer (0.5x SSC, 0.1% SDS, pH 7, heated to 37 °C), washed by agitation for 20 s, then let dry for 5 minutes before being imaged. Note that care must be taken so that the washing buffer does not dry and crystallize over the sample spots.

## 2.7 Sensitivity Assay

Sensitivity assays were performed directly on the microwell chips for all infectious disease DNA target strands and their respective conjugated barcode microbeads from Table 4.1. DNA target strands from Bio Basic Inc., purchased HPLC-purified, were prepared in increasing concentrations of 0, 5, 10, 50, 100, 500, 1000, and 2000 fmol/ $\mu$ L in TE buffer (pH 8). DNA detection strand from IDT DNA Technologies with Alexa647 fluorophore on the 5' end, purchased HPLC-purified, were prepared with concentration of 100 pmol/ $\mu$ L in TE buffer (pH 8). Both DNA target and detection strand samples were stored at 4 °C until further use. To perform the assay, 1  $\mu$ L of the conjugated bead sample, corresponding to approximately  $10^4$  conjugated beads, was deposited on a microwell chip for each assay condition and let dry for 1 hour. Then, 1  $\mu$ L of each DNA target strand sample (0, 5, 10, 50, 100, 500, 1000, and 2000 fmol) was mixed with 5  $\mu$ L of hybridization buffer (10x SSC, 0.1% SDS, pH 7, heated to 60 °C), 3  $\mu$ L of DD water, and 1  $\mu$ L of DNA detection strands (100 pmol) or DD water (for the blank condition). This resulted in a total hybridization volume of 10  $\mu$ L for each assay condition, which include blank, 0, 5, 10, 50, 100, 500, 1000, and 2000 fmol. The hybridization solution for each assay condition was deposited over the conjugated bead spots on the microwell chips and incubated at 37 °C for 20 minutes. The microwell chips were then submerged in 10 mL of washing buffer (0.5x SSC, 0.1% SDS, pH 7, heated to 37 °C), washed by agitation for 20 s, then let dry for 5 minutes before being imaged. Note that care must be taken so that the washing buffer does not dry and crystallize over the sample spots. Sensitivity assays performed by **K. Chen, A. Syed, and K. Ming.**

## 2.8 Multiplexing Assay

For the 3-plex multiplexing assay, 2  $\mu\text{L}$  of each conjugated barcode sample (B1-C1, B4-C4, and B6-C6 in Table 4.1), corresponding to approximately  $2 \times 10^4$  barcodes each, were mixed together with 18  $\mu\text{L}$  of DD water to produce a 4x dilution factor of the original. The dilution was to reduce bead aggregation after deposition on chip, which may confound barcode resolution during analysis. To perform the assay, 5  $\mu\text{L}$  of the conjugated barcode mixture, corresponding to approximately  $1.25 \times 10^3$  conjugated beads, was deposited on a microwell chip for each assay condition and let dry for 3 hours. Then, 2  $\mu\text{L}$  of T1 and T6 (concentration of 2 pmol/ $\mu\text{L}$  each, or 2 pmol each) was mixed with 40  $\mu\text{L}$  of hybridization buffer (10x SSC, 0.1% SDS, pH 7, heated to 60 °C), 14  $\mu\text{L}$  of DD water, and 16  $\mu\text{L}$  of the detection strand (concentration of 100 pmol/ $\mu\text{L}$ , or 1600 pmol). This resulted in a total hybridization volume of 70  $\mu\text{L}$ . From this, 10  $\mu\text{L}$  of the hybridization solution was deposited over the conjugated barcode spots on the microwell chip and incubated at 37 °C for 20 minutes. The microwell chip was then submerged in 10 mL of washing buffer (0.5x SSC, 0.1% SDS, pH 7, heated to 37 °C), washed by agitation for 20 s, washed again in another 10 mL of washing buffer to further reduce non-specific binding, then let dry for 5 minutes before being imaged. Note that care must be taken so that the washing buffer does not dry and crystallize over the sample spots.

Cross reactivity between all five DNA target strands and their corresponding conjugated barcodes, as well as negative and positive control cases, was studied from Table 4.1. First, 6  $\mu\text{L}$  of each conjugated barcode sample, corresponding to approximately  $6 \times 10^4$  barcodes each, were mixed together with 126  $\mu\text{L}$  of DD water to produce a 4x dilution factor of the original. The dilution was to reduce bead aggregation after deposition on chip, which may confound barcode resolution during analysis. To perform the assay, 8  $\mu\text{L}$  of the diluted conjugated barcode mixture, corresponding to approximately  $2 \times 10^4$  conjugated beads, was deposited on a microwell chip for each multiplexing case and let dry for 4 hours. Then, 2  $\mu\text{L}$  of each target case (DD water for the negative conditions, and corresponding DNA target strand sample with concentration of 2 pmol/ $\mu\text{L}$  for the positive conditions, or 2 pmol each) was mixed with 35  $\mu\text{L}$  of hybridization buffer (10x SSC, 0.1% SDS, pH 7, heated to 60 °C), 14  $\mu\text{L}$  of DD water, and 7  $\mu\text{L}$  of the detection strand (concentration of 100 pmol/ $\mu\text{L}$ , or 700 pmol). This resulted in a total hybridization volume of 70  $\mu\text{L}$  for each multiplexing case. From this, 20  $\mu\text{L}$  of the hybridization solution for each multiplexing case was deposited over the conjugated barcode spots on the

microwell chip and incubated at 37 °C for 20 minutes. The microwell chip was then submerged in 10 mL of washing buffer (0.5x SSC, 0.1% SDS, pH 7, heated to 37 °C), washed by agitation for 20 s, washed again in another 10 mL of washing buffer to further reduce non-specific binding, and then let dry for 5 minutes before being imaged. Note that care must be taken so that the washing buffer does not dry and crystallize over the sample spots. Multiplexing assays performed by **K. Chen, A. Syed, and K. Ming.**

## 2.9 Sample Imaging

All images were acquired using RETIGA EXi Fast Cooled Mono 12-bit CCD camera from QImaging or the iPhone 4S from Apple, as specified, mounted on an Olympus IX70 Inverted microscope at 20x magnification for all assays (20x objective, NA = 0.50) or 32x magnification for all photographs (20x objective, NA = 0.50, with 1.6x further magnification). Quantum dot barcodes and Alexa647 fluorophore were excited using a 100 W mercury lamp attached to the microscope, through excitation-emission filter sets [ $\lambda_{\text{ex}} = 350/50$ ,  $\lambda_{\text{em}} = 430\text{LP}$ ] (Thorlabs), [ $\lambda_{\text{ex}} = 480/40$ ,  $\lambda_{\text{em}} = 530/10$ ] (Thorlabs), [ $\lambda_{\text{ex}} = 480/40$ ,  $\lambda_{\text{em}} = 580/10$ ] (Thorlabs), [ $\lambda_{\text{ex}} = 480/40$ ,  $\lambda_{\text{em}} = 640/10$ ] (Thorlabs), and [ $\lambda_{\text{ex}} = 620/40$ ,  $\lambda_{\text{em}} = 692/40$ ] (Semrock, Brightline Cy5-4040A). The emission filters  $\lambda_{\text{em}} = 530/10$ ,  $\lambda_{\text{em}} = 580/10$ , and  $\lambda_{\text{em}} = 640/10$  corresponded with quantum dots “QD540”, “QD589”, and “QD640”, respectively, and were used to isolate for their fluorescence for resolving barcodes. The emission filter  $\lambda_{\text{em}} = 692/40$  was used to isolate for the detection strand Alexa647 fluorophore fluorescence as a means to measure the amount of analyte that hybridized with its corresponding capture strand. Image exposure times, adjustable using the software Image-Pro Plus from Media Cybernetics for the CCD were 50, 200, 200, 200, and 1000 ms for the emission filters  $\lambda_{\text{em}} = 430\text{LP}$ ,  $\lambda_{\text{em}} = 530/10$ ,  $\lambda_{\text{em}} = 580/10$ ,  $\lambda_{\text{em}} = 640/10$ , and  $\lambda_{\text{em}} = 692/40$ , respectively. Image exposure times, adjustable using the NightCap app from Apple’s App Store for the iPhone 4S were 1/20, 1/5, 1/5, 1/5, and 1 s for the emission filters  $\lambda_{\text{em}} = 430\text{LP}$ ,  $\lambda_{\text{em}} = 530/10$ ,  $\lambda_{\text{em}} = 580/10$ ,  $\lambda_{\text{em}} = 640/10$ , and  $\lambda_{\text{em}} = 692/40$ , respectively.

## 2.10 Image Analysis

A custom-made algorithm was written in MathWork’s MATLAB for all image analysis (see supplement section for the code). The algorithm accepts as inputs five emission filter images ( $\lambda_{\text{em}} = 430\text{LP}$ ,  $\lambda_{\text{em}} = 530/10$ ,  $\lambda_{\text{em}} = 580/10$ ,  $\lambda_{\text{em}} = 640/10$ , and  $\lambda_{\text{em}} = 692/40$ ) of a sample. The images were cropped to include microbeads of interest based on user selection. The cropped filter



images were aligned with the  $\lambda_{em} = 430\text{LP}$  filter image through the use of the Discrete Fourier Transform registration<sup>119,120</sup>. The algorithm then identified the size and location of each microbead, based on its appearances in the  $\lambda_{em} = 430\text{LP}$  filter image, using the Hough transform<sup>121,122</sup>. Erroneously identified microbeads (e.g. debris, imaging artefacts, overlapping microbeads) were excluded based on user input. Each microbead was then associated with the mean pixel intensity across its area at each of the four remaining filter images. For each microbead, the  $\lambda_{em} = 530/10$ ,  $\lambda_{em} = 580/10$ , and  $\lambda_{em} = 640/10$  filter image intensities comprised its intensity profile, while the  $\lambda_{em} = 692/40$  filter image intensity indicated the fluorescent secondary probe intensity. In order to identify the microbeads on the chip, known barcode intensity profiles were first established, in this case using the smartphone images (**Figure 4.3**). These profiles were obtained by imaging all the barcodes alone and calculating the mean filter intensity across all microbeads for each filter. Note that due to the high intensity at the  $\lambda_{em} = 692/40$  filter for some barcodes, each of the mean  $\lambda_{em} = 692/40$  filter intensity was subtracted from the assay signals when assays were performed. A microbead's intensity profile was then compared against each known barcode's intensity profile to identify the barcode of interest. Specifically, a barcode was classified according to its type (i.e. synthetic or clinical sample) and highest to lowest intensities among the filters  $\lambda_{em} = 530/10$ ,  $\lambda_{em} = 580/10$ , and  $\lambda_{em} = 640/10$ . This narrowed the selection down to either one barcode, in which case the barcode of interest was identified, or two barcodes. Between two possibilities “B<sub>high</sub>” (with higher mean intensities) and “B<sub>low</sub>” (with lower mean intensities) a threshold was defined for “B<sub>low</sub>”:

$$I_{barcode} = I_{mean} + I_{STD}$$

**Equation 4.1**

where

$I_{barcode}$  = Intensity threshold for “B<sub>low</sub>”.

$I_{mean}$  = Mean intensity of “B<sub>low</sub>”

$I_{STD}$  = Intensity standard deviation of “B<sub>low</sub>”.

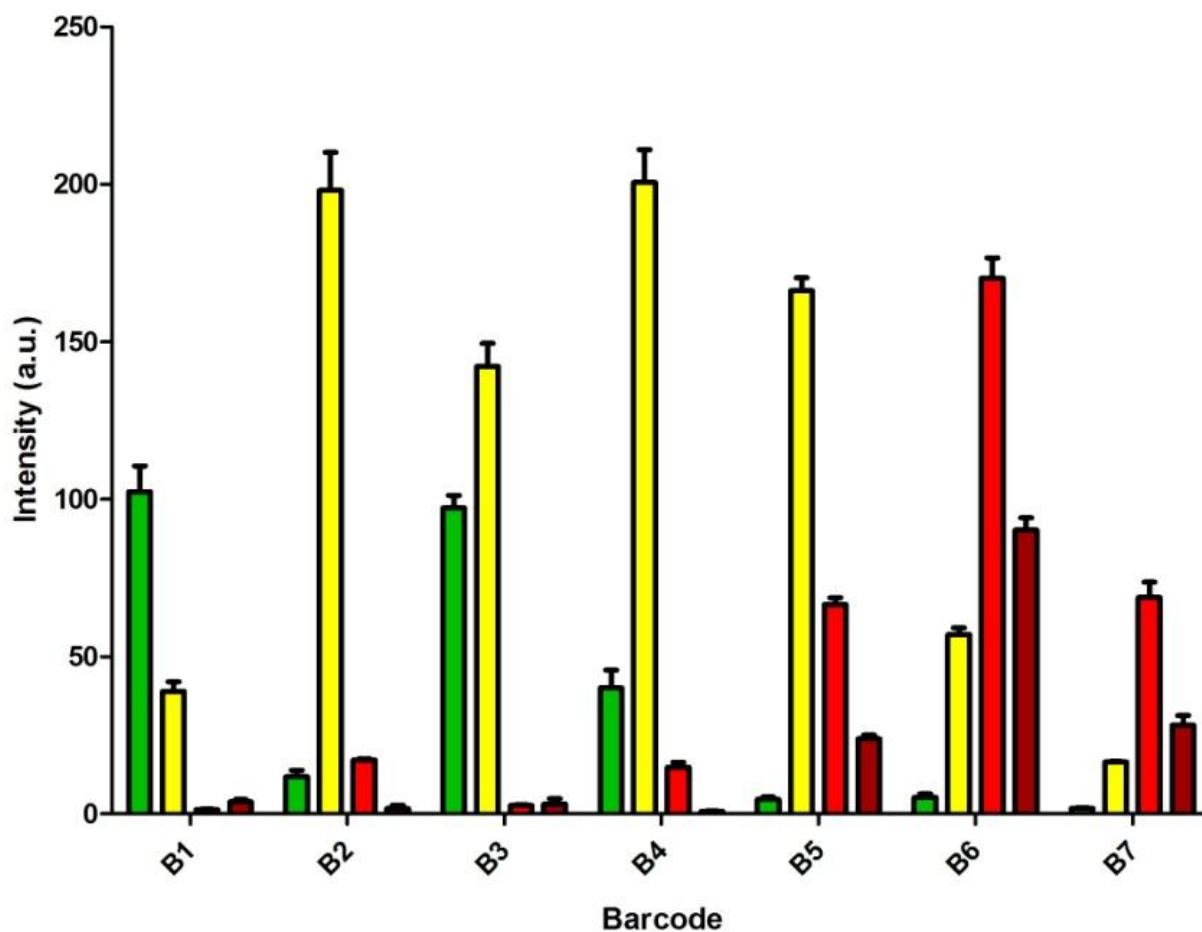


**Figure 4.3. Barcode intensity profiles.**

Barcode intensity profiles, from smartphone images, for the barcodes in **Table 4.1**. From left to right the coloured bars represent intensity observed in the filter  $\lambda_{em} = 530/10$  (green),  $\lambda_{em} = 580/10$  (yellow),  $\lambda_{em} = 640/10$  (red), and  $\lambda_{em} = 692/40$  (dark red). Data represent the mean and standard deviation from three replications. Figure created by the author. Reprinted (adapted) with permission from source<sup>113</sup>. Copyright 2015 American Chemical Society.

This threshold was calculated for the highest intensity amongst the three filters  $\lambda_{em} = 530/10$ ,  $\lambda_{em} = 580/10$ , and  $\lambda_{em} = 640/10$  for “B<sub>low</sub>”. If the highest intensities were similar in value between “B<sub>low</sub>” and “B<sub>high</sub>”, the second highest filter intensity was used. With this, if the microbead’s corresponding filter intensity was equal to or lower than  $I_{barcode}$ , the barcode of interest was “B<sub>low</sub>”, otherwise “B<sub>high</sub>” was chosen.

We determined whether the analyte of interest is present by using the intensity values from the  $\lambda_{em} = 692/40$  filter, which isolates for the Alexa Fluor 647 secondary probe signal. The mean intensity value across the microbead surface, for all barcodes of the same type, were used directly in all cases.

## 3 Results & Discussion

### 3.1 Solution- vs. Surface-based Genetic Assay

We compared the differences between (1) solution-based barcode assay detected using flow cytometer, (2) solution-based barcode assay imaged using CCD camera, and (3) surface-based barcode assay imaged using CCD camera. Unfortunately, surface-based barcode assays cannot be detected using flow cytometry as it requires samples to be in solution format. Three conditions were studied: (1) conjugated barcode, (2) conjugated barcode incubated with detection strand and no target (i.e. negative control), and (3) full hybridization with 100 fmol of target (i.e. positive control) (**Figure 4.4**). Note that this amount of target used (100 fmol) was based on a study conducted by our group previously<sup>50</sup>.

While the intensity values were not comparable between the flow cytometer and the CCD camera as they were generated from different instruments, we observed a large (~50x) difference between the negative and positive controls in the flow cytometry case (**Figure 4.4a**), which was not true for either imaging cases. This was puzzling for the case of solution assay imaging (**Figure 4.4b**) given that the same assay from flow cytometry was used. One explanation is in the instrumental sensitivity difference between them, which is logical given that the flow cytometer is a dedicated instrument, albeit larger and more expensive, compared to a microscope. As a further explanation, two factors need to be noted in the solution assay imaging case. It was observed that the deposition and drying of microbeads on the microwell chip after the assay resulted in more microbead aggregations compared to deposition and drying of the microbeads before the assay. This was likely due to interactions between the genetic strands on the microbeads. We also observed crystal-like structures forming on the surface after depositing the solution assay. These were suspected to be salt crystals from the washing buffer (consisting of 0.5x SSC and 0.1% SDS), in which the microbeads were suspending post-wash. Both factors can affect the resulting intensities and may explain the lack of difference between negative and positive controls in the solution assay imaging case. For the surface assay imaging case (**Figure 4.4c**) the lack of difference between the negative and positive controls can be attributed to, again, the reduced instrumental sensitivity, as well as the lack of optimization and characterization of its analytical sensitivity range.

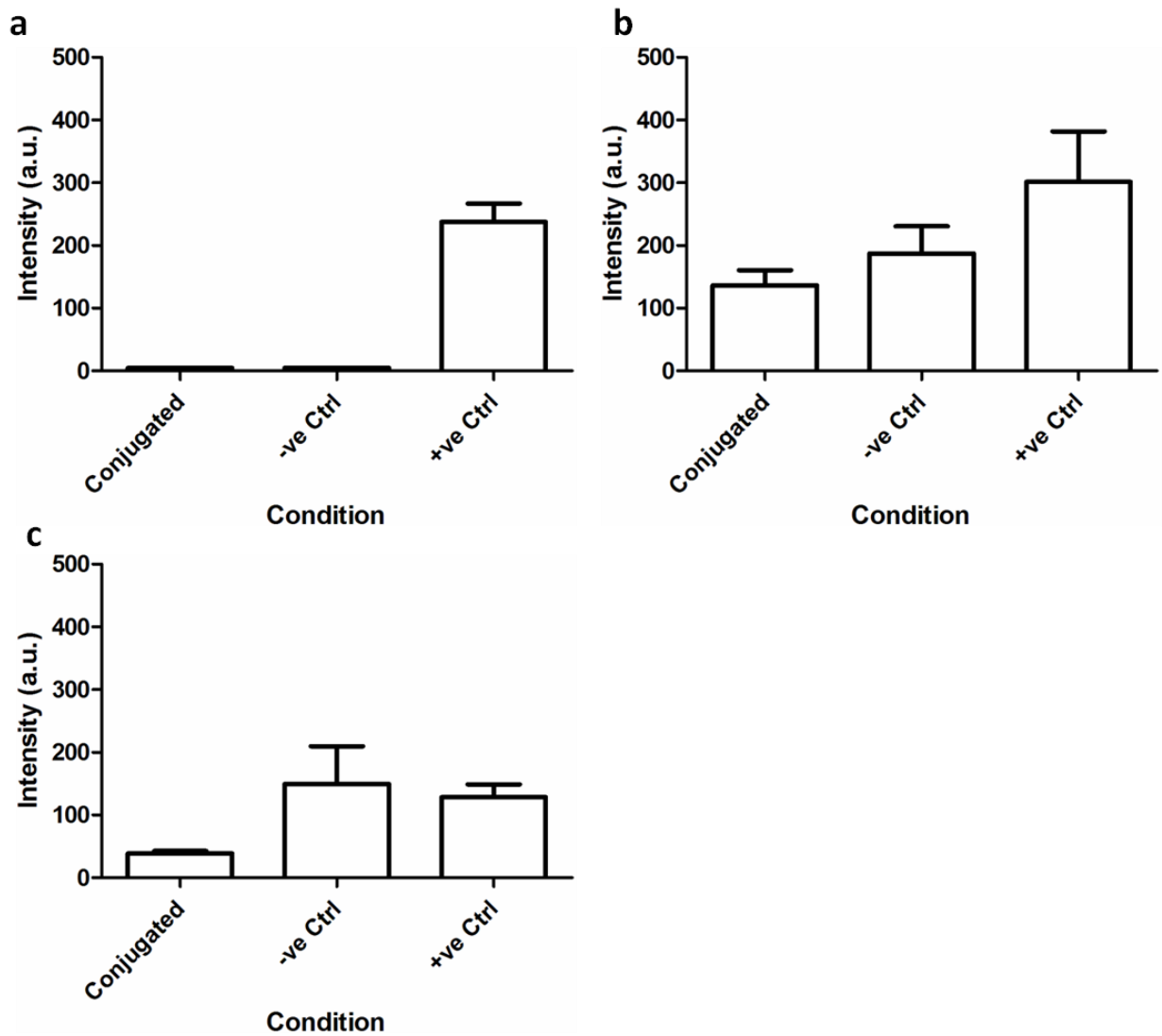


**Figure 4.4. Comparison of flow cytometry and CCD imaging genetic assays.**

Comparison of genetic assays performed and detected using (a) solution-based barcode assay and flow cytometry, (b) solution-based barcode assay and CCD imaging, and (c) surface-based barcode assay and CCD imaging. Custom-designed DNA captures strand (length: 30 nt; sequence: 5'- AAT ATA TTT GGT TTT CCC AAA CCA GTT TAA-3'), DNA target strand (length: 58 nt; sequence: 5'-CGG CGA TGA ATA CCT AGC ACA CTT ACT ATT AAA CTG GTT TGG GAA AAC CAA ATA TAT T-3'), and DNA detection strand (length: 25 nt; sequence: 5'-Alexa647-TAA GTG TGC TAG GTA TTC ATC GCC G-3') were used. Data represent the mean and standard error from three replications.

It should be noted that solution-based assays tend to be more homogeneous (i.e. even coverage of analytes) and result in better hybridization kinetics compared to surface-based assays (e.g. microarray or our microbead-coated chip). This is because in solution-based assays the microbeads are suspended in solution and free to move about, and can therefore refresh their depletion layer to hybridize with more analytes<sup>109</sup>. This is in contrast with surface-based assays where the capture strands are fixed in place, either directly on a substrate (microarray) or on the surface of microbeads (in our case). However, due to the increased surface area from the use of microbeads, we do expect our approach to be better than pure planar approaches like microarrays with regards to assay performances. In all, while our surface-based imaging system offers greater portability, economy, and ease of use compared to a solution-based flow cytometry setup, it also has its drawbacks.

## 3.2 Assay Optimization

In an effort to increase the assay intensity and thus increase the contrast between negative and positive detection cases of our surface-based barcode assay, we optimized for different assay conditions. Leveraging our group's knowledge and expertise in performing quantum dot barcode genetic assays in solution, we modeled the majority of our optimization conditions based on work done in the past<sup>29,50,75,109</sup>. In all cases 1 pmol of target strands were used to ensure saturation, and 10000 microbeads were used to ensure assay consistency from a large sample size.

### 3.2.1 DNA Sequence and Lengths

The design of DNA sequences for various infections<sup>29</sup>, and optimizations involving sequence lengths and hybridization structures<sup>50</sup>, were studied by our group in the past and used by this thesis.

### 3.2.2 Amount of Capture Strands for Conjugation

The amount of capture strands functionalized was optimized and determined to be  $10^{-12}$  mol DNA per  $10^5$  microbeads, selected based on the high intensity resulting from this condition (**Figure 4.5a**). As the number of captures strands conjugated to the microbeads increased, the resulting assay signal from hybridization increased with it until a certain point. Beyond the

optimal point the over abundance of surface conjugation by the capture strands resulted in steric hinderance<sup>109</sup>, which can block and reduce hybridization, indicated by the reduced intensities.

### 3.2.3 Amount of Detection Strands in the Assay

It is crucial that a sufficient amount of detection strands are present in the sample to hybridize with the bound target strands to ensure maximal detectable intensity. The amount of detection strand was optimized by increasing its ratio with respect to the target strand amount at 1 pmol (**Figure 4.5b**). As can be observed, saturation (i.e. the highest intensity) was reached at 1000x. However, due to cost considerations the 100x condition, or 100 pmol, was used.

### 3.2.4 Hybridization Buffer Type

Different types of buffer conditions were used to test for the condition that yielded the highest signal (**Figure 4.5c**). Both 5x and 10x SSC resulted in the highest signal due to the high presence of salt, which neutralizes the negative charge on the DNA backbone and thus facilitate hybridization. However, from literature<sup>50</sup>, because 10x SSC can cause microbead instability after long incubation (> 1 hour) due to the high concentrations of salt. Therefore 5x SSC condition was used.

### 3.2.5 Hybridization Temperature

To further increase hybridization kinetics and thus assay intensity, we tested assay incubation at 37 °C, up from room temperature of approximately 22 °C. Between the two conditions, the higher temperature resulted in a minor intensity increase and was thus used (**Figure 4.5d**).

### 3.2.6 Hybridization Kinetics

From the study, we observed that our genetic assay intensity reached the maximum in 35 minutes (**Figure 4.5e**). However, unlike with solution-based assays, it was observed that the 10-μL hybridization solution began to evaporate on the chip at an accelerated rate beyond the 20-minute point, even when the chip was covered. Complete drying, which was observed to happen past 25 minutes unless moisture was introduced, would cause the detection strand to adhere onto the barcode and unable to be removed despite vigorous washing. This was likely due to high ionic strengths from the salt in the hybridization buffer (10x SSC, 0.1% SDS). Therefore, to avoid this, 20 minutes of incubation time was adopted.

### 3.2.7 Continuous Excitation of the Detection Strand Fluorophore

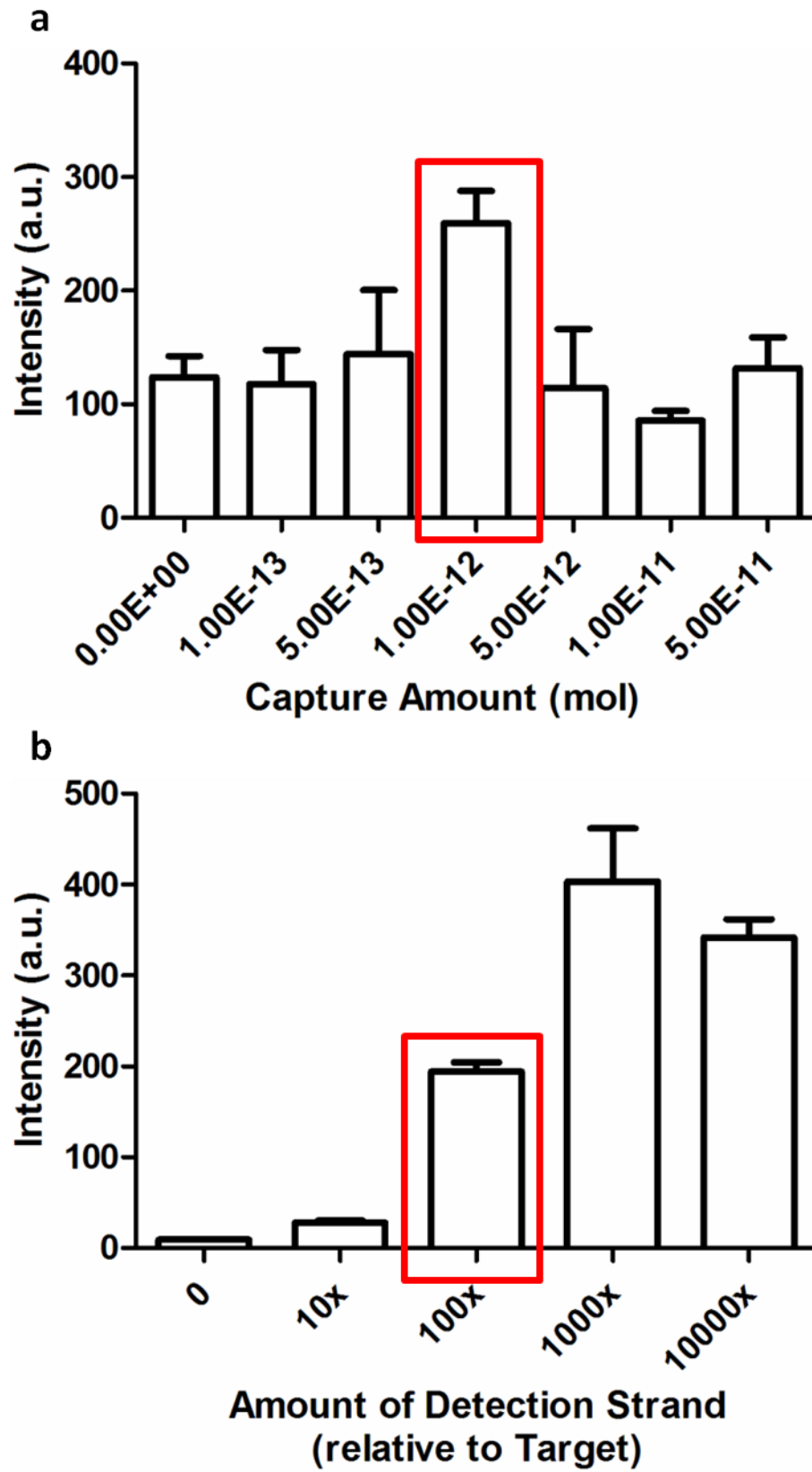
Finally, we characterized the photobleaching effect on the detection strand's Alexa647 fluorophore by subjecting it to continuous excitation during imaging (**Figure 4.5f**). This was to determine the longest duration for fluorophore excitation while avoiding significant photobleaching. While it did occur as expected, photobleaching was not significant (at most 12% reduction in intensity) within the first minute of excitation, which is well within the duration of our imaging time (typically 30 s).

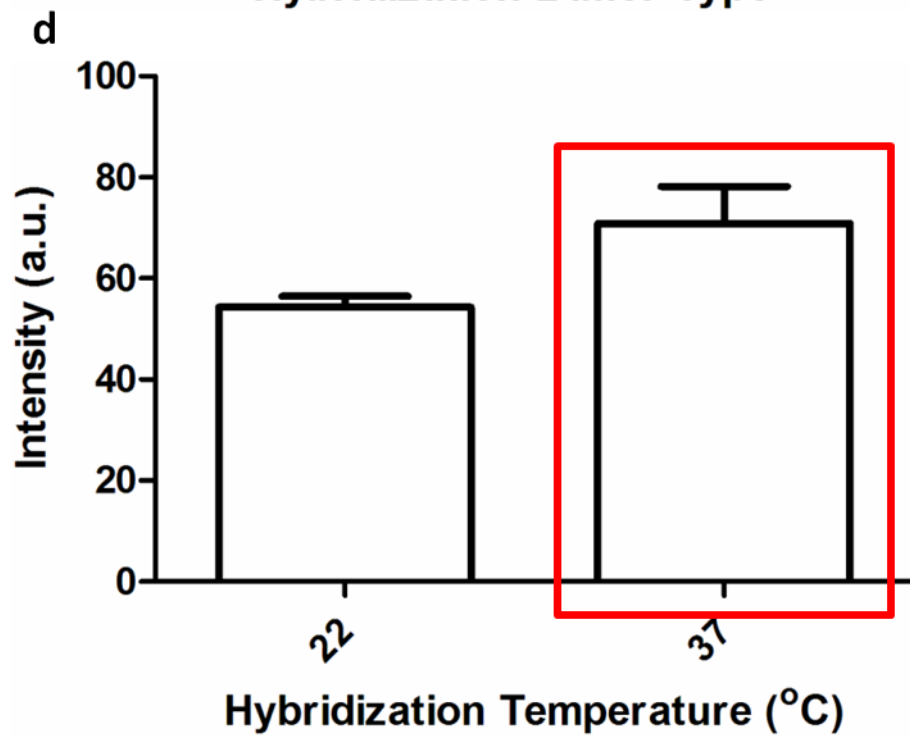
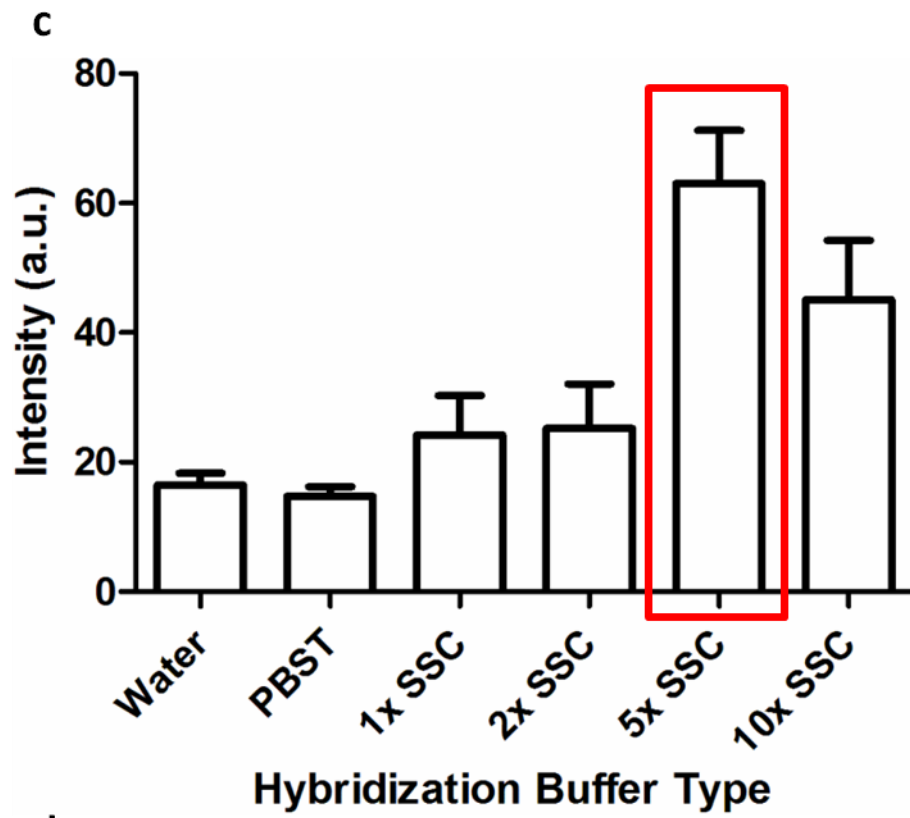
### 3.2.8 Background Intensity Adjustment

One important observation we made after the optimizations was the variability of intensity ranges between experiments, in particular the “negative” conditions. For example, the 0 fmol capture condition (**Figure 4.5a**) has a mean intensity of 124, whereas the water hybridization buffer condition (**Figure 4.5c**) has a mean intensity of 16; the incubation time experiment (**Figure 4.5e**) even has its mean intensities in the 1000's. Unsurprisingly, this was the result of high background signal, both from the environment and in some case the barcodes' themselves (see  $\lambda_{em} = 692/40$  filter intensity for B5-B7 in **Figure 4.3**). Fortunately, this does not affect the optimization results as each study was performed using the same barcode and imaging setup between the conditions, so the relative differences in intensities would remain, resulting in the same optimal conditions. However, from here on, all experiments using microscopy imaging were adjusted for intensities from the environment and barcode by first imaging the conjugated barcodes on the chip in ambient environmental lighting, then subtracting this mean intensity from all further intensities obtained in the same environment.

While background intensity had a significant impact on the  $\lambda_{em} = 692/40$  filter images due to their high imaging exposure times (1 s) and relatively low secondary probe signal, the barcode intensities (i.e.  $\lambda_{em} = 530/10$ ,  $580/10$ , and  $640/10$  filter images) were relatively immune. This was because the imaging exposure times used for them were low (200 ms or  $1/5$  s) and that the barcodes fluoresced at much high intensities compared the secondary probe. Thus background intensity adjustment did not need to be applied to the barcodes, and their intensity profiles remained the same.







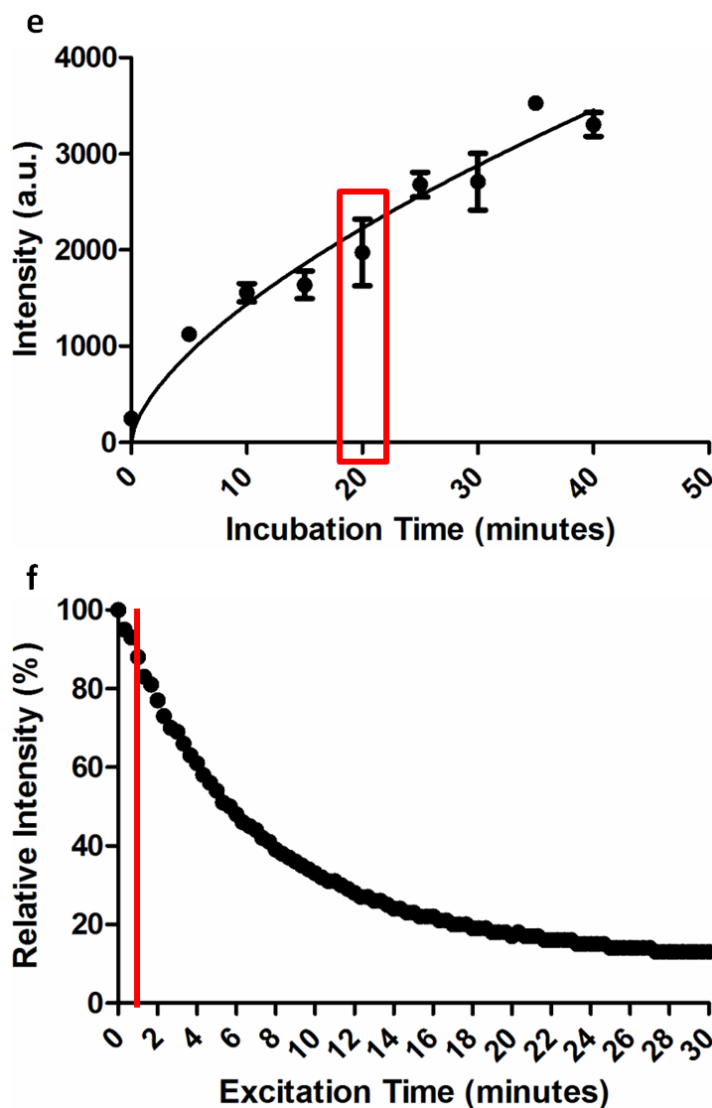


**Figure 4.5. Surface assay optimization.**

Optimization of our surface-based genetic assay for (a) amount of capture strands, (b) amount of detection strands, (c) hybridization buffer type, (d) hybridization temperature, (e) incubation time, and (f) length of excitation time. Red highlights indicate the optimized condition adopted for the final protocol. Custom-designed DNA captures strand (length: 30 nt; sequence: 5'- AAT ATA TTT GGT TTT CCC AAA CCA GTT TAA-3'), DNA target strand (length: 58 nt; sequence: 5'-CGG CGA TGA ATA CCT AGC ACA CTT ACT ATT AAA CTG GTT TGG GAA AAC CAA ATA TAT T-3'), and DNA detection strand (length: 25 nt; sequence: 5'- Alexa647-TAA GTG TGC TAG GTA TTC ATC GCC G-3') were used. Data represent the mean and standard deviation from three replications.

### 3.3 Camera Usage

Up to this point, a CCD camera was used for imaging as an initial proof-of-concept for imaging-based assay detection. However, the CCD camera is expensive and not prevalent. Indeed, most of the current detection platforms for identifying quantum dot barcodes found in literature require expensive instruments and detectors, and would be prohibitive in their use in resource-limited settings<sup>29,76</sup>. Having optimized the various surface assay parameters using the established CCD-based instrumental setup, we began work on imaging using a smartphone (**Figure 4.6**). First, we needed to confirm the smartphone's (in this case Apple's iPhone 4S) imaging capabilities for our purposes. Our system consisted of the smartphone mounted onto the front port of a microscope and a mercury lamp to excite the barcodes on the chip. We demonstrated that an iPhone camera was able to capture the distinct optical emission of each barcode in the microwell (**Figure 4.7a**). We also showed that the barcodes' optical signals can be differentiated from that of the secondary probe's using proper filtering (**Figure 4.7b**).

Next, we compared the analytical performance of the iPhone 4S camera against that of the CCD camera's in detecting target analytes on a chip. Sensitivity curves were established by depositing conjugated microbeads on the microwell chip then incubated with the detection strand and their corresponding target strands in increasing amounts, from 5 fmol to 2 pmol, for one target sequence. Images were taken with both the CCD camera and Apple's iPhone 4S, and assay intensities (i.e. detection strand intensities observed through filter  $\lambda_{em} = 692/40$ , indicating hybridization) analyzed using our custom MATLAB algorithm (**Figure 4.8**). It was observed that the CCD camera was more sensitive (steeper slope in the linear dynamic range), and had a slightly higher saturation point on the sensitivity curve (beyond 2 pmol) (**Figure 4.8a**) than that of the iPhone's (~1 pmol) (**Figure 4.8b**). Despite this, the iPhone camera produced a similar limit of detection and dynamic range, albeit at different intensity ranges. Note how after background intensity adjustment the 5 fmol data point were on or near the base line in both cases. This study confirmed that an iPhone camera can image barcodes on the chip surface, be used as a detector for biological assays, and can reduce the cost and size of a quantum dot barcode readout device. The iPhone was thus used for detection in all further studies.

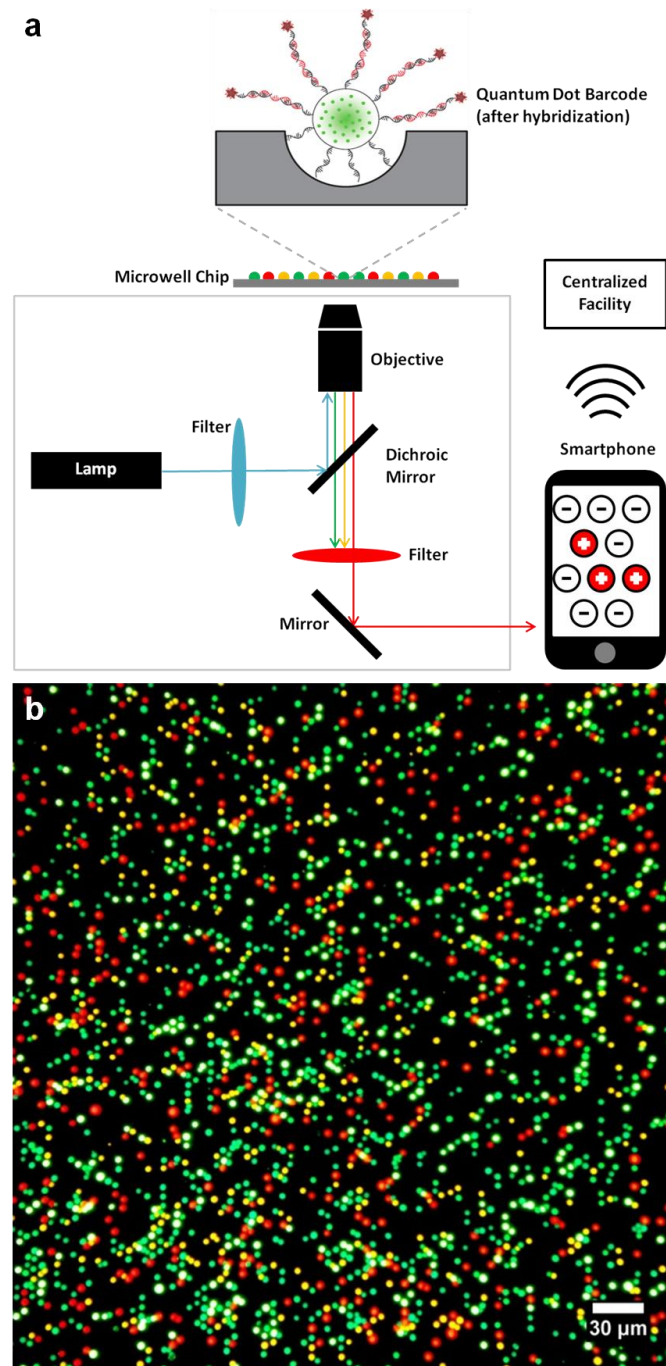


**Figure 4.6. Microscopy-smartphone imaging setup.**

Microscope-smartphone setup for quantum dot barcode imaging. (a) Illustration of the microscope-smartphone setup. (b) An example demonstrating smartphone-captured image of various colours of barcodes on the microwell chip.

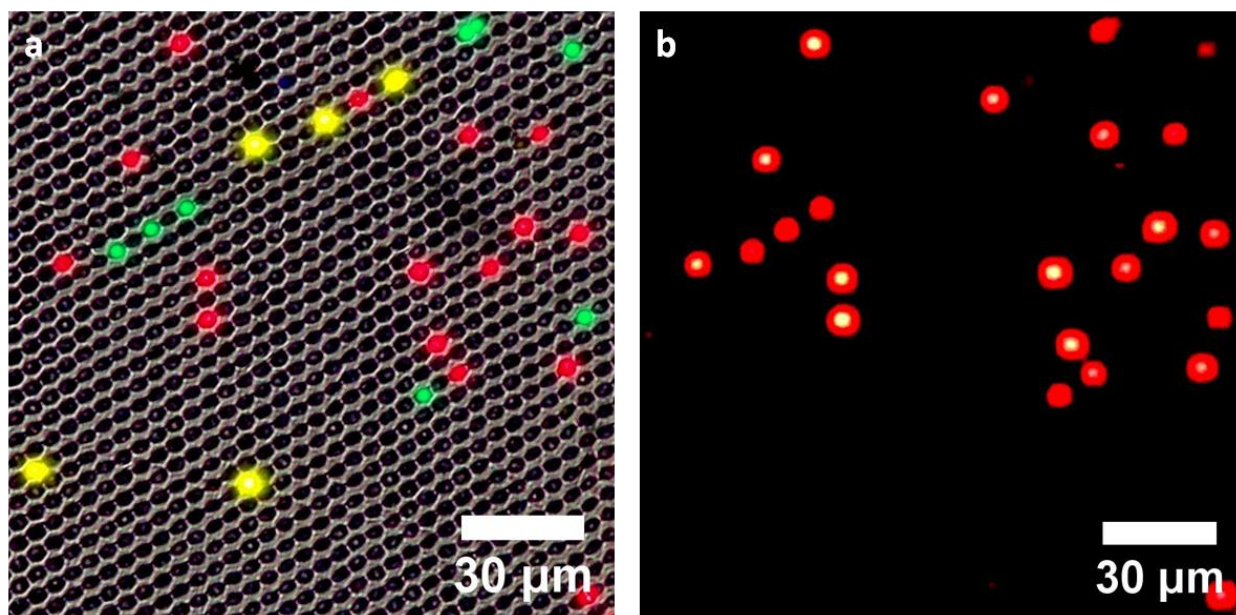


**Figure 4.7. Barcode genetic assay imaging on the smartphone.**

(a) Green, yellow, and red barcodes (identified as B1, B4, and B6 in **Table 4.1**, respectively) are deposited on the chip and imaged using an iPhone camera (fluorescence microscopy parameters: objective of 20x at  $NA = 0.50$ ,  $\lambda_{ex} = 350/50$ ,  $\lambda_{em} = 430LP$ , exposure time = 0.05 s). The microwells are visualized using bright-field microscopy. The fluorescence and bright-field images are super-imposed. (b) After the assay, the smartphone camera-acquired fluorescence image of the microbeads bound with the target analyte and secondary probe (fluorescence microscopy parameters: objective of 20x at  $NA = 0.50$ ,  $\lambda_{ex} = 640/40$ ,  $\lambda_{em} = 692/40$ , exposure time = 1 s). Both green and red beads had positive signals. This demonstrates that T1 and T6 genomic targets are present in the sample but not T4. Of note, the white spots on the barcodes are due to overexposure from the high combined intensity of the Alexa647 fluorophore and the 640 nm quantum dots impregnated within B6.

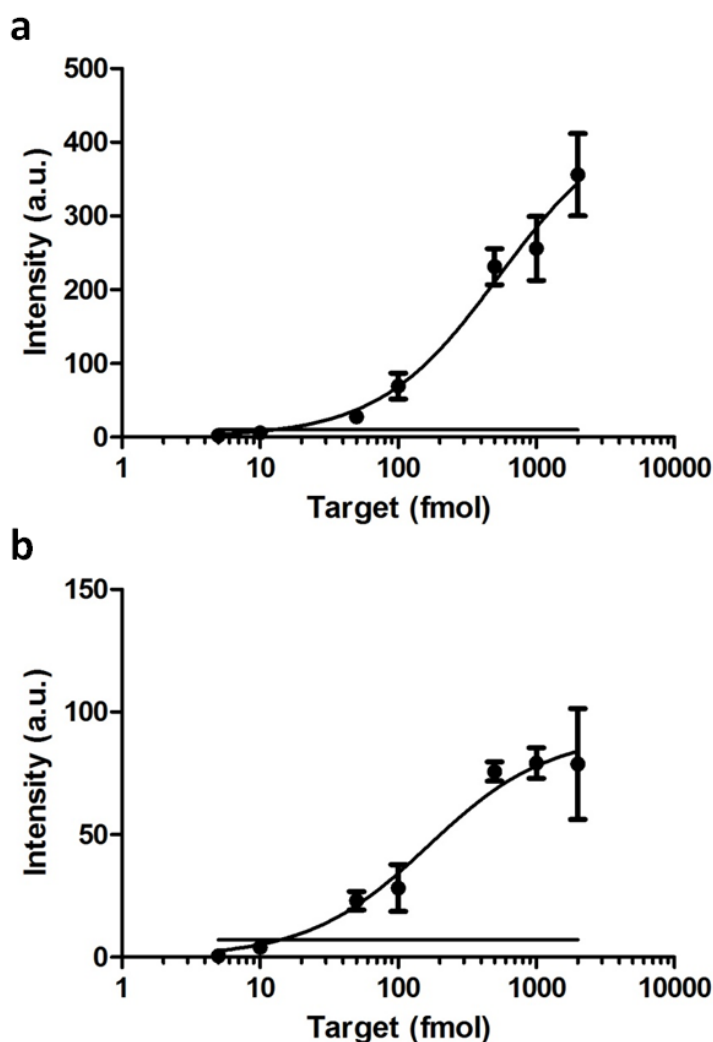


**Figure 4.8. Comparison of CCD and smartphone camera assay sensitivity.**

A comparison of sensitivity curves obtained from images taken with (a) a charge-coupled device (CCD) camera (Retiga EXi Fast 1394, QImaging) and (b) an iPhone camera (iPhone 4S, Apple Inc.), for a custom-designed sequence (capture sequence: 5'-GAG ACC ATC AAT GAG GAA GCT GCA GAA TGG GAT-3'; target sequence: 5'-CGG CGA TGA ATA CCT AGC ACA CTT A CTA AT CCC ATT CTG CAG CTT CCT CAT TGA TGG TCT C-3'; secondary probe sequence: 5'-Alexa647-TAA GTG TGC TAG GTA TTC ATC GCC G-3'). The horizontal lines represent the limits of detection and are ~15 fmol for both cases. Data represent the mean and standard deviation from three replications.

### 3.4 Assay Sensitivity

We proceeded to establish the sensitivity curves for a variety of infectious disease types (influenza type A H1N1, H3N2, H5N1, and HBV/C) using synthetic samples (**Figure 4.9**). We observed that the range of intensity levels varied for each target type, likely due to differences in conjugation efficiency between each barcode type and their respective capture strands from **Table 4.1**. This affects the total allowable binding of target strands and in turn detection strands. The intensity differences may also be due to differences in hybridization efficiency between each target strand and their respective capture and detection strands, likely resulting from differences in the various sequences and lengths used. Both of these highlight the importance of sensitivity characterization prior to use whenever a new barcode and/or genetic sequence is introduced. However, a sigmoid behaviour was observed in all cases, with the start and end of the linear region located between 50-100 fmol and 1-2 pmol, respectively. Intensity increases between consecutive points varying by twice the amount of target strand (e.g. 500 and 1000 fmol) were also observable. Not only does this demonstrate the system's usability for DNA-based analyte detection, but also its sensitivity to minor increases in assay signal, i.e. analyte concentration. Finally, all curves had a detection limit of approximately 10-50 fmol (not shown in figure), as defined by three standard deviations above the mean intensity of the negative control. From this, taking into account the assay volume (10  $\mu$ L), the *analytical* sensitivity (i.e. detection limit divided by assay volume) of the system for synthetic samples is calculated to be 1-5 nM. The *clinical* sensitivity, defined as the number of true positives divided by the total number of sick individuals in the population for clinical samples, does not apply here.

### 3.5 Multiplexing and Specificity

Having established the sensitivity curves, the final step in validating our surface-based assay system was to utilize the quantum dot barcodes for multiplexed detection, i.e. simultaneous detection of negative and positive conditions for multiple targets. This was demonstrated using the same five infectious diseases, as well as positive and negative controls as internal control cases. While the overall assay procedures remained the same as those of the sensitivity curves, it was found that some parameters had to be further optimized. This stemmed from that fact that using the same concentration of microbeads resulted in large aggregations between the different types of barcodes, which is unfavourable for barcode resolution. And while the underlying



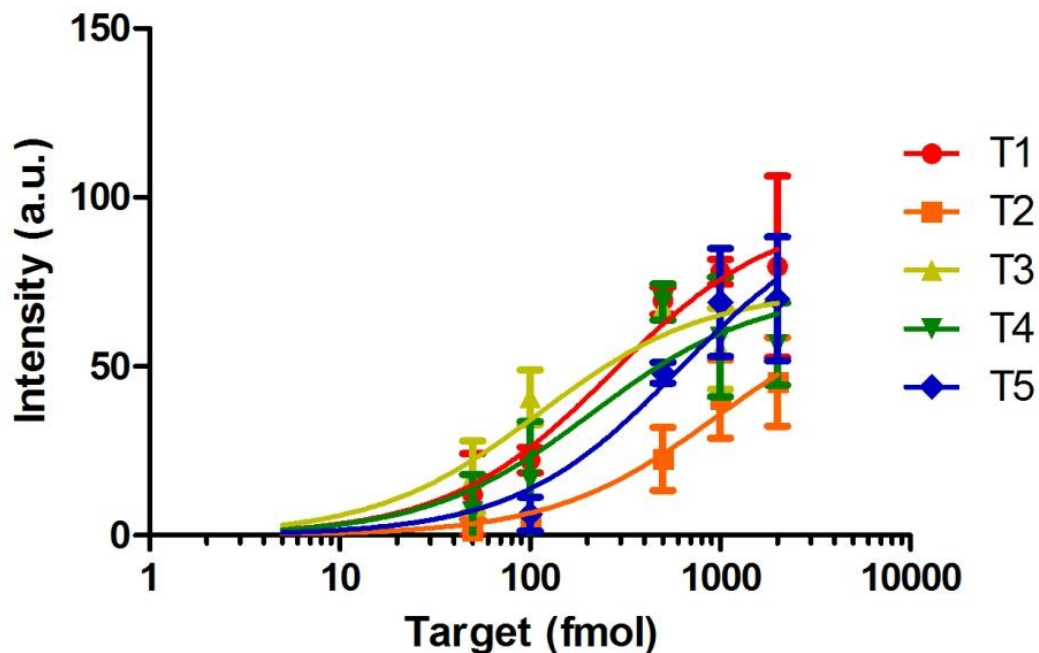


**Figure 4.9. Smartphone sensitivity curves.**

Sensitivity curves for genetic biomarkers for the influenza A viruses H1N1 (red), H3N5 (orange), and H5N1 (yellow), as well as HBV (green) and HCV (blue) from **Table 4.1**. Detection limit for all (not shown) is between 10-50 fmol. Data represent the mean and standard deviation from three replications.

mechanism is not well understood and warrants future investigation, it is suspected that the heterogeneity of the different barcode microbead sizes – resulting from different batches of barcode synthesis – played a role, as many of the barcode did not settle into the microwells. Interestingly, this phenomenon was in a way similar to our fill efficiency study when microbeads larger than 3  $\mu\text{m}$  were used. Thus, to perform the multiplexing assay, the final microbead concentration needed to be diluted by 4x before deposition onto the chip to minimize microbead aggregation. In addition, to account for the increase in hybridization volume due to the large number of samples involved, and to ensure that the target and detection strands were near-saturation during hybridization, the amount of target and detection strands used were increased. We chose six cases to demonstrate the 7-plex assays (**Figure 4.10**). Positive and negative control conditions were also included for each case, as internal controls that serve to indicate proper functioning of the assay. In all cases the assays and detections performed accordingly. This indicates the system's high *analytical* specificity for synthetic samples (i.e. low cross-reactivity). The *clinical* specificity, defined as the number of true negatives divided by the total number of well individuals in the population for clinical samples, does not apply here.

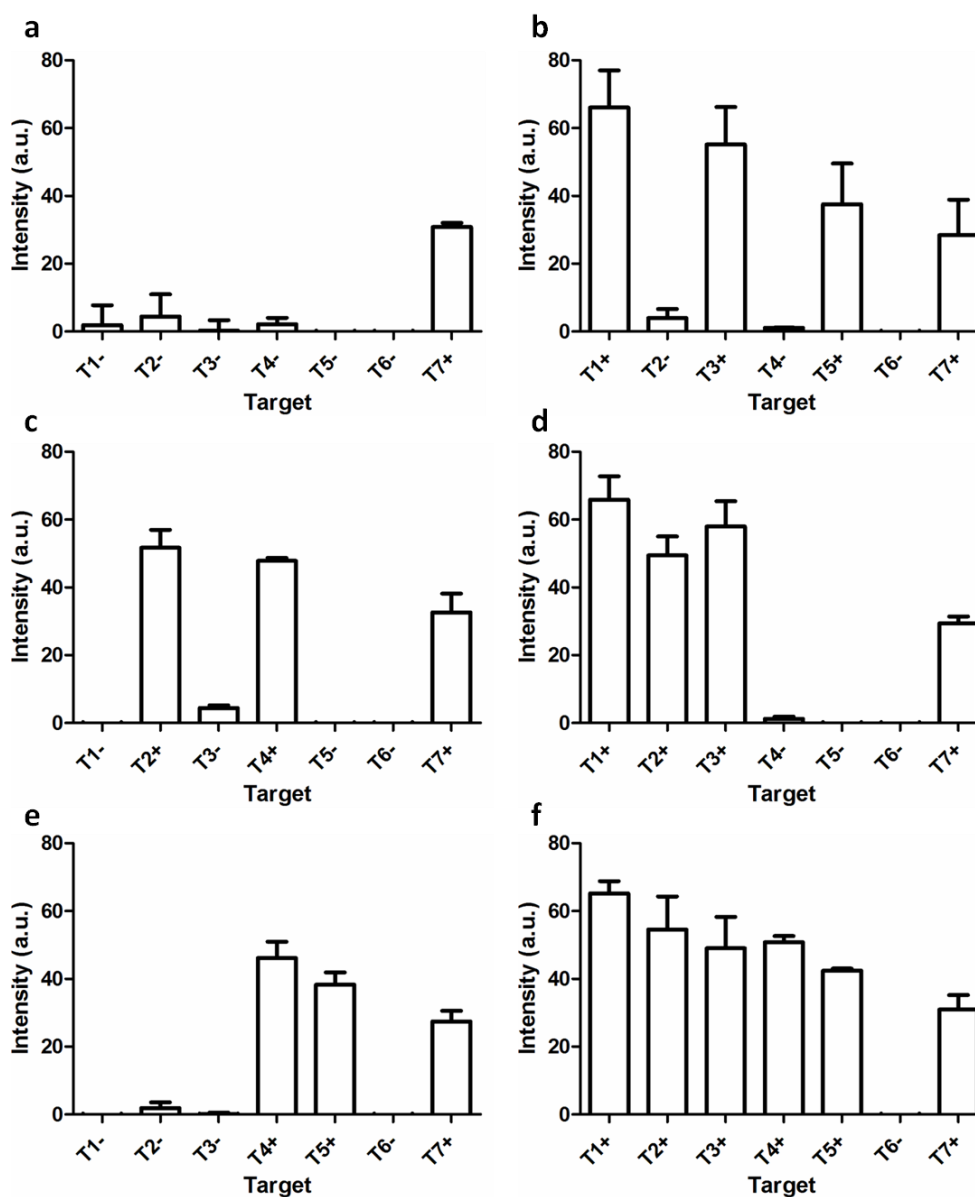


**Figure 4.10. Smartphone multiplexed detection.**

Demonstrations of multiplexed detection of all five infectious disease target strands T1 to T5 as well as a negative control T6 and a positive control T7 from **Table 4.1**. (a) Only T7 was present during hybridization. (b) Targets T1, T3, T5, and T7 were present during hybridization. (c) Targets T2, T4, and T7 were present during hybridization. (d) Targets T1, T2, T3, and T7 were present during hybridization. (e) Targets T4, T5, and T7 were present during hybridization. (f) All targets except for T6 were present during hybridization. Data represent the mean and standard deviation from three replications.

## 4 Chapter Summary

In this chapter we compared the analytical performance of traditional solution-based genetic assay to that of a surface-based one utilizing the quantum dot barcode chip developed in the previous chapter. We further optimized for all the necessary assay parameters for the chip platform, and compared its analytical sensitivity between a CCD-based imaging system to a smartphone-based one. We concluded this chapter by establishing the assay sensitivity for, and demonstrating multiplexed detection of, five types of infectious disease synthetic samples. Combined, we have shown that genetic assays can be performed on our barcode chip, and that the results can be analyzed using images taken from a smartphone.

## 5 Author Contributions

The experiments were designed by **K. Ming** and **W.C.W. Chan**. Experiments were performed by **D. Li** (quantum dot synthesis), **A. Lam** (quantum dot barcode synthesis), **K. Chen** (solution assay, barcode conjugation and validation, sensitivity and multiplexing assays), **A. Syed** (barcode conjugation and validation, sensitivity and multiplexing assays), and **K. Ming** (all others). Analyses were performed by **K. Ming**. Algorithms were written by **K. Ming**. This chapter was written by **K. Ming**.

## Chapter 5

### Construction and Validation of Smartphone Device

#### 1 Introduction

The objective for this thesis was to develop a point-of-care smartphone-based infectious disease diagnostic device utilizing quantum dot barcodes for multiplexing. Thus far we have used a microscopy setup to test our microwell chip platform functionalized with quantum dot barcodes. In Chapter 3, we confirmed that microscopy imaging can be used to identify and resolve up to nine quantum dot barcodes immobilized on the microwell chip. In Chapter 4, we validated that a smartphone, in conjunction with microscopy, can be used to image the barcodes on our chip, and whose images can be used to detect and analyze genetic assays involving five different types of infectious disease synthetic samples. We then established the system's analytical performance to be 10-50 fmol, and demonstrated its ability to perform 7-plex detection involving five targets and two controls. Utilizing cell phones or smartphones as part of a point-of-care diagnostics has been a popular theme in recent years, as Chapter 1 has illustrated<sup>64,65</sup>. The majority of these exploit the phone's camera functionality for detection, either for direct imaging of samples<sup>66</sup> or imaging of commercially-available test kits<sup>71</sup>. Using the smartphone in a similar manner, in this chapter we illustrate the design and construction of a portable imaging device – that replaces the microscope – such that, when used in conjunction with our quantum dot barcode chip, molecular detection can be performed for various types of infectious diseases. We validated this by detecting for both synthetic and clinical samples, as well as in both simplex and multiplex settings. Note that for the custom-designed synthetic sequences, hybridization between the capture and target strands, and target with detection strands are perfectly congruent (i.e. no base pair mismatches). Base pair mismatches will be discussed later in the context of diagnosing clinical samples.

#### 2 Experimental Methods

##### 2.1 Quantum Dot Synthesis

Same procedures as those in Chapter 4 were used. Quantum dot synthesis and characterization performed by **D. Li**.

## 2.2 Quantum Dot Barcode Synthesis

Same procedures as those in Chapter 4 were used. The barcodes synthesized are presented (**Table 5.1**) along with their synthesis parameters (**Table 5.2**). Quantum dot barcode synthesis and characterization performed by **A. Lam**.

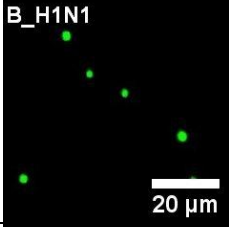
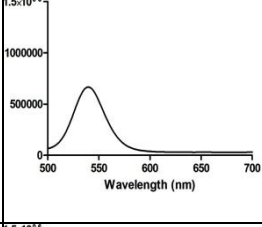
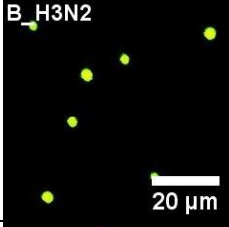
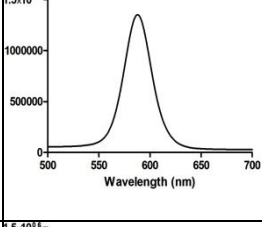
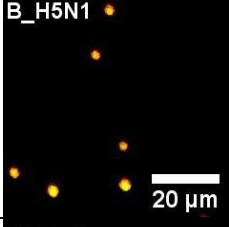
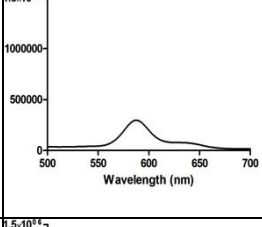
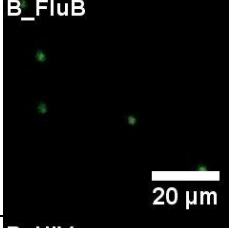
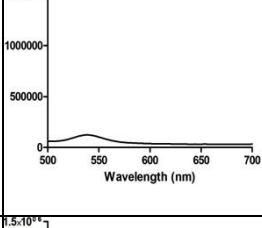
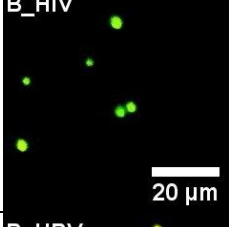
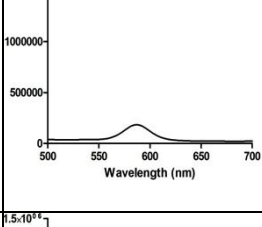
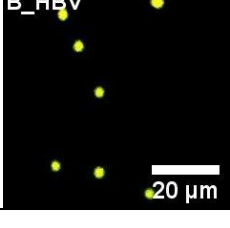
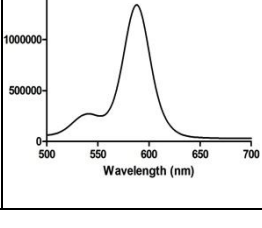
## 2.3 Barcode Microbead Conjugation and Validation

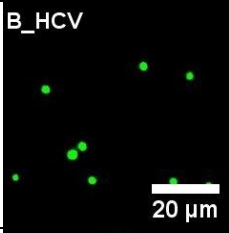
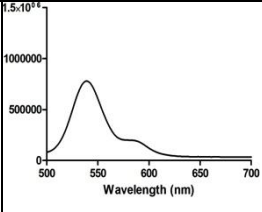
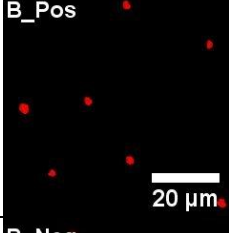
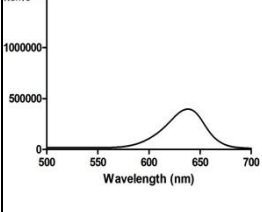
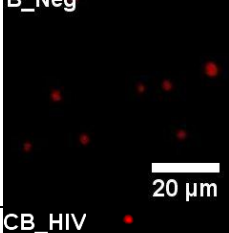
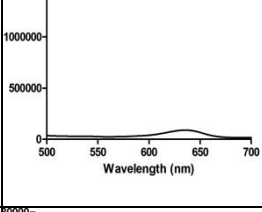
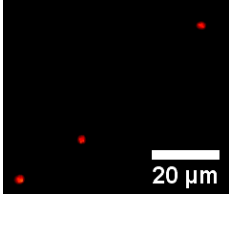
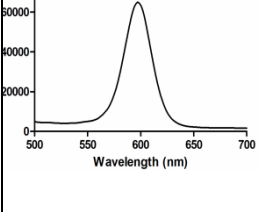
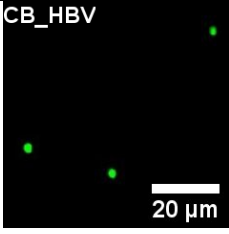
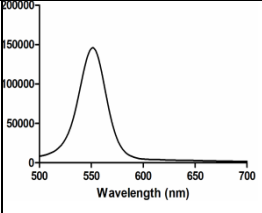
Same procedures as those in Chapter 4 were used, performed by **A. Syed**.

## 2.4 Sensitivity Assay

Sensitivity assays were performed directly on the microwell chips for all infectious disease DNA target strands (T\_H1N1, T\_H3N2, T\_H5N1, T\_FluB, T\_HIV, T\_HBV, and T\_HCV of Table 5.1) and their respective conjugated barcode microbeads (B\_H1N1, B\_H3N2, B\_H5N1, B\_FluB, B\_HIV, B\_HBV, and B\_HCV of Table 5.1). DNA target strands from Bio Basic Inc., purchased HPLC-purified, were prepared in increasing concentrations of 0, 5, 10, 50, 100, 300, 500, 1000, and 2000 fmol/ $\mu$ L in TE buffer (pH 8). DNA detection strand from IDT DNA Technologies with Alexa647 fluorophore on the 5' end, purchased HPLC-purified, were prepared with concentration of 100 pmol/ $\mu$ L in TE buffer (pH 8). Both DNA target and detection strand samples were stored at 4 °C until further use. To perform the assay, 1  $\mu$ L of the conjugated microbead sample, corresponding to approximately  $10^4$  conjugated microbeads, was deposited on a microwell chip for each assay condition and let dry for 1 hour. Then, 1  $\mu$ L of each DNA target strand sample (0, 5, 10, 50, 100, 300, 500, 1000, and 2000 fmol) was mixed with 5  $\mu$ L of hybridization buffer (10x SSC, 0.1% SDS, pH 7, heated to 60 °C), 3  $\mu$ L of DD water, and 1  $\mu$ L of DNA detection strands (1 pmol) or DD water (for the blank condition). This resulted in a total hybridization volume of 10  $\mu$ L for each assay condition, which include blank, 0, 10, 50, 100, 300, 500, 1000, and 2000 fmol target DNA. The hybridization solution for each assay condition was deposited over the conjugated microbead spots on the microwell chips and incubated at 37 °C for 20 minutes. The microwell chips were then submerged in 10 mL of washing buffer (0.5x SSC, 0.1% SDS, pH 7, heated to 37 °C), washed by agitation for 20 s, then let dry for 5 minutes before being imaged. Note that care must be taken so that the washing buffer does not dry and crystallize over the sample spots. Sensitivity assays performed by **A. Syed, J. Kim, and K. Ming**.

**Table 5.1. List of barcodes synthesized and their corresponding DNA strands.**

Disease/ Biomarker	Capture Name/Length/ Sequence (5' to 3')	Target / Amplicon Name/Length/ Sequence (5' to 3')	Secondary Probe Name/Len./ Sequence	Corresponding Barcode	Corresponding Barcode Spectrum
<b>Influenza</b>  Hemagglutinin – Influenza Type A (H1N1)	<b>C_H1N1/ 30 nt/ CCC TCT TAG TTT GCA TAG TTT CCC GTT ATG</b>	<b>T_H1N1/ 58 nt/ CGG CGA TGA ATA CCT AGC ACA CTT A CTA CA TAA CGG GAA ACT ATG CAA ACT AAG AGG G</b>	<b>D/ 25 nt/ 5'- Alexa647- TAA GTG TGC TAG GTA TTC ATC GCC G-3'</b>	<b>B_H1N1</b> 	
<b>Influenza</b>  Neuraminidase – Influenza Type A (H3N2)	<b>C_H3N2/ 30 nt/ ACT TGG TTG TTT GGG GGG GAG TTG AAT TCA</b>	<b>T_H3N2/ 58 nt/ CGG CGA TGA ATA CCT AGC ACA CTT A CTA TG AAT TCA ACT CCC CCC CAA ACA ACC AAG T</b>		<b>B_H3N2</b> 	
<b>Influenza</b>  Hemagglutinin – Influenza Type A (H5N1)	<b>C_H5N1/ 30 nt/ CCA TTC CCT GCC ATC CTC CCT CTA TAA AAC</b>	<b>T_H5N1/ 58 nt/ CGG CGA TGA ATA CCT AGC ACA CTT A CTA GT TTT ATA GAG GGA GGA TGG CAG GGA ATG G</b>		<b>B_H5N1</b> 	
<b>Influenza</b>  Influenza Type B	<b>C_FluB/ 27 nt/ CAC CGC AGT TTC AGC TGC TCG AAT TGG</b>	<b>T_FluB/ 55 nt/ CGG CGA TGA ATA CCT AGC ACA CTT A CTA CC AAT TCG AGC AGC TGA AAC TGC GGT G</b>		<b>B_FluB</b> 	
<b>Human Immuno- deficiency Virus (HIV)</b>  SK102 HIV-1	<b>C_HIV/ 33 nt/ GAG ACC ATC AAT GAG GAA GCT GCA GAA TGG GAT</b>	<b>T_HIV/ 61 nt/ CGG CGA TGA ATA CCT AGC ACA CTT A CTA AT CCC ATT CTG CAG CTT CCT CAT TGA TGG TCT C</b>		<b>B_HIV</b> 	
<b>Hepatitis B (HBV)</b>  PB-2 – HBV	<b>C_HBV/ 25 nt/ TCA GAA GGC AAA AAA GAG AGT AAC T</b>	<b>T_HBV/ 53 nt/ CGG CGA TGA ATA CCT AGC ACA CTT A CTA AG TTA CTC TCT TTT TTG CCT TCT GA</b>		<b>B_HBV</b> 	

<b>Hepatitis C (HCV)</b> KY 150 – HCV	<b>C_HCV/</b> <b>26 nt/</b> CAT AGT GGT CTG CGG AAC CGG TGA GT	<b>T_HCV/</b> <b>54 nt/</b> CGG CGA TGA ATA CCT AGC ACA CTT A CTA AC TCA CCG GTT CCG CAG ACC ACT ATG		<b>B_HCV</b>  20 μm	
<b>Positive Control</b>	<b>C_Pos/</b> <b>22 nt/</b> GAC AAT GCT CAC TGA GGA TAG T	<b>T_Pos/</b> <b>50 nt/</b> CGG CGA TGA ATA CCT AGC ACA CTT A CTA AC TAT CCT CAG TGA GCA TTG TC		<b>B_Pos</b>  20 μm	
<b>Negative Control</b>	<b>C_Neg/</b> <b>15 nt/</b> CCA ATA TCG GCG GCC	<b>T_Neg/</b> <b>43 nt/</b> CGG CGA TGA ATA CCT AGC ACA CTT A CTA GG CCG CCG ATA TTG G		<b>B_Neg</b>  20 μm	
<b>Clinical HIV Sample</b>	<b>CC_HIV/</b> <b>116 nt/</b> GAA AGG TGA AGG GGC AGT AGT AAT ACA AGA C AAT AGT GAC ATA AAG GTA GTA CCA AGA AGA AAA GCA AAG ATC ATT AGG GAT TAT GGA AAA CAG ATG GCA GGT GAT GAT TGT GTG G	<b>CT_HIV/</b> <b>66 nt/</b> TTT TTT TTT GCC ACA CAA TCA TCA CCT GCC ATC TGT TTT CCA TAA TCC CTA ATG ATC TTT GCT TTT	<b>CD_HIV/</b> <b>57 nt/</b> 5'- Alexa647- TTG GTA CTA CCT TTA TGT CAC TAT TGT CTT GTA TTA CTA CTG CCC CTT CAC CTT TCC-3'	<b>CB_HIV</b>  20 μm	
<b>Clinical HBV Sample</b>	<b>CC_HBV/</b> <b>100 nt/</b> GGC ATG GAC ATT GAC CCT TAT AAA GAA TTT GGA GCT TCT GTG GAG TTA CTC TCT TTT TTG CCT TCT GAT TTC TTT CCG TCT ATT CGG GAC CTT CTC GAC A	<b>CT_HBV/</b> <b>56 nt/</b> AAA AAA AAA TGT CGA GAA GGT CCC GAA TAG ACG GAA AGA AAT CAG AAG GCA AAA AA	<b>CD_HBV/</b> <b>47 nt/</b> 5'-AAC TCC ACA GAA GCT CCA AAT TCT TTA TAA GGG TCA ATG TCC ATG CC- Alexa647-3'	<b>CB_HBV</b>  20 μm	



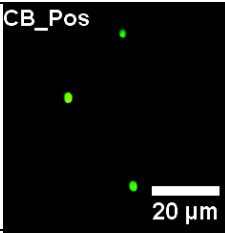
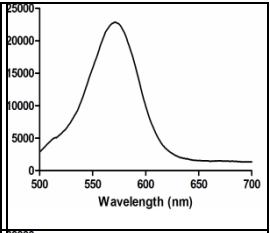
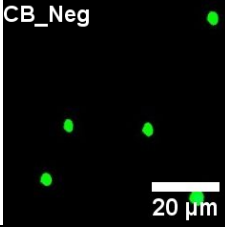
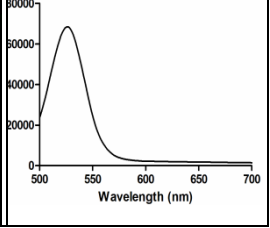
<b>Clinical Positive Control</b>	<b>CC_Pos/</b> <b>22 nt/</b> GAC AAT GCT CAC TGA GGA TAG T	<b>CT_Pos/</b> <b>50 nt/</b> CGG CGA TGA ATA CCT AGC ACA CTT A CTA AC TAT CCT CAG TGA GCA TTG TC	<b>CD/</b> <b>25 nt/</b> 5'- Alexa647- TAA GTG TGC TAG GTA TTC ATC GCC G-3'	<b>CB_Pos</b>  20 μm	
<b>Clinical Negative Control</b>	<b>CC_Neg/</b> <b>15 nt/</b> CCA ATA TCG GCG GCC	<b>CT_Neg/</b> <b>43 nt/</b> CGG CGA TGA ATA CCT AGC ACA CTT A CTA GG CCG CCG ATA TTG G		<b>CB_Neg</b>  20 μm	

Table created by the author. Reprinted (adapted) with permission from source<sup>113</sup>. Copyright 2015 American Chemical Society.

**Table 5.2. List of barcode synthesis parameters.**

<b>Barcode</b>	<b>Diameter (<math>\mu\text{m}</math>)</b>	<b>QD540 Concentration (<math>\mu\text{L/mL}</math>)</b>	<b>QD589 Concentration (<math>\mu\text{L/mL}</math>)</b>	<b>QD640 Concentration (<math>\mu\text{L/mL}</math>)</b>
B_H1N1	$2.70 \pm 1.61$	60		
B_H3N2	$2.70 \pm 1.36$		57	
B_HCV	$2.70 \pm 1.60$	60	11.4	
B_FluB	$2.70 \pm 1.60$	12	57	
B_HIV	$2.70 \pm 1.34$		57	182
B_HBV	$3.50 \pm 1.19$			910
B_H5N1	$2.70 \pm 1.51$			182

<b>Barcode*</b>	<b>Diameter (<math>\mu\text{m}</math>)</b>	<b>QD515 Concentration (<math>\mu\text{L/mL}</math>)</b>	<b>QD547 Concentration (<math>\mu\text{L/mL}</math>)</b>	<b>QD560 Concentration (<math>\mu\text{L/mL}</math>)</b>	<b>QD596 Concentration (<math>\mu\text{L/mL}</math>)</b>	<b>QD615 Concentration (<math>\mu\text{L/mL}</math>)</b>
CB_HIV	$3.5 \pm 1.66$			5	5	5
CB_HBV	$3.5 \pm 0.96$		200			
CB_Pos	$3.5 \pm 1.02$			50		
CB_Neg	$3.5 \pm 0.81$	100				

\*All microbeads were encoded with 150  $\mu\text{L}$  of 7 nm FeO Magnetic Nanoparticles (36.5 ng/mL). The magnetic iron (II,III) oxide nanoparticles were synthesized via the thermal decomposition of iron triacetylacetonate<sup>133</sup>.

Tables created by A. Lam. Reprinted (adapted) with permission from source<sup>113</sup>. Copyright 2015 American Chemical Society.

## 2.5 Multiplexing Assay

For the 3-plex multiplexing assay, 2  $\mu\text{L}$  of each conjugated barcode sample (B\_HBV, B\_HCV, and B\_Pos of Table 5.1), corresponding to approximately  $2 \times 10^4$  barcodes each, were mixed together with 18  $\mu\text{L}$  of DD water to produce a 4x dilution factor of the original. The dilution was to reduce microbead aggregation after deposition on chip, which may confound barcode resolution during analysis. To perform the assay, 5  $\mu\text{L}$  of the conjugated barcode mixture, corresponding to approximately  $1.25 \times 10^3$  conjugated beads, was deposited on a microwell chip for each assay condition and let dry for 3 hours. Then, 2  $\mu\text{L}$  of B\_HBV and B\_Pos (concentration of 2 pmol/ $\mu\text{L}$  each, or 4 pmol each) was mixed with 40  $\mu\text{L}$  of hybridization buffer (10x SSC, 0.1% SDS, pH 7, heated to 60 °C), 14  $\mu\text{L}$  of DD water, and 16  $\mu\text{L}$  of the detection strand (concentration of 100 pmol/ $\mu\text{L}$ , or 1600 pmol). This resulted in a total hybridization volume of 70  $\mu\text{L}$ . From this, 10  $\mu\text{L}$  of the hybridization solution was deposited over the conjugated barcode spots on the microwell chip and incubated at 37 °C for 20 minutes. The microwell chip was then submerged in 10 mL of washing buffer (0.5x SSC, 0.1% SDS, pH 7, heated to 37 °C), washed by agitation for 20 s, washed again in another 10 mL of washing buffer to further reduce non-specific binding, then let dry for 5 minutes before being imaged. Note that care must be taken so that the washing buffer does not dry and crystallize over the sample spots.

Cross reactivity between the bloodborne virus DNA target strands (T\_HIV, T\_HBV, and T\_HCV of Table 5.1) and their corresponding conjugated barcodes (B\_HIV, B\_HBV, and B\_HCV), as well as positive and negative control cases (B\_Pos and T\_Pos, and B\_Neg and T\_Neg, respectively), was studied. First, 6  $\mu\text{L}$  of each conjugated barcode sample, corresponding to approximately  $6 \times 10^4$  barcodes each, were mixed together with 90  $\mu\text{L}$  of DD water to produce a 4x dilution factor of the original. The dilution was to reduce microbead aggregation after deposition on chip, which may confound barcode resolution during analysis. To perform the assay, 8  $\mu\text{L}$  of the diluted conjugated barcode mixture, corresponding to approximately  $2 \times 10^4$  conjugated microbeads, was deposited on a microwell chip for each multiplexing case and let dry for 4 hours. Then, 4  $\mu\text{L}$  of each target case (DD water for the negative conditions, and corresponding DNA target strand sample with concentration of 2 pmol/ $\mu\text{L}$  for the positive conditions, or 8 pmol each) was mixed with 40  $\mu\text{L}$  of hybridization buffer (10x SSC, 0.1% SDS, pH 7, heated to 60 °C) and 20  $\mu\text{L}$  of the detection strand (concentration of 100 pmol/ $\mu\text{L}$ , 2000

pmol). This resulted in a total hybridization volume of 80  $\mu$ L for each multiplexing case. From this, 20  $\mu$ L of the hybridization solution for each multiplexing case was deposited over the conjugated barcode spots on the microwell chip and incubated at 37 °C for 20 minutes. The microwell chip was then submerged in 10 mL of washing buffer (0.5x SSC, 0.1% SDS, pH 7, heated to 37 °C), washed by agitation for 20 s, washed again in another 10 mL of washing buffer to further reduce non-specific binding, and then let dry for 5 minutes before being imaged. Note that care must be taken so that the washing buffer does not dry and crystallize over the sample spots. Multiplexing assays performed by **A. Syed, J. Kim, and K. Ming.**

## 2.6 Whole Blood Collection/Separation, Viral DNA/RNA Extraction, and Reverse Transcription

Whole blood was collected by venipuncture in either a Vacutainer (serum) or anticoagulant-treated tubes (plasma). Tubes were inverted several times, and stood upright for 30-60 minutes (for serum collection). Samples were then spun in a refrigerated centrifuge, and serum or plasma was aliquoted and stored at -80 °C. HBV or HIV nucleic acid was extracted using the Chemagic Viral DNA/RNA Kit (PerkinElmer), and HIV RNA was then reverse transcribed as per the iScript cDNA Synthesis kit (Bio-Rad). Whole blood was collected and prepared by **M.J. Biondi.**

## 2.7 Recombinase Polymerase Amplification (RPA) and Purification

RPA was performed using either extracted DNA or reverse-transcribed cDNA using the TwistAmp Basic kit (TwistDx, UK). For HBV detection, a premix solution containing 0.48 pmol/ $\mu$ L of each forward and reverse primers (5'-GGC ATG GAC ATT GAC CCT TAT AAA GAA TTT GG-3', 5'-TGT CGA GAA GGT CCC GAA TAG ACG GAA AGA-3'), 9.2  $\mu$ L of nuclease-free water, 29.5  $\mu$ L of rehydration buffer, and 4  $\mu$ L of the either extracted non-infected or infected DNA was prepared in a volume of 47.5  $\mu$ L. This solution was then transferred to a tube containing the reaction pellet and mixed. The reaction was initiated by the addition of 2.5  $\mu$ L of 280 mM magnesium acetate, and incubated at 37 °C for 10 minutes to produce 100 base-pair amplicon.

For HIV detection, a premix solution containing 0.48 pmol/ $\mu$ L of each forward and reverse primers (5'-GAA AGG TGA AGG GGC AGT AGT AAT ACA AGA CA-3', 5'-CCA CAC

AAT CAT CAC CTG CCA TCT GTT TTC CA-3'), 11.2  $\mu\text{L}$  of nuclease-free water, 29.5  $\mu\text{L}$  of rehydration buffer, and 2  $\mu\text{L}$  of the either extracted and reverse-transcribed non-infected or infected cDNA was prepared for a total volume of 47.5  $\mu\text{L}$ . This solution was then transferred to a tube containing the reaction pellet and mixed. The reaction was initiated by the addition of 2.5  $\mu\text{L}$  of 280 mM magnesium acetate, and incubated at 37 °C for 30 minutes to produce 116 base-pair amplicon.

RPA products were purified using EZ-10 Spin Column DNA Gel Extraction Kit (Bio Basic), and eluted into 50  $\mu\text{L}$  for detection. Purified DNA was visualized by gel electrophoresis, and kept at 4 °C until later use. RPA and sample purification performed by **J. Kim**.

## 2.8 Mono-Infection Assays using Amplified Clinical Samples

Clinical mono-infection assays were performed directly on the microwell chips using HIV- and HBV-negative, as well as HIV- and HBV-positive samples after amplification. DNA detection strands from IDT DNA Technologies with Alexa647 fluorophore on either 5' end (CD\_HIV of Table 5.1) or 3' end (CD\_HBV of Table 5.1), purchased HPLC-purified, for the HIV and HBV target sequences, were prepared with concentration of 100 pmol/ $\mu\text{L}$  in TE buffer (pH 8) and stored at 4 °C until further use. To perform the assay, 1  $\mu\text{L}$  of the conjugated microbead sample, corresponding to approximately  $10^4$  conjugated microbeads, was deposited on a microwell chip for each assay condition and let dry for 1 hour. During this time 20  $\mu\text{L}$  of the amplified sample (unknown amount) was mixed with 5  $\mu\text{L}$  of the corresponding detection strand (500 pmol) and denatured at 100 °C for 15 minutes. Then, the 25- $\mu\text{L}$  denaturation solution was mixed with 25  $\mu\text{L}$  of hybridization buffer (10x SSC, 0.1% SDS, pH 7, heated to 60 °C). The 50- $\mu\text{L}$  hybridization solution was deposited over the dried conjugated microbead spot on the microwell chip and incubated at 37 °C for 60 minutes, and let cool at room temperature for 5 minutes. The microwell chip was then submerged in 200 mL of washing buffer (0.5x SSC, 0.1% SDS, pH 7, heated to 37 °C), washed by agitation for 10 s, washed again in another 200 mL of washing buffer to further reduce non-specific binding, and let dry for 5 minutes before being imaged. Note that care must be taken so that the washing buffer does not dry and crystallize over the sample spots.

## 2.9 Co-Infection Assays using Amplified Clinical Samples

Cross-reactivity between the amplified HIV and HBV clinical samples (CT\_HIV and CT\_HBV of Table 5.1) and their corresponding conjugated barcodes (CB\_HIV and CB\_HBV of Table 5.1), as well as positive and negative control cases (CB\_Pos and CT\_Pos, and CB\_Neg and CT\_Neg of Table 5.1, respectively), was studied. First, 5  $\mu\text{L}$  of each conjugated barcode sample, corresponding to approximately  $5 \times 10^4$  barcodes each, were mixed together with 20  $\mu\text{L}$  of DD water to produce a 2x dilution factor of the original. The dilution was to reduce microbead aggregation after deposition on chip, which may confound barcode resolution during analysis. To perform the assay, 1  $\mu\text{L}$  of the diluted conjugated barcode mixture, corresponding to approximately  $5 \times 10^3$  conjugated microbeads, was deposited on a microwell chip for each multiplexing case and let dry for 1 hour. During this time 10  $\mu\text{L}$  of each amplified sample (unknown amount for each), 10  $\mu\text{L}$  of the positive control (10 pmol), and 10  $\mu\text{L}$  of DD water (for negative control) were mixed with 5  $\mu\text{L}$  of each of the corresponding detection strands (5  $\mu\text{L}$  of CD\_HIV, 5  $\mu\text{L}$  CD\_HBV, and 10  $\mu\text{L}$  of CD for both CT\_Pos and CT\_Neg, corresponding to 500 pmol for each target type) and denatured at 100 °C for 15 minutes. Then, the 60- $\mu\text{L}$  denaturation solution was mixed with 60  $\mu\text{L}$  of hybridization buffer (10x SSC, 0.1% SDS, pH 7, heated to 60 °C). The 120- $\mu\text{L}$  hybridization solution was deposited over the dried conjugated microbead spot on the microwell chip and incubated at 37 °C for 60 minutes, and let cool at room temperature for 5 minutes. The microwell chip was then submerged in 400 mL of washing buffer (0.5x SSC, 0.1% SDS, pH 7, heated to 37 °C), washed by agitation for 10 s, washed again in another 400 mL of washing buffer to further reduce non-specific binding, and let dry for 5 minutes before being imaged. Note that care must be taken so that the washing buffer does not dry and crystallize over the sample spots.

## 2.10 Device Design and Construction

The device was designed using SolidWorks 2012 and 3D printed commercially (ReproDux, North York, Ontario, Canada). Laser diode excitation sources of 405 nm 50 mW (<http://www.ebay.com/itm/170719374707>), and 650 nm 50 mW ([http://www.ebay.com/itm/1pcs-650nm-50mw-Red-Laser-Diode-Dot-Module-/370650098149?pt=LH\\_DefaultDomain\\_0&hash=item564c77a9e5](http://www.ebay.com/itm/1pcs-650nm-50mw-Red-Laser-Diode-Dot-Module-/370650098149?pt=LH_DefaultDomain_0&hash=item564c77a9e5)) were purchased online and secured into the device as delivered. The device was designed such that both lasers could excite

the same spot on the chip. An excitation filter  $\lambda_{\text{ex}} = 655/15$  nm (Edmund Optics) was fixed in front of the 650 nm laser diode source to reduce background signal. Both laser diodes were electrically connected to 2x AA batteries via a battery holder and single-pole triple-throw switch (both purchased from a local electronics shop) that switches between the two sources as well as an OFF state. A generic 160x-200x pocket microscope was purchased online (<http://www.gadgetplus.ca/science/Microscope160-200x.html>). It was disassembled to extract the eyepiece and objective lenses, and installed into the device manually. The eyepiece was fixed in place but the objective was made to be movable long a track to allow focusing on the sample.

## 2.11 Sample Imaging

All images were acquired using the iPhone 4S from Apple (unless otherwise specified) mounted in our device. Quantum dot barcodes and Alexa647 fluorophore were excited using laser diodes of wavelengths 405 nm and 650 nm, respectively. Emission filters  $\lambda_{\text{em}} = 430\text{LP}$  (Thorlabs),  $\lambda_{\text{em}} = 530/10$  (Thorlabs),  $\lambda_{\text{em}} = 580/10$  (Thorlabs),  $\lambda_{\text{em}} = 640/10$  (Thorlabs), and  $\lambda_{\text{em}} = 692/40$  (Semrock, Brightline Cy5-4040A) were placed in the device's emission filter slot one at a time during imaging. The emission filter  $\lambda_{\text{em}} = 430\text{LP}$  was used in conjunction with a neutral density filter OD = 1.3 (Thorlabs) to image all barcodes to determine their size and location, while avoiding intensity saturation. The emission filters  $\lambda_{\text{em}} = 530/10$ ,  $\lambda_{\text{em}} = 580/10$ , and  $\lambda_{\text{em}} = 640/10$  corresponded with quantum dots QD540, QD589, and QD640, respectively, and were used to isolate for their fluorescence for resolving barcodes. The emission filter  $\lambda_{\text{em}} = 692/40$  was used to isolate for the detection strand Alexa647 secondary label fluorescence as a means to measure the amount of analyte that hybridized with its corresponding capture strand. Image exposure times, made adjustable with the use of the NightCap app from Apple's App Store, was maintained at 1 s for all filters. In the case of fluorophore particles, they were excited using only the 405 nm laser diode source and imaged using only the emission filter  $\lambda_{\text{em}} = 430\text{LP}$ , the images of which were used for subsequence intensity analysis. The  $\lambda_{\text{em}} = 430\text{LP}$  emission filter was also acquired through a neutral density filter (Thorlabs) of OD = 0.6 to avoid overexposure.

## 2.12 Image Analysis

A custom-made algorithm was written in MathWork's MATLAB for all image analysis (see supplement section for the code). The algorithm accepts as inputs five emission filter images ( $\lambda_{\text{em}} = 430\text{LP}$ ,  $\lambda_{\text{em}} = 530/10$ ,  $\lambda_{\text{em}} = 580/10$ ,  $\lambda_{\text{em}} = 640/10$ , and  $\lambda_{\text{em}} = 692/40$ ) of a sample. The images

were cropped to include microbeads of interest based on user selection. The cropped filter images were aligned with the  $\lambda_{em} = 430\text{LP}$  filter image through the use of the Discrete Fourier Transform registration<sup>119,120</sup>. The algorithm then identified the size and location of each microbead, based on its appearances in the  $\lambda_{em} = 430\text{LP}$  filter image, using the Hough transform<sup>121,122</sup>. Erroneously identified microbeads (e.g. debris, imaging artefacts, overlapping microbeads) were excluded based on user input. Each microbead was then associated with the mean pixel intensity across its area at each of the four remaining filter images. For each microbead, the  $\lambda_{em} = 530/10$ ,  $\lambda_{em} = 580/10$ , and  $\lambda_{em} = 640/10$  filter image intensities comprised its intensity profile, while the  $\lambda_{em} = 692/40$  filter image intensity indicated the fluorescent secondary probe intensity. In order to identify the microbeads on the chip, known barcode intensity profiles were first established (**Figure 5.1**). These profiles were obtained by imaging all the barcodes alone and calculating the mean filter intensity across all microbeads for each filter. A microbead's intensity profile was then compared against each known barcode's intensity profile to identify the barcode of interest. Specifically, a barcode was classified according to its type (i.e. synthetic or clinical sample) and highest to lowest intensities among the filters  $\lambda_{em} = 530/10$ ,  $\lambda_{em} = 580/10$ , and  $\lambda_{em} = 640/10$ . This narrowed the selection down to either one barcode, in which case the barcode of interest was identified, or two barcodes. Between two possibilities “B<sub>high</sub>” (with higher mean intensities) and “B<sub>low</sub>” (with lower mean intensities) a threshold was defined for “B<sub>low</sub>”:

$$I_{barcode} = I_{mean} + I_{STD}$$

**Equation 5.1**

where

$I_{barcode}$  = Intensity threshold for “B<sub>low</sub>”.

$I_{mean}$  = Mean intensity of “B<sub>low</sub>”

$I_{STD}$  = Intensity standard deviation of “B<sub>low</sub>”.

This threshold was calculated for the highest intensity amongst the three filters  $\lambda_{em} = 530/10$ ,  $\lambda_{em} = 580/10$ , and  $\lambda_{em} = 640/10$  for B<sub>low</sub>. If the highest intensities were similar in value between B<sub>low</sub> and B<sub>high</sub>, the second highest filter intensity was used. With this, if the microbead's



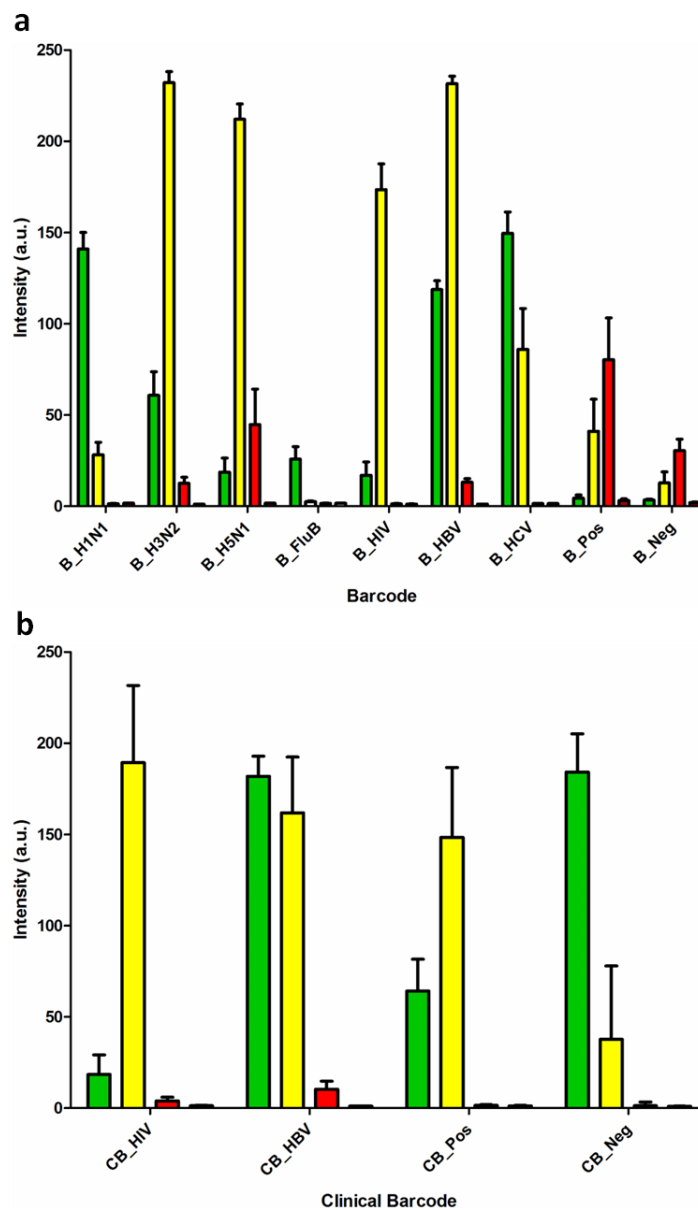


**Figure 5.1. Barcode intensity profiles.**

Barcode intensity profiles, from smartphone images, for the barcodes synthesized. From left to right the coloured bars represent intensity observed in the filter  $\lambda_{em} = 530/10$  (green),  $\lambda_{em} = 580/10$  (yellow),  $\lambda_{em} = 640/10$  (red), and  $\lambda_{em} = 692/40$  (dark red). Profiles are shown for (a) barcodes used with synthetic samples, and (b) barcodes used with clinical samples. Data represent the mean and standard deviation from three replications. Figure created by the author. Reprinted (adapted) with permission from source<sup>113</sup>. Copyright 2015 American Chemical Society.

corresponding filter intensity was equal to or lower than  $I_{barcode}$ , the barcode of interest was  $B_{low}$ , otherwise  $B_{high}$  was chosen.

We determined whether the analyte of interest is present by using the intensity values from the  $\lambda_{em} = 692/40$  filter, which isolates for the Alexa Fluor 647 secondary probe signal. Here, we developed a histogram of the fluorescence intensity from the secondary probe and compare that signal to those of the negative sample:

$$\% \text{ Population} = \frac{\text{population of barcode whose } \lambda_{em}=692/40 \text{ filter intensity} \geq I_{assay}}{\text{(total barcode population)}}$$

**Equation 5.2**

That is, the barcodes whose secondary probe intensities were equal to or above the threshold  $I_{assay}$ , established empirically from negative controls, were counted and a percentage “% Population”, relative to the microbead’s total population, was calculated (**Figure 5.2**). The population thresholds, “% Threshold”, above which a detection was considered positive, were 30% and 3% for the synthetic sample and clinical samples, respectively, and also established based on negative controls.

## 2.13 PCR Amplification and Purification

No more than 10% of the reverse-transcribed product was added to the PCR reaction, as per product guidelines. Conventional PCR was carried out using the GoTaq G2 Hot Start Colorless Master Mix (Promega) as per company amplification guidelines. The 100 base-pair amplicon for HBV was generated based on the pre-core/core open reading frame using forward primer 5'-GGCATGGACATTGACCCTTA-3' and reverse primer 5'-TGTCGAGAAGGTCCCGAATA-3' at a final concentration of 1  $\mu$ M in a 50  $\mu$ l reaction, and eluted into 30  $\mu$ l for detection. Primers for the HIV detection product were designed to generate a 118 base-pair amplicon in the integrase gene, with forward primer 5'-GGAAAGGTGAAGGGGCAGTAGTAATAC-3' and reverse primer 5'-GCCACACAATCATCACCTGCC-3' also at a final concentration of 1  $\mu$ M in a 50  $\mu$ l reaction, and eluted into 30  $\mu$ l. PCR programs were carried out as per Promega guidelines for small amplification products.

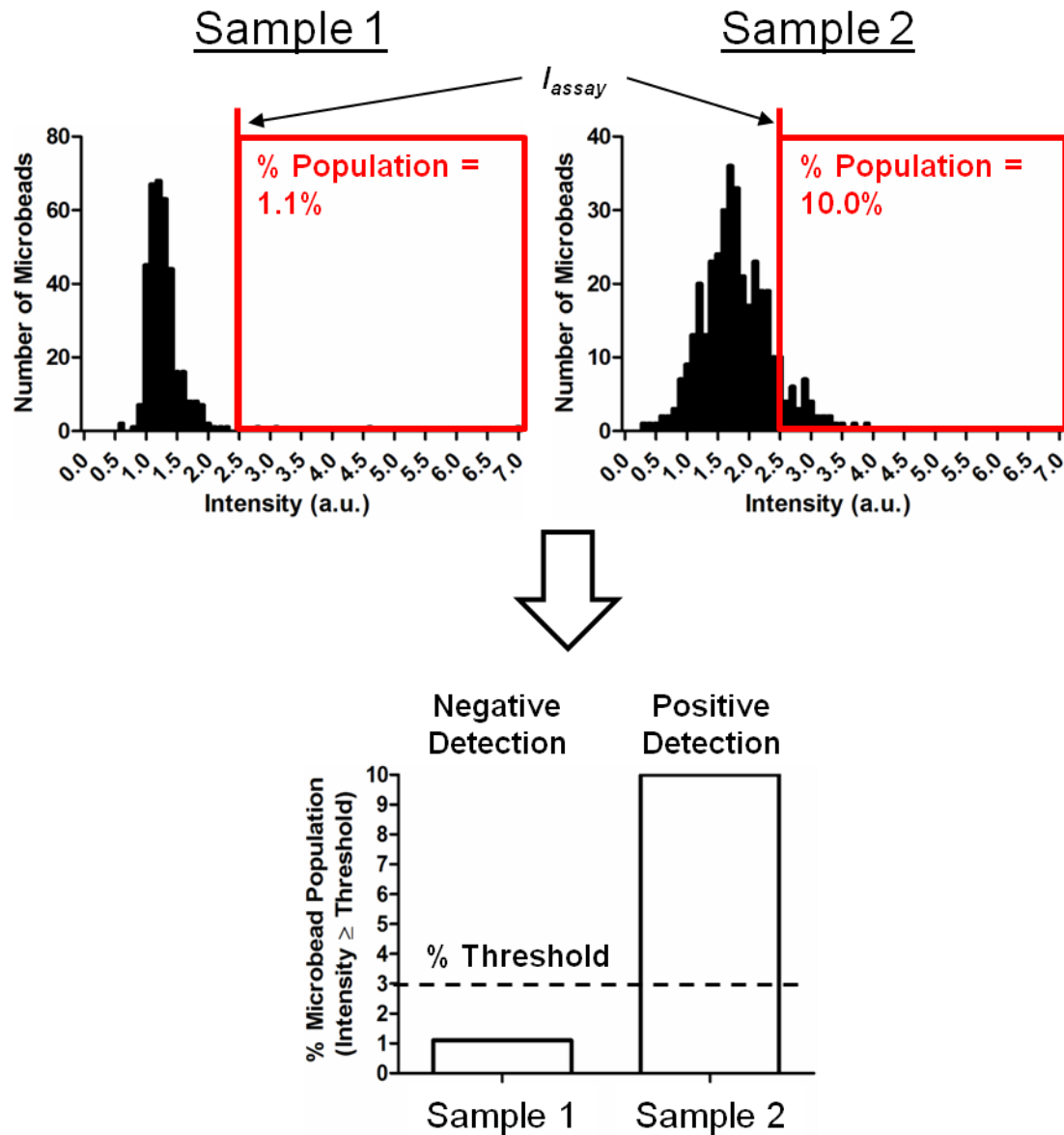


**Figure 5.2. Detection using histogram analysis.**

An illustration of how positive and negative detections were determined using histogram analysis. In this example Sample 1, which has a % Population below % Threshold = 3%, is considered negative detection; Sample 2, which has % Population above % Threshold = 3%, is considered positive detection.

Amplification products were verified using gel electrophoresis and purified with the Gel/PCR DNA Fragments Extraction Kit (Geneaid) using the PCR clean-up protocol. These products were used in the barcode assay, and sent for sequencing to determine the number of single-nucleotide polymorphisms (SNPs). HBV genotyping was also conducted using conventional PCR with primers previously published<sup>134</sup>, and genotype was determined using HBVseq from the Stanford University HIV Drug Resistance Database<sup>135</sup>. PCR amplification and purification performed by **M. Ostrowski**.

## 2.14 Quantum Dot Barcode Assay in Solution

Purified RPA and PCR products were denatured by heating at 100 °C for 10 minutes and stored in ice immediately. 1 µL of denatured amplicon was then transferred to the assay solution containing 1 µL of conjugated microbeads (~10,000 beads), 1 µL of detection oligonucleotides (100 pmol/µL), 7 µL of DD water and 10 µL of hybridization buffer (10X SSC, 0.1% SDS, pH 7, heated to 60 °C) making up a total volume of 20 µL. The solution was mixed and incubated at 37 °C for 30 minutes. The assay product was washed by mixing with 200 µL of washing buffer (0.5x SSC, 0.1% SDS, pH 7) and let stand in a magnetic rack (MagnaRack, Life Technologies) for 10 minutes to allow magnetically encoded microbeads to settle to the wall of a microcentrifuge tube. The supernatant was removed, and the washing was repeated two more times. Washed product was resuspended in 200 µL of PBST buffer (pH 7.4) for flow cytometry (BD FACSCalibur). Quantum dot barcode solution assays performed by **J. Kim**.

## 2.15 HBV/HIV Multiplexed Assay in Solution

Purified RPA and PCR products were denatured by heating at 100 °C for 10 minutes and stored on ice. For all multiplexing conditions, synthetic DNA strand (CT\_Pos, Table 5.1) was added as a positive control, which was designed to hybridize with CC\_Pos capture DNA (Table 5.1) conjugated to CB\_Pos barcode. CB\_Neg barcode conjugated with CC\_Neg (Table 1) capture DNA was also added in all cases as a negative control, CB\_HIV barcode was conjugated with HIV capture DNA (CC\_HIV), and CB\_HBV barcode was conjugated with HBV capture DNA (CC\_HBV, Table 5.1). A total of 2 µL of denatured amplicon (a combination of 1 µL HBV positive or negative patient sample plus 1 µL of HIV positive or negative patient samples corresponding to the four multiplexing cases) was added to the assay solution containing 1 µL of

CB\_HIV (10,000 beads), 1  $\mu$ L of CB\_HBV (10,000 beads), 1  $\mu$ L of CB\_Pos (10,000 beads), 1  $\mu$ L of CB\_Neg (10,000 beads), 1  $\mu$ L of HIV detection oligonucleotides (100 pmol/ $\mu$ L, CD\_HIV, Table 5.1), 1  $\mu$ L of HBV detection oligonucleotides (100 pmol/ $\mu$ L, CD\_HBV, Table 5.1), 2  $\mu$ L of positive and negative control detection oligonucleotides (100 pmol/ $\mu$ L, CD, Table 5.1), 11  $\mu$ L of hybridization buffer (10X SSC, 0.1% SDS, pH 7, heated to 60 °C), and 1  $\mu$ L of positive control target DNA (1 pmol/ $\mu$ L, CT\_Pos, Table 5.1). The solution was mixed and incubated at 37 °C for 30 minutes. The assay product was washed by mixing with 200  $\mu$ L of washing buffer (0.5x SSC, 0.1% SDS, pH 7) and let stand in a magnetic rack (MagnaRack, Life Technologies) for 10 minutes to allow magnetically encoded microbeads to settle to the wall of a microcentrifuge tube. The supernatant was removed, and the washing was repeated two more times. Washed product was resuspended in 200  $\mu$ L of PBST buffer for flow cytometry (BD FACSCalibur). HBV/HIV multiplex assay were performed by **J. Kim**.

## 2.16 Data Analysis for Solution-based Assay

FL1 (530/30 nm BP), FL2 (585/42 nm BP) and FL4 (661/16 nm BP) signals were acquired from flow cytometer (BD FACSCalibur) and analyzed with FlowJo software. Each barcode signal was gated by plotting FL2 vs. FL1 signals (Supplementary Fig. S1), and the median FL4 intensity was calculated from the gated populations. Final figures were plotted using GraphPad Prism 6, and all statistical analysis was calculated using ordinary one-way ANOVA function. Data analysis for solution-based assays performed by **J. Kim**.

## 2.17 Human Subjects

The de-identified clinical samples were obtained from the Toronto Western Hospital Liver Clinic and St. Michael's Hospital biobank repository. The protocol was approved by the Research Ethics Board of the University Health Network and St. Michael's Hospital, both affiliates of the University of Toronto. All patients provided written informed consent for storage and use of their specimens for research. Human subject samples provided by **J.J. Feld**.

## 3 Results & Discussion

### 3.1 Device Design and Construction

Essentially, the objective was to miniaturize the microscope for fluorescence imaging. Towards this we needed the following components: (1) interchangeable emission filters for spectral imaging, (2) excitation source for the sample, (3) power for the excitation source, (4) optics system to interface with the iPhone camera for imaging the micrometer-sized barcodes, and (5) chassis for the smartphone, microwell, and all the above components. All these needed to be accomplished in a portable and light-weight design.

#### 3.1.1 Emission Filters and Dichroic Mirrors

While the emission filters from the microscope setup were readily deployable in our device, we needed to confirm that the dichroic mirrors could be omitted. We thus tested the imaging of several barcodes in the absence of the dichroics. No significant differences were found between images obtained with and without them (**Figure 5.3**). Thus dichroic mirrors did not need to be designed into the device.

#### 3.1.2 Excitation Source and Power

We tested for the appropriate source and configuration (i.e. oblique illumination versus transillumination) for excitation. Light-emitting diodes (LEDs) are inexpensive, easy to power, and light-weight, so we first experimented with a 405 nm wavelength LED to excite the barcodes under oblique illumination (**Figure 5.4a and b**). While the barcodes fluoresced under excitation, we also observed a high background signal compared to excitation using the mercury lamp (**Figure 5.4c and d**) due to the un-collimated nature of the LED light and its wide emission wavelength. To overcome this, we elected to use a 405 nm diode laser (**Figure 5.4e and f**), as the source is collimated and whose wavelength does not “leak” into the filter. To further reduce the higher overall signal in the  $\lambda_{em} = 430\text{LP}$  filter, we used a neutral density filter ( $\text{OD} = 1.3$ ) during imaging. Performance of transillumination, where the excitation light had to pass through the microwell chip to reach the sample, depended on the angle of excitation. Expectedly, a large angle relative to the sample plane ( $> 45^\circ$ ) resulted in high background due to more incident light into the objective (**Figure 5.5a and b**), whereas a low angle ( $< 45^\circ$ ) resulted in low background, but also resulting in less excitation (**Figure 5.5c and d**). Because of these reasons as well as

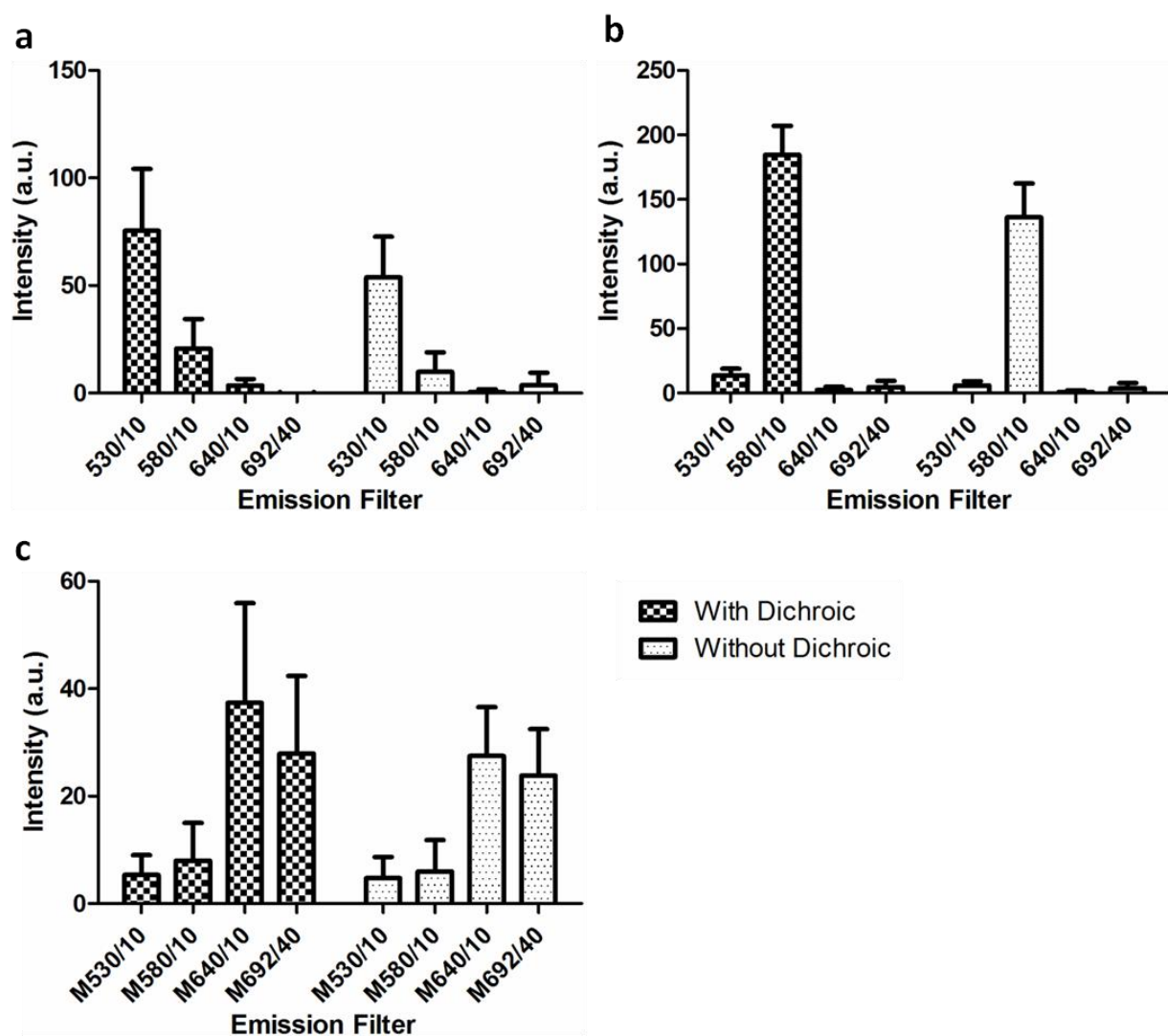


**Figure 5.3. Effect of dichroic mirror on intensity profiles.**

Intensity profiles of (a) B1, (b) B2, and (c) B6 from **Table 4.1**, imaged with and without dichroic mirrors. Data represent the mean and standard deviation from three replications.

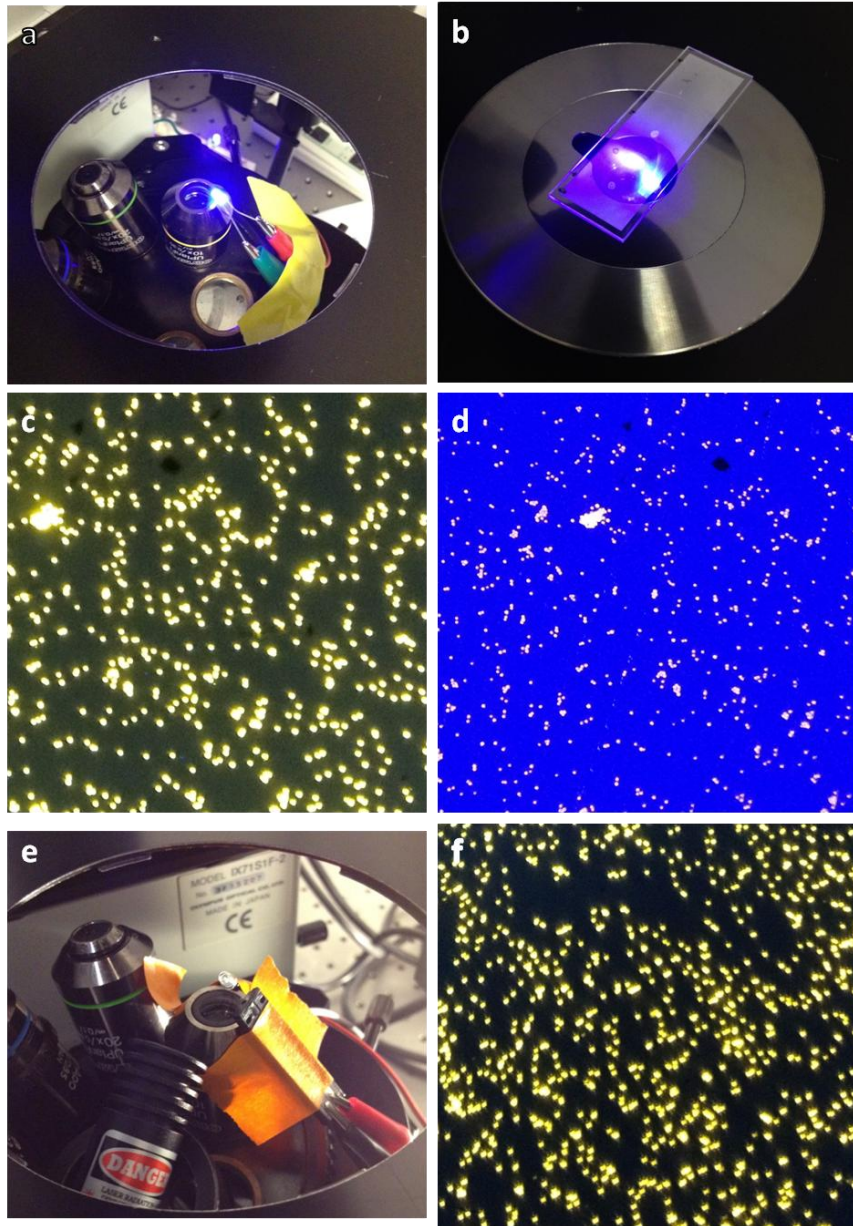


**Figure 5.4. LED and diode laser excitation of quantum dot barcodes.**

Microscopy imaging (10x objective, NA = 0.30) of quantum dot barcodes excited using different sources and configurations. (a, b) Oblique barcode excitation configuration using 405 nm diode. (c)  $\lambda_{\text{em}} = 430\text{LP}$  filter image of barcode excited using mercury lamp. (d)  $\lambda_{\text{em}} = 430\text{LP}$  filter image of barcode excited using 405 nm diode. (e) Oblique barcode excitation configuration using 405 nm diode laser. (f)  $\lambda_{\text{em}} = 430\text{LP}$  filter image of barcode excited using 405 nm diode laser.



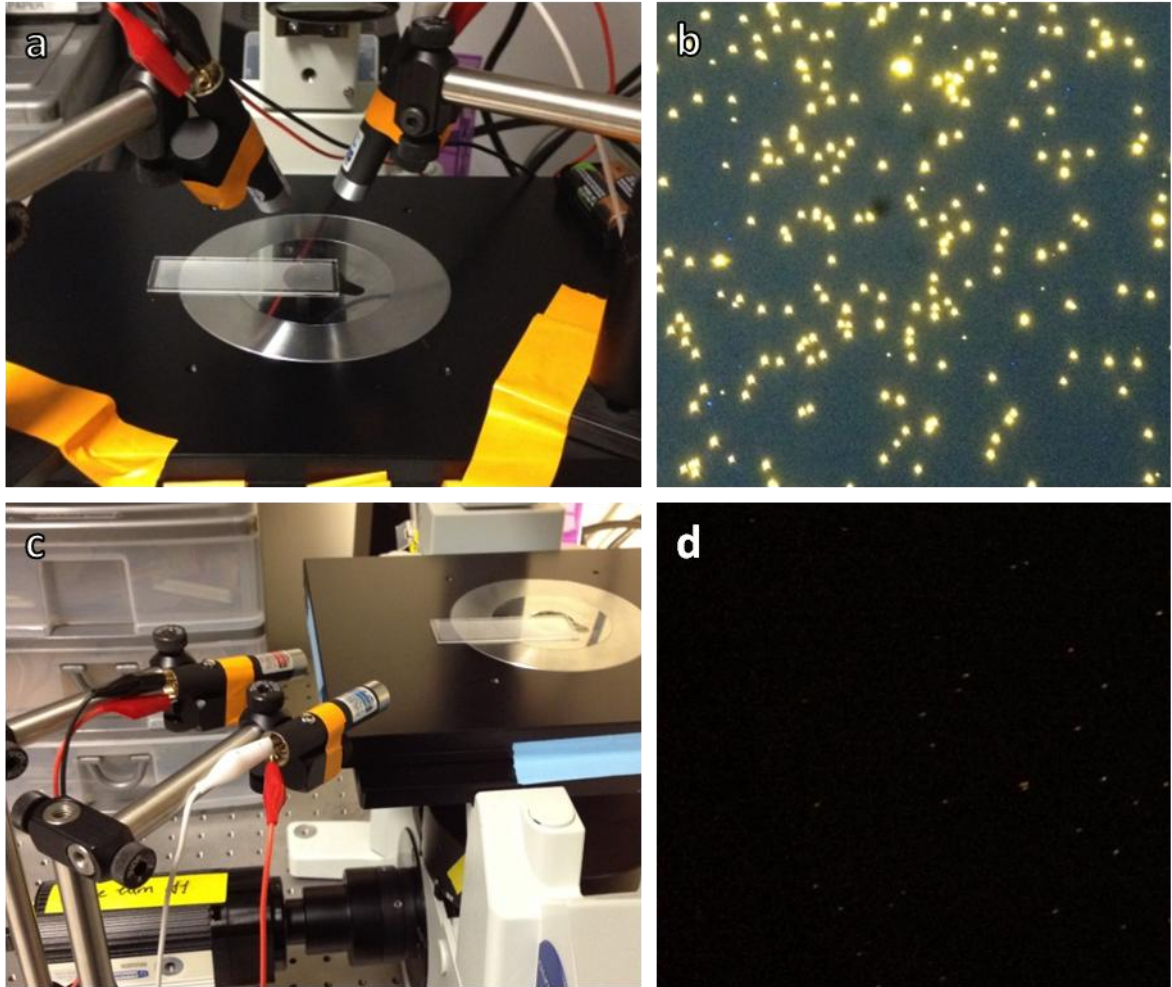


**Figure 5.5. Transillumination of quantum dot barcodes.**

An example illustrating the effect of angle on transillumination of quantum dot barcodes on chip, under microscopy imaging (10x objective,  $NA = 0.30$ ). (a, b) Configuration and result of transillumination of barcodes using 405 nm at diode laser at high angle ( $> 45^\circ$ ). (c, d) Configuration and result of transillumination of barcodes using 405 nm at diode laser at low angle ( $< 45^\circ$ ).

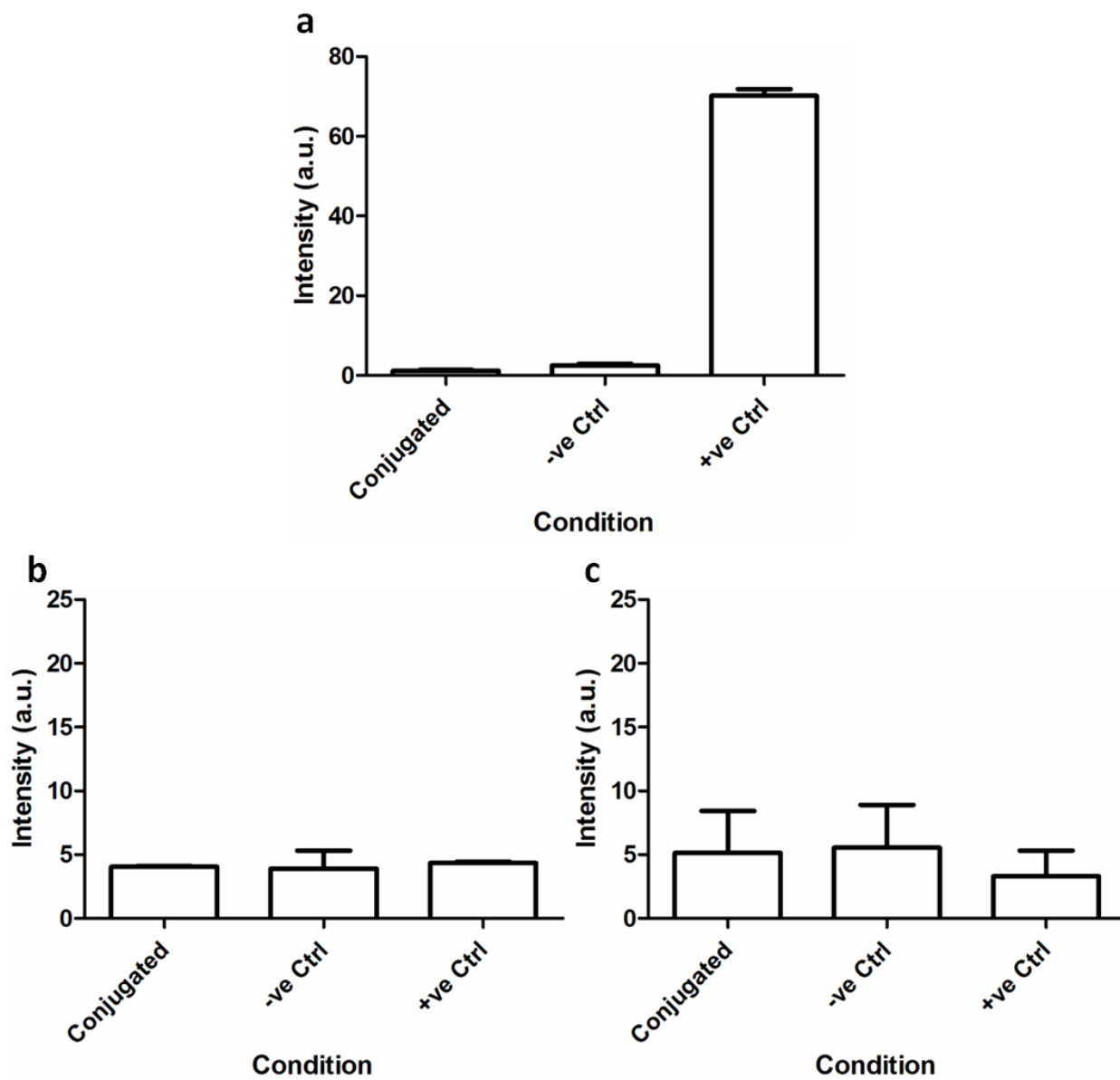
design considerations – transillumination would require more space when accommodated into a device – oblique illumination was selected as the orientation of choice.

Next we tested for excitation of the detection strand fluorophore. Several cost-effective options were available: 40 mW LED, 1050 mW LED, 0.8 mW diode laser, and 5 mW diode laser, arranged in both oblique illumination and transillumination. They all emit in the red, 650-655 nm range, to match the peak absorption wavelength of 650 nm for the Alexa647 dye. Here, the 5 mW laser showed the largest contrast between negative and positive assay conditions while requiring only 3 V to power (**Figure 5.6**). Between oblique illumination and transillumination we do indeed see a larger difference between negative/background and positive in the former case, similar to the barcode excitation case. We later identified diode lasers that were smaller in physical size and easier to connect electronically than the 5 mW ones used here, but higher in power (50 mW) for both 405 and 650 nm. These were used for all proceeding experiments. At a rating of 3 V, these were also favourable because they can be powered by two 1.5-V AA or AAA batteries, as was the case with the 5 mW lasers. To limit the wavelength and background intensity from the high powered 50 mW 650 nm source, which impacts the detection results, we fixed an excitation filter  $\lambda_{\text{ex}} = 655/15$  nm in front of it.

### 3.1.3 Optical System

The last component, the optics system for microbead magnification, was crucial to the entire design and indeed success of our device. Surveying the literature, one attempt was to model our device after one with a similar purpose<sup>68</sup>. This design was chosen because they demonstrated the ability to image 2-4  $\mu\text{m}$ -sized fluorescent microbeads, albeit in solution, which is within the size range of our  $\sim 3$   $\mu\text{m}$  barcodes. The design itself was also highly portable. Unfortunately, the major design challenge we could not overcome involved the size (0.6 mm in diameter) and positioning of the plano-convex lens, which also needed to be placed exactly 0.6 mm away from the sample in order to enable proper magnification. The high level of mechanical precision required also made it unattractive from a point-of-care diagnostics perspective, as it meant the manufacturing would be more technically intensive and that the device is more prone to breakages in the field (e.g. slight misalignment in the lens would render it obsolete).

Another attempt was to model our device after another cell phone-based microscopy system<sup>66</sup>. This setup was unattractive to us at first due to its size and need for costly microscopy-grade



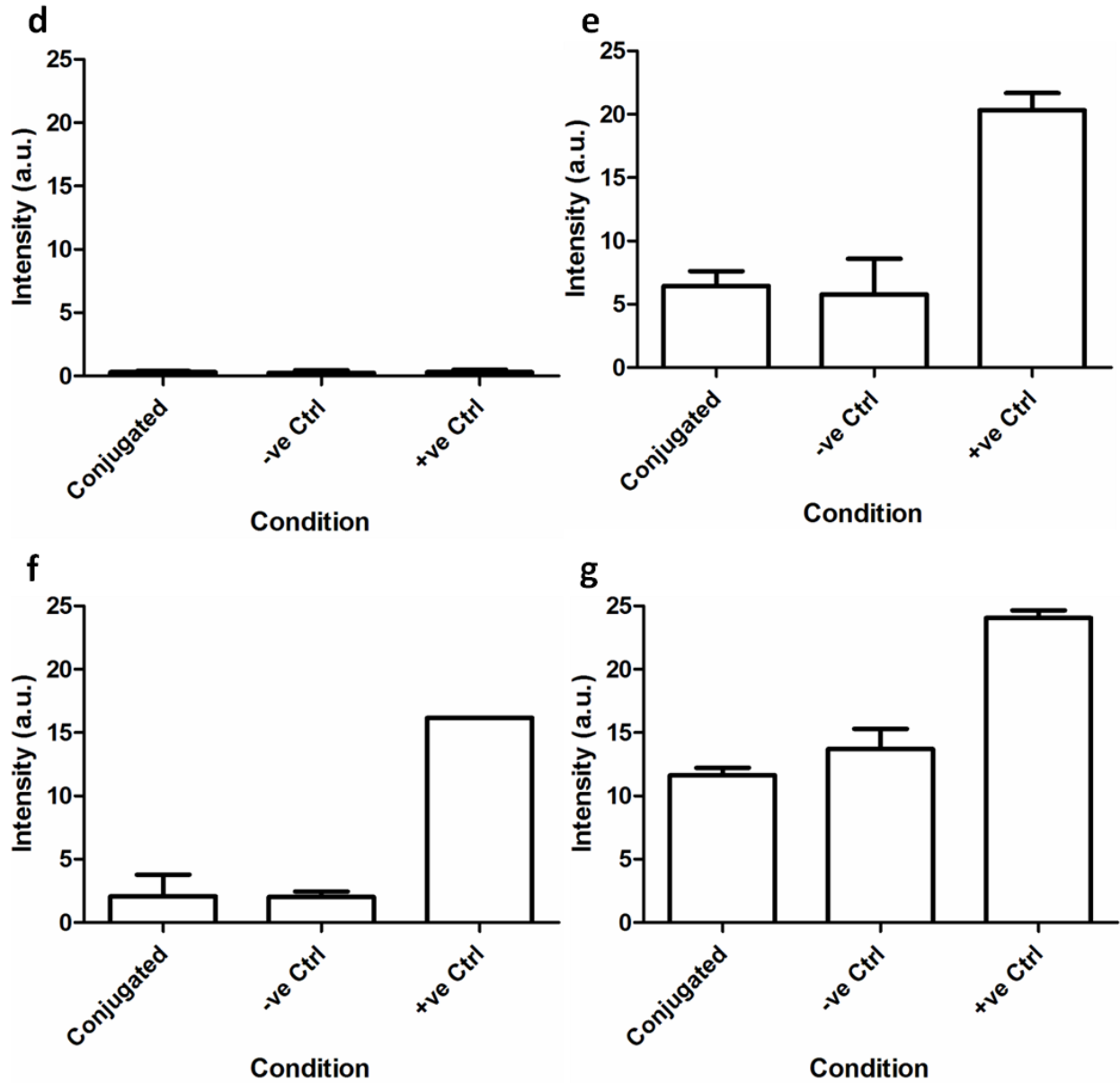


**Figure 5.6.** Excitation sources for genetic assays.

Excitation of conjugated barcodes, negative control condition assay, and positive control condition assay using (a) mercury lamp under oblique illumination, (b) 40 mW LED with 12 V source under oblique illumination, (c) 1050 mW LED with 12 V source under oblique illumination, (d) 0.8 mW diode laser using 3 V source under oblique illumination, (e) 0.8 mW diode laser using 12 V source under oblique illumination, (f) 5 mW diode laser using 3 V source under oblique illumination, and (g) 5 mW diode laser using 3 V source under transillumination. The capture, target, and detection strands correspond to those for Influenza Type B in **Table 5.1**. Data represent the mean and standard deviation from three replications.

components. We resolved this by replacing the eyepiece and objective with a miniature pocket microscope magnifier possessing 160x-200x magnification power, which would be similar to using an objective of 10x to 20x on our microscope (i.e. the eyepiece would be an additional 10x, to bring the total magnification to 100x-200x). These were integrated in with the remaining designs (**Figure 5.7**).

### 3.1.4 Construction

The device was built and we were able to successfully demonstrate the imaging of quantum dot barcodes (**Figure 5.8**). Crucially, the components – batteries, switch, laser diodes, lenses, and filters – and 3D-printed plastic chassis were all light-weight and able to fit in one hand. The two laser diodes were switched on independently via a manual switch: Excitation Laser 1 (405 nm) excited the barcodes and Excitation Laser 2 (650 nm) excited the secondary label with a filter ( $\lambda_{\text{ex}} = 655/15$ ) that limited the excitation wavelength. The angles used for the two source – 25° for the 405 nm source and 10° for the 650 nm source, both relative to the sample plane – were chosen such that the incident light would be as orthogonal to the sample plane as possible without being obscured by the maximally extended distance of the objective lens. The eyepiece and movable objective lens magnify and focus barcodes on the chip to allow them to be viewable clearly by the naked eye on the smartphone display. The smartphone camera, Apple's iPhone 4S as before, then captures that view.

## 3.2 Synthetic Sample Validation

Here we evaluated whether our device can differentiate the optical signals between the barcodes and secondary fluorescent probe used in our genetic assays (**Figure 5.9**). It was demonstrated that an iPhone camera was able to capture the distinct optical emissions of each barcode on the microwell chip, and proper filtering enabled the differentiation of barcode optical signals from the secondary probe's signal. These studies confirmed that an iPhone camera can image barcodes on the chip surface and be used as a detector for biological assays.

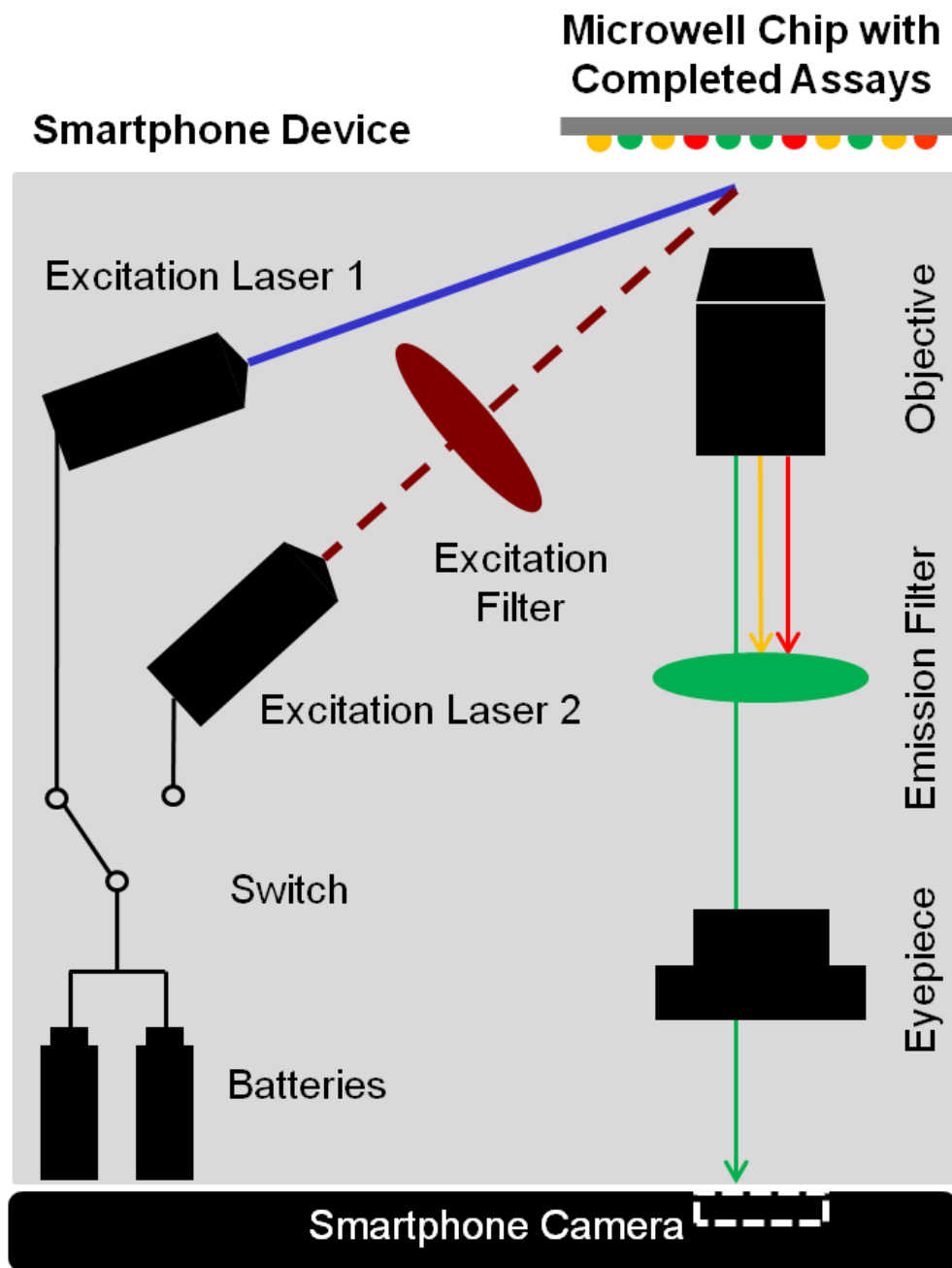


**Figure 5.7. Smartphone device design.**

Two excitation sources excite the quantum dot barcoded chip independently. The optical emission is collected by a set of objective and eyepiece lenses, imaged using a smartphone camera. Figure created by the author. Reprinted (adapted) with permission from source<sup>113</sup>. Copyright 2015 American Chemical Society.

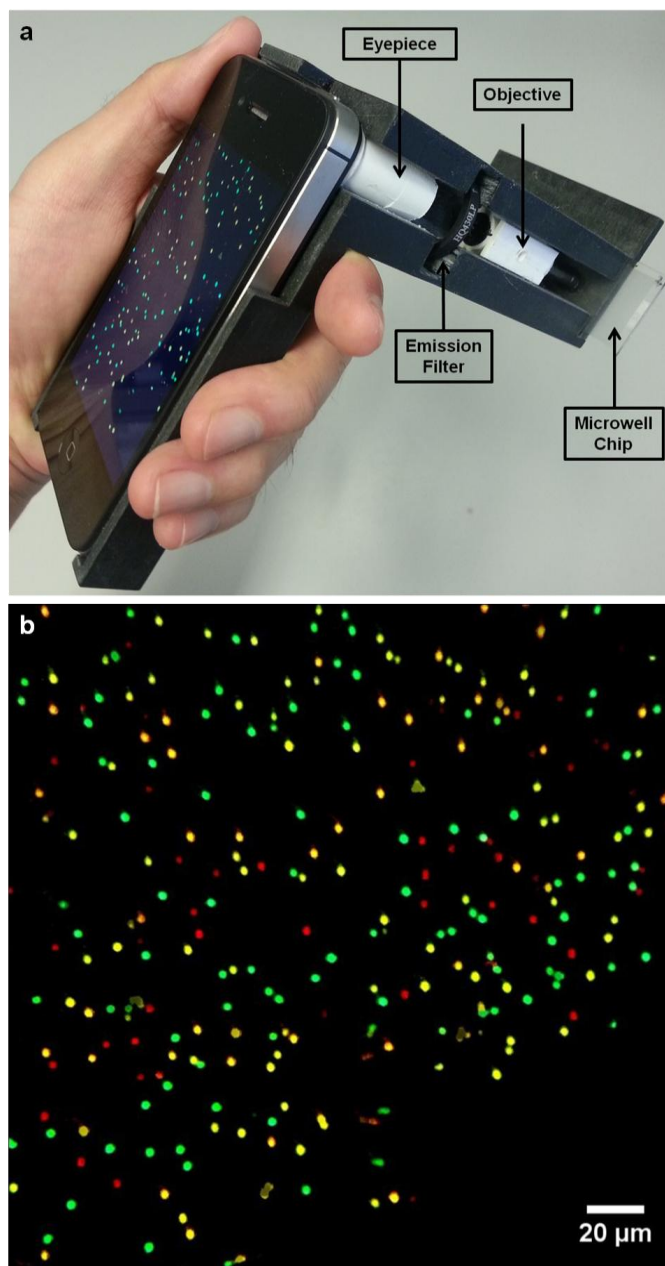


**Figure 5.8. Smartphone device and imaging.**

(a) Image of the smartphone device. (b) A smartphone camera captures the image of four different quantum dot barcodes arrayed on the surface of the chip. These barcodes are excited with a violet laser source ( $\lambda_{\text{ex}} = 405 \text{ nm}$ , 50 mW), optical signals collected by a set of lenses, filtered with 430 nm long-pass filter, and imaged using an Apple iPhone 4S smartphone with an exposure time of 0.05 s. Figure created by the author. Reprinted (adapted) with permission from source<sup>113</sup>. Copyright 2015 American Chemical Society.

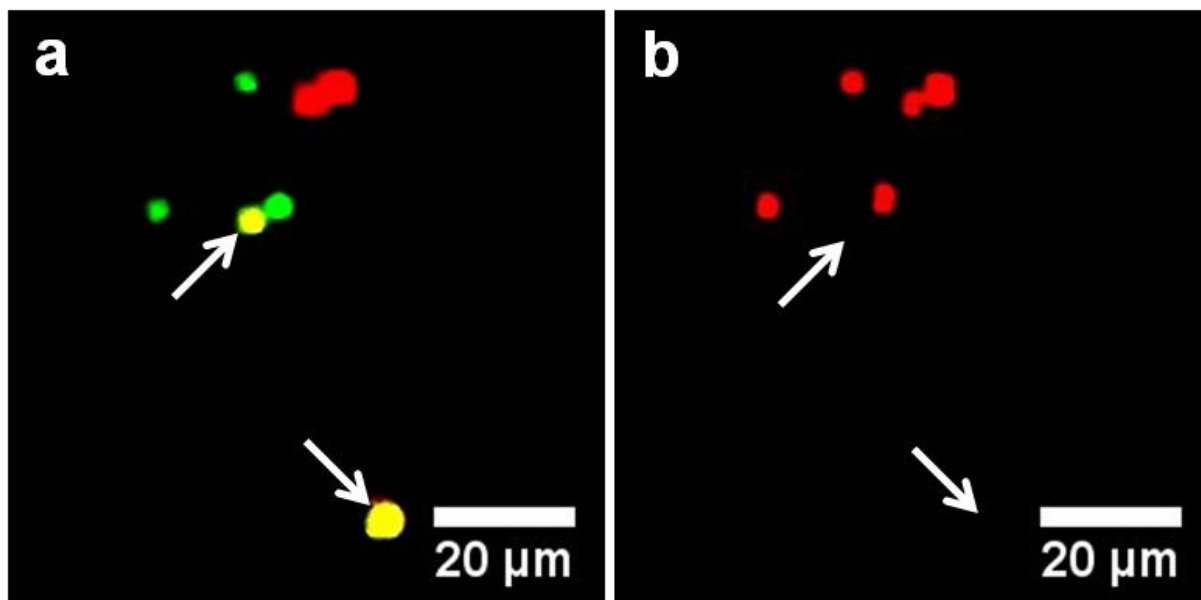


**Figure 5.9. Signal differentiation of device images.**

(a) Yellow, green, and red barcodes (identified as B\_HBV, B\_HCV, and B\_Pos in Table 1, respectively) are deposited on the chip and imaged using the device ( $\lambda_{\text{ex}} = 405 \text{ nm}$ ,  $\lambda_{\text{em}} = 430\text{LP}$ , exposure time = 1 s). (b) After the assay, the device-acquired fluorescence image of the microbeads bound with the target analyte and secondary probe ( $\lambda_{\text{ex}} = 655/15$ ,  $\lambda_{\text{em}} = 692/40$ , exposure time = 1 s). Both green and red microbeads had positive signals. This demonstrates that their respective genomic targets are present in the sample but not for the yellow barcode. Figure created by the author. Reprinted (adapted) with permission from source<sup>113</sup>. Copyright 2015 American Chemical Society.



### 3.2.1 Assay Sensitivity

We then determined the analytical performance of the microbead-based sandwich assay using our engineered smartphone reader (**Figure 5.10**). We designed seven barcodes for detecting seven infectious disease biomarker targets: influenza type A (H1N1, H3N2, H5N1), influenza type B, HIV, and hepatitis B and C (**Table 5.1**). The limits of detection and linear dynamic ranges for each of the targets were between 10-50 fmol ( $6 \times 10^9$  to  $3 \times 10^{10}$  copies) and up to 40-fold, respectively, in a final hybridization sample volume of 10  $\mu$ L, translating to an *analytical* sensitivity of 1-5 nM for the device for synthetic samples. Again, the *clinical* sensitivity, defined as the number of true positives divided by the total number of sick individuals in the population for clinical samples, does not apply here. This suggested that analytical performance was independent of the infectious disease targets. As was the case previously with the sensitivity curves of our microscopy setup, differences between the curves were due to differences between the size of the barcodes, conjugation efficiency, and hybridization efficiency. However, no conclusions could be made between the microscopy setup and the device since, aside from the barcodes used for H1N1 and H3N2, the pairings between barcodes and their diseases were changed between the microscopy experiments in Chapter 4 and the device experiments here.

### 3.2.2 Microbead-Counting Analysis Approach

For the sensitivity assays the intensities were used directly to establish the limits of detection and dynamic ranges, for both the microscope and the device. Here, however, we used a microbead-counting method to determine positive/negative detection, i.e. presence/absence of target molecular of interest. We observed that samples that had the target of interest had more microbeads whose secondary probe signals were above a threshold. We chose this method of analysis rather than directly using absolute intensity values because we found this approach to obtain greater consistency in the analysis due to reduction in skewing of the measurements from a small population of microbeads (i.e. outliers with extreme intensity values). Furthermore, this measurement strategy was adapted from flow cytometry, currently the gold standard in fluorescent microbead analysis.

In flow cytometry analysis, where data are shown in the form of a scatter plot (i.e. signal from one microbead results in one count in the plot), “gating” is performed. Established empirically from negative controls, a “gate” is essentially a threshold that delineates the boundary inside

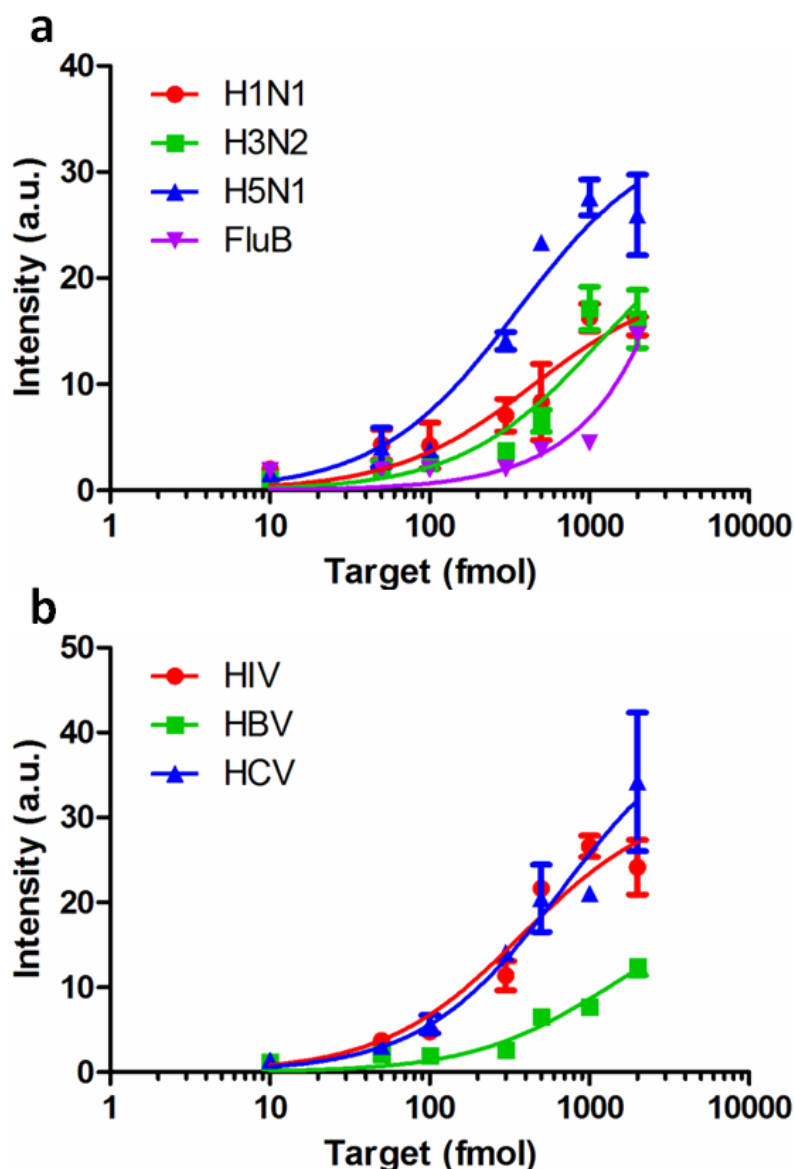


**Figure 5.10. Device sensitivity assays.**

Sensitivity curves for genetic biomarkers for (a) the influenza A viruses H1N1, H3N5, and H5N1; influenza B virus (FluB) from **Table 5.1**; as well as (b) the bloodborne viruses human immunodeficiency virus (HIV), hepatitis B virus (HBV) and hepatitis C virus (HCV) from **Table 5.1**. Detection limit for all (not shown) is between 10-50 fmol. Data represent the mean and standard deviation from three replications. Figure created by the author. Reprinted (adapted) with permission from source<sup>113</sup>. Copyright 2015 American Chemical Society.

which data from the scatter plot are to be evaluated. Traditionally, the percent population of microbeads within the gate, relative to the total sample microbead population (i.e. inside and outside of gate), is calculated and used to differentiate between positive and negative detections, i.e. positive detections are samples with high percent populations within the gate, and negative detections are those with low percent populations.

In our analysis, analogous to flow cytometry's scatter plot, we first develop a histogram of the microbeads' secondary probe intensities. Then, modeling after the process of gating, we apply a threshold intensity,  $I_{assay}$ , to the histogram to determine the number of microbeads whose intensities are above this threshold. Finally, just as in the case of flow cytometry analysis, the percent population of microbeads above  $I_{assay}$ , relative to the total sample microbead population in the sample, is calculated. Samples whose percent population are above a population threshold, “%Threshold”, are considered positive detections, otherwise they are negative detections (refer to **Figure 5.2** for example).

For simplex detections (i.e. detection of a one target of interest within an assay), the  $I_{assay}$  are established empirically like in flow cytometry using known negative controls; and %Threshold is established by first applying  $I_{assay}$  to the negative controls, determining their respective percent populations, then calculating their mean plus twice standard deviation rounded to the nearest whole number to yield 30% and 3% for the synthetic and clinical samples (discussed later), respectively. Having established the %Threshold for the sample type, for multiplex detections (i.e. detection of multiple targets of interest, as well as internal positive and negative controls, within an assay), the same 30% and 3% for synthetic and clinical samples were used, respectively. That is, using the appropriate %Threshold, the multiplexing assay's  $I_{assay}$  is first determined using the assay's internal negative control (i.e.  $I_{assay}$  at which the assay's internal negative control percent population < %Threshold), then it is applied to the other targets of interest within the multiplexing assay (e.g. HIV, HBV, HCV) to determine their respective percent population, resulting in either positive or negative detection.

### 3.2.3 Multiplexing Assay and Specificity

We demonstrated the ability to simultaneously detect multiple synthetic genetic targets from the bloodborne virus panel of HIV, HBV, and HCV (**Figure 5.11**). We prepared six different mock genetic samples by mixing the secondary fluorescent probe sequence with various combinations

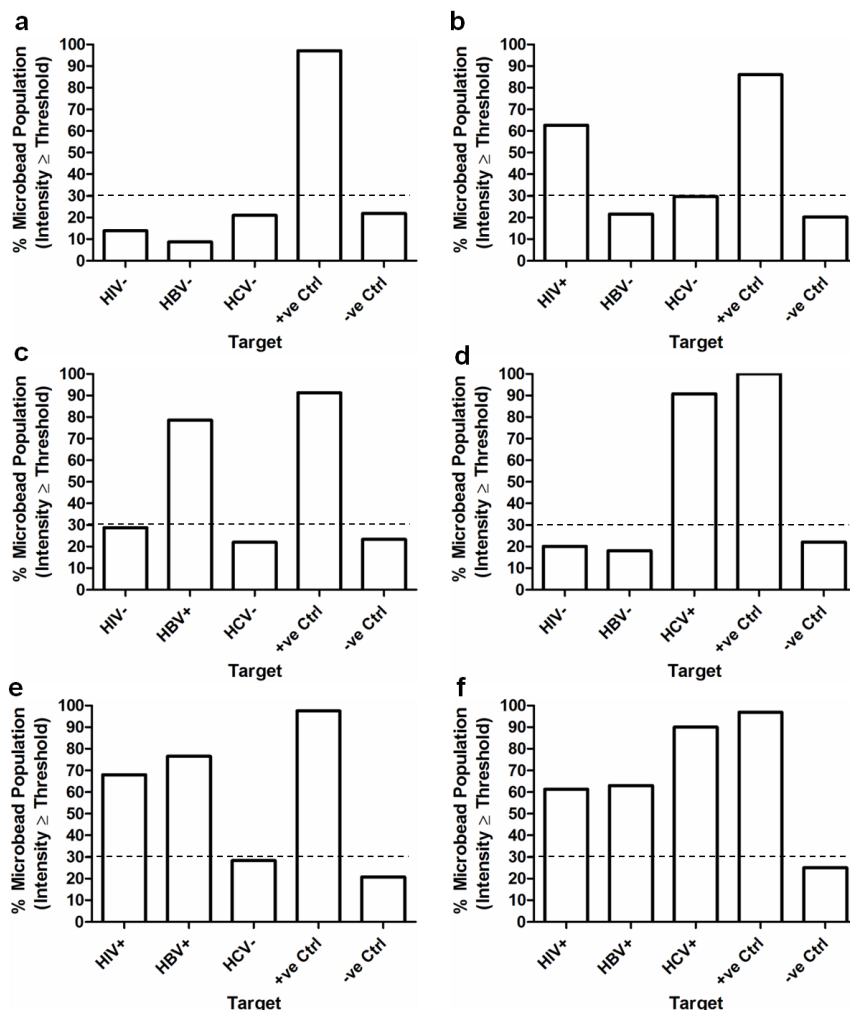


**Figure 5.11. Device multiplexing assays.**

Demonstrations of multiplexed detection of synthetic HIV, HBV, and HCV, as well as synthetic positive and negative controls target strands from **Table 5.1**. (a) Only positive control was present during hybridization. (b) Targets for HIV and positive control were present during hybridization. (c) Targets for HBV and positive control were present during hybridization. (d) Targets for HCV and positive control were present during hybridization. (e) Targets for HIV, HBV, and positive control were present during hybridization. (f) All targets except for negative control were present during hybridization. Results represent data from three experimental replications of each condition combined into a single data set. Note that samples above the dashed 30% line are considered positive detection, otherwise they are considered negative detection. Figure created by the author. Reprinted (adapted) with permission from source<sup>113</sup>. Copyright 2015 American Chemical Society.

of the genetic target sequences for each of the three pathogens of interest – HIV, HBV, and HCV – plus a positive control sequence to ensure that the barcodes are working as designed. For example, we would prepare solutions that were spiked with the target sequences for HIV and positive control sequence in one combination (**Figure 5.11b**), then HIV, HBV, HCV and positive control sequence in another combination (**Figure 5.11f**). A final hybridization sample of 20  $\mu$ L was added to the chip and incubated at 37 °C for 20 minutes, rinsed with a washing buffer, dried, imaged, and analyzed using the algorithm. In all cases the target sequences were correctly identified by the assay, indicating the device's high *analytical* specificity for synthetic samples (i.e. low cross-reactivity). The *clinical* specificity, defined as the number of true negatives divided by the total number of well individuals in the population for clinical samples, does not apply here. For example, in our solution containing the sequences for HCV and positive control (**Figure 5.11d**), the bar graph shows our technique can discriminate between barcodes bound with secondary probes (i.e. HCV and positive control) versus those not bound (i.e. HIV, HBV and negative control). All of the probe recognition sequences for the bloodborne viral panels were carefully designed *in silico* to minimize cross-reactivity with closely related viruses using subtypes against the gag gene of HIV, core protein gene of HBV and nucleocapsid protein gene of HCV, as per gold standard testing standards.

### 3.3 Clinical Sample Validation

We determined whether the device was capable of detecting and differentiating samples from patients with HIV and HBV (i.e., HIV- or HBV-positive subjects) from those without (i.e., HIV- or HBV-negative subjects). The sensitivity assays using synthetic targets showed that the device has a limit of detection of 10-50 fmol but to use the device for diagnosing patient samples, the limit of detection needed to be lowered by a factor of  $10^6$ . Conventional PCR amplification methods require bulky and expensive equipment that cannot be incorporated into a point-of-care device. To address this issue, we optimized an isothermal amplification step, which can be performed in 10-30 minutes, is simple, and does not require precise temperature control (operates at 37-42 °C).

#### 3.3.1 Mono-Infection of HIV and HBV

Patient samples were collected using standard protocols and we extracted the hepatitis B viral DNA and HIV viral RNA using magnetic microbeads (**Table 5.3**). The viral loads are reported

as per a clinical setting, and represent a viral load range from treatment-naïve patients. They do not necessarily indicate the clinical limit of detection. The HBV-infected samples were comprised of multiple genotypes to ensure our test would be widely applicable. To obtain the genetic samples, the cell membrane was first disrupted by the addition of lysis buffer, and the surface functionalized magnetic microbeads captured viral nucleic acid. The sample was then placed in a magnetic separator to collect magnetic microbeads. Before use in our assay, the HIV RNA was reverse-transcribed into complementary DNA (cDNA). All samples were then amplified using recombinase polymerase amplification. The recombinase proteins were added to the isolated genetic targets to form nucleoprotein complex, which facilitates strand-transfer at the homologous sequence of the template DNA. Single-stranded binding proteins then stabilize the displaced strand of the template DNA, and the DNA polymerase extends the complimentary strand<sup>136</sup>. Of the final amplified sample, 20 µL of the double-stranded DNAs were denatured and added to the chip, incubated at 40 °C, rinsed with a washing buffer, dried, imaged, and analyzed using the algorithm in a manner that is similar to detection of the synthetic targets. We demonstrated the successful diagnosis of individual patient samples with HIV and HBV, respectively, of varying viral loads before amplification (**Figure 5.12 a and b**). In order to determine whether the measurement results were significant, we combined the measurements from all samples of non-infected subjects, and then compared them to the combined measurements from the infected patients with either HIV or HBV (**Figure 5.12 c and d**). Our results showed a significant difference with a p-value of 0.05 and 0.01, respectively. We further confirmed the results using flow cytometry (**Figure 5.13**) and showed comparable outcomes. With this we had demonstrated that our diagnostic device was capable of detecting viral loads in the range of  $10^3$  to  $10^9$  copies/mL and different genotypes.

**Table 5.3. List of HBV genotypes and HBV/HIV viral loads.**

HBV					HIV		
Sample ID	HBV Genotype	Viral Load (IU/mL)*	Viral Load (Copies/mL)	Viral Load (mol/ $\mu$ L)	Sample ID	Viral Load (Copies/mL)*	Viral Load (mol/ $\mu$ L)
HBV+ 1	C	4.38E7	2.55E8	4.23E-19	HIV+ 1	2.41E4	4.00E-23
HBV+ 2	C	1.7E8	9.89E8	1.64E-18	HIV+ 2	4.87E4	8.09E-23
HBV+ 3	B	1.01E6	5.88E6	9.77E-21	HIV+ 3	1.48E4	2.46E-23
HBV+ 4	D	1.68E9	9.78E9	1.62E-17	HIV+ 4	7.23E3	1.20E-23
HBV+ 5	C	4.51E5	2.63E6	4.36E-21	HIV+ 5	3.00E5	4.98E-22
HBV+ 6	B	1.31E9	7.62E9	1.27E-18	HIV+ 6	1.00E5	1.66E-22
HBV+ 7	C	1.47E5	8.56E5	1.42E-21	HIV+ 7	5.00E5	8.31E-22
					HIV+ 8	2.53E4	4.20E-23
					HIV+ 9	2.43E4	4.04E-23
					HIV+ 10	3.10E4	5.15E-23

\*As reported by gold standard automated equipment.

Table created by M.J. Biondi and O. Ostrowski. Reprinted (adapted) with permission from source<sup>113</sup>. Copyright 2015 American Chemical Society.

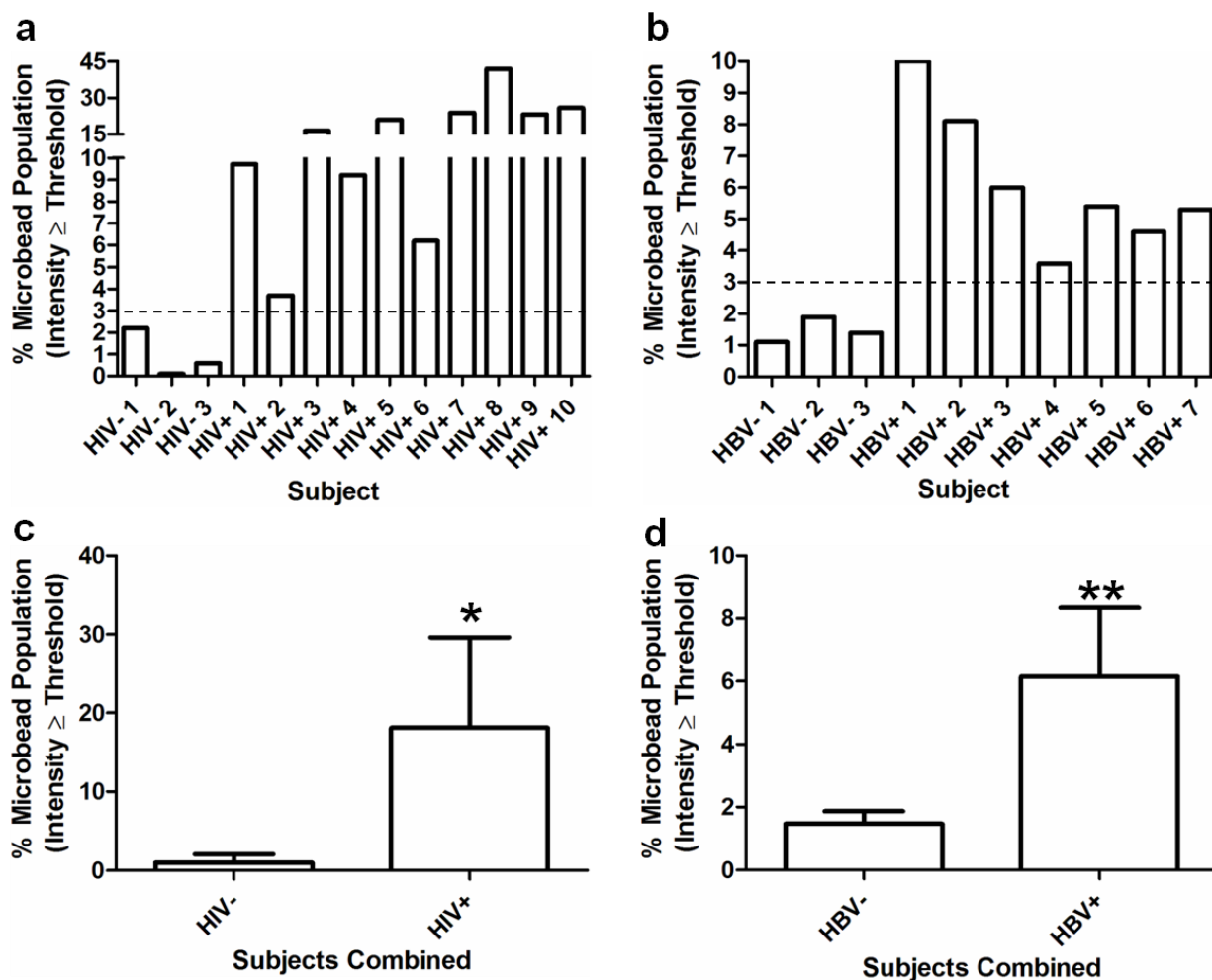


**Figure 5.12. Detection of HIV and HBV clinical mono-infections.**

Demonstrations of detection of clinical HIV and HBV DNA targets from **Table 5.3**. (a) Detection of mono-infected amplified samples from 3 HIV-negative subjects and 10 HIV-positive patients. (b) Detection of mono-infected amplified samples from 3 HBV-negative subjects and 7 HBV-positive patients. (c) Comparison between the average combined statistics of all subjects of the HIV-negative group (3 subjects) and HIV-positive group (10 patients) from (a); error bars represent standard deviation, with statistical significance ( $P < 0.05$ ) indicated and determined using two-sided  $t$ -test. (d) Comparison between the average combined statistics of all subjects of the HBV-negative group (3 subjects) and HBV-positive group (7 patients) from (b); error bars represent standard deviation, with statistical significance ( $P < 0.01$ ) indicated and determined using two-sided  $t$ -test. Figure created by the author. Reprinted (adapted) with permission from source<sup>113</sup>. Copyright 2015 American Chemical Society.



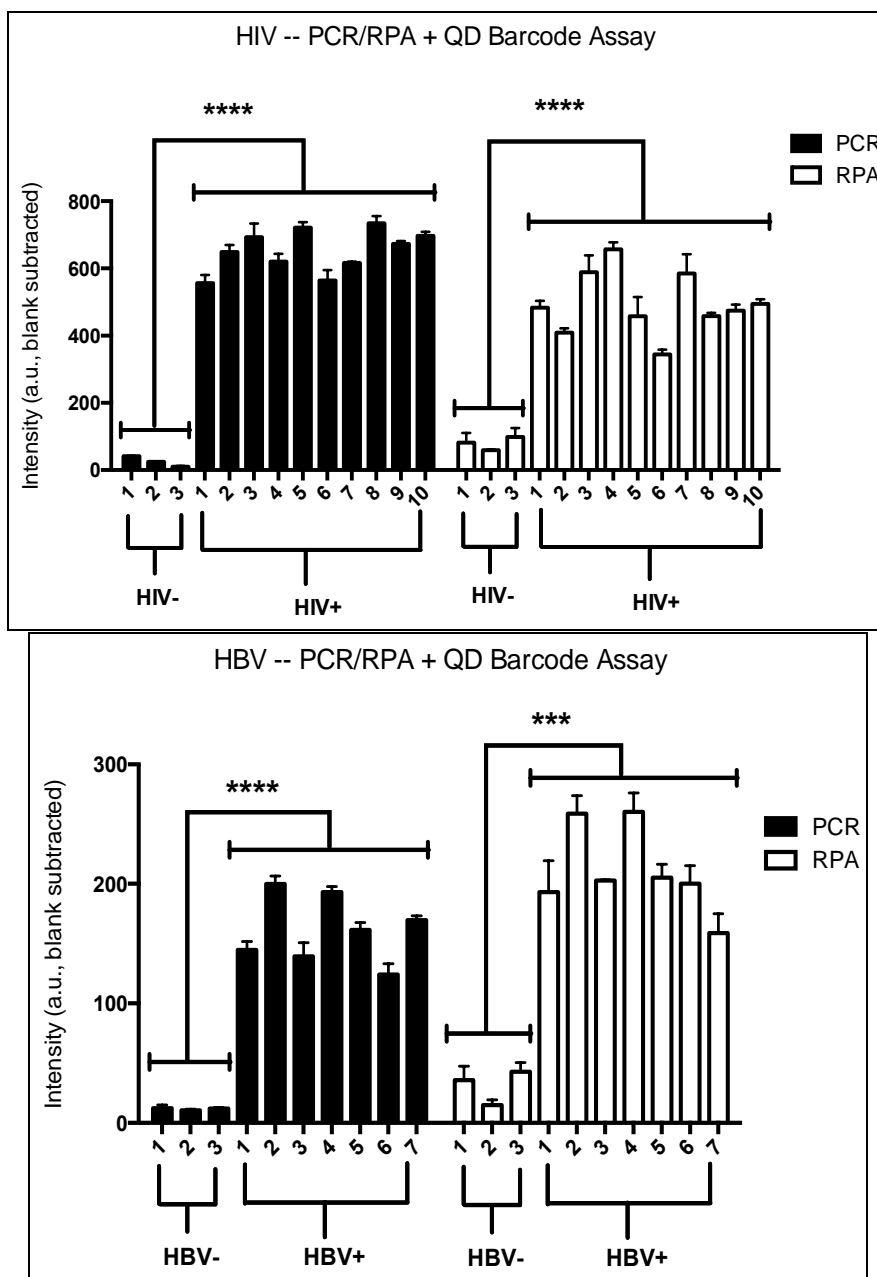


**Figure 5.13. Detection of HIV and HBV clinical mono-infections in solution.**

Quantum dot barcode assay in solution using PCR and RPA products for HBV (top) and HIV (bottom) patient samples. All error bars represent standard error of the mean of experimental triplicates. Note that statistical significance is indicated as \*\*\* for  $p \leq 0.001$ , and \*\*\*\* for  $p \leq 0.0001$ . Data represent the mean and standard deviation from three replications. Figure created by **J. Kim**. Reprinted (adapted) with permission from source<sup>113</sup>. Copyright 2015 American Chemical Society.

### 3.3.2 Co-Infection of HIV and HBV

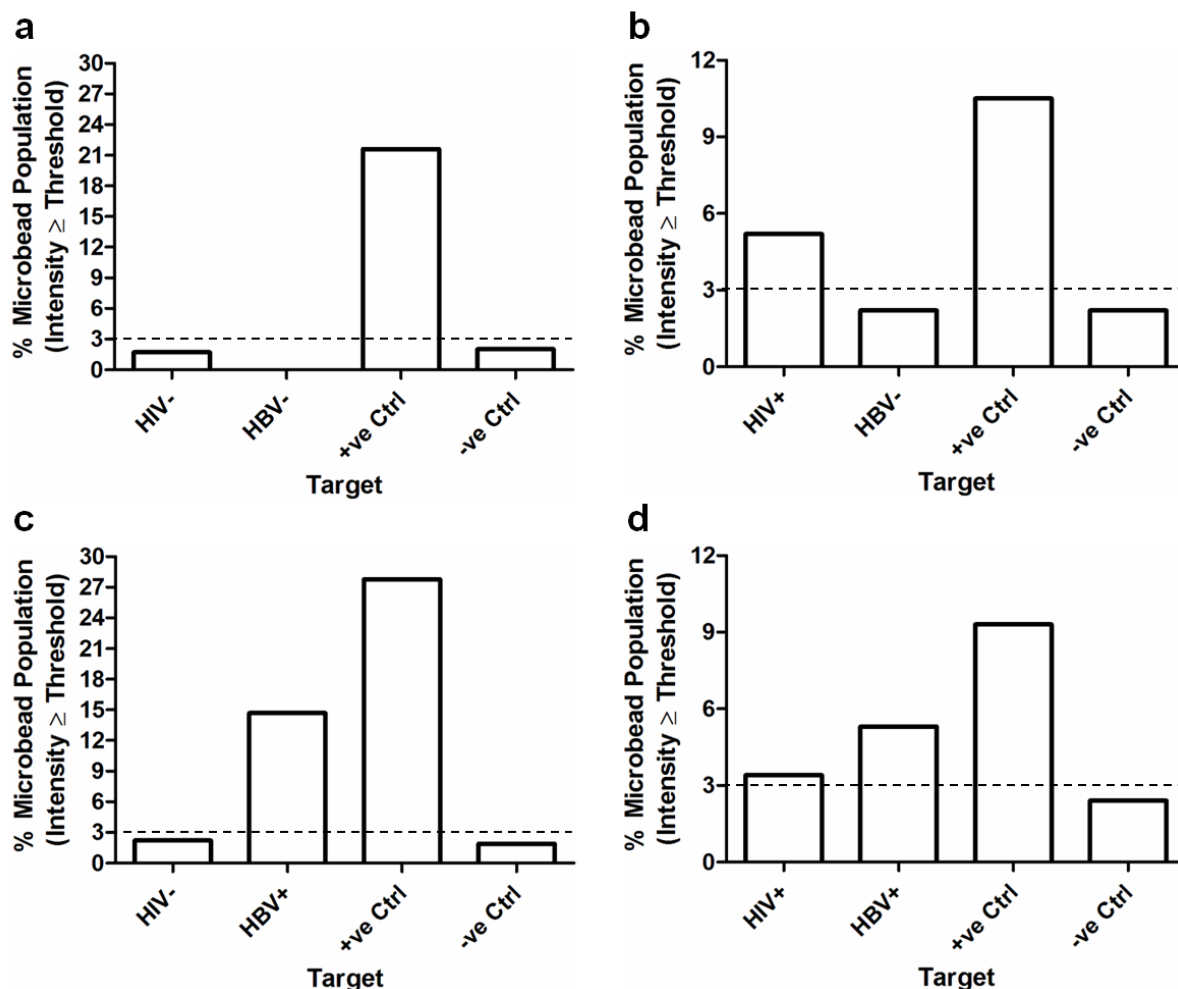
To confirm our device is capable of multiplex detection of patient samples, we mixed 10  $\mu\text{L}$  of each amplified patient samples containing HIV and/or HBV. We performed 4-plex assays (HIV, HBV, as well as positive and negative controls), and the results of which clearly demonstrated that the device is capable of differentiating between the two viruses (**Figure 5.14**). These results were confirmed again using flow cytometry (**Figure 5.15**). Our clinical validation with real-world HBV- and HIV-infected patient samples demonstrates the effectiveness of the proposed detection platform for diagnosing infectious diseases in point-of-care settings.

### 3.3.3 Clinical Sample Sensitivity and Specificity

From the clinical mono-infection and co-infection results shown above, the highest measurable *analytical* sensitivity is 0.24 aM (i.e.  $1.2 \times 10^{-23}$  mol / 50  $\mu\text{L}$ ) after amplification with high *analytical* specificity (i.e. low cross-reactivity). Furthermore, since no false positives or negatives were detected, the *clinical* sensitivity and specificity would be 100%. However, due to the limited number of samples tested (13 for HIV and 10 for HBV), these values are not good representations of the device's clinical capabilities. To better characterize the device's clinical sensitivity and specificity, and establish their optimal values using a Receiver Operating Characteristics curve, a large number of clinical samples (e.g. in the neighbourhood of at least 100 subjects) will need to be tested in a future study.

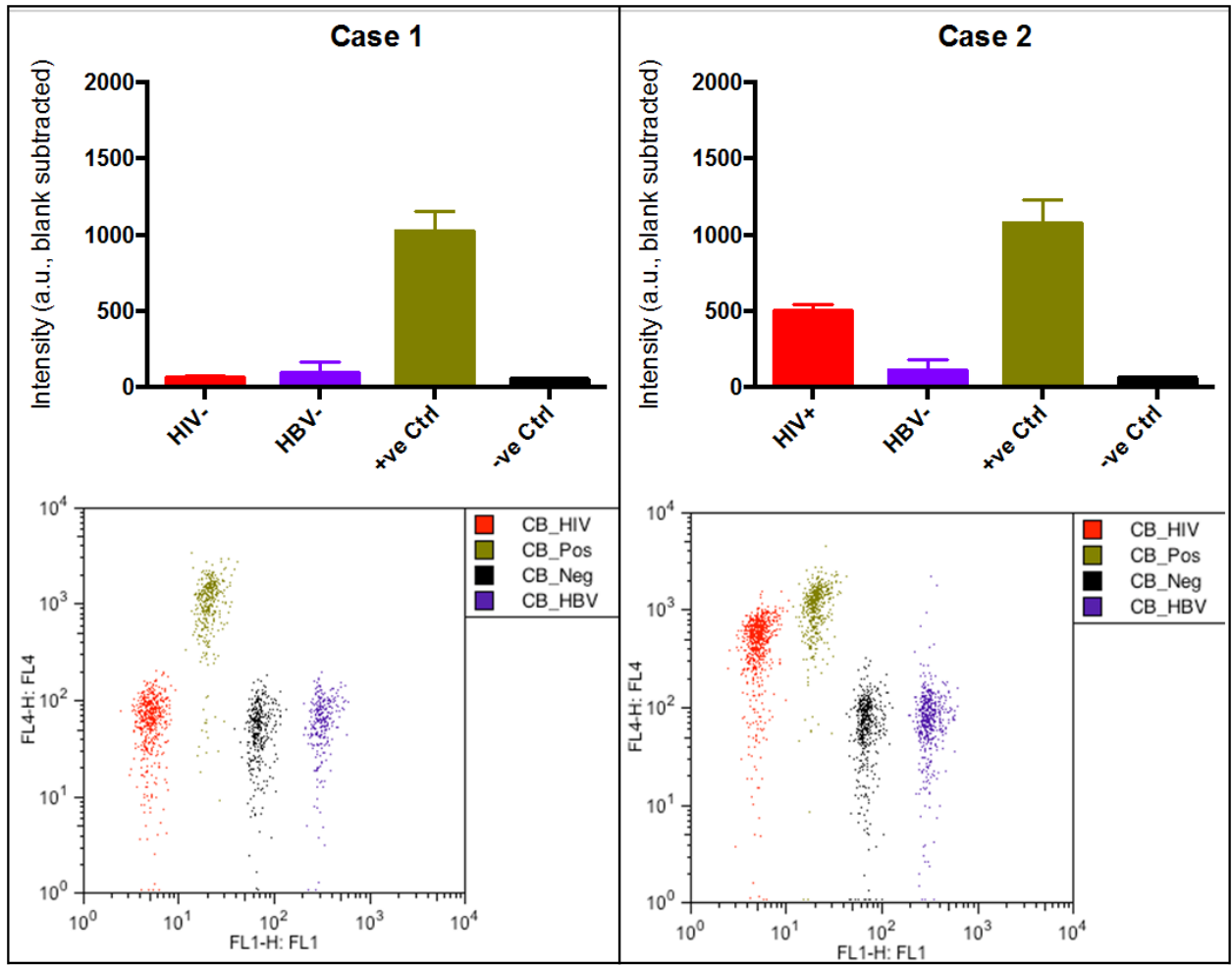
### 3.3.4 Base Pair Mismatches

Finally, we investigated the level of genetic specificity with our genetic assay by sequencing the 10 HIV and 7 HBV patient samples (**Figure 5.16**). We found that there were 3 to 4 and 5 to 9 mismatches within the HIV and HBV probe-binding regions used for the assay, respectively. Although we acknowledge that we have only used wild-type probes to detect patient samples in this thesis, we believe that the level of specificity can be further improved to detect single base pair mismatch by following approach of Liong and co-workers. They used mutant probes that were designed specifically to match mutated region and therefore bind stronger with mutated target than the wild-type target<sup>137</sup>. The development of our device for diagnosing single-nucleotide polymorphisms was not a focus here but will be studied in the future.



**Figure 5.14. Detection of HIV and HBV clinical co-infections.**

Demonstrations of co-infection detection of clinical HIV and HBV DNA targets, as well as synthetic positive and negative control synthetic targets. (a) Only positive control was present during hybridization. (b) HIV-positive patient sample and positive control were present during hybridization. (c) HBV-positive patient sample and positive control were present during hybridization. (d) HIV- and HBV-positive patient samples, and positive control, were present during hybridization. Results represent data from three replications of each condition combined into a single data set. Note that samples above the dashed 3% line are considered positive detection, otherwise they are considered negative detection. All samples were amplified. Figure created by the author. Reprinted (adapted) with permission from source<sup>113</sup>. Copyright 2015 American Chemical Society.



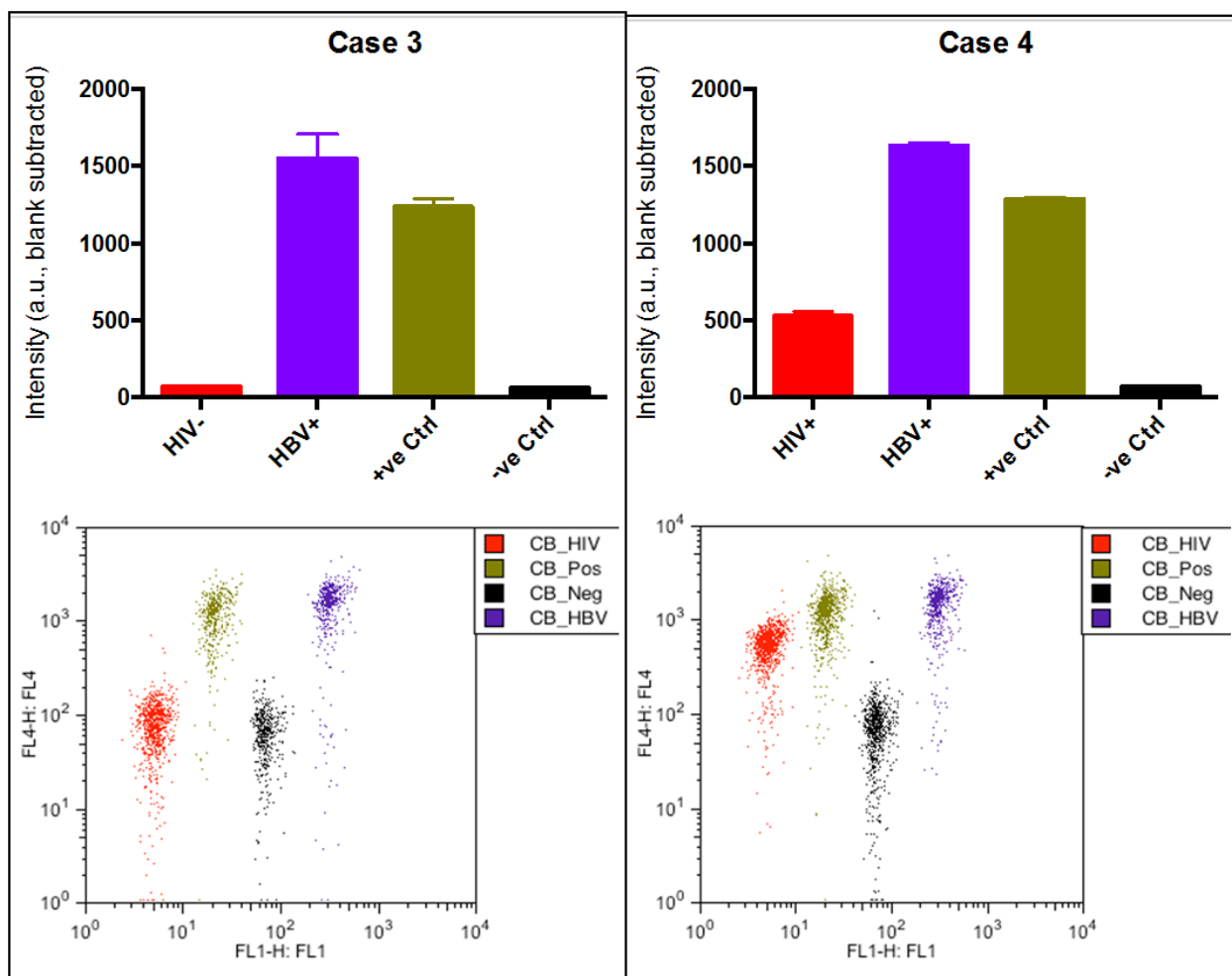


**Figure 5.15. Detection of HIV and HBV clinical co-infections in solution.**

The use of flow cytometry to verify the HBV/HIV multiplexed assay. (Case 1) Only positive control DNA was present during hybridization. (Case 2) Targets for HIV and positive control were present during hybridization. (Case 3) Targets for HBV and positive control were present during hybridization. (Case 4) Targets for HIV, HBV and positive control were present during hybridization. All error bars represent standard error of the mean of experimental triplicates. Figure created by **J. Kim**. Reprinted (adapted) with permission from source<sup>113</sup>. Copyright 2015 American Chemical Society



## 4 Chapter Summary

In this chapter, we described the design and construction of a smartphone-based point-of-care infectious disease diagnostic device that utilized our quantum dot barcode chip for genetic testing. It was validated using synthetic as well as clinical samples (post-RPA), from patients of HIV and HBV. Furthermore, both mono- and co-infection detection were performed to ensure that the device can be used in clinical multiplexing. In addition to these pathogens our device, due to the versatility of quantum dot barcodes, could be extended to develop molecular testing panels for other important pathogens underlying sexually transmitted infections, malaria, influenzas A and B, and tuberculosis by simply modifying the barcode recognition molecules to the target of choice.

## 5 Author Contributions

The experiments were designed by **K. Ming** and **W.C.W. Chan**. Experiments were performed by **D. Li** (quantum dot synthesis), **A. Lam** (quantum dot barcode synthesis), **A. Syed** (barcode conjugation and validation, sensitivity and multiplexing assays), **M.J. Biondi** (clinical sample extraction and preparation), **M. Ostrowski** (PCR), **J. Kim** (sensitivity and multiplexing assays, RPA, solution-based assay, flow cytometry), and **K. Ming** (all others). Analyses were performed by **J. Kim** (solution assays) and **K. Ming** (all others). Device was designed and constructed by **K. Ming**. Algorithms were written by **K. Ming**. The manuscript from which this chapter was adapted was written by **K. Ming**, with major contributions from **J. Kim**, **M.J. Biondi**, **A. Rebbapragada**, **J.J. Feld**, and **W.C.W. Chan**.

## Chapter 6

### Summary & Future Directions

#### 1 Summary

Modern medicine and improved sanitation have drastically lowered the incidences of infectious diseases around the world. However, much more is required to control and potentially eradicate them. For rapidly spreading pathogens, speedy implementation of infection control measures and enhanced surveillance to curb the spread of disease will be critical. To achieve this, an effective means of diagnostics at the point-of-care is paramount. This thesis illustrated one such device that combines quantum dot barcodes with smartphone technology, integrating the capabilities of multiplexed molecular diagnosis with portability and wireless transmission. First we demonstrated the superiority of quantum dot barcodes compared to those incorporating traditional fluorophores with regards to their absorption/excitation and emission spectra, emission under varying excitation, resistance to photobleaching, and single-source fluorescence imaging. Next, we functionalized and characterized them on a microwell chip-based platform in order to improve transportability and ease of handling, and developed a custom-made algorithm to identify and resolve up to nine different barcodes with 95% accuracy using an imaging-based approach. Building on this, we developed and optimized genetic assays performed directly over top of the barcode chip, demonstrated the ability to perform our imaging analysis using smartphone images, and characterized the assays' analytical sensitivity (10-50 fmol) and validated the platform's multiplexing capabilities using five types of infectious diseases. Finally, combining all these, we constructed a portable smartphone-based device and validated it using seven synthetic samples (H1N1, H3N2, H5N1 of type A influenza; type B influenza; HIV, and hepatitis B and C) before demonstrating its ability to detect HIV/HBV mono- and co-infections from clinical samples.

#### 2 Significance

There has been a surge in publications in recent years pertaining to cell phone or smartphone-based diagnostics. This is because these mobile devices, which are widely available, enable diagnostics to be performed in even remote regions of the world, which in turn reduces the need for clinicians and/or large diagnostic infrastructures. The ability for wireless transmission further



allows the sharing of information pertaining to diagnoses, vastly increasing infection control potentials. However, a key difference in our current proposed system is that we have integrated a versatile molecular diagnostic platform of the quantum dot barcodes, with the imaging and wireless capabilities of a smartphone. Moreover this study describes the first quantitative analysis of detecting multiple genomic targets based on smartphone camera imaging of optical signals from different wavelengths and sources (i.e. quantum dot barcodes and fluorescent secondary probe). This is followed by analysis using a custom-made algorithm that can differentiate the barcodes' optical signals, and quantify the amount of the probe bound to the microbead surface. In a clinical setting, following standard sample collection procedures, there are only four steps in our assay: (1) extraction of the genetic target, (2) amplification of the target and denaturation, (3) recognition and hybridization to barcodes on chip and secondary probe, and (4) readout of the chip optical signal with the smartphone (**Figure 6.1**). Compared to other diagnostic technologies found in literature (**Table 6.1**), the proposed system has comparable analytical sensitivity and speed, while being portable, economical, and able to perform multiplexed detection. And compared to other mobile phone-based technologies, to our knowledge, this is the first study to demonstrate the use of a smartphone for quantum dot barcode readout, as well as for molecular detection of multiple diseases simultaneously from patient sample.

### 3 Future Directions

Having provided a proof-of-concept device in this thesis, future work will focus on studying and improving the various components of the systems. In terms of the assay, our group will or have been focused on improving/simplifying the sample preparation, analytical sensitivity or amplification process (worked on by Dr. Kun Chen, Jisung Kim), barcode transport and storage (work in progress by Buddhisha Udugama), and the overall assay process (worked on by Albert Lam). In parallel to these, we will also be conducting a clinical trial with greater sample size in order to establish the optimal clinical sensitivity and specificity, as described previously (work in progress by Pranav Kadhireshan). Regarding hardware engineering, we will improve upon the imaging quality of the sample images (work in progress by Pranav Kadhireshan). And although we have conducted our studies using a specific brand of smartphone, the concept lends itself to further device engineering such that it can physically accommodate any cell phone or smartphone (work in progress by Pranav Kadhireshan). Finally, to make the device as easy to use

as possible, a packaged analysis program and/or smartphone app software will need to be written. Ultimately, we envision a final blackbox unit containing all of the necessary components, integrating the various steps of the assay with specific chambers for each (**Figure 6.2**). Furthermore, each compartment would contain disposable lyophilized samples that can be dissolved by buffers, and transferred from one compartment to the next using capillaries and electrically-driven flow. Constructing such a single unit device is conventionally done as technologies advance from academic development to commercial use once each step in the process has been confirmed to work as design. The device may also be custom-designed for different types of target molecules and the number of chambers in the device can be engineered according to the target molecule. For example, this device could also screen for proteomic targets, and detect and profile other diseases such as cancer and heart disease.

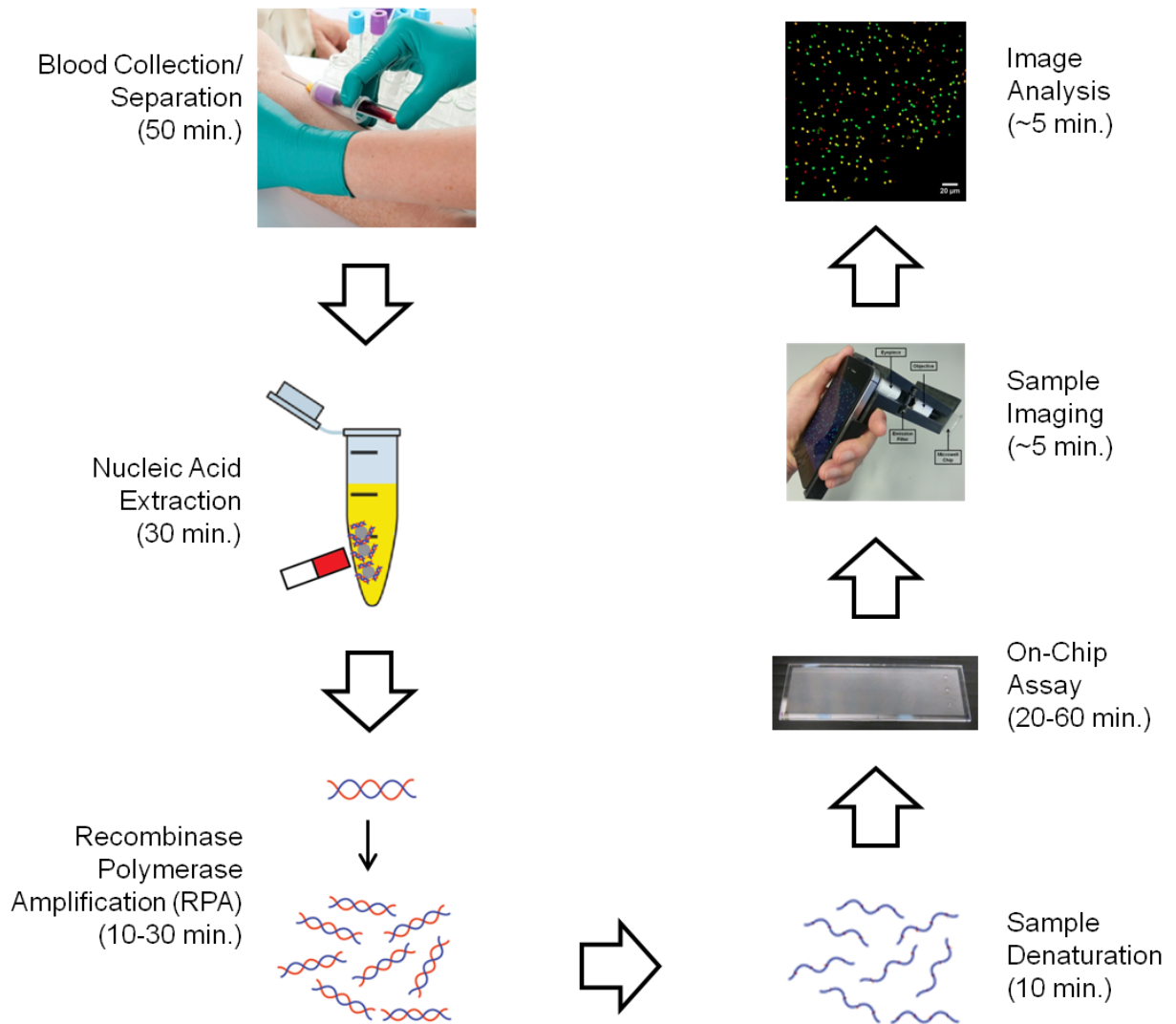


**Figure 6.1. Device procedures flow chart.**

Flow chart illustrating the overall procedure from sample acquisition to final readout. The entire process takes 2-3 hours. First image adopted from (<http://www.turnerlawoffices.com/dui/bac-testing-in-tennessee/blood-test/>).

**Table 6.1. Comparison of Diagnostic Technologies and the Proposed System.**

<b>Platform</b>	<b>Sensitivity Range</b>	<b>Speed (Assay + Readout)</b>	<b>Portable</b>	<b>Simple to Use</b>	<b>Multiplexing</b>
Paper <sup>43,44</sup>	mM – nM	10-60 min.	Yes	Yes	No
Lateral Flow <sup>15,43,45,46</sup>	nM – pM	20-30 min.	Yes	Yes	No
Microfluidics <sup>33,47-49</sup>	nM – fM	20-60 min.	No	No	Yes
Flow Cytometry <sup>29,50-53</sup>	pM – fM	20-60 min.	No	No	Yes
Microarray <sup>19,54,55</sup>	pM – fM	2-3 hr.	No	No	Yes
Fibre Optics <sup>25,56,57</sup>	fM – zM	2-3 hr.	No	No	Yes
PCR <sup>58-60</sup>	aM – zM	2-3 hr.	No	No	Yes
Proposed System	1 nM (Synthetic)  0.24 aM (Clinical)	30 min. (Synthetic)  2 hr. (Clinical)	Yes	Yes	Yes

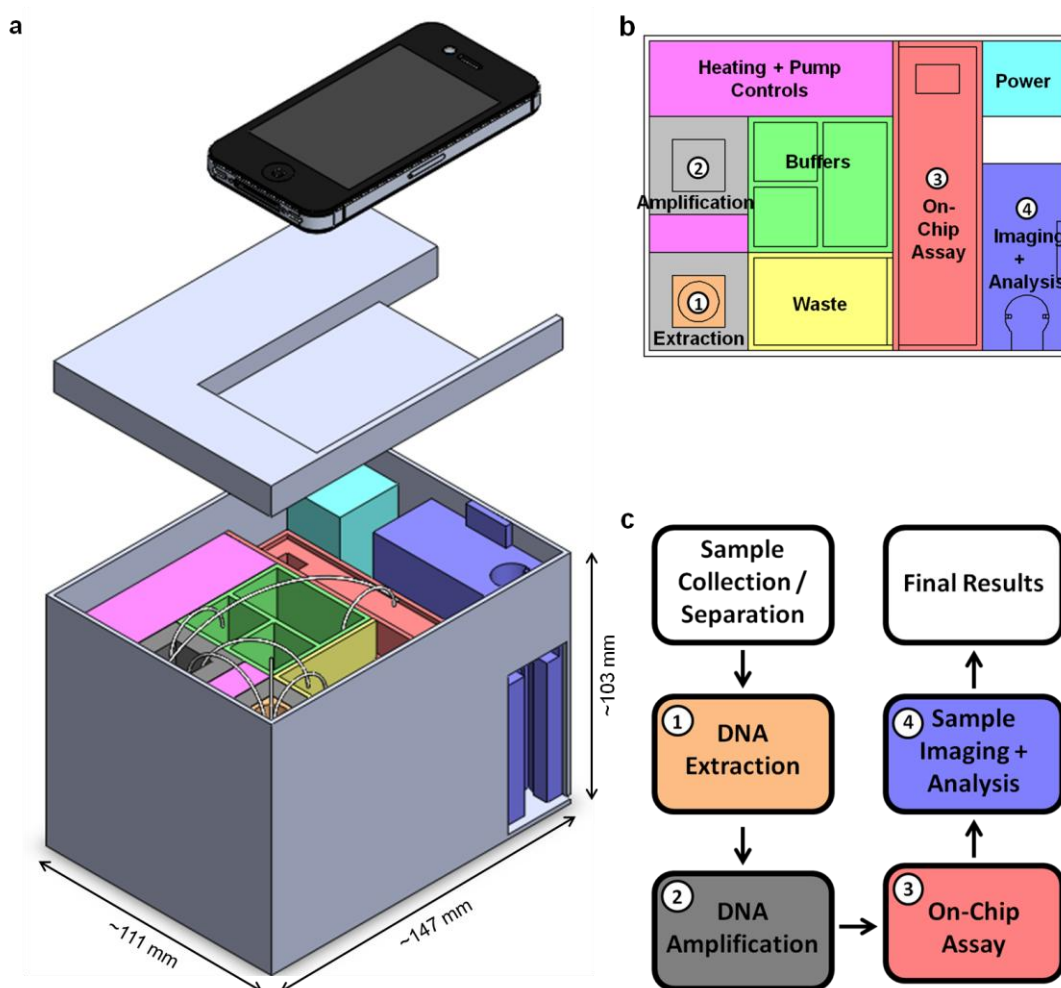


**Figure 6.2. Envisioned diagnostic unit.**

(a) A visual representation of the envisioned final device, with the different compartments coloured for clarity, capillary tubes to show the flow of solutions between them, and a smartphone for scale. (b) Schematics of the envisioned final device with colors matching the various compartments in (a) and numbers indicating the movement of sample in these compartments. (c) A flow diagram illustrating the steps required for detecting pathogen targets using the envisioned final device, from patient sample to imaging and analysis, with colors and numbers matching the compartments in (a) and (b). The liquid can be moved from one compartment to the next using electrically-driven flow. Figure created by the author. Reprinted (adapted) with permission from source<sup>113</sup>. Copyright 2015 American Chemical Society.

## References

1. World Health Organization. Infectious Diseases. at [http://www.who.int/topics/infectious\\_diseases/en/](http://www.who.int/topics/infectious_diseases/en/)
2. Fauci, A. S., Touchette, N. A. & Folkers, G. K. Emerging infectious diseases: a 10-year perspective from the National Institute of Allergy and Infectious Diseases. *Emerg. Infect. Dis.* **11**, 519–25 (2005).
3. Jones, K. E. *et al.* Global trends in emerging infectious diseases. *Nature* **451**, 990–3 (2008).
4. Hauck, T. S., Giri, S., Gao, Y. & Chan, W. C. W. Nanotechnology diagnostics for infectious diseases prevalent in developing countries. *Adv. Drug Deliv. Rev.* **62**, 438–48 (2010).
5. Ebola in graphics: The toll of a tragedy. *Econ.* (2014). at <http://www.economist.com/blogs/graphicdetail/2014/12/ebola-graphics>
6. Ebola virus epidemic in West Africa. *Wikipedia* (2015). at [http://en.wikipedia.org/wiki/Ebola\\_virus\\_epidemic\\_in\\_West\\_Africa](http://en.wikipedia.org/wiki/Ebola_virus_epidemic_in_West_Africa)
7. World Health Organization. Urgently needed: rapid, sensitive, safe and simple Ebola diagnostic tests. (2014). at <http://www.who.int/mediacentre/news/ebola/18-november-2014-diagnostics/en/>
8. Hartman, M. R. *et al.* Point-of-care nucleic acid detection using nanotechnology. *Nanoscale* **5**, 10141–54 (2013).
9. Kingsmore, S. F. Multiplexed protein measurement: technologies and applications of protein and antibody arrays. *Nat. Rev. Drug Discov.* **5**, 310–20 (2006).
10. Wongsrichanalai, C., Barcus, M. J., Muth, S., Sutamihardja, A. & Wernsdorfer, W. H. A Review of Malaria Diagnostic Tools : Microscopy and Rapid Diagnostic Test ( RDT ). **77**, 119–127 (2007).

11. Engvall, E. & Perlmann, P. ENZYME-LINKED IMMUNOSORBENT ASSAY, ELISA. *J. Immunology* **109**, 129–135 (1972).
12. Voller, a, Bartlett, a, Bidwell, D. E., Clark, M. F. & Adams, a N. The detection of viruses by enzyme-linked immunosorbent assay (ELISA). *J. Gen. Virol.* **33**, 165–7 (1976).
13. Corstjens, P. L. a M. *et al.* Lateral-flow and up-converting phosphor reporters to detect single-stranded nucleic acids in a sandwich-hybridization assay. *Anal. Biochem.* **312**, 191–200 (2003).
14. Ngom, B., Guo, Y., Wang, X. & Bi, D. Development and application of lateral flow test strip technology for detection of infectious agents and chemical contaminants: a review. *Anal. Bioanal. Chem.* **397**, 1113–35 (2010).
15. Qiu, W. *et al.* Carbon nanotube-based lateral flow biosensor for sensitive and rapid detection of DNA sequence. *Biosens. Bioelectron.* **64C**, 367–372 (2014).
16. Hughes, T. R. *et al.* Expression profiling using microarrays fabricated by an ink-jet oligonucleotide synthesizer. *Nat. Biotechnol.* **19**, 342–7 (2001).
17. Wang, D. *et al.* Microarray-based detection and genotyping of viral pathogens. *Proc. Natl. Acad. Sci. U. S. A.* **99**, 15687–92 (2002).
18. Kim, D., Daniel, W. L. & Mirkin, C. a. Microarray-based multiplexed scanometric immunoassay for protein cancer markers using gold nanoparticle probes. *Anal. Chem.* **81**, 9183–7 (2009).
19. Zheng, Z., Wu, Y., Yu, X. & Shang, S. DNA Microarray Technology for Simultaneous Detection and Species Identification of Seven Human Herpes Viruses. *J. Med. Virol.* **80**, 1042–1050 (2008).
20. Drosten, C. *et al.* Identification of a novel coronavirus in patients with severe acute respiratory syndrome. *N. Engl. J. Med.* **348**, 1967–76 (2003).

21. Sanchez, J. A., Pierce, K. E., Rice, J. E. & Wang, L. J. Linear-after-the-exponential (LATE)-PCR: an advanced method of asymmetric PCR and its uses in quantitative real-time analysis. *Proc. Natl. Acad. Sci. U. S. A.* **101**, 1933–8 (2004).
22. Vetter, E. A., Yao, J. D. C., Wengenack, N. L., Iii, F. R. C. & Smith, T. F. Real-Time PCR in Clinical Microbiology: Applications for Routine Laboratory Testing. *Clin. Microbiol. Rev.* **19**, 165–256 (2006).
23. Walt, D. Bead-based fiber-optic arrays. *Science*. **287**, 451–452 (2000).
24. Walt, D. R. Fibre optic microarrays. *Chem. Soc. Rev.* **39**, 38–50 (2010).
25. Li, Z., Hayman, R. B. & Walt, D. R. Detection of single-molecule DNA hybridization using enzymatic amplification in an array of femtoliter-sized reaction vessels. *J. Am. Chem. Soc.* **130**, 12622–3 (2008).
26. Jani, I. V, Janossy, G., Brown, D. W. G. & Mandy, F. Multiplexed immunoassays by flow cytometry for diagnosis and surveillance of infectious diseases in resource-poor settings. *Lancet* **2**, 243–250 (2002).
27. Yan, X. *et al.* Multiplexed Flow Cytometric Immunoassay for Influenza Virus Detection and Differentiation. *Anal. Chem.* **77**, 7673–7678 (2005).
28. Deng, W., Drozdowicz-Tomsia, K., Jin, D. & Goldys, E. M. Enhanced flow cytometry-based bead immunoassays using metal nanostructures. *Anal. Chem.* **81**, 7248–55 (2009).
29. Giri, S., Sykes, E. A., Jennings, T. L. & Chan, W. C. W. Rapid screening of genetic biomarkers of infectious agents using quantum dot barcodes. *ACS Nano* **5**, 1580–7 (2011).
30. Sia, S. K., Linder, V., Parviz, B. A., Siegel, A. & Whitesides, G. M. An integrated approach to a portable and low-cost immunoassay for resource-poor settings. *Angew. Chem. Int. Ed. Engl.* **43**, 498–502 (2004).
31. Yager, P. *et al.* Microfluidic diagnostic technologies for global public health. *Nature* **442**, 412–8 (2006).



32. Chin, C. D. *et al.* Microfluidics-based diagnostics of infectious diseases in the developing world. *Nat. Med.* **17**, 1015–9 (2011).
33. Zhang, H., Xu, T., Li, C.-W. & Yang, M. A microfluidic device with microbead array for sensitive virus detection and genotyping using quantum dots as fluorescence labels. *Biosens. Bioelectron.* **25**, 2402–7 (2010).
34. Martinez, A. W., Phillips, S. T. & Whitesides, G. M. Three-dimensional microfluidic devices fabricated in layered paper and tape. *Proc. Natl. Acad. Sci. U. S. A.* **105**, 19606–11 (2008).
35. Martinez, A. W., Phillips, S. T., Whitesides, G. M. & Carrilho, E. Diagnostics for the developing world: microfluidic paper-based analytical devices. *Anal. Chem.* **82**, 3–10 (2010).
36. Fu, E. *et al.* Enhanced sensitivity of lateral flow tests using a two-dimensional paper network format. *Anal. Chem.* **83**, 7941–7946 (2011).
37. Cheng, C.-M. *et al.* Paper-based ELISA. *Angew. Chem. Int. Ed. Engl.* **49**, 4771–4 (2010).
38. Chin, C. D., Linder, V. & Sia, S. K. Lab-on-a-chip devices for global health: past studies and future opportunities. *Lab Chip* **7**, 41–57 (2007).
39. Giljohann, D. a & Mirkin, C. a. Drivers of biodiagnostic development. *Nature* **462**, 461–4 (2009).
40. El Ekiaby, M., Lelie, N. & Allain, J.-P. Nucleic acid testing (NAT) in high prevalence-low resource settings. *Biologicals* **38**, 59–64 (2010).
41. Zou, Z. *et al.* Quantum dot-based immunochromatographic fluorescent biosensor for biomonitoring trichloropyridinol, a biomarker of exposure to chlorpyrifos. *Anal. Chem.* **82**, 5125–33 (2010).
42. Xu, Y. *et al.* Fluorescent probe-based lateral flow assay for multiplex nucleic acid detection. *Anal. Chem.* **86**, 5611–4 (2014).

43. Hu, J. *et al.* Advances in paper-based point-of-care diagnostics. *Biosens. Bioelectron.* **54**, 585–597 (2014).
44. Ge, X. *et al.* Nanomaterial-enhanced paper-based biosensors. *TrAC - Trends Anal. Chem.* **58**, 31–39 (2014).
45. Yetisen, A. K., Akram, M. S. & Lowe, C. R. Paper-based microfluidic point-of-care diagnostic devices. *Lab Chip* **13**, 2210–51 (2013).
46. Pelton, R. Bioactive paper provides a low-cost platform for diagnostics. *TrAC - Trends Anal. Chem.* **28**, 925–942 (2009).
47. Nahavandi, S. *et al.* Microfluidic platforms for biomarker analysis. *Lab Chip* **14**, 1496–514 (2014).
48. Song, Y. *et al.* Point-of-care technologies for molecular diagnostics using a drop of blood. *Trends Biotechnol.* **32**, 132–139 (2014).
49. Kang, D. K., Monsur Ali, M., Zhang, K., Pone, E. J. & Zhao, W. Droplet microfluidics for single-molecule and single-cell analysis in cancer research, diagnosis and therapy. *TrAC - Trends Anal. Chem.* **58**, 145–153 (2014).
50. Gao, Y., Stanford, W. L. & Chan, W. C. W. Quantum-dot-encoded microbeads for multiplexed genetic detection of non-amplified DNA samples. *Small* **7**, 137–46 (2011).
51. Thiollot, S., Bessant, C. & Morgan, S. L. Application of multiple response optimization design to quantum dot-encoded microsphere bioconjugates hybridization assay. *Anal. Biochem.* **414**, 23–30 (2011).
52. Ozanich, R. M. *et al.* Rapid multiplexed flow cytometric assay for botulinum neurotoxin detection using an automated fluidic microbead-trapping flow cell for enhanced sensitivity. *Anal. Chem.* **81**, 5783–93 (2009).
53. Krishnan, V. V, Khan, I. H. & Luciw, P. a. Multiplexed microbead immunoassays by flow cytometry for molecular profiling: Basic concepts and proteomics applications. *Crit. Rev. Biotechnol.* **29**, 29–43 (2009).

54. Cretich, M., Bagnati, M., Damin, F., Sola, L. & Chiari, M. Overcoming mass transport limitations to achieve femtomolar detection limits on silicon protein microarrays. *Anal. Biochem.* **418**, 164–166 (2011).
55. Duer, R., Lund, R., Tanaka, R., Christensen, D. a & Herron, J. N. In-Plane Parallel Scanning: A Microarray Technology for Point-of-Care Testing. *Anal. Chem.* **82**, 8856–8865 (2010).
56. Rissin, D. M. *et al.* Single-molecule enzyme-linked immunosorbent assay detects serum proteins at subfemtomolar concentrations. *Nat. Biotechnol.* **28**, 595–599 (2010).
57. Blicharz, T. M. *et al.* Fiber-optic microsphere-based antibody array for the analysis of inflammatory cytokines in saliva. *Anal. Chem.* **81**, 2106–14 (2009).
58. Miao, P., Tang, Y., Wang, B., Yin, J. & Ning, L. Signal amplification by enzymatic tools for nucleic acids. *TrAC Trends Anal. Chem.* **67**, 1–15 (2015).
59. Bustin, S. a & Mueller, R. Real-time reverse transcription PCR (qRT-PCR) and its potential use in clinical diagnosis. *Clin. Sci. (Lond)*. **109**, 365–379 (2005).
60. Mackay, I. M., Arden, K. E. & Nitsche, A. Real-time PCR in virology. *Nucleic Acids Res.* **30**, 1292–1305 (2002).
61. International Telecommunication Union. International Telecommunication Union Statistics. at <[http://www.itu.int/en/ITU-D/Statistics/Documents/statistics/2014/ITU\\_Key\\_2005-2014\\_ICT\\_data.xls](http://www.itu.int/en/ITU-D/Statistics/Documents/statistics/2014/ITU_Key_2005-2014_ICT_data.xls)>
62. Data and development: Off the map. *Econ.* (2014). at <<http://www.economist.com/news/international/21632520-rich-countries-are-deluged-data-developing-ones-are-suffering-drought>>
63. Wesolowski, A. *et al.* Commentary: Containing the Ebola Outbreak - the Potential and Challenge of Mobile Network Data. *PLoS Curr.* 1–17 (2014). doi:10.1371/currents.outbreaks.0177e7fcf52217b8b634376e2f3efc5e

64. Zhu, H., Isikman, S. O., Mudanyali, O., Greenbaum, A. & Ozcan, A. Optical imaging techniques for point-of-care diagnostics. *Lab Chip* **13**, 51–67 (2013).
65. Preechaburana, P., Suska, A. & Filippini, D. Biosensing with cell phones. *Trends Biotechnol.* **32**, 351–5 (2014).
66. Breslauer, D. N., Maamari, R. N., Switz, N. a, Lam, W. a & Fletcher, D. a. Mobile phone based clinical microscopy for global health applications. *PLoS One* **4**, e6320 (2009).
67. Wei, Q. *et al.* Fluorescent Imaging of Single Nanoparticles and Viruses on a Smart-Phone. *ACS Nano* (2013). doi:10.1021/nn4037706
68. Zhu, H., Mavandadi, S., Coskun, A. F., Yaglidere, O. & Ozcan, A. Optofluidic fluorescent imaging cytometry on a cell phone. *Anal. Chem.* **83**, 6641–7 (2011).
69. Zhu, H., Yaglidere, O., Su, T.-W., Tseng, D. & Ozcan, A. Cost-effective and compact wide-field fluorescent imaging on a cell-phone. *Lab Chip* **11**, 315–22 (2011).
70. Zhu, H. *et al.* Cost-effective and rapid blood analysis on a cell-phone. *Lab Chip* **13**, 1282–8 (2013).
71. Mudanyali, O. *et al.* Integrated rapid-diagnostic-test reader platform on a cellphone. *Lab Chip* (2012). doi:10.1039/c2lc40235a
72. Wang, S. *et al.* Integration of cell phone imaging with microchip ELISA to detect ovarian cancer HE4 biomarker in urine at the point-of-care. *Lab Chip* **11**, 3411–8 (2011).
73. Stedtfeld, R. D. *et al.* Gene-Z: a device for point of care genetic testing using a smartphone. *Lab Chip* **12**, 1454–62 (2012).
74. Preechaburana, P., Gonzalez, M. C., Suska, A. & Filippini, D. Surface Plasmon Resonance Chemical Sensing on Cell Phones. *Angew. Chem. Int. Ed. Engl.* 11585–11588 (2012). doi:10.1002/anie.201206804
75. Fournier-Bidoz, S. *et al.* Facile and rapid one-step mass preparation of quantum-dot barcodes. *Angew. Chem. Int. Ed. Engl.* **47**, 5577–81 (2008).

76. Klostranec, J. M. *et al.* Convergence of quantum dot barcodes with microfluidics and signal processing for multiplexed high-throughput infectious disease diagnostics. *Nano Lett.* **7**, 2812–8 (2007).
77. Gao, Y., Lam, A. W. Y. & Chan, W. C. W. Automating Quantum Dot Barcode Assays Using Microfluidics and Magnetism for the Development of a Point-of-Care Device. (2013).
78. Korteweg, C. & Gu, J. Pandemic influenza A (H1N1) virus infection and avian influenza A (H5N1) virus infection: a comparative analysis. *Biochem. Cell Biol.* **88**, 575–87 (2010).
79. Smith, G. J. D. *et al.* Dating the emergence of pandemic influenza viruses. *Proc. Natl. Acad. Sci. U. S. A.* **106**, 11709–12 (2009).
80. Yamada, S. *et al.* Haemagglutinin mutations responsible for the binding of H5N1 influenza A viruses to human-type receptors. *Nature* **444**, 378–82 (2006).
81. Russell, C. J. & Webster, R. G. The genesis of a pandemic influenza virus. *Cell* **123**, 368–71 (2005).
82. Barr, I. G. *et al.* Epidemiological, antigenic and genetic characteristics of seasonal influenza A(H1N1), A(H3N2) and B influenza viruses: basis for the WHO recommendation on the composition of influenza vaccines for use in the 2009-2010 Northern Hemisphere season. *Vaccine* **28**, 1156–67 (2010).
83. Lindstrom, S. *et al.* Human infections with novel reassortant influenza A(H3N2)v viruses, United States, 2011. *Emerg. Infect. Dis.* **18**, 834–7 (2012).
84. World Health Organization. Influenza vaccine viruses and reagents. at <<http://www.who.int/influenza/vaccines/virus/en/>>
85. Yerly, S. *et al.* Nosocomial outbreak of multiple bloodborne viral infections. *J. Infect. Dis.* **184**, 369–72 (2001).

86. Chu, C. *et al.* Hepatitis C : Comparison with acute hepatitis B - Comparison of clinical, virologic and pathologic features in patients with acute hepatitis B and C. *J. Gastroenterol. Hepatol.* **16**, 209–214 (2001).
87. Brook, M. G. Sexual transmission and prevention of the hepatitis viruses A-E and G. *Sex. Transm. Infect.* **74**, 395–398 (1998).
88. Kane, A., Lloyd, J., Zaffran, M., Simonsen, L. & Kane, M. Transmission of hepatitis B , hepatitis C and human immunodeficiency virus through unsafe injections in the developing world: model-based regional estimates. *Bull. World Health Organ.* **77**, 801–807 (1999).
89. Freitag-Koontz, M. J. Prevention of Hepatitis B and C Transmission during Pregnancy and the First Year of Life. *J. Perinat. Neonatal Nurs.* **10**, 40–55 (1996).
90. Hogben, M. & Kachur, R. Internet partner notification: another arrow in the quiver. *Sex. Transm. Dis.* **35**, 117–8 (2008).
91. Hogben, M., McNally, T., McPheeters, M. & Hutchinson, A. B. The effectiveness of HIV partner counseling and referral services in increasing identification of HIV-positive individuals a systematic review. *Am. J. Prev. Med.* **33**, S89–100 (2007).
92. Kania, D. *et al.* Combining rapid diagnostic tests and dried blood spot assays for point-of-care testing of human immunodeficiency virus, hepatitis B and hepatitis C infections in Burkina Faso, West Africa. *Clin. Microbiol. Infect.* **19**, E533–41 (2013).
93. Appleyard, D. C., Chapin, S. C. & Doyle, P. S. Multiplexed protein quantification with barcoded hydrogel microparticles. *Anal. Chem.* **83**, 193–9 (2011).
94. Lee, J. *et al.* Universal process-inert encoding architecture for polymer microparticles. *Nat. Mater.* **13**, 524–9 (2014).
95. Lin, C. *et al.* Submicrometre geometrically encoded fluorescent barcodes self-assembled from DNA. *Nat. Chem.* **4**, 832–9 (2012).

96. Li, Q. *et al.* Color-encoded microcarriers based on nano-silicon dioxide film for multiplexed immunoassays. *Analyst* **137**, 3760–6 (2012).
97. Nam, J.-M., Thaxton, C. S. & Mirkin, C. a. Nanoparticle-based bio-bar codes for the ultrasensitive detection of proteins. *Science* **301**, 1884–6 (2003).
98. Chung, H. J., Castro, C. M., Im, H., Lee, H. & Weissleder, R. A magneto-DNA nanoparticle system for rapid detection and phenotyping of bacteria. *Nat. Nanotechnol.* **8**, 369–75 (2013).
99. Han, M., Gao, X., Su, J. Z. & Nie, S. Quantum-dot-tagged microbeads for multiplexed optical coding of biomolecules. *Nat. Biotechnol.* **19**, 631–5 (2001).
100. Wang, G. *et al.* Highly Efficient Preparation of Multi-Scaled Quantum Dot Barcodes for Multiplexed Hepatitis B Detection. *ACS Nano* (2012). doi:10.1021/nn3045215
101. Klostranec, J. M. & Chan, W. C. W. Quantum Dots in Biological and Biomedical Research: Recent Progress and Present Challenges. *Adv. Mater.* **18**, 1953–1964 (2006).
102. Alivisatos, P. The use of nanocrystals in biological detection. *Nat. Biotechnol.* **22**, 47–52 (2004).
103. Jin, Z. & Hildebrandt, N. Semiconductor quantum dots for in vitro diagnostics and cellular imaging. *Trends Biotechnol.* **30**, 394–403 (2012).
104. Kairdolf, B. A. *et al.* Semiconductor quantum dots for bioimaging and biodiagnostic applications. *Annu. Rev. Anal. Chem. (Palo Alto. Calif.)* **6**, 143–62 (2013).
105. Morris, S. Translating Cancer Targets into Nanotechnology-based Therapeutics: Accelerating Research Through Collaborations. at <<https://ocg.cancer.gov/news-publications/e-newsletter-issue/issue-11>>
106. Medintz, I. L., Uyeda, H. T., Goldman, E. R. & Mattoussi, H. Quantum dot bioconjugates for imaging, labelling and sensing. *Nat. Mater.* **4**, 435–46 (2005).

107. Boldt, K., Bruns, O. T., Gaponik, N. & Eychmüller, A. Comparative examination of the stability of semiconductor quantum dots in various biochemical buffers. *J. Phys. Chem. B* **110**, 1959–63 (2006).
108. Lee, J. a. *et al.* Toward the Accurate Read-out of Quantum Dot Barcodes: Design of Deconvolution Algorithms and Assessment of Fluorescence Signals in Buffer. *Adv. Mater.* **19**, 3113–3118 (2007).
109. Jennings, T. L., Rahman, K. S., Fournier-Bidoz, S. & Chan, W. C. W. Effects of microbead surface chemistry on DNA loading and hybridization efficiency. *Anal. Chem.* **80**, 2849–56 (2008).
110. Martín-Banderas, L. *et al.* Towards High-Throughput Production of Uniformly Encoded Microparticles. *Adv. Mater.* **18**, 559–564 (2006).
111. Peng, X., Schlamp, M. C., Kadavanich, A. V & Alivisatos, A. P. Epitaxial Growth of Highly Luminescent CdSe / CdS Core / Shell Nanocrystals with Photostability and Electronic Accessibility. *J. Am. Chem. Soc.* **119**, 7019–7029 (1997).
112. Hines, M. A. & Guyot-Sionnest, P. Synthesis and Characterization of Strongly Luminescing ZnS-Capped CdSe Nanocrystals. *J. Phys. Chem.* **100**, 468–471 (1996).
113. Ming, K. *et al.* An Integrated Quantum Dot Barcode Smartphone Optical Device for Wireless Multiplexed Diagnosis of Infected Patients. *ACS Nano* **9**, 3060–3074 (2015).
114. Carrillo-Carrión, C., Cárdenas, S., Simonet, B. M. & Valcárcel, M. Quantum dots luminescence enhancement due to illumination with UV/Vis light. *Chem. Commun. (Camb)*. 5214–26 (2009). doi:10.1039/b904381k
115. Wang, H.-Q. *et al.* A flow cytometric assay technology based on quantum dots-encoded beads. *Anal. Chim. Acta* **580**, 18–23 (2006).
116. Liu, W.-T. *et al.* Microfluidic device as a new platform for immunofluorescent detection of viruses. *Lab Chip* **5**, 1327–30 (2005).



117. Lucas, L. J., Chesler, J. N. & Yoon, J.-Y. Lab-on-a-chip immunoassay for multiple antibodies using microsphere light scattering and quantum dot emission. *Biosens. Bioelectron.* **23**, 675–81 (2007).
118. Riegger, L. *et al.* Read-out concepts for multiplexed bead-based fluorescence immunoassays on centrifugal microfluidic platforms. *Sensors Actuators A Phys.* **126**, 455–462 (2006).
119. Guizar-Sicairos, M., Thurman, S. T. & Fienup, J. R. Efficient subpixel image registration algorithms. *Opt. Lett.* **33**, 156–8 (2008).
120. Guizar-Sicairos, M. Efficient subpixel image registration by cross-correlation. at <http://www.mathworks.com/matlabcentral/fileexchange/18401-efficient-subpixel-image-registration-by-cross-correlation>
121. Ballard, D. H. Generalizing the Hough Transform to detect arbitrary shapes. *Pattern Recognit.* **13**, 111–122 (1981).
122. Peng, T. Detect circles with various radii in grayscale image via Hough Transform. at <http://www.mathworks.com/matlabcentral/fileexchange/9168-detect-circles-with-various-radii-in-grayscale-image-via-hough-transform>
123. Huang, N.-T. *et al.* Multiplexed spectral signature detection for microfluidic color-coded bioparticle flow. *Anal. Chem.* **82**, 9506–12 (2010).
124. Lee, W.-M. *et al.* High-throughput, sensitive, and accurate multiplex PCR-microsphere flow cytometry system for large-scale comprehensive detection of respiratory viruses. *J. Clin. Microbiol.* **45**, 2626–34 (2007).
125. Dunbar, S. a. Applications of Luminex xMAP technology for rapid, high-throughput multiplexed nucleic acid detection. *Clin. Chim. Acta.* **363**, 71–82 (2006).
126. Mahony, J. *et al.* Development of a respiratory virus panel test for detection of twenty human respiratory viruses by use of multiplex PCR and a fluid microbead-based assay. *J. Clin. Microbiol.* **45**, 2965–70 (2007).

127. Song, L., Ahn, S. & Walt, D. R. Fiber-Optic Microsphere-Based Arrays for Multiplexed Biological Warfare Agent Detection. *Anal. Chem.* **78**, 1023–1033 (2006).
128. Agrawal, A., Deo, R., Wang, G. D., Wang, M. D. & Nie, S. Nanometer-scale mapping and single-molecule detection with color-coded nanoparticle probes. *Proc. Natl. Acad. Sci. U. S. A.* **105**, 3298–303 (2008).
129. Dickinson, M. E., Bearman, G., Tille, S., Lansford, R. & Fraser, S. E. Multi-Spectral Imaging and Linear Unmixing Add a Whole New Dimension to Laser Scanning Fluorescence Microscopy. *Biotechniques* **31**, 1272–1278 (2001).
130. Zimmermann, T., Rietdorf, J. & Pepperkok, R. Spectral imaging and its applications in live cell microscopy. *FEBS Lett.* **546**, 87–92 (2003).
131. Levenson, R. M. Spectral Imaging and Pathology: Seeing More. *Lab. Med.* **35**, 244–251 (2004).
132. Reddy, B. S. & Chatterji, B. N. An FFT-Based Technique for Translation, Rotation, and Scale-Invariant Image Registration. *IEEE Trans. Image Process.* **5**, 1266–1271 (1996).
133. Uni, B. & Uni, P. Oleylamine as Both Reducing Agent and Stabilizer in a Facile Synthesis of Magnetite Nanoparticles. *Chem. Mater.* 1778–1780 (2009).
134. Huy, T. T.-T. *et al.* Genotype C of hepatitis B virus can be classified into at least two subgroups. *J. Gen. Virol.* **85**, 283–92 (2004).
135. Stanford University. HBVseq. (2012).
136. Piepenburg, O., Williams, C. H., Stemple, D. L. & Armes, N. a. DNA detection using recombination proteins. *PLoS Biol.* **4**, e204 (2006).
137. Liong, M. *et al.* Magnetic barcode assay for genetic detection of pathogens. *Nat. Commun.* **4**, 1752 (2013).